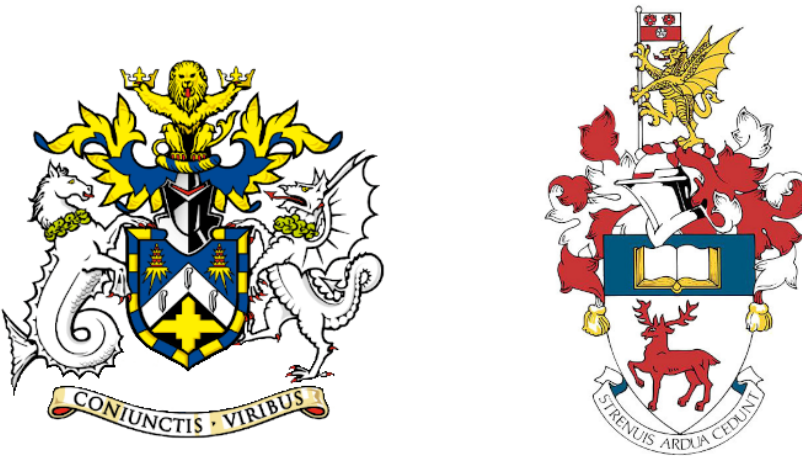


<sup>1</sup> EXPANDING THE PHYSICS REACH  
<sup>2</sup> OF DUNE IN THE NEAR AND  
<sup>3</sup> FAR DETECTORS



<sup>4</sup>

<sup>5</sup> Francisco Martínez López

<sup>6</sup> Submitted in partial fulfillment of the requirements  
<sup>7</sup> of the Degree of Doctor of Philosophy

<sup>8</sup> School of Physical and Chemical Sciences  
<sup>9</sup> Queen Mary University of London

<sup>10</sup> School of Physics and Astronomy  
<sup>11</sup> University of Southampton

<sup>12</sup> December 2024



## Statement of originality

- 14 I, Francisco Martínez López, confirm that the research included within this thesis is my  
15 own work or that where it has been carried out in collaboration with, or supported by  
16 others, that this is duly acknowledged below and my contribution indicated. Previously  
17 published material is also acknowledged below.
- 18 I attest that I have exercised reasonable care to ensure that the work is original, and  
19 does not to the best of my knowledge break any UK law, infringe any third party's  
20 copyright or other Intellectual Property Right, or contain any confidential material.
- 21 I accept that the University has the right to use plagiarism detection software to check  
22 the electronic version of the thesis.
- 23 I confirm that this thesis has not been previously submitted for the award of a degree  
24 by this or any other university.
- 25 The copyright of this thesis rests with the author and no quotation from it or information  
26 derived from it may be published without the prior written consent of the author.
- 27 Signature: [can be digital signature]
- 28 Date:
- 29 Details of collaboration and publications:  
30 [insert details here if applicable]



# Abstract

31

32 Work in progress ...



*¡Oh memoria, enemiga mortal de mi descanso!*

---

*El ingenioso hidalgo don Quijote de la Mancha*

MIGUEL DE CERVANTES SAAVEDRA



## Acknowledgements

34 Work in progress ...



# Contents

Statement of originality . . . . .	3
Abstract . . . . .	5
Acknowledgements . . . . .	9
<b>Contents</b>	<b>14</b>
<b>List of Figures</b>	<b>15</b>
<b>List of Tables</b>	<b>29</b>
<b>List of Abbreviations</b>	<b>31</b>
<b>1 Introduction</b>	<b>33</b>
<b>2 Neutrino physics</b>	<b>37</b>
2.1 Neutrinos in the SM . . . . .	37
2.2 Trouble in the neutrino sector . . . . .	41
2.2.1 The solar neutrino problem . . . . .	41
2.2.2 The atmospheric neutrino problem . . . . .	43
2.3 Massive neutrinos . . . . .	45
2.4 Neutrino oscillation formalism . . . . .	47
2.4.1 Oscillations in vacuum . . . . .	49
2.4.2 Oscillations in matter . . . . .	52
2.4.3 Current status of neutrino oscillations . . . . .	54
2.5 Open questions in the neutrino sector . . . . .	55
2.6 Neutrino interactions . . . . .	56

## CONTENTS

<b>3 The Deep Underground Neutrino Experiment</b>	<b>61</b>
3.1 Overview . . . . .	61
3.2 Physics goals of DUNE . . . . .	63
3.3 LBNF beamline . . . . .	66
3.4 Near Detector . . . . .	66
3.4.1 ND-LAr . . . . .	68
3.4.2 TMS/ND-GAr . . . . .	69
3.4.3 PRISM . . . . .	70
3.4.4 SAND . . . . .	72
3.5 A More Capable Near Detector . . . . .	72
3.5.1 Requirements . . . . .	73
3.5.2 Reference design . . . . .	73
3.5.3 R&D efforts . . . . .	76
3.6 Far Detector . . . . .	79
3.6.1 Horizontal Drift . . . . .	80
3.6.2 Vertical Drift . . . . .	82
3.6.3 FD Data Acquisition System . . . . .	84
<b>4 Matched Filter approach to Trigger Primitives</b>	<b>87</b>
4.1 Motivation . . . . .	87
4.2 Signal-to-noise ratio definition . . . . .	89
4.3 Low-pass FIR filter design . . . . .	91
4.4 Matched filters . . . . .	94
4.5 Monte Carlo studies . . . . .	101
4.5.1 Angular dependence . . . . .	106
4.5.2 Distortion and peak asymmetry . . . . .	108
4.5.3 Hit sensitivity . . . . .	112
4.6 VD ColdBox data taking . . . . .	120

## CONTENTS

<b>5 Dark Matter searches with neutrinos from the Sun</b>	<b>123</b>
5.1 Gravitational capture of DM by the Sun . . . . .	123
5.2 Neutrino flux from DM annihilations . . . . .	130
5.3 Computing limits from solar neutrino fluxes . . . . .	131
5.4 Example: Kaluza-Klein Dark Matter . . . . .	135
5.5 High energy DM neutrino signals . . . . .	139
5.5.1 DIS-like events . . . . .	142
5.5.2 Single proton QE-like events . . . . .	145
5.5.3 Results . . . . .	149
5.6 Example: Leptophilic Dark Matter . . . . .	151
5.7 Systematic uncertainties . . . . .	156
5.7.1 Systematic uncertainties in the solar WIMP signal . . . . .	156
5.7.2 Systematic uncertainties in the atmospheric background . . . . .	157
5.7.3 Common systematic uncertainties . . . . .	158
<b>6 Particle identification in ND-GAr</b>	<b>159</b>
6.1 GArSoft . . . . .	159
6.1.1 Event generation . . . . .	160
6.1.2 Detector simulation . . . . .	161
6.1.3 Reconstruction . . . . .	162
6.2 $dE/dx$ measurement in the TPC . . . . .	164
6.2.1 Energy calibration . . . . .	166
6.2.2 Truncated $dE/dx$ mean . . . . .	176
6.2.3 Mean $dE/dx$ parametrisation . . . . .	179
6.3 Muon and pion separation in the ECal and MuID . . . . .	184
6.3.1 Track-ECal matching . . . . .	186
6.3.2 Classification strategy . . . . .	191
6.3.3 Feature selection and importance . . . . .	195
6.3.4 Hyperparameter optimisation . . . . .	206

## CONTENTS

6.3.5	Probability calibration . . . . .	210
6.3.6	Performance . . . . .	212
6.4	ECal time-of-flight . . . . .	214
6.4.1	Arrival time estimations . . . . .	216
6.4.2	Proton and pion separation . . . . .	217
6.5	Charged pion decay in flight . . . . .	220
6.5.1	Track breakpoints . . . . .	222
6.6	Neutral particle identification . . . . .	228
6.6.1	ECal clustering . . . . .	228
6.6.2	$\pi^0$ reconstruction . . . . .	232
6.7	Integration in GArSoft . . . . .	233
<b>7</b>	<b>Event selection in ND-GAr</b>	<b>237</b>
7.1	Data sample . . . . .	237
7.2	$\nu_\mu$ CC selection . . . . .	239
7.2.1	Selection optimisation . . . . .	242
7.2.2	Selection performance . . . . .	248
7.2.3	Primary muon kinematics . . . . .	250
7.3	Charged pion identification . . . . .	254
7.3.1	$\nu_\mu$ CC $1\pi^\pm$ selection . . . . .	262
7.4	Neutral pion identification . . . . .	266
7.5	Neutrino energy reconstruction . . . . .	268
7.6	Systematic uncertainties . . . . .	271
7.6.1	Flux uncertainties . . . . .	271
7.6.2	Cross section uncertainties . . . . .	272
7.6.3	Detector uncertainties . . . . .	275
<b>8</b>	<b>Conclusion and outlook</b>	<b>279</b>
<b>Bibliography</b>		<b>283</b>

# List of Figures

2.1	Solar neutrino fluxes for the solar model BS05(OP). . . . .	42
2.2	Zenith angle distributions for the selected $\nu_e$ and $\nu_\mu$ events in the SK detector. . . . .	44
2.3	$K^0 \rightleftharpoons \bar{K}^0$ mixing through $W^\pm$ exchange. . . . .	48
2.4	Feynman diagrams of the four most relevant CC interactions to long baseline neutrino oscillation experiments. . . . .	57
2.5	Total muon neutrino CC cross section per nucleon as a function of the neutrino energy. . . . .	58
2.6	Schematic representation of a $\nu_\mu$ CCQE interaction with a neutron inside a nucleus. . . . .	59
3.1	Schematic diagram of the DUNE experiment and the LBNF beamline. .	62
3.2	Schematic longitudinal section of the LBNF beamline at Fermilab. . .	65
3.3	Predicted neutrino fluxes at the FD in FHC mode and RHC mode. . .	67
3.4	Representation of the ND hall in Phase II, showing the different subcomponents. .	68
3.5	Schematic representation of the external components of ND-LAr, including the cryostat and the PRISM movable system and detailed drawing of one ArgonCube module. . . . .	69
3.6	Schematic view of the TMS detector, highlighting its main parts. . . .	70
3.7	Cross section of the ND-GAr geometry, showing the HPgTPC, ECal and magnet. . . . .	71
3.8	Predicted beam muon neutrino flux at the ND location for different off-axis positions. . . . .	72

## LIST OF FIGURES

3.9	Diagram of the ALICE TPC, showing the two drift chambers, inner and outer field cages and readout chambers. . . . .	74
3.10	Diagram of the ALICE TPC, showing the two drift chambers, inner and outer field cages and readout chambers. . . . .	75
3.11	Photographs of the TOAD pressure vessel at RHUL. . . . .	77
3.12	Electron microscope image and schematic diagram of a GEM electrode. . . . .	78
3.13	Schematic diagram showing the operating principle of a LArTPC with wire readout. . . . .	79
3.14	Proposed design for the FD-2 module following the HD principle. . . . .	80
3.15	Schematic representation of an APA frames showing the U, V, X and G wires. . . . .	81
3.16	A PDS module containing 24 X-ARAPUCAs and the location of the modules on the APAs. . . . .	82
3.17	Proposed design for the FD-1 and FD-3 modules following the VD principle. . . . .	83
3.18	Schematic representation of the electrode strip configuration for a top and bottom CRU. . . . .	84
3.19	Detailed diagram of the DUNE FD DAQ system. . . . .	85
4.1	Schematic representation of the Trigger Primitive Generation chain in the DUNE FD. . . . .	88
4.2	Example unfiltered waveform from a ProtoDUNE-SP raw data capture. . . . .	90
4.3	Example filtered waveform from a ProtoDUNE-SP raw data capture. . . . .	92
4.4	Power spectra for the current low-pass FIR filter and the optimal filter obtained using the Parks-McClellan algorithm. . . . .	93
4.5	Relative change in the S/N of the ProtoDUNE-SP raw data capture for different values of the cutoff frequency $f_c$ and the transition width $\delta f$ . . . . .	94
4.6	Distribution of the relative change of the S/N on the different wire planes after the optimal FIR filter was applied. . . . .	95

## LIST OF FIGURES

4.7 Example matched filtered waveform from a ProtoDUNE-SP raw data capture. . . . .	96
4.8 Relative change in the S/N for the ProtoDUNE-SP raw data capture for different values of $\delta$ and $\sigma$ from the matched filter parametrisation. . . . .	99
4.9 Distribution of the relative change of the S/N on the induction planes from the ProtoDUNE-SP raw data capture after their respective optimal matched filters were applied. . . . .	101
4.10 Distributions of the particles track length in the liquid argon for the generated single particle monoenergetic samples. . . . .	102
4.11 Schematic representation of the two rotated reference frames used in the analysis of the MC filter performance. . . . .	104
4.12 Distributions of the mean S/N change per event for the different MC samples after applying the matched filters. . . . .	105
4.13 Angular dependence of the mean S/N and the S/N improvement for the monoenergetic muon sample. . . . .	106
4.14 Angular dependence of the mean S/N and the S/N improvement for the monoenergetic electron sample. . . . .	107
4.15 Waveforms for two muon events, one parallel to the APA and to the wires in the U plane and other normal to the APA plane and perpendicular to the U plane wires. . . . .	109
4.16 Distribution of the peak asymmetry for the monoenergetic muon sample and dependence of the S/N change on the mean peak asymmetry of the event. . . . .	110
4.17 Raw event display for an electron event showing the true, standard, and matched filter hits produced. . . . .	112
4.18 Dependence of the precision, sensitivity, and $F_1$ scores on the threshold values used in the hit finder for the FIR and matched filters. . . . .	114

## LIST OF FIGURES

4.19 Dependence of the averaged hit sensitivity on the kinetic energy of the events for the matched filter and standard hits, for the case of the muon and electron samples. . . . .	116
4.20 Distributions of the hit sensitivity in the U and V planes versus the sensitivity in the X plane for the standard hits and the matched filter hits in the electron sample. . . . .	117
4.21 Standard residuals and quantile-quantile plots for the hit sensitivity of the X and U planes. . . . .	118
4.22 Schematic diagram of the vertical drift ColdBox setup at CERN. . . . .	120
4.23 Event display of the data taken with the matched filter and HMA trigger at the VD ColdBox. . . . .	121
4.24 Comparison between firmware-produced and simulated TP quantities for a matched filter run at the VD ColdBox. . . . .	122
5.1 Input solar parameters used in the capture rate computation as a function of the solar radius. . . . .	127
5.2 Capture rates as a function of the DM mass for the DM-electron interactions, SD DM-nucleons interactions, and SI DM-nucleons interactions. . . . .	128
5.3 NuWro computed $\nu_\mu - {}^{40}\text{Ar}$ charged-current scattering cross section as a function of the neutrino energy. . . . .	132
5.4 Expected atmospheric neutrino flux as a function of the neutrino energy $E_\nu$ at Homestake at solar minimum. . . . .	134
5.5 Feynman diagrams for $B^1B^1$ annihilation into SM fermions. . . . .	136
5.6 Feynman diagrams for $B^1B^1$ annihilation into a Higgs boson pair. . . . .	136
5.7 Computed spectra of muon neutrinos at the DUNE FD site from $B^1$ annihilations in the Sun for various values of $M_{\text{LKP}}$ . . . . .	137
5.8 Projected 90% confidence level upper limit for DUNE (400 kT yr) on the spin-dependent $B^1$ -proton scattering cross section as a function of $M_{\text{LKP}}$ . .	138

## LIST OF FIGURES

5.9 Computed spectra of muon neutrinos at the DUNE FD site from $\tau^+\tau^-$ and $b\bar{b}$ annihilations in the Sun for different DM masses. . . . .	139
5.10 Distribution of the muon neutrino energies from the $\tau^+\tau^-$ and $b\bar{b}$ annihilation channels. . . . .	141
5.11 Angular distributions for the $b\bar{b}$ DIS sample with $m_{\text{DM}} = 10 \text{ GeV}$ and the atmospheric background. . . . .	141
5.12 Signal efficiency and background rejection for the $b\bar{b}$ sample with $m_{\text{DM}} = 10 \text{ GeV}$ as a function of the angular cuts. . . . .	143
5.13 Signal efficiencies for the $\tau^+\tau^-$ and $b\bar{b}$ DIS samples as functions of the DM mass. . . . .	144
5.14 Angular distributions for the $\tau^+\tau^-$ QE sample with $m_{\text{DM}} = 5 \text{ GeV}$ and the atmospheric background. . . . .	146
5.15 Performance of the MLP classifier for the $\tau^+\tau^-$ QE signal with $m_{\text{DM}} = 5 \text{ GeV}$ . . . . .	147
5.16 Signal efficiencies for the $\tau^+\tau^-$ and $b\bar{b}$ single proton QE samples as functions of the DM mass. . . . .	148
5.17 Projected 90% confidence level upper limit for DUNE (400 kT yr) on the spin-dependent DM-nucleon scattering cross section as a function of $m_{\text{DM}}$ , for the annihilation channels $\tau^+\tau^-$ and $b\bar{b}$ separated by interaction mode	150
5.18 Projected 90% confidence level sensitivity of DUNE (400 kT yr) to the scale $\Lambda$ of an EFT containing only leptophilic DM axial-axial interactions.	154
6.1 Schematic diagram showing the different modules involved in the ND-GAr production. . . . .	163
6.2 Distribution of the fraction of energy deposits with residual range less than 20% of the total track length, and distribution of the ionisation per unit length after removing the tracks with less than 30% of their energy deposits in the last 20% of the track. . . . .	168

## LIST OF FIGURES

6.3	Distribution of the reconstructed ionisation charge per unit length for different reclustering values, and distribution of the median change in $dQ/dx$ per track for the $N_{group} = 4$ reclustering. . . . .	169
6.4	Distribution of the Geant4-simulated energy losses per unit length versus residual range for the stopping proton sample. . . . .	170
6.5	Fitted most probable $dQ/dx$ values for each $dE/dx$ bin, together with best fit to the logarithmic calibration function. . . . .	171
6.6	Fitted most probable $dQ/dx$ values for each $dE/dx$ bin for three different ADC bit limits. . . . .	173
6.7	Area normalised $dE/dx$ distributions for the true and the reconstructed energy deposits in the stopping proton sample, both after applying the calibration and the calibration and the normalisation correction. . . . .	174
6.8	Fractional residuals between the true and the corrected $dE/dx$ means and the 60% truncated means, and fractional residuals between the true and the uncorrected, corrected and uncalibrated $dE/dx$ 60% truncated means. . . . .	176
6.9	Estimated values of the mean $dE/dx$ bias and resolution for the stopping proton sample at different values of the truncation factor. . . . .	177
6.10	Examples of the truncated mean $dE/dx$ LanGauss fits for various $\beta\gamma$ bins, from a simulated FHC neutrino sample. . . . .	179
6.11	Resulting one and two dimensional projections of the posterior probability distributions of the ALEPH $\langle dE/dx \rangle$ parameters obtained by fitting the 60% truncated mean $dE/dx$ values from a FHC neutrino sample. . . . .	181
6.12	Truncated mean $dE/dx$ obtained for the FHC neutrino sample as a function of the $\beta\gamma$ product, together with the fitted most probable values for each $\beta\gamma$ bin and the best fit obtained using the ALEPH parametrisation.	182
6.13	Distribution of the 60% truncated mean $dE/dx$ versus reconstructed momentum for the FHC neutrino sample. . . . .	183

## LIST OF FIGURES

6.14 Estimated values of the mean $dE/dx$ bias and resolution obtained for the true protons in a FHC neutrino sample. . . . .	184
6.15 True momentum distribution for the primary muon in $\nu_\mu$ CC $N\pi^\pm$ interactions inside the fiducial volume of ND-GAr, compared to the post FSI charged pion spectrum. . . . .	185
6.16 Distributions of energy deposits in the ECal for a muon and a charged pion with similar momenta. . . . .	187
6.17 Left panel: comparison between the precision (blue), sensitivity (yellow) and $F_1$ score (red) obtained for the default (horizontal lines) and new algorithms, both with the $\chi^2$ -based direction estimator (squares) and cheating the directions (circles), for different values of the $\chi^2$ cut. Right panel: comparison of the performance of the new algorithm when applying the cluster $t_0$ correction (squares) and when (circles). . . . .	188
6.18 Schematics of a possible option to deal with track-ECal associations in non-zero $t_0$ neutrino interaction events, trying to correct for the drift direction uncertainty in a cluster-by-cluster basis using the cluster time, $t_{cluster}$ . . . . .	190
6.19 Momentum distribution for the reconstructed muons (top panel) and charged pions (bottom panel) in a FHC neutrino sample, together with the fraction of them reaching the ECal (red) and MuID (blue). Each entry corresponds to a reconstructed track, backtracked to a true muon or pion which has not produced any other reconstructed track. . . . .	192
6.20 Predicted truncated mean $dE/dx$ versus momentum, for electrons, muons, charged pions and protons, obtained using the ALEPH parametrisation. The vertical dashed lines represent the boundaries of the six regions used for the muon and pion classification training. . . . .	193
6.21 Example ECal feature distributions for muons and charged pions in the five different momentum ranges considered. . . . .	197

## LIST OF FIGURES

6.22 Example MuID feature distributions for muons and charged pions in the three different momentum ranges considered. . . . .	198
6.23 Left panel: cumulative explained variance for the first three principal components (top panel) and contribution of the different features to the principal axes in feature space (bottom panel). Right panel: Shapley (blue) and Gini (red) feature importances for the different input features. Both figures correspond to the samples in the momentum range $0.3 \leq p < 0.8 \text{ GeV}/c$ . . . . .	200
6.24 Left panel: cumulative explained variance for the first three principal components (top panel) and contribution of the different features to the principal axes in feature space (bottom panel). Right panel: Shapley (blue) and Gini (red) feature importances for the different input features. Both figures correspond to the samples in the momentum range $0.8 \leq p < 1.5 \text{ GeV}/c$ . . . . .	201
6.25 Evolution of the SHAP importance for the top six most important features across all five momentum ranges. . . . .	203
6.26 Permutation importances for the ten most important features in the different momentum ranges (from left to right, top to bottom, in increasing momentum order). The bars indicate the effect that permutations of each feature have on the purity (blue) and the sensitivity (yellow), the translucent regions representing one standard deviation around the central value. . . . .	205
6.27 Values of the precision and sensitivity obtained for 10000 BDT hyperparameter configurations, for the momentum regions I, III and V. . . . .	208
6.28 Reliability diagrams for the BDT classifier used in the momentum range $0.3 \leq p < 0.8 \text{ GeV}/c$ , both for the original (blue circles) and calibrated (yellow squares) responses. For reference, the response of a perfectly calibrated classifier is also shown (black dashed line). . . . .	210

## LIST OF FIGURES

6.29 Uncalibrated (left panel) and calibrated (right panel) predicted probabilities assigned by the BDT classifiers for true muons (blue) and charged pions (red) in the momentum range $0.3 \leq p < 0.8$ GeV/c . . . . .	211
6.30 Calibrated predicted probabilities assigned by the BDT classifiers for the true muons and charged pions in a FHC neutrino sample. . . . .	212
6.31 Efficiency and purity of the muon selection as a function of the reconstructed momentum for the FHC neutrino sample. . . . .	213
6.32 Schematic of the hit selection used for the ToF measurement. The grid represents the layers of the inner ECal, with coloured squares indicating the tiles with hits. Green squares indicate the selected hits. . . . .	215
6.33 Particle velocity versus momentum measured with different ECal arrival time estimations. From left to right: earliest hit time, average hit time, and fitted hit time. In all cases the time resolution is $\Delta\tau = 0.1$ ns. . . . .	216
6.34 Mass spectra for $p$ (blue) and $\pi^\pm$ (yellow) particles, using different ECal time resolution values (from top to bottom, in ascending order), and arrival time estimates. From left to right: earliest hit time, average hit time, and fitted hit time. The dashed lines indicate the true masses of the particles. . . . .	218
6.35 Efficiency (top panel) and purity (bottom panel) for the proton selection as a function of the momentum, for $\Delta\tau = 0.10$ ns. . . . .	219
6.36 Distributions of the velocities measured by ToF with the inner ECal, for different momentum bins, in a FHC neutrino interaction sample. The Gaussian fits are performed around the maxima for each particle species.	220
6.37 Left panel: number of non-decaying, decaying and decaying in the fiducial volume pions for a MC sample of 100000, $p = 500$ MeV/c isotropic positively charged pions inside the TPC. Right panel: event display for a positive pion decaying inside the fiducial volume, with a single reconstructed track for the pion and muon system. . . . .	221

## LIST OF FIGURES

6.38 Values of $\chi_k^{2(FB)}$ (top left panel), $F_k$ (top right panel), $D_k^{1/R}$ (bottom left panel) and $D_k^\phi$ (bottom right panel) versus position along the drift direction for a reconstructed track in a positive pion decay event. The vertical red dashed line indicates the true location of the decay point. . .	223
6.39 Fractional residual distributions of the true and reconstructed decay position along the drift coordinate, using the position of the maximum of $\chi_k^{2(FB)}$ (left panel) and $F_k$ (right panel) as estimates of the decay position. Also shown are double Gaussian fits to these points (red lines). . .	224
6.40 Distributions of the extreme values of $\chi_k^{2(FB)}$ (top left panel), $F_k$ (top right panel), $D_k^{1/R}$ (bottom left panel) and $D_k^\phi$ (bottom right panel) for non-decaying reconstructed pion tracks (blue) and tracks which include the decay inside the fiducial volume (red). . . . .	226
6.41 Left panel: distributions of the predicted probabilities assigned by the BDT classifier to a test sample of decaying pion+muon tracks (blue) and non-decaying pion tracks (red). Left: signal efficiency versus background acceptance (ROC curve) obtained from the BDT for the test sample. . .	227
6.42 Left panel: dependence of the decay position finding resolution on the true value of the decay angle for the $\chi_k^{2(FB)}$ (red) and $F_k$ (blue) methods. Right panel: signal efficiency (blue line) and background rejection (red line) from the BDT classifier versus true decay angle. . . . .	227
6.43 Mean values of the $F_1$ -score marginal distributions for the different free parameters of the new clustering algorithm, with the error bars representing one standard deviation around the mean. The $F_1$ -score values were computed for the 6561 possible parameter configurations using 1000 $\nu_\mu$ CC interaction events. . . . .	230

## LIST OF FIGURES

6.44 Left panel: distributions of the number of ECal clusters per photon from $\pi^0$ decays for the standard (red) and new (blue) clustering algorithms. Right panel: reconstructed invariant mass distributions for photon pairs from single $\pi^0$ events using the standard (red) and new (blue) ECal clustering algorithms. . . . .	231
6.45 Distributions of proton $dE/dx$ and ToF scores for a sample of 100000 FHC neutrino interactions in the HPgTPC. . . . .	234
7.1 Schematic diagram of the HPgTPC including the fiducial volume. . . . .	241
7.2 True positive, false positive, and false negative true neutrino energy distributions for a $\nu_\mu$ CC selection. . . . .	242
7.3 Efficiency and purity for the $\nu_\mu$ CC selection as a function of the different cuts. . . . .	244
7.4 Significance for the $\nu_\mu$ CC selection as a function of the different cuts. . . . .	244
7.5 Normalised 2D distributions of efficiency, purity and significance for the $\nu_\mu$ CC selection. The $S/\sqrt{S+B}$ is normalised to the highest value achieved. The vertical dashed line indicates a purity value of 0.85, whereas the horizontal one corresponds to an efficiency of 0.80. . . . .	245
7.6 Cumulative efficiency and purity for the $\nu_\mu$ CC selection. . . . .	246
7.7 True neutrino energy spectra for the $\nu_\mu$ CC selection. . . . .	247
7.8 True neutrino energy spectra for the $\nu_\mu$ CC selection. . . . .	248
7.9 True neutrino energy spectra for the $\nu_\mu$ CC selection with (blue) and without (red) sign selection. The selected events are broken down by true positives (signal) and false positives (background). The true distribution is also shown (black data points). The bottom panel shows the ratios between the number of false positives and total selected events per bin. . . . .	249
7.10 Efficiency 2D distributions for the $\nu_\mu$ CC selection given the true position of the interaction vertex. . . . .	250

## LIST OF FIGURES

7.11 Distributions for the reconstructed versus truth primary muon momentum, longitudinal momentum, transverse momentum, and angle. . . . .	251
7.12 Efficiency and purity of the $\nu_\mu$ CC selection as a function of the primary muon true momentum and beam angle. . . . .	252
7.13 Fractional residual distributions for the position of the primary vertex in the $\nu_\mu$ CC selection. . . . .	253
7.14 Distribution of events given their true and reconstructed $\pi^\pm$ multiplicity, for a given selection. . . . .	255
7.15 Efficiency and purity for the $\nu_\mu$ CC $0\pi^\pm$ selection as a function of the different cuts. . . . .	257
7.16 Efficiency and purity for the $\nu_\mu$ CC $1\pi^\pm$ selection as a function of the different cuts. . . . .	258
7.17 Row and column normalised distributions of events given their true and reconstructed $\pi^\pm$ multiplicity, for the selection that maximises the significance of the $\nu_\mu$ CC $1\pi^\pm$ selection. . . . .	260
7.18 Purity versus efficiency achieved for the different cut configurations explored separated by the various $\nu_\mu$ CC $N\pi^\pm$ selections. . . . .	261
7.19 Efficiency of the $\nu_\mu$ CC $N\pi^\pm$ selections as a function of the hadronic invariant mass. . . . .	262
7.20 Reconstructed kinematic distributions for the pion candidate in the $\nu_\mu$ CC $1\pi^\pm$ selection. . . . .	263
7.21 Distributions for the reconstructed versus truth pion kinetic energy and angle between the pion and muon in the $\nu_\mu$ CC $1\pi^\pm$ selection. . . . .	264
7.22 Efficiency of the $\nu_\mu$ CC $1\pi^\pm$ selection as a function of the true pion kinetic energy and pion-muon angle. . . . .	265
7.23 Invariant mass distribution obtained for the unassociated ECal cluster pair in the event with the value closest to the true $\pi^0$ mass. . . . .	267
7.24 Reconstructed neutrino energy spectra for the $\nu_\mu$ CC selection obtained using the truth and reconstructed information . . . . .	270

## LIST OF FIGURES

7.25 Neutrino energy residuals distributions for the $\nu_\mu$ CC selection obtained using the truth and reconstructed information . . . . .	271
7.26 Estimated $dE/dx$ resolution as a function of the track length for true muons and protons in a $\nu_\mu$ CC sample. . . . .	276



# List of Tables

2.1	Values of $T_3$ and $Y/2$ assigned to the first generation of fermions. . . . .	39
2.2	Neutral current couplings. . . . .	40
2.3	Summary of neutrino oscillation parameters determined in the Neutrino Global Fit of 2020. . . . .	55
3.1	Summary of the two-phased plan for DUNE. . . . .	63
3.2	Exposure and time required to achieve the different physics milestones of the two phases. . . . .	64
4.1	Characteristic parameters of the two monoenergetic muon events selected for the peak asymmetry study. . . . .	109
5.1	Systematic uncertainties for the solar WIMP signal events. . . . .	156
5.2	Systematic uncertainties for the solar WIMP atmospheric background events. . . . .	157
6.1	Calibration parameters obtained from the fit of the ND-GAr simulated stopping proton sample to the calibration function, for different ADC limits.	173
6.2	Momentum ranges and description of the PID approach assumed for the muon and pion classification task. . . . .	194
6.3	Optimal values of the hyperparameters used by the BDT, for each momentum range. . . . .	209
6.4	Performance metrics of the BDTs with optimal hyperparameters, for the different momentum ranges. . . . .	209

## LIST OF TABLES

6.5	Summary of parameters and sampled values used in the optimisation of the clustering algorithm. . . . .	229
7.1	Estimated event rates in ND-GAr. . . . .	239
7.2	Step-by-step $\nu_\mu$ CC selection cuts and cumulative passing rates. . . . .	246
7.3	Neutrino interaction systematic parameters implemented in <b>GENIE</b> used in the DUNE TDR LBL analysis. . . . .	273
7.4	Neutrino interaction systematic parameters used in the DUNE TDR LBL analysis not present in <b>GENIE</b> . . . . .	274

# List of Abbreviations

<b>ADC</b>	Analog to Digital Converter	<b>LBNF</b>	Long Baseline Neutrino Facility
<b>ALEPH</b>	Apparatus for LEP Physics	<b>MEC</b>	Meson-Exchange Current
<b>ALICE</b>	A Large Ion Collider Experiment	<b>MuID</b>	Muon IDentification system
<b>BDT</b>	Boosted Decision Tree	<b>NC</b>	Neutral Current
<b>CAF</b>	Common Analysis File	<b>ND</b>	Near Detector
<b>CC</b>	Charged Current	<b>ND-GAr</b>	Near Detector Gaseous Argon
<b>DIS</b>	Deep Inelastic Scattering	<b>ND-LAr</b>	Near Detector Liquid Argon
<b>DM</b>	Dark Matter	<b>PDG</b>	Particle Data Group
<b>DUNE</b>	Deep Underground Neutrino Experiment	<b>POT</b>	Protons On Target
<b>ECal</b>	Electromagnetic Calorimeter	<b>QE</b>	QuasiElastic
<b>FD</b>	Far Detector	<b>RES</b>	RESonant
<b>FHC</b>	Forward Horn Current	<b>RHC</b>	Reverse Horn Current
<b>GAr</b>	Gaseous Argon	<b>SIS</b>	Shallow Inelastic Scattering
<b>HPgTPC</b>	High Pressure gaseous Time Projection Chamber	<b>SM</b>	Standard Model
<b>LAr</b>	Liquid Argon	<b>SNB</b>	Supernova Neutrino Burst
<b>LBL</b>	Long BaseLine	<b>TP</b>	Trigger Primitive
		<b>WIMP</b>	Weakly Interacting Massive Particle



## Introduction

*The beginning is the most important part of any work.*

<sup>38</sup> – Plato, *The Republic*

The Standard Model (SM) of particle physics [1–3] has provided a deep understanding of the electromagnetic, weak and strong interactions, and over the past decades it has passed all kind of precision tests [4]. However, the SM by itself can not explain certain observed phenomena, such as the baryon asymmetry of the universe [5], the existence of Dark Matter (DM) [6], or the origin of neutrino masses [7].

One of the biggest puzzles in physics nowadays is how the universe came to be matter-dominated. Following the Big Bang, matter and antimatter were created in equal amounts. A. D. Sakharov described what are the necessary conditions to generate a matter-antimatter asymmetry in the early universe [8]. One of them is the existence of interactions that violate the CP symmetry. It has already been established that the amount of CP violation in the quark sector is not enough to generate the baryon asymmetry [9]. Leptons could contribute to the CP violation through the neutrino oscillation mechanism [10]. However, there is no experimental evidence for this so far.

Another yet to be solved mystery of modern physics concerns the nature of DM. From astrophysical observations (see Ref. [6] and references therein), we are aware of the existence of some unknown matter which only interacts gravitationally with other particles. Usually, extensions of the SM include feasible DM candidates. These are usually very stable, heavy particles with small interactions (if any) with SM particles. These

## CHAPTER 1. INTRODUCTION

57 states are known as weakly interacting massive particles (WIMPs) [11, 12]. Experiments  
58 looking for DM have set the interaction cross section between DM and SM particles to  
59 be very small for DM masses below 1 TeV [13].

60 Among other next generation particle experiments, the Deep Underground Neutrino  
61 Experiment (DUNE) stands out. Conceived as a neutrino oscillation experiment, it will  
62 provide definitive answers to different open questions in the neutrino sector. Its main  
63 goals are the discovery of CP violation in the leptonic sector and the determination  
64 of the neutrino mass ordering [14]. It will also provide precision measurements of the  
65 oscillation parameters within the three-flavour picture.

66 The DUNE far detector (FD) will also search for baryon-number violation and  
67 neutrinos originated from supernova explosions. Moreover, its near detector (ND)  
68 complex will sit next to the most powerful neutrino beam to date, allowing for a  
69 rich neutrino cross section programme. This broad physics range requires a superb  
70 performance from the detectors, which can also be used to look for other BSM phenomena.

71 In this thesis, I explore three different aspects of DUNE. Focusing on the data  
72 acquisition system of the far detector, I start by proposing a method to enhance the  
73 sensitivity of the online processing to low energy events. The idea is to modify the  
74 processing chain in order to have more information available to form trigger decisions.  
75 I motivate this new approach using both ProtoDUNE data and Monte Carlo (MC)  
76 samples, as well as with the results from a test in a real detector setup.

77 Then, I investigate the potential of detecting neutrino fluxes from DM annihilations  
78 inside the Sun with DUNE. Although this is the territory of the large volume neutrino  
79 telescopes, a detector with the high resolution and pointing capabilities of the DUNE  
80 FD can provide complementary information in certain regimes. I present here the results  
81 of a preliminary analysis, showing the projected sensitivities for the general case and  
82 two particular DM scenarios.

83 Finally, I discuss my work on the reconstruction of ND-GAr, the gaseous argon  
84 component of the DUNE ND. These efforts were focused towards the development of  
85 the particle identification strategy in the detector. Following a series of additions and

86 upgrades in the reconstruction, I make use of that to perform the first event selection  
87 studies with fully reconstructed events in this detector.

88 This thesis opens with an overview of the status of neutrino physics in Chapter  
89 2. I start summarising the role that neutrinos play in the SM, to then focus on the  
90 developments that lead to the discovery of neutrino oscillations and how to accommodate  
91 massive neutrinos in the model. I then discuss the phenomenology of the neutrino  
92 oscillations, as well as the current experimental landscape and open questions. In the  
93 final section, I review the basics of the neutrino-nucleus interaction modelling, which is  
94 of great importance for DUNE.

95 Chapter 3 introduces DUNE, its physics programme and various components. I give  
96 detail descriptions of the LBNF beamline, the near detector and the far detector designs.  
97 I also discuss the current staging plans for DUNE. This leads to the of ND-GAr, the  
98 more capable near detector planned for DUNE Phase II.

99 In Chapter 4 I start by reviewing how the trigger primitives (TPs), the basic building  
100 blocks of the DUNE far detector trigger chain, are formed. I then motivate how to  
101 use the filtering to enhance the TP generation in the induction channels. I describe  
102 the concept of matched filter, and how to optimise it using ProtoDUNE-SP data. I  
103 use different MC samples to study its performance, and assess how it improves the hit  
104 finding. Finally, I present the results of the tests we performed at the VD ColdBox setup  
105 at CERN, were for the first time we collected TP data with a matched filter.

106 The solar DM analysis is presented in Chapter 5. After reviewing the theoretical  
107 basis for the solar DM capture and how capture and annihilation rates are related,  
108 I introduce the analysis framework used. I then focus on the event selection studies  
109 based on two topologies: high-energy DIS events and low-energy  $1\mu 1p$  QE events. I  
110 use these to extract the projected sensitivities for the DM-nucleon scattering cross  
111 section, and compare them to the current status of other direct and indirect DM searches.  
112 Additionally, I discuss the potential of DUNE in two specific DM models. I end with a  
113 discussion of the systematic uncertainties relevant for this analysis.

114 Chapter 6 starts with a description of GArSoft, the simulation and reconstruction

## CHAPTER 1. INTRODUCTION

software of ND-GAr. Then, I describe the charge calibration procedure I implemented using a MC sample of stopping protons. I use this to compute the mean ionisation loss per unit length of the tracks, and show how this procedure can be used for particle separation. Next, I summarise my investigations on the muon and pion separation using the information from the calorimeter. I outline the strategy I followed for the training and testing of the classifiers, commenting on the achieved performance using a neutrino interaction sample. Following this, I introduce the possibility of using the fast timing of the calorimeter to perform a time-of-flight measurement. It will allow to separate pions and protons in a momentum range not accessible to other methods. Additionally, I present a method to identify the decays of charged pions in the TPC, when the decay angle is too small and the pion and muon get merged into a single track. I construct a collection of variables from the track fit that allow to locate the position of the decay. Lastly, I propose a new clustering algorithm optimised for our calorimeter. I then demonstrate its impact in the context of the neutral pion reconstruction. The Chapter finishes with an overview of the integration of these reconstruction items in GArSoft.

The event selection studies are covered in Chapter 7. I start by describing the MC neutrino interaction sample I use for the studies. Then, I focus on the  $\nu_\mu$  CC selection, which includes an optimisation of the fiducial volume. I also explore the kinematics of the selected primary muon and the location of the neutrino vertex. Next, I study the performance of the selections based on the reconstructed charged pion multiplicity, paying special attention to the  $1\pi^\pm$  selection. I briefly discuss the possibility of adding the neutral pions in the analysis. Following that, I present the results on the energy reconstruction for the selected charged-current events. I finish with a detailed discussion of the different sources of systematic error relevant for ND-GAr. These include flux and neutrino interaction modelling uncertainties, as well as detector effects.

Eventually, the thesis concludes with Chapter 8. There, I summarise the main results presented in this work, and discuss future plans for the different projects.

# 2

143

144

## Neutrino physics

145        *Little particles of inspiration sleet through the universe all the time traveling  
146        through the densest matter in the same way that a neutrino passes through a  
147        candyfloss haystack, and most of them miss.*

148

– Terry Pratchett, *Sourcery*

149        Ever since they were postulated in 1930 by Wolfgang Pauli to explain the continuous  
150         $\beta$  decay spectrum [15] and later found by F. Reines and C. Cowan at the Savannah  
151        River reactor in 1953 [16], neutrinos have had a special place among all other elementary  
152        particles. They provide a unique way to probe a wide range of quite different physics,  
153        from nuclear physics to cosmology, from astrophysics to colliders. Moreover, there is  
154        compelling evidence to believe that the study of neutrinos may be key to unveil different  
155        aspects of physics beyond the SM, difficult to test elsewhere.

156        In this Chapter, I will review the basics of neutrino physics, from its role within the  
157        SM to the main open questions related to the neutrino sector, paying special attention  
158        to the phenomenology of neutrino oscillations.

### 159        2.1 Neutrinos in the SM

160        The SM of fundamental interactions was initially proposed in 1967 by S. Glashow,  
161        S. Weinberg and A. Salam[1–3]. This theoretical framework describes the dynamics  
162        of leptons and quarks, by introducing a collection of mediating gauge vector bosons  
163        and one scalar particle, known as the Higgs boson. It assumes that the local  $SU(3) \times$

## CHAPTER 2. NEUTRINO PHYSICS

164  $SU(2)_L \times U(1)_Y$  gauge symmetry is an internal symmetry of the system, with  $SU(3)$   
165 describing quantum chromodynamics, and  $SU(2)_L \times U(1)_Y$  being the gauge groups of  
166 the electroweak sector. For a detailed overview of the SM of electroweak interactions,  
167 see Ref. [17].

168 In the SM, neutrinos appear in three flavours, namely  $\nu_e$ ,  $\nu_\mu$ , and  $\nu_\tau$ . These are  
169 associated with the corresponding charged leptons,  $e$ ,  $\mu$ , and  $\tau$ . Neutrinos exist only  
170 as left-handed particles, grouped in doublets with the charged leptons, while the later  
171 come in both chirality states:

$$\begin{pmatrix} \nu_e \\ e_L^- \end{pmatrix}, \quad \begin{pmatrix} \nu_\mu \\ \mu_L^- \end{pmatrix}, \quad \begin{pmatrix} \nu_\tau \\ \tau_L^- \end{pmatrix}, \quad e_R^-, \quad \mu_R^-, \quad \tau_R^-. \quad (2.1)$$

172 Similarly, quarks also exist in both chirality states, and are grouped as:

$$\begin{pmatrix} u_L \\ d_L \end{pmatrix}, \quad \begin{pmatrix} s_L \\ c_L \end{pmatrix}, \quad \begin{pmatrix} t_L \\ b_L \end{pmatrix}, \quad u_R, \quad d_R, \quad s_R, \quad c_R, \quad t_R, \quad b_R. \quad (2.2)$$

173 The fact that there are no right-handed neutrino fields implies that neutrinos are  
174 strictly massless within the SM. This restriction follows from the experimental observation  
175 that all neutrinos produced via weak interactions are pure left-handed helicity states  
176 (and similarly antineutrinos are pure right-handed states). The hypothetical existence  
177 of right-handed neutrinos could be indirectly inferred from the observation of non-zero  
178 neutrino masses, nevertheless the existence of neutrino masses is not a sufficient condition  
179 for the existence of such fields.

180 Left and right-handed fermions transform differently under  $SU(2)_L \times U(1)_Y$  rotations,  
181 as the right-handed particles are singlets under  $SU(2)_L$ . Applying a local transformation,  
182 they change as:

$$\begin{aligned} \psi_L &\longrightarrow e^{-iY\beta(x)/2} e^{-iT_a\alpha_a(x)} \psi_L, \\ \psi_R &\longrightarrow e^{-iY\beta(x)/2} \psi_R, \end{aligned} \quad (2.3)$$

183 where  $Y/2$  and  $T_a$  are the generators of  $SU(2)_L$  and  $U(1)_Y$ , respectively, and  $\beta(x)$  and

## 2.1. NEUTRINOS IN THE SM

**Table 2.1:** Values of  $T_3$  and  $Y/2$  assigned to the first generation of fermions.

	$e_L$	$\nu_e$	$e_R$	$u_L$	$d_L$	$u_R$	$d_R$
$T_3$	-1/2	1/2	0	1/2	-1/2	0	0
$Y/2$	-1/2	-1/2	-1	1/6	1/6	2/3	-1/3

<sup>184</sup>  $\alpha_a(x)$  are the parameters of the rotation.

<sup>185</sup> The values of the quantum numbers  $Y/2$  and  $T_3$ , the third component of the weak  
<sup>186</sup> isospin, have to be assigned to the different particles. The values of  $T_3$  follow from the  
<sup>187</sup> commutation relations of the generators of SU(2). After the spontaneous symmetry  
<sup>188</sup> breaking  $SU(2)_L \times U(1)_Y \rightarrow U(1)_{EM}$ , one finds the relation which determines the electric  
<sup>189</sup> charge:

$$Q = T_3 + \frac{Y}{2}, \quad (2.4)$$

<sup>190</sup> Setting the electric charge to  $-1$  for electrons, we can find the values of the hypercharge  
<sup>191</sup> for the rest of the fermions. The resulting values for the first generation of leptons and  
<sup>192</sup> quarks are shown in Tab. 2.1.

<sup>193</sup> It is clear that the free Lagrangian of the theory is not be invariant under the gauge  
<sup>194</sup> transformations, as the kinetic terms contain derivatives. Therefore, to make it invariant,  
<sup>195</sup> one needs to introduce a set of gauge bosons. They appear in the so-called covariant  
<sup>196</sup> derivative, which replaces the common derivative and transforms in the same way as the  
<sup>197</sup> fermion fields under local rotations. This constrain fixes completely the transformations  
<sup>198</sup> of the spin-1 fields. For left and right-handed particles, the covariant derivatives are  
<sup>199</sup> given by:

$$\begin{aligned} D_\mu \psi_L &= \left( \partial_\mu + ig' \frac{Y}{2} B_\mu + ig T_a W_\mu^a \right) \psi_L, \\ D_\mu \psi_R &= \left( \partial_\mu + ig' \frac{Y}{2} B_\mu \right) \psi_R, \end{aligned} \quad (2.5)$$

<sup>200</sup> where  $W_\mu^i$ ,  $i = 1, 2, 3$  and  $B_\mu$  are the gauge bosons for the  $SU(2)_L$  and  $U(1)_Y$  factors,  
<sup>201</sup> respectively, and  $g$  and  $g'$  are the corresponding gauge couplings. It can be shown that  
<sup>202</sup> these fields transform in the adjoint representation of the gauge group.

## CHAPTER 2. NEUTRINO PHYSICS

**Table 2.2:** Neutral current couplings.

	$u$	$d$	$\nu_e$	$e$
$2v_f$	$1 - \frac{8}{3}\sin^2\theta_W$	$-1 + \frac{4}{3}\sin^2\theta_W$	1	$-1 + 4\sin^2\theta_W$
$2a_f$	1	-1	1	-1

So far, the theory only contains massless particles, as adding bare mass terms to the Lagrangian would spoil the gauge symmetry. Therefore, the mass terms need to be induced by a spontaneous violation of the symmetries. In the SM, the responsible for this is the Higgs mechanism. The Higgs doublet is coupled to the gauge bosons through the covariant derivative, and to the fermions through the Yukawa couplings. Upon spontaneous symmetry breaking, the vacuum expectation value of the Higgs field generate the mass terms of the particles.

In order to obtain the physical intermediate vector boson states, we need to perform the following redefinitions:

$$\begin{aligned} A_\mu &= \sin \theta_W W_\mu^3 + \cos \theta_W B_\mu, \\ Z_\mu &= \cos \theta_W W_\mu^3 - \sin \theta_W B_\mu, \\ W_\mu^\pm &= \frac{1}{\sqrt{2}} (W_\mu^1 \mp i W_\mu^2), \end{aligned} \tag{2.6}$$

where  $A_\mu$  is the photon field, and  $Z_\mu$  and  $W_\mu^\pm$  are the neutral and the charged weak boson fields, respectively. The Weinberg angle,  $\theta_W$ , relates the weak coupling constants and the electric charge:

$$e = g' \cos \theta_W = g \sin \theta_W. \tag{2.7}$$

At this point, the interacting part of the electroweak Lagrangian can be re-written as the sum of three contributions: the electromagnetic (EM), charged-current (CC) and neutral-current (NC) components:

$$\begin{aligned} \mathcal{L}_{\text{EW}}^{\text{int}} &= \mathcal{L}_{\text{EM}} + \mathcal{L}_{\text{CC}} + \mathcal{L}_{\text{NC}} \\ &= -e A_\mu J_{\text{EM}}^\mu - \frac{g}{2\sqrt{2}} (W_\mu^+ J_{\text{CC}}^\mu + \text{h.c.}) - \frac{g}{2\cos\theta_W} Z_\mu J_{\text{NC}}^\mu, \end{aligned} \tag{2.8}$$

## 2.2. TROUBLE IN THE NEUTRINO SECTOR

218 with the currents defined as:

$$\begin{aligned} J_{\text{EM}}^\mu &= \sum_f Q_f \bar{f} \gamma^\mu f, \\ J_{\text{CC}}^\mu &= \sum_\ell \bar{\nu}_\ell \gamma^\mu (1 - \gamma_5) \ell + \sum_f \bar{u}_f \gamma^\mu (1 - \gamma_5) d_f, \\ J_{\text{NC}}^\mu &= \sum_f \bar{f} \gamma^\mu (v_f - a_f \gamma_5) f, \end{aligned} \quad (2.9)$$

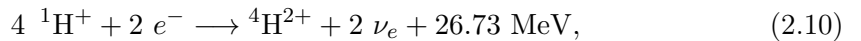
219 where  $f$  denotes any SM fermion,  $\ell$  and  $\nu_\ell$  a charged lepton and a neutrino of any flavour,  
220 and  $u_f$  and  $d_f$  an up-like and a down-like quarks of any flavour. For the NC case, the  
221 values of the  $v_f$  and  $a_f$  couplings are given in Tab. 2.2.

222 As seen in Eq. (5.8), in the electroweak theory neutrinos are coupled to the  $Z$  boson  
223 in a universal way. Therefore, by measuring the so-called invisible decay width of the  $Z$   
224 boson we have an estimate of the number of light (i.e. lighter than the  $Z$  boson) neutrino  
225 flavours. This number was measured by LEP in a combined analysis of  $e^+ e^- \rightarrow \mu^+ \mu^-$   
226 and  $e^+ e^- \rightarrow \text{hadrons}$  to be  $N_\nu = 2.9840 \pm 0.0082$  [18].

## 227 2.2 Trouble in the neutrino sector

### 228 2.2.1 The solar neutrino problem

229 Neutrinos are produced everywhere in vast amounts. One of the most prominent sources  
230 of neutrinos in our vicinity is our Sun. The Sun is powered mainly by two nuclear fusion  
231 reactions, the p – p chain and the CNO cycle. In both cases, the overall reaction is:



232 where part of the released energy is lost to the neutrinos. The electron neutrinos  
233 produced are often labelled after the processes that generate them. Figure 2.1 shows the  
234 solar neutrino flux as a function of the neutrino energy, broken down by the production  
235 process.

## CHAPTER 2. NEUTRINO PHYSICS

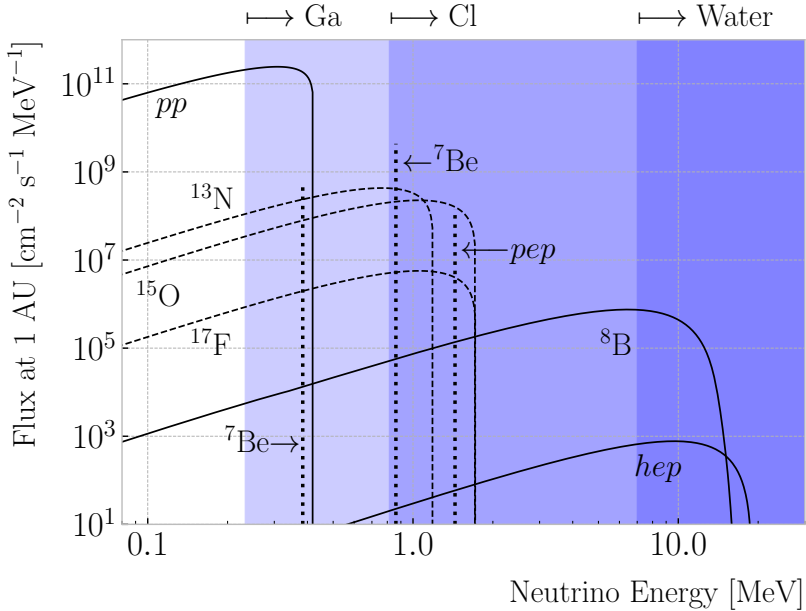


**Figure 2.1:** Solar neutrino fluxes for the solar model BS05(OP). The detection thresholds for Gallium, Chlorine and water-based experiments are also shown. Figure adapted from Ref. [20].

In the late 1960s, the Brookhaven Solar Neutrino Experiment, led by R. Davis, started

data taking with the goal of measuring the solar neutrino flux [19]. The experiment

used a tank containing  $380 \text{ m}^3$  of tetrachloroethene ( $\text{C}_2\text{Cl}_4$ ), a liquid commonly used

in dry-cleaning, located 1.5 km underground in the Homestake mine, in Lead, South

Dakota. The incoming neutrinos would get captured following the reaction:

$$\nu_e + {}^{37}\text{Cl} \longrightarrow {}^{37}\text{Ar} + e^-, \quad (2.11)$$

therefore allowing to measure the neutrino flux by counting the  ${}^{37}\text{Ar}$  isotopes. The

threshold for this reaction is 0.814 MeV, just below the 0.862 MeV line from the  ${}^7\text{Be}$

ground state transition.

The results of the experiment were compared to the theoretical predictions made by

J. Bahcall [21]. During its operation from 1968 to 2002, the experiment observed a solar

$\nu_e$  flux that was approximately a third of the total prediction [22].

In the early 1990s, the SAGE [23] and GALLEX [24] experiments started operations.

## 2.2. TROUBLE IN THE NEUTRINO SECTOR

248 The detection principle used for both experiments was similar to that of the Homestake  
 249 experiment, but using  $^{71}\text{Ga}$  instead of  $\text{C}_2\text{Cl}_4$ . With a detection threshold of 0.233 MeV,  
 250 the Gallium-based experiments were able to observe the  $pp$  neutrino flux. Both  
 251 experiments measured a solar electron neutrino flux that was a factor of two lower  
 252 than the predictions, demonstrating that this deficit was energy-dependent.

253 In the early 2000s, the SNO experiment put an end to the solar neutrino puzzle  
 254 [25, 26]. Thanks to its directionality capabilities, being a Cherenkov light detector, as  
 255 well as to its heavy water target, SNO measured the total solar neutrino flux through  
 256 the NC process:

$$\nu_\alpha + d \longrightarrow n + p + \nu_\alpha, \quad (2.12)$$

257 where  $\alpha = e, \mu, \tau$ . This measurement agreed with the solar model predictions. Then,  
 258 measuring the CC reaction:

$$\nu_e + d \longrightarrow p + p + e^-, \quad (2.13)$$

259 they were able to establish that the  $\nu_\mu$  and  $\nu_\tau$  solar fluxes are in fact non-zero, revealing  
 260 that electron neutrinos were transitioning into different flavours.

### 261 2.2.2 The atmospheric neutrino problem

262 When cosmic-rays interact with the atoms in the upper atmosphere, a plethora of  
 263 hadrons, mainly  $\pi$  and  $K$  mesons, are produced. In particular, for the charged pions,  
 264 we have the following decay chain dominates:

$$\begin{aligned} \pi^+ &\longrightarrow \mu^+ + \nu_\mu, \\ \mu^+ &\longrightarrow e^+ + \bar{\nu}_\mu + \nu_e, \end{aligned} \quad (2.14)$$

265 and similar for the antiparticles. For neutrino energies  $< 1$  GeV, the ratio:

$$\frac{N(\nu_\mu + \bar{\nu}_\mu)}{N(\nu_e + \bar{\nu}_e)}, \quad (2.15)$$

266 of produced neutrinos and antineutrinos is, in good approximation, equal to two [27].

## CHAPTER 2. NEUTRINO PHYSICS

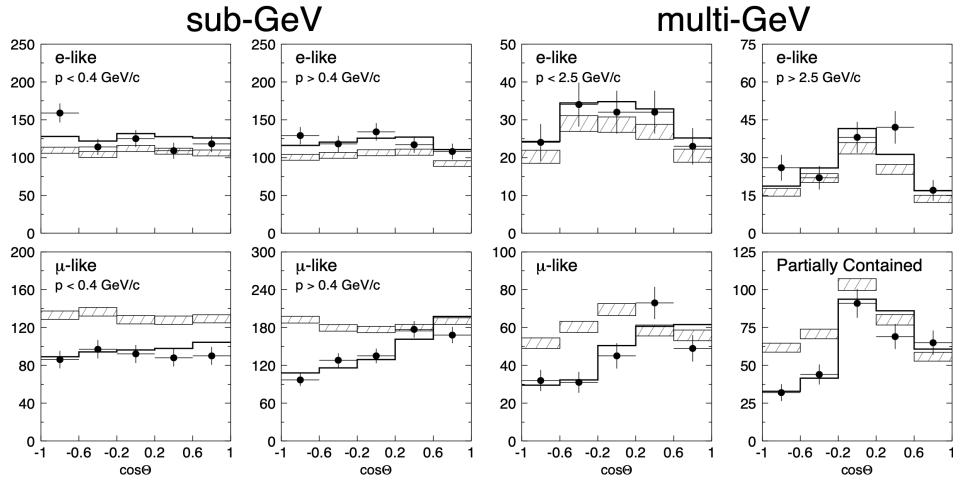


**Figure 2.2:** Zenith angle distributions for the selected  $\nu_e$  (top row) and  $\nu_\mu$  (bottom row) events in the SK detector. The hatched region corresponds to the expectation in the case of no oscillations, whereas the solid line indicates the best-fit in the case of  $\nu_\mu \rightarrow \nu_\tau$  oscillations. Figure taken from Ref. [32].

267 During the 1980s, several proton decay experiments, like Kamiokande [28], IMB [29],

268 MACRO [30], and Soudan-2 [31], measured the flux of atmospheric neutrinos. This was

269 an important part of their research programme, as the atmospheric neutrinos constitute

270 their main background. All these experiments reported an atmospheric neutrino ratio

271 lower than the predictions.

272 A few years before the SNO discovery, in 1998, Super-Kamiokande (SK) collaboration

273 measured the atmospheric  $\nu_e$  and  $\nu_\mu$  spectra as a function of the zenith angle [32].

274 Upward-going particles have negative zenith angle,  $\cos \Theta < 0$ , indicating that they

275 entered from the bottom of the detector. These upward-going neutrinos had to travel

276 through the Earth in order to reach the detector, allowing SK to probe a broad range

277 of baselines. Figure 2.2 shows the reported distributions (black dots), compared to the

278 no oscillations prediction (hatched region). This measurement confirmed that muon

279 neutrinos transition to other flavours, and that this phenomenon depends both on the

280 energy and the path length of the neutrino.

281 The SK and SNO findings provided definitive evidence for the existence of neutrino

282 oscillations, and therefore non-zero neutrino masses. This constitutes one of the

283 groundbreaking discoveries of modern physics and has acted as driving force for beyond

### 2.3. MASSIVE NEUTRINOS

284 the Standard Model (BSM) physics. The minimal extension of the SM we can do to  
 285 address these phenomena is introducing different masses for at least two of the neutrinos.  
 286 This way, we are left with three neutrino mass eigenstates  $\nu_1$ ,  $\nu_2$ , and  $\nu_3$ , with masses  $m_1$ ,  
 287  $m_2$ , and  $m_3$  respectively, which in general will not coincide with the flavour eigenstates,  
 288  $\nu_e$ ,  $\nu_\mu$ , and  $\nu_\tau$ .

## 289 2.3 Massive neutrinos

290 The existence of neutrino oscillations imply that neutrinos are massive particles. However,  
 291 as we have seen before, within the SM neutrinos are massless, as they do not have a  
 292 mass term in the Lagrangian. If one wants to give neutrinos a mass, the particle content  
 293 of the SM needs to be expanded.

294 A way of generating massive neutrinos while maintaining gauge invariance is by  
 295 introducing an arbitrary number of sterile neutrinos  $N_i$ ,  $i = 1, \dots, m$ . These allow for  
 296 two different types of neutrino mass terms:

$$-\mathcal{L}_{M_\nu} = \sum_{i=1}^m \sum_{j=1}^3 M_D^{ij} \bar{N}_i \nu_{Lj} + \frac{1}{2} \sum_{i=1}^m \sum_{j=1}^m M_N^{ij} \bar{N}_i N_j^c + \text{h.c.}, \quad (2.16)$$

297 where  $M_D$  is a complex  $m \times 3$  matrix and  $M_N$  a complex and symmetric  $m \times m$  matrix.  
 298 The first term, often referred to as the Dirac mass term, arises from the corresponding  
 299 Yukawa interaction after the spontaneous electroweak symmetry breaking, similar to  
 300 the other fermions. The second term, called the Majorana mass term, is allowed in the  
 301 Lagrangian, as it is a singlet of the gauge group. However, it violates lepton number  
 302 conservation by two units.

303 If one imposes lepton number symmetry conservation, the Majorana term must  
 304 banish,  $M_N = 0$ . In this case, if  $m = 3$  we can identify the sterile neutrinos as the  
 305 right-handed component of the neutrino field. The Dirac mass matrix can be diagonalised  
 306 using two unitary matrices,  $V_R^\nu$  and  $V_L^\nu$ , as:

$$M_D = V_R^\nu \text{ diag}(m_1, m_2, m_3) V_L^{\nu\dagger}, \quad (2.17)$$

## CHAPTER 2. NEUTRINO PHYSICS

307 where  $m_i$ ,  $i = 1, 2, 3$  are the masses of the three neutrino mass eigenstates.

308 The neutrino mass term can be written in term of the resulting eigenstates as:

$$-\mathcal{L}_{M_\nu} = \sum_{i=1}^3 m_i \bar{\nu}_{Di} \nu_{Di}, \quad (2.18)$$

309 with:

$$\nu_{Di} = \left( V_L^{\nu\dagger} \nu_L \right)_i + \left( V_R^{\nu\dagger} N \right)_i. \quad (2.19)$$

310 In this scenario, both the low energy particle budget and the symmetries of the SM  
 311 have to be modified. Moreover, the masses of the neutrinos are generated exclusively  
 312 through the Higgs mechanism, which does not explain why they are much smaller than  
 313 those of the charged leptons.

314 Going back to the general case, we can re-write Eq. (2.16) in matrix form as:

$$-\mathcal{L}_{M_\nu} = \frac{1}{2} \left( \bar{\nu}_L^c, \bar{N} \right) \begin{pmatrix} 0 & M_D^T \\ M_D & M_N \end{pmatrix} \begin{pmatrix} \nu_L \\ N^c \end{pmatrix} + \text{h.c.} = \bar{\nu}^c M_\nu \nu + \text{h.c.}, \quad (2.20)$$

315 with  $\nu = (\nu_L, N^c)^T$  being a  $(3+m)$ -dimensional vector grouping the active and the  
 316 sterile neutrinos. The matrix  $M_\nu$ , which is a complex  $(3+m) \times (3+m)$  symmetric  
 317 matrix, can be diagonalised by means of a unitary matrix  $V^\nu$ , yielding:

$$M_\nu = V^\nu \text{ diag}(m_1, m_2, \dots, m_{3+m}) V^{\nu T}. \quad (2.21)$$

318 Using this eigendecomposition, the neutrino mass term can be expressed as:

$$-\mathcal{L}_{M_\nu} = \frac{1}{2} \sum_{i=1}^{3+m} m_i \bar{\nu}_{Mi} \nu_{Mi}, \quad (2.22)$$

319 where the states  $\nu_{Mi}$ , commonly referred to as Majorana neutrinos, are defined as:

$$\nu_{Mi} = \left( V^{\nu\dagger} \nu \right)_i + \left( V^{\nu\dagger} \nu \right)_i^c, \quad (2.23)$$

320 in such a way that the Majorana condition,  $\nu_M^c = \nu_M$ , holds true.

## 2.4. NEUTRINO OSCILLATION FORMALISM

321 As a consequence of the Majorana condition, the neutrino and the antineutrino states  
 322 can be described in terms of a single field. As opposed to the charged leptons, which  
 323 need to be represented by a four-component or Dirac spinor, the Majorana neutrino is  
 324 described by a two-component or Weyl spinor.

325 If the eigenvalues of the Majorana mass matrix,  $M_N$ , are much larger than the  
 326 electroweak symmetry breaking scale, the diagonalisation of  $M_\nu$  leads to 3 light and  $m$   
 327 heavy neutrino states:

$$-\mathcal{L}_{M_\nu} = \frac{1}{2}\bar{\nu}_l M_l \nu_l + \frac{1}{2}\bar{\nu}_h M_h \nu_h, \quad (2.24)$$

328 where the two mass matrices are given by:

$$\begin{aligned} M_l &\simeq -V_l^T M_D^T M_N^{-1} M_D V_l, \\ M_h &\simeq V_h^T M_N V_h, \end{aligned} \quad (2.25)$$

329 with  $V_l$  and  $V_h$  two unitary matrices.

330 This scenario represents the so-called see-saw mechanism [33–37]. The name comes  
 331 from the fact that the masses of the heavy states are proportional to  $M_N$ , whereas for  
 332 the light states they are proportional to  $M_N^{-1}$ . While both the heavy and the light  
 333 neutrinos are Majorana particles, it can be shown that the heavy states are mainly  
 334 right-handed, whereas the light ones are mostly left-handed.

## 335 2.4 Neutrino oscillation formalism

336 Neutrino oscillations were first proposed in 1958 by B. Pontecorvo [38], inspired by the  
 337 neutral kaon oscillation phenomenon [39]. Neutral kaons,  $K^0$  and  $\bar{K}^0$ , have opposite  
 338 strangeness ( $\pm 1$ ) and are produced in strong processes. It was observed that, when  
 339 having a beam initially pure of neutral kaons of one type, these would transition into  
 340 their antiparticles while propagating. Because the weak interaction does not conserve  
 341 strangeness, neutral kaons can change their identity via the processes shown in Fig. 2.3.

342 The mixing considered initially by Pontecorvo was between the neutrino and the

## CHAPTER 2. NEUTRINO PHYSICS

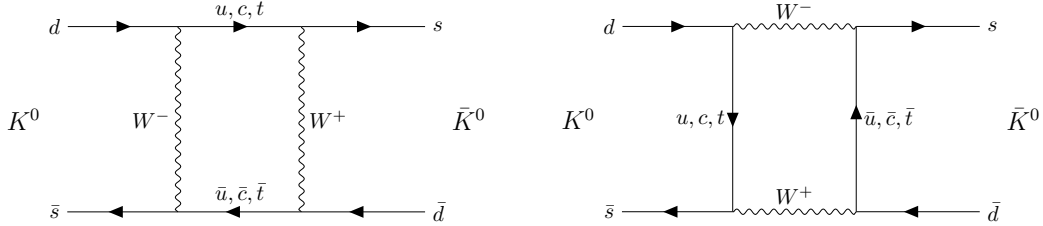


**Figure 2.3:**  $K^0 \rightleftharpoons \bar{K}^0$  mixing through  $W^\pm$  exchange.

343 antineutrino states, as only one neutrino flavour was known at the time. After the  
 344 discovery of the muon neutrino, the mixing between flavours was also explored [40].

345 In the general case, we have 3 active and  $m$  sterile neutrinos, resulting in  $3 + m$   
 346 neutrino mass eigenstates. Working in the mass basis, the leptonic charged-current  
 347 Lagrangian can be written as:

$$-\mathcal{L}_{CC}^{lep} = \frac{g}{\sqrt{2}} (\bar{e}_L, \bar{\mu}_L, \bar{\tau}_L) \gamma^\mu U \begin{pmatrix} \nu_1 \\ \nu_2 \\ \vdots \\ \nu_{3+m} \end{pmatrix} W_\mu^+ + \text{h.c.}, \quad (2.26)$$

348 where  $U$  is a  $3 \times (3 + m)$  matrix which obeys  $UU^\dagger = I_{3 \times 3}$ , but in general will not be  
 349 unitary,  $U^\dagger U \neq I_{(3+m) \times (3+m)}$ .

350 The leptonic mixing matrix,  $U$ , establishes how the neutrino mass states couple to  
 351 the charged leptons. In general, a complex  $n \times n$  matrix can be fully specified by  $2n^2$  real  
 352 parameters. If the matrix is unitary, then the number of independent parameters reduces  
 353 to  $n^2$ , as one has to impose  $n$  normalisation and  $n(n - 1)$  orthogonality constraints.  
 354 In our case, we can further reduce the number of parameters by performing a phase  
 355 redefinition of the charged lepton fields, without affecting the physics. This is not true  
 356 for the neutrinos. As they may be their own antiparticles, one is not allowed to remove  
 357 any physically relevant phases. If we consider  $n$  generations of leptons, the total number  
 358 of parameters in the mixing matrix is  $n^2 - n$ . Out of these, half of them are mixing  
 359 angles, while the other half are complex phase factors.

360 Considering the extended SM without any additional sterile neutrino states, the  
 361 resulting  $3 \times 3$  mixing matrix is unitary. This matrix, often called the Pontecorvo-Maki-

## 2.4. NEUTRINO OSCILLATION FORMALISM

362 Nakagawa-Sakata (PMNS) matrix [41, 42], relates the set of active neutrinos and the  
363 three mass eigenstates as:

$$|\nu_\alpha\rangle = \sum_{i=1}^3 U_{\alpha i}^* |\nu_i\rangle, \quad (2.27)$$

364 where the Greek index  $\alpha$  denotes the flavour  $\{e, \mu, \tau\}$  and the Latin index  $i$  the mass state  
365  $\{1, 2, 3\}$ . This leptonic mixing matrix may be parametrized in terms of 6 parameters,  
366 of which are mixing angles  $\theta_{12}$ ,  $\theta_{13}$  and  $\theta_{23}$ , one CP-violating phase  $\delta_{CP}$  and 2 Majorana  
367 phases  $\alpha$  and  $\beta$ :

$$U = \begin{pmatrix} 1 & 0 & 0 \\ 0 & c_{23} & s_{23} \\ 0 & -s_{23} & c_{23} \end{pmatrix} \begin{pmatrix} c_{13} & 0 & s_{13} e^{-i\delta_{CP}} \\ 0 & 1 & 0 \\ -s_{13} e^{i\delta_{CP}} & 0 & c_{13} \end{pmatrix} \begin{pmatrix} c_{12} & s_{12} & 0 \\ -s_{12} & c_{12} & 0 \\ 0 & 0 & 1 \end{pmatrix} \begin{pmatrix} 1 & 0 & 0 \\ 0 & e^{i\alpha} & 0 \\ 0 & 0 & e^{i\beta} \end{pmatrix}, \quad (2.28)$$

368 where  $c_{ij} \equiv \cos \theta_{ij}$  and  $s_{ij} \equiv \sin \theta_{ij}$ . This matrix is analogous to the Cabibbo-Kobayashi-  
369 Maskawa (CKM) matrix in the quark sector. If neutrinos are Dirac fermions, we can  
370 drop the Majorana phases in the PMNS matrix, as in this case we can perform the  
371 phase redefinitions. However, these phases play no role on the neutrino oscillation  
372 phenomenology.

373 In the case that additional sterile neutrinos states are present, the full leptonic mixing  
374 matrix would not be unitary in general. For instance, in the see-saw scenario, the  $3 \times 3$   
375 submatrix for the three light Majorana neutrinos is not unitary. However, the deviations  
376 from unitarity are of the order  $\mathcal{O}(M_D/M_N)$ , and therefore expected to be negligible.

### 377 2.4.1 Oscillations in vacuum

378 Consider the case where a neutrino of flavour  $\alpha$  is produced at  $t = 0$ , and then it  
379 propagates through vacuum. Such a state will evolve in time according to the relation:

$$|\nu_\alpha(\vec{x}, t)\rangle = \sum_{i=1}^3 U_{\alpha i}^* e^{-i(E_i t - \vec{p}_i \cdot \vec{x})} |\nu_i(\vec{x} = \vec{0}, t = 0)\rangle, \quad (2.29)$$

380 in the plane wave approximation, as the mass eigenstates are also eigenstates of the free  
381 Hamiltonian.

## CHAPTER 2. NEUTRINO PHYSICS

382 This way, the probability for the neutrino to transition from flavour  $\alpha$  to flavour  $\beta$   
383 will be given by:

$$P(\nu_\alpha \rightarrow \nu_\beta) = |\langle \nu_\beta | \nu_\alpha(\vec{x}, t) \rangle|^2 = \left| \sum_{i=1}^3 \sum_{j=1}^3 U_{\alpha i}^* U_{\beta j} e^{-i(E_i t - \vec{p}_i \cdot \vec{x})} \langle \nu_j | \nu_i \rangle \right|^2 \\ = \left| \sum_{i=1}^3 U_{\alpha i}^* U_{\beta i} e^{-i(E_i t - \vec{p}_i \cdot \vec{x})} \right|^2, \quad (2.30)$$

384 where we have used the orthogonality relation  $\langle \nu_i | \nu_j \rangle = \delta_{ij}$ . A usual approximation to  
385 take at this point is to consider ultra-relativistic neutrinos, i.e.  $p_i \simeq E$ , so we can write  
386 the dispersion relations as:

$$E_i = \sqrt{p_i^2 + m_i^2} \approx E + \frac{m_i^2}{2E}. \quad (2.31)$$

387 In the end, assuming  $t \approx L$  where  $L$  is the distance between the production and the  
388 detection points, the probability for the  $\nu_\alpha \rightarrow \nu_\beta$  transition becomes:

$$P(\nu_\alpha \rightarrow \nu_\beta) = \sum_{i,j} U_{\alpha i}^* U_{\beta i} U_{\alpha j} U_{\beta j} e^{-i \frac{\Delta m_{ij}^2}{2E} L} \\ = \delta_{\alpha\beta} - 4 \sum_{i < j} \Re e [U_{\alpha i}^* U_{\beta i} U_{\alpha j} U_{\beta j}^*] \sin^2 \left( \frac{\Delta m_{ij}^2}{4E} L \right) \\ + 2 \sum_{i < j} \Im m [U_{\alpha i}^* U_{\beta i} U_{\alpha j} U_{\beta j}^*] \sin \left( \frac{\Delta m_{ij}^2}{2E} L \right), \quad (2.32)$$

389 where  $\Delta m_{ij}^2$  is the difference of the squared masses of the  $j$ th and  $i$ th neutrino mass  
390 eigenvalues. At this point, it is usual to write the phase responsible for the oscillations  
391 as:

$$\Delta_{ij} \equiv \frac{\Delta m_{ij}^2}{4E} L \simeq 1.27 \frac{\Delta m_{ij}^2}{(\text{eV}^2)} \frac{L}{(\text{km})} \frac{(\text{GeV})}{E}. \quad (2.33)$$

392 Notice that, in the case of antineutrinos, the only difference would be the sign of the  
393 last term in the oscillation probability. As the process  $\bar{\nu}_\alpha \rightarrow \bar{\nu}_\beta$  is the CP-mirror image  
394 of  $\nu_\alpha \rightarrow \nu_\beta$ , the differences between their oscillation probabilities would be a measure of

## 2.4. NEUTRINO OSCILLATION FORMALISM

395 CP symmetry violation:

$$\begin{aligned} A_{CP}^{\alpha\beta} &= P(\nu_\alpha \rightarrow \nu_\beta) - P(\bar{\nu}_\alpha \rightarrow \bar{\nu}_\beta) \\ &= 4 \sum_{i<j} \Im \left[ U_{\alpha i}^* U_{\beta i} U_{\alpha j} U_{\beta j}^* \right] \sin 2\Delta_{ij}. \end{aligned} \quad (2.34)$$

396 Assuming that CPT invariance holds, then the following relation must be true:

$$P(\nu_\alpha \rightarrow \nu_\beta) = P(\bar{\nu}_\beta \rightarrow \bar{\nu}_\alpha), \quad (2.35)$$

397 as these two process are related by the CPT symmetry. From the definition of probability,  
398 we also must have:

$$\sum_{\beta} P(\nu_\alpha \rightarrow \nu_\beta) = \sum_{\beta} P(\bar{\nu}_\alpha \rightarrow \bar{\nu}_\beta) = 1, \quad (2.36)$$

399 where the sum includes all flavours, including  $\alpha$ . From these two constraints, one can  
400 probe that:

$$A_{CP}^{\alpha\beta} = -A_{CP}^{\beta\alpha}, \quad (2.37)$$

401 and in particular:

$$A_{CP}^{\alpha\alpha} = 0. \quad (2.38)$$

402 A direct consequence of this last relation is that there are no observable CP-violating  
403 effects in the so-called disappearance experiments. One needs to perform appearance  
404 experiments, where the flavour detected is different from the original flavour, in order  
405 to measure the CP asymmetry. Neutrino experiments often report the amount of CP-  
406 violation through the Jarlskog invariant. In terms of the parametrisation typically used  
407 to write the PMNS matrix, it is given by:

$$J = \frac{1}{8} \cos \theta_{13} \sin 2\theta_{12} \sin 2\theta_{13} \sin 2\theta_{23} \sin \delta_{CP}. \quad (2.39)$$

408 The Jarlskog invariant can be used to compare the amount of CP-violation in the lepton  
409 and the quark sectors, where  $J = 3.12^{+0.13}_{-0.12} \times 10^{-5}$  in the latter [43].

## CHAPTER 2. NEUTRINO PHYSICS

### 410 2.4.2 Oscillations in matter

411 When neutrinos propagate through matter, their oscillation can be affected in mainly  
 412 two ways. First, neutrinos can inelastically scatter with nuclei, thus destroying the  
 413 coherent propagation of their quantum state. Nevertheless, in most cases this effect is  
 414 negligible (even in very dense mediums like the core of the Sun). Second, neutrinos can  
 415 also experience coherent or forward scatterings, that can affect their oscillation but not  
 416 lose the coherent propagation of the state.

417 The first proposed model to account for neutrino oscillations in matter was proposed  
 418 by Mikhaev, Smirnov and Wolfenstein (MSW) [44]. It relies on the fact that, as the  
 419 only charged lepton present in ordinary matter is the electron, electron neutrinos can  
 420 undergo both charged and neutral-current interactions with matter whereas for muon  
 421 and tau neutrinos just neutral currents are possible.

422 An illustrative way to introduce the MSW mechanism is by considering the two  
 423 flavours case. It can be shown that the evolution of the two flavour eigenstates in vacuum  
 424 is given by the following time-dependent Schrödinger equation:

$$i \frac{d}{dt} \begin{pmatrix} \nu_e \\ \nu_\mu \end{pmatrix} = H_V \begin{pmatrix} \nu_e \\ \nu_\mu \end{pmatrix}, \quad (2.40)$$

425 with a vacuum Hamiltonian given by:

$$H_V = \frac{\Delta m^2}{4E} \begin{pmatrix} -\cos 2\theta & \sin 2\theta \\ \sin 2\theta & \cos 2\theta \end{pmatrix}, \quad (2.41)$$

426 where  $\Delta m^2$  is the mass splitting between the two neutrino states and  $\theta$  the only mixing  
 427 angle. For simplicity, I omit the terms of the Hamiltonian that are proportional to the  
 428 identity, as they do not affect the oscillation phenomenology.

429 The NC contribution to the matter potential is identical for all the flavours, and has  
 430 the form:

$$V_{NC} = -\frac{G_F}{\sqrt{2}} N_n(x), \quad (2.42)$$

## 2.4. NEUTRINO OSCILLATION FORMALISM

431 where  $G_F$  is the Fermi constant and  $N_n(x)$  the local neutron density. Because it is  
 432 common to all flavours, I do not take it into account in the effective Hamiltonian, as it  
 433 would appear as a term proportional to the identity. The CC component only affects  
 434 the electron neutrino (and antineutrino). It can be written as:

$$V_{\text{CC}} = \pm \sqrt{2} G_F N_e(x), \quad (2.43)$$

435 with  $N_e(x)$  being the local electron density in the material. In the end, the effective  
 436 Hamiltonian which describes the propagation of the flavour eigenstates in matter only  
 437 contains an extra  $\nu_e - \nu_e$  element:

$$H_M = H_V + \begin{pmatrix} V_{\text{CC}} & 0 \\ 0 & 0 \end{pmatrix}. \quad (2.44)$$

438 The solution to the Schrödinger equation greatly simplifies if one considers the case  
 439 of a constant matter density. In that case, the effective Hamiltonian can be diagonalised,  
 440 obtaining the effective neutrino mass eigenstates in matter. It can be re-written in the  
 441 same form as the vacuum Hamiltonian:

$$H_M = \frac{\Delta m_m^2}{4E} \begin{pmatrix} -\cos 2\theta_m & \sin 2\theta_m \\ \sin 2\theta_m & \cos 2\theta_m \end{pmatrix}, \quad (2.45)$$

442 where the effective mass splitting and the effective mixing angle are given by:

$$\begin{aligned} \Delta m_m^2 &= \lambda \Delta m_m^2, \\ \sin 2\theta_m &= \frac{\sin 2\theta_m}{\lambda} \end{aligned} \quad (2.46)$$

443 with:

$$\begin{aligned} \lambda &= \sqrt{(\cos 2\theta - A)^2 + \sin^2 2\theta}, \\ A &= \pm \frac{2\sqrt{2} G_F N_e E}{\Delta m^2}. \end{aligned} \quad (2.47)$$

444 In terms of the effective matter oscillation parameters, the transition probability

## CHAPTER 2. NEUTRINO PHYSICS

445  $\nu_e \rightarrow \nu_\mu$  (in the two flavour approximation) reads:

$$P(\nu_e \rightarrow \nu_\mu) = \sin^2 2\theta_m \sin^2 \left( \frac{\Delta m_m^2}{2E} L \right) \quad (2.48)$$

446 From this last equation one can see that, when  $\cos 2\theta = A > 0$  the oscillations are  
447 greatly enhanced. This effect is known as the MSW resonance. For the neutrinos, this  
448 resonant condition is only satisfied if  $\Delta m^2 > 0$  (the opposite is true for antineutrinos).  
449 This is can be exploited by long baseline experiments, which can gain sensitivity to the  
450 neutrino mass hierarchy through matter effects.

### 451 2.4.3 Current status of neutrino oscillations

452 A wide range of neutrino experiments provide experimental input to the neutrino  
453 oscillation framework, both using natural or synthetic neutrino sources. The results  
454 from one of the neutrino global fit analyses, shown in Tab. 2.3<sup>1</sup>, summarise well our  
455 current understanding of the different oscillation parameters.

456 **Solar neutrino experiments** detect neutrinos produced in thermonuclear reactions  
457 inside the Sun, mainly from the so-called *pp* chain and the CNO cycle. These neutrinos  
458 have a typical energy in the range from 0.1 to 20 MeV. These experiments (Homestake  
459 [45], GALLEX [24], SAGE [23], Borexino [46], Super-Kamiokande [47] and SNO [48])  
460 provide the best sensitivities to  $\theta_{12}$  and  $\Delta m_{21}^2$ .

461 **Atmospheric neutrino experiments** detect the neutrino flux produced when  
462 cosmic rays scatter with particles in Earth's atmosphere. These collisions generate particle  
463 showers that eventually produce electron and muon neutrinos (and antineutrinos). Their  
464 energies range from few MeV to about  $10^9$  GeV. Experiments, like Super-Kamiokande  
465 [49] and IceCube [50] use atmospheric neutrinos to measure oscillations and are specially  
466 sensitive to  $\theta_{23}$  and  $\Delta m_{32}^2$ .

467 **Reactor neutrino experiments** look for the  $\bar{\nu}_e$  spectrum produced by nuclear  
468 reactors, with energies in the MeV scale. Depending on the distance to the source,

<sup>1</sup>These are the results reported during M. Tórtola's talk at Neutrino 2024 (see this link). I need to keep an eye and see if they publish these or other updated results in the near future.

## 2.5. OPEN QUESTIONS IN THE NEUTRINO SECTOR

**Table 2.3:** Summary of neutrino oscillation parameters determined in the Neutrino Global Fit of 2020 [61].

Parameter	Best fit $\pm 1\sigma$	$3\sigma$ range
$\Delta m_{21}^2$ [eV $^2 \times 10^{-5}$ ]	$7.55^{+0.22}_{-0.20}$	6.98 – 8.19
$ \Delta m_{31}^2 $ [eV $^2 \times 10^{-3}$ ] (NO)	$2.51^{+0.02}_{-0.03}$	2.43 – 2.58
$ \Delta m_{31}^2 $ [eV $^2 \times 10^{-3}$ ] (IO)	$2.41^{+0.03}_{-0.02}$	2.34 – 2.49
$\sin^2 \theta_{12}/10^{-1}$	$3.04 \pm 0.16$	2.57 – 3.55
$\sin^2 \theta_{23}/10^{-1}$ (NO)	$5.64^{+0.15}_{-0.21}$	4.23 – 6.04
$\sin^2 \theta_{23}/10^{-1}$ (IO)	$5.64^{+0.15}_{-0.18}$	4.27 – 6.03
$\sin^2 \theta_{13}/10^{-2}$ (NO)	$2.20^{+0.05}_{-0.06}$	2.03 – 2.38
$\sin^2 \theta_{13}/10^{-2}$ (IO)	$2.20^{+0.07}_{-0.04}$	2.04 – 2.38
$\delta_{CP}/\pi$ (NO)	$1.12^{+0.16}_{-0.12}$	0.76 – 2.00
$\delta_{CP}/\pi$ (IO)	$1.50^{+0.13}_{-0.14}$	1.11 – 1.87

469 long-baseline experiments like KamLAND [51] are sensitive to the solar mass splitting  
470  $\Delta m_{21}^2$  whereas much shorter baseline experiment such as RENO [52] or DayaBay [53]  
471 measure  $\theta_{13}$  and  $\Delta m_{31}^2$ .

472 **Accelerator experiments** measure neutrino fluxes generated in particle accelerators.  
473 Usually mesons are produced in the accelerator to be focused into a beam, then some  
474 decay to muon neutrinos and the rest are absorbed by a target. Depending on the  
475 configuration one can obtain a beam made of mostly neutrinos or antineutrinos. The  
476 typical energies of these neutrinos are in the GeV range. Experiments such as NOvA  
477 [54], T2K [55], MINOS [56], OPERA [57] and K2K [58] (and in the future DUNE [59])  
478 are primarily sensitive to  $\theta_{13}$ ,  $\theta_{23}$  and  $\Delta m_{32}^2$ . Also, in the coming years DUNE [59] and  
479 Hyper-Kamiokande [60] will be sensitive to  $\delta_{CP}$ .

## 480 2.5 Open questions in the neutrino sector

481 A crucial question that remains open these days, and is of vital importance for oscillation  
482 phenomena, is whether the mass eigenvalue  $\nu_3$  is the heaviest (what we call normal  
483 ordering) or the lightest (referred to as inverted ordering) of the mass eigenstates. In

## CHAPTER 2. NEUTRINO PHYSICS

484 other words, this means that we do not know the sign of  $\Delta m_{32}^2$ , so we can either have  
485  $m_1 < m_2 < m_3$  (NO) or  $m_3 < m_1 < m_2$  (IO).

486 Another big puzzle is related to the value of  $\delta_{CP}$ . Nowadays it is poorly constrained,  
487 with all values between  $\pi$  and  $2\pi$  being consistent with data. A prospective measurement  
488 different from  $\delta_{CP} = 0, \pi$  will predict CP-violation in the leptonic sector, and thus  
489 contribute along with the one measured in the quark sector to the total amount of  
490 CP-violation. Although it is true that these two contributions by themselves are not  
491 enough to explain the matter anti-matter asymmetry in our universe, the amount of  
492 CP-violation in the leptonic sector can be key to explain such imbalance.

493 Both of these questions, because of their nature, could be understood thanks to  
494 future oscillation experiments.

495 Notwithstanding, there are other mysteries that can not be unveiled just by conducting  
496 oscillation experiments, as certain quantities do not influence these phenomena. Among  
497 these there is the question of the absolute values of the neutrino masses. Depending  
498 on the value of the lightest of the neutrino masses we can have different mass spectra,  
499 from hierarchical  $m_1 \ll m_2 < m_3$  (NO) or  $m_3 \ll m_1 < m_2$  (IO) to quasi-degenerate  
500  $m_1 \simeq m_2 \simeq m_3$ .

501 Other open question concerns the nature itself of the neutrinos. If neutrinos are Dirac  
502 particles then their mass term can be generated through the usual Higgs mechanism  
503 by adding right-handed neutrino fields. However, if they are Majorana particles and  
504 therefore their own antiparticles, there is no need to add extra fields to have the mass  
505 term in the Lagrangian. Experiments like SuperNEMO [62], SNO+ [63] and NEXT  
506 [64], which search for neutrino-less double beta decay, will be able to determine whether  
507 neutrinos are Dirac or Majorana.

## 508 2.6 Neutrino interactions

509 The study of neutrino-nucleus interactions is of great importance for long baseline  
510 neutrino oscillation experiments. The interaction model provides a mapping between

## 2.6. NEUTRINO INTERACTIONS

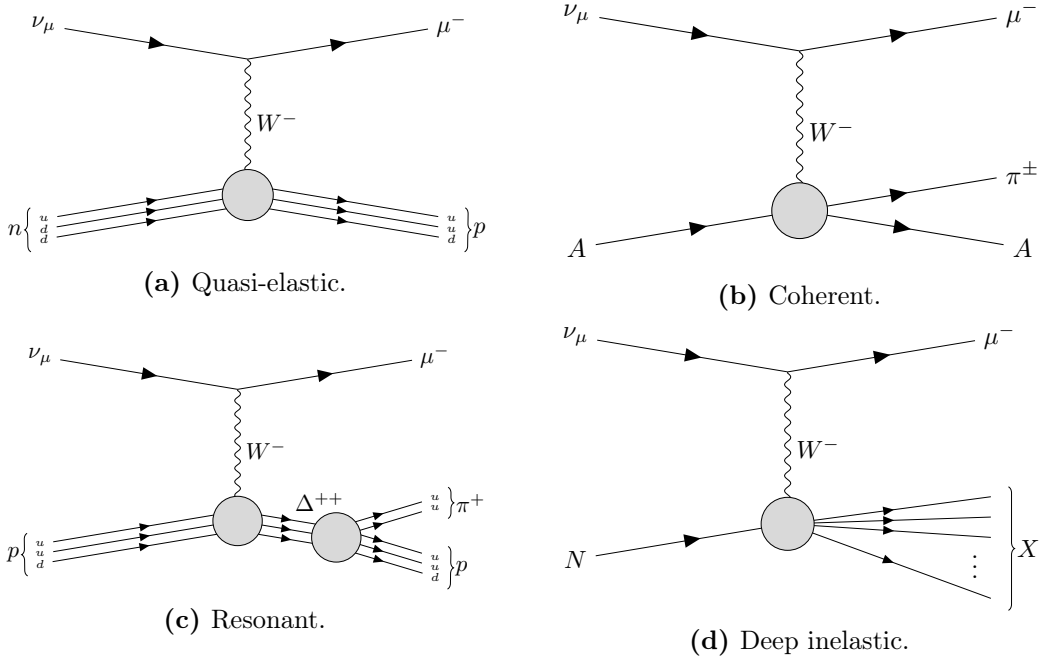


**Figure 2.4:** Feynman diagrams of the four most relevant CC interactions to long baseline neutrino oscillation experiments.

the energy of the incoming neutrino and the final state particles after the interaction.  
 Because in this kind of experiments neutrinos are obtained as secondary decay products of mesons, typically charged pions and kaons, their energies are not known a priori. Not only that, but the kinematics of the interacting nucleon are also unknown. Therefore, we rely on the neutrino interaction models to provide this relation between the observables in the detector and the true kinematics of the neutrino. Interaction modelling is expected to be the one of the leading sources of systematic uncertainties in the next generation of long baseline experiments [65–67].

In the case of neutrino interactions with nuclei, at the energies relevant for long baseline oscillation experiments, around the GeV-scale, the process is dominated by the interaction between the neutrino and a single nucleon within the nuclear medium. Figure 2.4 shows examples of the four most common neutrino CC interactions. In this diagrams  $A$  indicated that the interaction happened with the nucleas as a whole, whereas  $N$  denotes a single nucleon.

At low energies, below 1 GeV, quasi-elastic (QE) interactions dominate. In a CCQE

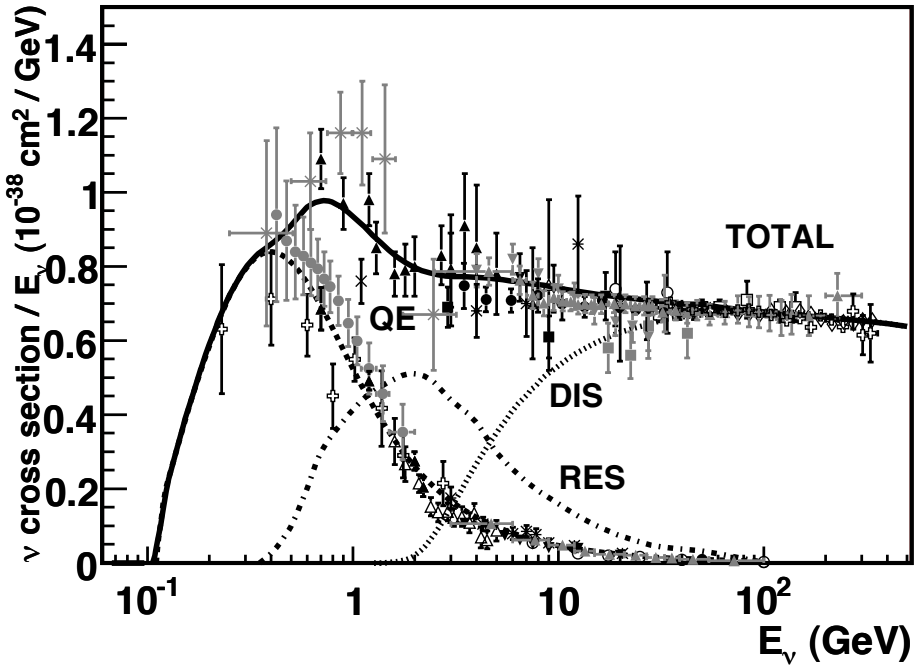


**Figure 2.5:** Total  $\nu_\mu$  CC cross section per nucleon as a function of the neutrino energy. The contributions from the different channels are shown. Figure taken from Ref. [68].

interaction a neutrino (antineutrino) interacts with a neutron (proton), converting it into a proton (neutron) which is then ejected from the nucleus together with the resulting charged lepton. At energies above 1 GeV the neutrino is able to excite the nucleon into a baryonic resonance, which promptly decays into a nucleon and a pion. These are the so-called resonant (RES) interactions. Neutrinos also interact with entire nucleus coherently, in the process known as coherent (COH) interaction. This kind of reactions also produce a single pion in the final state. At high neutrino energies, above 5 GeV, deep inelastic scattering (DIS) takes place. In these processes, the neutrino interacts with a single quark within the nucleon, breaking the nucleon and producing a hadronic shower.

Figure 2.5 shows a compilation of measurements of the total  $\nu_\mu$  CC cross section (see Ref. [68] for the details of the different experimental results). Also shown are the contributions from the different interaction modes. The contribution of the CCCOH interaction is omitted, as it is negligible compared to the others. This shows how the

## 2.6. NEUTRINO INTERACTIONS

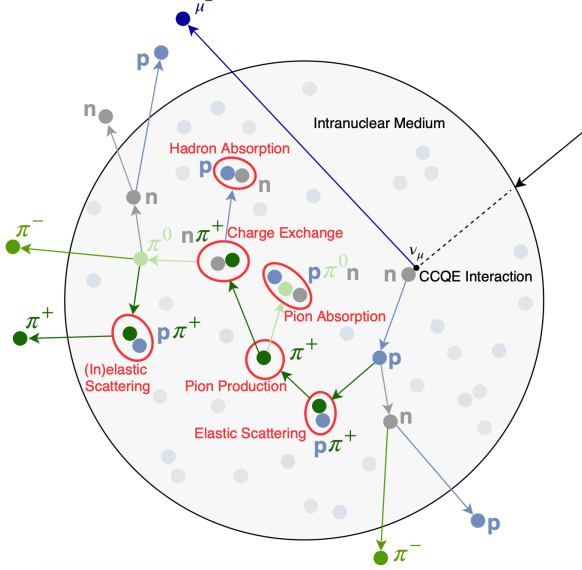


**Figure 2.6:** Schematic representation of a  $\nu_\mu$  CCQE interaction with a neutron inside a nucleus. The reaction produces a muon and a proton, which travel through the nuclear medium. The outgoing proton undergoes various kinds of hadronic FSIs on its way out. Figure taken from Ref. [69].

540 interaction model needs to accurately predict the neutrino-nucleon cross section for the  
 541 different interaction modes across a broad energy range, to obtain the correct relative  
 542 contributions.

543 Nuclear effects alter the neutrino cross section, as well as the multiplicities of the  
 544 final state particles. Therefore, the interaction models need to account for the effects  
 545 introduced by the nuclei. There are several models available to describe the initial state  
 546 of the nucleus, like the relativistic Fermi gas model [70], spectral functions [71] or the  
 547 random phase approximation [72]. The other main effect that interaction models have to  
 548 deal with are the so-called final state interactions (FSI). These are the interactions of the  
 549 particles produced in the neutrino-nucleon scattering as they travel through the nuclear  
 550 medium. Typically, the lepton exits the nucleus without interacting. However, hadrons  
 551 tend to get scattered, absorbed or re-emitted. These effects are usually described by  
 552 means of intra-nuclear cascade models [73]. Figure 2.6 illustrates the effects of FSI on  
 553 the observable particle content in the detector after a  $\nu_\mu$  CCQE interaction.

554 There exists a rich experimental programme dedicated to the measurement of neutrino

## CHAPTER 2. NEUTRINO PHYSICS

555 cross sections. The list of such experiments in the recent years include MiniBooNE  
556 [74], MINERvA [75], MicroBooNE [76] and SBND [77]. Additionally, thanks to their  
557 near detectors, long baseline experiments can perform cross section measurements.  
558 Some recent examples are NOvA [78] or T2K [79]. Future oscillation experiments  
559 will greatly benefit from these measurements, as the measurement of the oscillation  
560 parameters depends on the cross section modelling. However, there are alternative  
561 data-driven approaches to extract the oscillation probabilities without relying on a  
562 neutrino interaction model, which are planned to be explored in the next generation of  
563 experiments [80, 81].

565

# The Deep Underground Neutrino Experiment

567

*Deep in the human unconscious is a pervasive need for a logical universe that makes sense. But the real universe is always one step beyond logic.*

568

– Frank Herbert, *Dune*

569

570 The Deep Underground Neutrino Experiment (DUNE) is a next generation long-  
571 baseline neutrino oscillation experiment [14]. It will address several questions in neutrino  
572 physics, study neutrinos from astrophysical sources and search for beyond the standard  
573 model physics.

574

This Chapter reviews the main goals of DUNE, the operating principle of the LBNF  
575 beamline, the role that the near detector plays in the oscillation measurement, and the  
576 design of the far detector modules and their data acquisition (DAQ) system.

577

## 3.1 Overview

578

The main physics goals of DUNE are:

579

- measure the neutrino mass hierarchy, the amount of CP violation in the leptonic sector and the  $\theta_{23}$  octant,

580

- detect rare low energy neutrino events, like neutrinos from supernova bursts, and

581

- search for proton decay and other beyond the standard model phenomena.

## CHAPTER 3. THE DEEP UNDERGROUND NEUTRINO EXPERIMENT

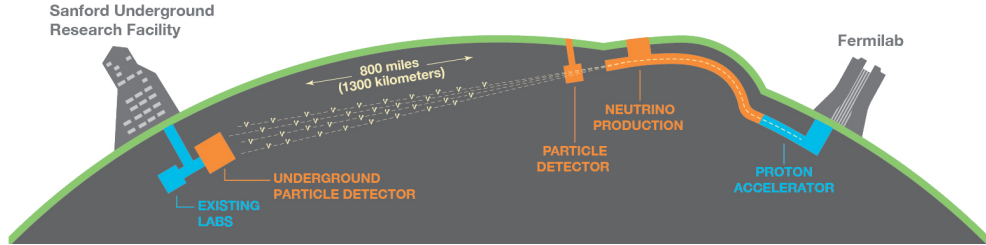


**Figure 3.1:** Schematic diagram of the DUNE experiment and the LBNF beamline [14].

The design of DUNE has been tailored with these goals in mind. It will consist of two neutrino detectors. A near detector (ND) complex will be placed at Fermilab, 574 m downstream of the neutrino production point, whereas a larger far detector (FD) will be built in the Sandford Underground Research Facility (SURF), South Dakota, approximately 1300 km away. Figure 3.1 shows a simplified diagram with the various components of DUNE (not to scale).

The beam neutrinos will be provided by the Long-Baseline Neutrino Facility (LBNF) beamline, the multi-megawatt wide-band neutrino beam planned for Fermilab. It will produce neutrinos travelling in the direction of SURF, with the capability to switch between neutrino and antineutrino mode.

Before arriving to the FD, the neutrino beam meets the ND complex, which serves as the experiment's control. The design of the DUNE ND is mainly driven by the needs of the oscillation physics programme, as its main role is to measure the unoscillated neutrino energy spectra. From these we can predict the unoscillated spectra at the FD, which can be compared to the spectra measured at the FD to extract the oscillation parameters. Additionally, the ND has a physics programme of its own, including cross section measurements and BSM physics searches.

The technology chosen for the FD modules of DUNE is the liquid Argon time projection chamber (LArTPC). Its four modules will record neutrino interactions from the accelerator-produced beam arriving at predictable times. As it also aims at recording rare and low energy events, like supernovae and solar neutrinos, the FD requires trigger

### 3.2. PHYSICS GOALS OF DUNE

**Table 3.1:** Summary of the two-phased plan for DUNE. Adapted from Ref. [82].

Parameter	Phase I	Phase II	Benefit
FD mass	20 kt fiducial	40 kt fiducial	FD statistics
Beam power	up to 1.2 MW	2.4 MW	FD statistics
ND config.	ND-LAr, TMS, SAND	ND-LAr, ND-GAr, SAND	Systematic constraints

604 schemes which can deal with both kinds of physics, and also maximum uptime.

605 DUNE is planned to be built using a staged approach consisting on two phases,  
 606 which are summarised in Tab. 3.1. Phase I consists of a FD with 50% of the total  
 607 fiducial mass, a reduced version of the ND complex and a 1.2 MW proton beam. It will  
 608 be sufficient to achieve some early physics goals, like the determination of the neutrino  
 609 mass ordering. For its Phase II, DUNE will feature the full four FD modules, a more  
 610 capable ND and a 2.4 MW proton beam. The physics milestones for the two phases are  
 611 given in Tab. 3.2, in a staging scenario which assumes that Phase II is completed after  
 612 6 years of operation.

613 A summary of the DUNE science programme can be found in the DUNE FD  
 614 Technical Design Report (TDR) Volume I [14]. For a detailed discussion on the two-  
 615 phased approach the reader is referred to the DUNE Snowmass 2021 report [82].

## 616 3.2 Physics goals of DUNE

617 As noted in the literature (see for instance Ref. [61] for a review), the parameter space of  
 618 the neutrino oscillation phenomena within the three-flavour picture is quite constrained  
 619 by current experimental data. However, there are still crucial open questions, like the  
 620 mass ordering, the value of  $\delta_{CP}$  or the  $\theta_{23}$  octant. One of the main goals of DUNE is to  
 621 determine precisely the values of these parameters [83].

622 To address these questions DUNE can look to the subdominant oscillation channel  
 623  $\nu_\mu \rightarrow \nu_e$  ( $\bar{\nu}_\mu \rightarrow \bar{\nu}_e$ ) and study the energy dependence of the  $\nu_e$  ( $\bar{\nu}_e$ ) appearance probability.  
 624 When we focus on the antineutrino channel  $\bar{\nu}_\mu \rightarrow \bar{\nu}_e$  there is a change in the sign of  $\delta_{CP}$ ,  
 625 thus introducing CP-violation. Moreover, due to the fact that there are no positrons in

### CHAPTER 3. THE DEEP UNDERGROUND NEUTRINO EXPERIMENT

**Table 3.2:** Exposure and time required to achieve the different physics milestones of the two phases. The predictions assume a Phase II staging scenario where FD modules 3 and 4 are deployed in years 4 and 6 and both the beam and ND are upgraded after 6 years. Adapted from Ref. [82].

Stage	Physics milestone	Exposure (kt-MW-years)	Years (staged)
Phase I	$5\sigma$ MO ( $\delta_{CP} = -\pi/2$ )	16	1-2
	$5\sigma$ MO (100% of the $\delta_{CP}$ values)	66	3-5
	$3\sigma$ CPV ( $\delta_{CP} = -\pi/2$ )	100	4-6
Phase II	$5\sigma$ CPV ( $\delta_{CP} = -\pi/2$ )	334	7-8
	$\delta_{CP}$ resolution of 10 degrees ( $\delta_{CP} = 0$ )	400	8-9
	$5\sigma$ CPV (50% of the $\delta_{CP}$ values)	646	11
	$3\sigma$ CPV (75% of the $\delta_{CP}$ values)	936	14
	$\sin^2(2\theta_{13})$ resolution of 0.004	1079	16

the composition of Earth, there is a sign difference for the matter effect contribution when looking to the antineutrino channel. This asymmetry is proportional to the baseline length  $L$  and is sensitive to the sign of  $\Delta m_{31}^2$ , and thus to the neutrino mass ordering.

Another of the main physics goals of DUNE is the search for baryon-number violating processes. Specifically, it will try to answer the question of whether protons are stable or not. There is no symmetry argument that forbids protons from decaying, but its apparent stability seems to suggest that baryon number is conserved [84]. However, proton decay is a usual feature of grand-unified theories, where electromagnetic, weak and strong interactions are unified above a certain energy scale [85].

As the energy deposition scale for this kind of searches is nearly the same as the one for long-baseline neutrino oscillations, DUNE will be able to look for them. It has several advantages over other experiments, such as excellent imaging and particle identification, which can be translated into lower backgrounds.

The last of the main objectives of DUNE is the detection of neutrinos originated in supernovae explosions, what is called a supernova neutrino burst (SNB). These neutrinos carry with them information about the core-collapse process, from the progenitor to the explosion and the remnant; but also may have information about new exotic physics. So far, the only neutrino events ever recorded from such a process were a few dozens of  $\bar{\nu}_e$

### 3.3. LBNF BEAMLINE

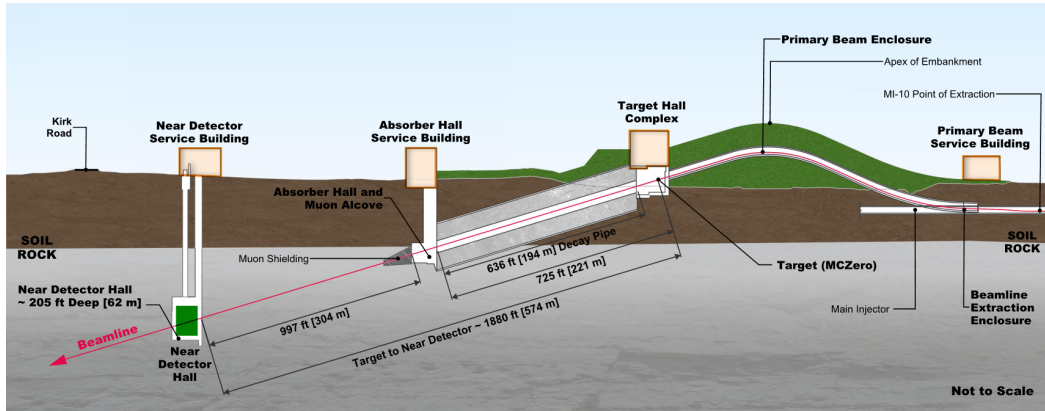


**Figure 3.2:** Schematic longitudinal section of the LBNF beamline at Fermilab (not to scale). Figure taken from Ref. [88].

644 events from the 1987A supernova located in the Magellanic Cloud, 50 kpc away from  
 645 Earth [86,87].

646 DUNE aims to collect SNB events. Although these are quite rare, as the expected  
 647 supernovae explosion events are about one every few decades for our galaxy and  
 648 Andromeda, the long lifetime of the experiment (around a couple of decades as well)  
 649 makes it reasonable to expect some. Nowadays the main sensitivity to SNB of most  
 650 experiments is to the  $\bar{\nu}_e$  flux through inverse beta decay. One of the advantages of  
 651 DUNE is its expected sensitivity to MeV-scale  $\nu_e$  events, since the dominant channel  
 652 will be  $\nu_e$  CC scattering.

653 Moreover, due to the stringent requirements that the main physics goals set for  
 654 DUNE, it will allow also to perform searches for all kind of BSM physics. Among  
 655 others, DUNE will be able to look for: active-sterile neutrino mixing, non-unitarity of  
 656 the PMNS matrix, non-standard interactions, Lorentz and CPT violations, neutrino  
 657 trident production, light-mass DM, boosted DM and heavy neutral leptons. The reader  
 658 is referred to the DUNE FD TDR Volume II [83] for a full discussion of the physics  
 659 scope of DUNE.

## CHAPTER 3. THE DEEP UNDERGROUND NEUTRINO EXPERIMENT

### 660 3.3 LBNF beamline

661 The LBNF project is responsible for producing the neutrino beam for the DUNE detectors.  
662 A detailed discussion of the LBNF programme can be found in the DUNE/LBNF CDR  
663 Volume III [88].

664 A schematic diagram of the longitudinal section of the LBNF beamline is shown in  
665 Fig. 3.2. First, a beam of 60 – 120 GeV protons is extracted from the Fermilab Main  
666 Injector. This beam is aimed towards the target area, where it collides with a cylindrical  
667 graphite target to produce charged pions and kaons.

668 The diffuse, secondary beam of particles is focused by a pair of magnetic horns.  
669 These select the positively charged particles when operated in Forward Horn Current  
670 (FHC) mode, or the negatively charged ones when the current is reversed, also known as  
671 Reverse Horn Current (RHC) mode. The focused secondary beam then enters a 194 m  
672 decay pipe where the pions and kaons will predominantly produce  $\mu^+ \nu_\mu$  pairs when in  
673 FHC mode (or  $\mu^- \bar{\nu}_\mu$  in RHC mode).

674 At the end of the decay pipe a hadron absorber removes the undecayed hadrons and  
675 muons from the beam, which reduces the  $\nu_e$  ( $\bar{\nu}_e$ ) and  $\bar{\nu}_\mu$  ( $\nu_\mu$ ) contamination coming  
676 from the  $\mu^+$  ( $\mu^-$ ) decays. The resulting neutrino flux at the FD is shown in Fig. 3.3,  
677 both for FHC (left) and RHC (right) modes. These predictions show the intrinsic  $\langle \bar{\nu}_e \rangle$   
678 contamination and wrong sign component from wrong sign and neutral meson decays,  
679 as well as muons decaying before reaching the absorber.

### 680 3.4 Near Detector

681 To estimate the oscillation parameters we measure the neutrino energy spectra at the FD.  
682 This reconstructed energy arises from a convolution of the neutrino flux, cross section,  
683 detector response and the oscillation probability. Using theoretical and empirical models  
684 to account for the other effects, one can extract the oscillation probability using the  
685 measurement. However, these models have associated a number of uncertainties that

### 3.4. NEAR DETECTOR

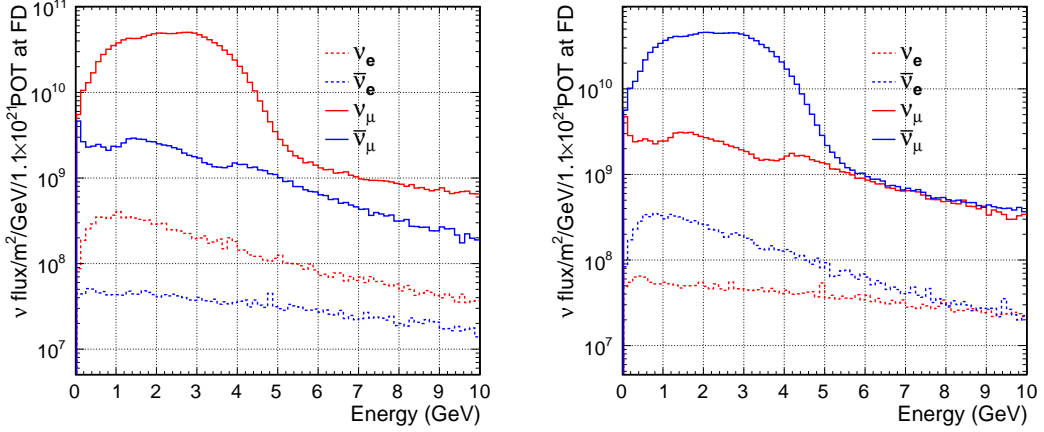


**Figure 3.3:** Predicted neutrino fluxes at the FD in FHC mode (left panel) and RHC mode (right panel). Figures taken from Ref. [83].

686 are then propagated to the oscillation parameters.

687 One of the main roles of the ND is to measure the neutrino interaction rates before  
 688 the oscillation effects become relevant, i.e. close to the production point. By measuring  
 689 the  $\nu_\mu$  and  $\nu_e$  energy spectra, and that of their corresponding antineutrinos, at the ND  
 690 we can constrain the model uncertainties. A complete cancellation of the uncertainties  
 691 when taking the ratio between the FD and ND measurements is not possible, as that  
 692 would require both detectors to have identical designs and the neutrino fluxes seen by  
 693 them to be the same. Because of the distance, the flux probed by the FD will have a  
 694 different energy and flavour composition than that at the ND, as neutrinos oscillate and  
 695 the beam spreads. The differences in the flux also determine the design of the detectors,  
 696 therefore the ND is limited in its capability to match the FD design.

697 Nevertheless, having a highly capable ND, DUNE can minimise the systematic  
 698 uncertainties affecting the observed neutrino energy. The ND data can be used to  
 699 tune the model parameters by comparison with the prediction. Then, one uses the  
 700 tuned model to predict the unoscillated FD spectra. Comparing the prediction with the  
 701 measured spectra it is possible to extract the oscillation parameters.

702 Additionally, the ND will have a physics programme of its own. In particular, it will  
 703 measure neutrino cross sections that will then be used to constrain the model used in

## CHAPTER 3. THE DEEP UNDERGROUND NEUTRINO EXPERIMENT

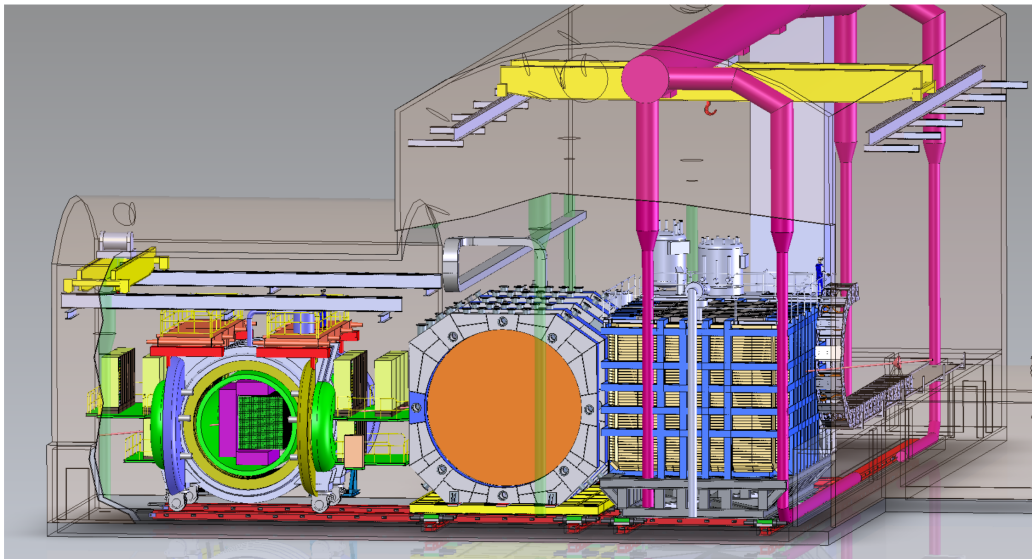


**Figure 3.4:** Representation of the ND hall in Phase II, showing the different subcomponents. From right to left, in the direction of the beam, we have ND-LAr, ND-GAr and SAND. Figure taken from Ref. [89].

704 the long-baseline oscillation analysis. It will also be used to search for BSM phenomena  
 705 such as heavy neutral leptons, dark photons, millicharged particles, etc.

706 The DUNE ND can be divided in three main components, a LArTPC known as ND-  
 707 LAr, a magnetised muon spectrometer, which will be the Temporary Muon Spectrometer  
 708 (TMS) in Phase I and ND-GAr in Phase II, and the System for on-Axis Neutrino  
 709 Detection (SAND). The layout of the Phase II DUNE ND can be seen in Fig. 3.4. The  
 710 first two components of the ND will be able to move off-axis, in what is called the  
 711 Precision Reaction-Independent Spectrum Measurement (PRISM) concept. More details  
 712 on the purpose and design of the ND can be found in the DUNE ND Conceptual Design  
 713 Report (CDR) [89].

### 714 3.4.1 ND-LAr

715 ND-LAr is a LArTPC, as the ND needs a LAr component to reduce cross section and  
 716 detector systematic uncertainties in the oscillation analysis. However, its design differs  
 717 significantly from those proposed for the FD modules. Because of the high event rates  
 718 at the ND, approximately 55 neutrino interaction events per 10  $\mu$ s spill, ND-LAr will be

### 3.4. NEAR DETECTOR

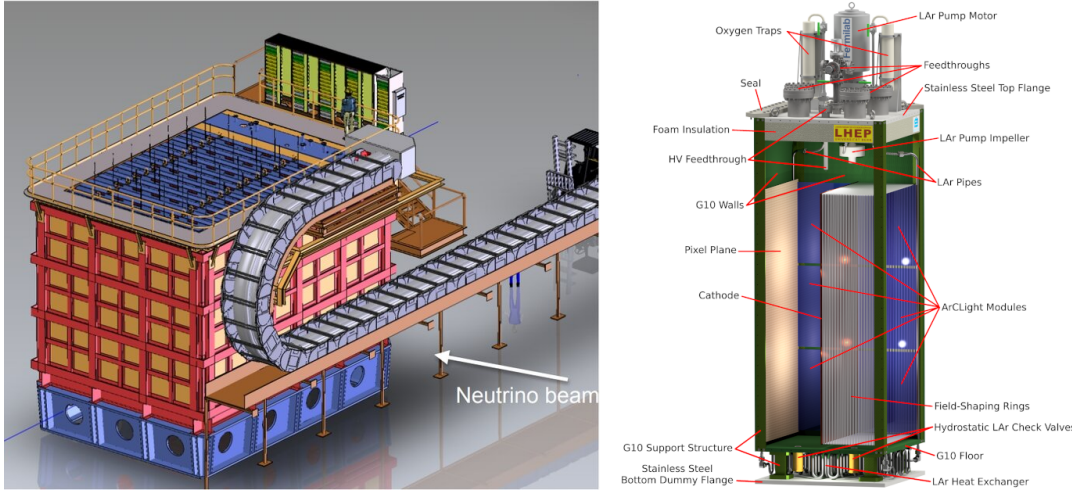


**Figure 3.5:** Schematic representation of the external components of ND-LAr, including the cryostat and the PRISM movable system (left) and detailed drawing of one ArgonCube module (right). Figure adapted from Ref. [14].

719 built in a modular way. Each of the modules, based on the ArgonCube technology, is a  
 720 fully instrumented, optically isolated TPC with a pixelated readout [90]. The pixelisation  
 721 allows for a fully 3D reconstruction and the optical isolation reduces the problems due  
 722 to overlapping interactions. Figure 3.5 shows a representation of the external parts of  
 723 ND-LAr (left) and a detailed diagram of an ArgonCube module (right).

724 With a fiducial mass of 67 t and dimensions 7 m (w)  $\times$  3 m (h)  $\times$  5 m (l), ND-LAr  
 725 will be able to provide high statistics and contain the hadronic systems from the beam  
 726 neutrino interactions, but muons with a momentum higher than 0.7 GeV will exit the  
 727 detector.

#### 728 3.4.2 TMS/ND-GAr

729 To accurately estimate the neutrino energy, the momentum of the outgoing muons needs  
 730 to be determined. That is the reason why a muon spectrometer is needed downstream  
 731 of ND-LAr.

732 In Phase I that role will be fulfilled by TMS. It is a magnetised sampling calorimeter,  
 733 with alternating steel and plastic scintillator layers. Figure 3.6 shows a schematic view  
 734 of the TMS detector. The magnetic field allows a precise measurement of the sign of the

## CHAPTER 3. THE DEEP UNDERGROUND NEUTRINO EXPERIMENT

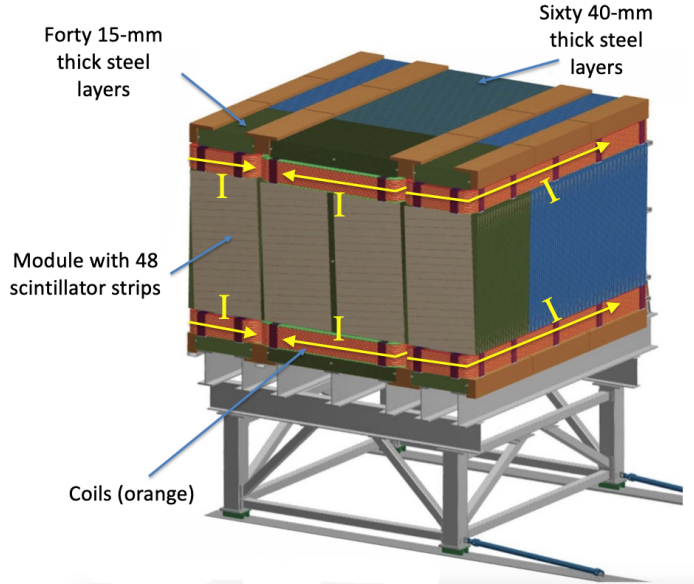


**Figure 3.6:** Schematic view of the TMS detector, highlighting its main parts. Figure adapted from Ref. [14].

735 muon, so one can distinguish between neutrino and antineutrino interactions.

736 After the Phase II upgrade, TMS will be replaced with a more capable near detector.

737 The current technology considered is ND-GAr. This detector is a magnetised, high-  
 738 pressure gaseous argon (GAr) TPC (often denoted as HPgTPC) surrounded by an  
 739 electromagnetic calorimeter (ECal) and a muon tagger. A cross section of its geometry  
 740 can be seen in Fig. 3.7. ND-GAr will be able to measure the momenta of the outgoing  
 741 muons while also detect neutrino interactions inside the GAr volume. This allows  
 742 ND-GAr to constrain the systematic uncertainties even further, as it will be able to  
 743 accurately measure neutrino interactions at low energies thanks to the lower tracking  
 744 thresholds of GAr.

### 745 3.4.3 PRISM

746 In general, the observed peak neutrino energy of a neutrino beam decreases as the  
 747 observation angle with respect to the beam direction increases. This feature has been  
 748 used in other long-baseline neutrino experiments, like T2K ( $2.5^\circ$  off-axis) and NOvA  
 749 ( $0.8^\circ$  off-axis), to achieve narrower energy distributions. The DUNE PRISM concept

### 3.4. NEAR DETECTOR

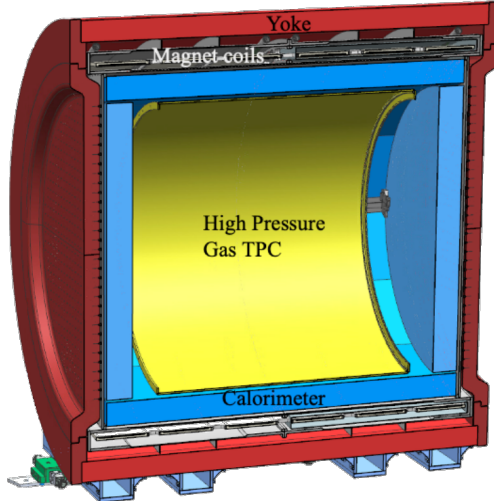


**Figure 3.7:** Cross section of the ND-GAr geometry, showing the HPgTPC, ECal and magnet. Figure adapted from Ref. [91].

750 exploits this effect using a movable ND. Within PRISM both ND-LAr and the muon  
 751 spectrometer (TMS in Phase I and ND-GAr in Phase II) can be moved up to  $3.2^\circ$   
 752 off-axis, equivalent to moving the detectors 30.5 m laterally through the ND hall.

753 This allows us to record additional data samples with different energy compositions.  
 754 Figure 3.8 compares the on-axis muon neutrino flux at the ND with the fluxes at different  
 755 off-axis positions. As the off-axis position increases the neutrino flux becomes closer to  
 756 a monoenergetic beam with a lower peak energy. These samples can be used to perform  
 757 a data-driven determination of the relation between true and reconstructed neutrino  
 758 energy, to reduce the dependence on the interaction model. The off-axis samples are  
 759 linearly combined to produce a narrow Gaussian energy distribution centered on a target  
 760 true energy. From the combination coefficients one can build a sample of reconstructed  
 761 neutrino events that will determine the energy mapping.

762 The PRISM samples will also be used to form a flux at the ND location similar in  
 763 shape to the oscillated flux measured by the FD. This method can be used to extract  
 764 the oscillation parameters with minimal input from the neutrino interaction model [81].

## CHAPTER 3. THE DEEP UNDERGROUND NEUTRINO EXPERIMENT

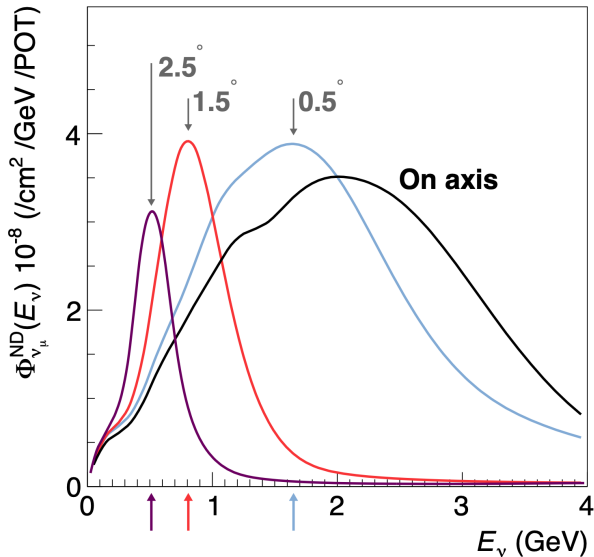


**Figure 3.8:** Predicted beam muon neutrino flux at the ND location for different off-axis positions. Figure taken from Ref. [89].

### 3.4.4 SAND

The role of SAND is to monitor the beam stability by measuring the on-axis neutrino energy spectra. As the PRISM program requires that ND-LAr and its downstream muon spectrometer spend about half of the time in off-axis positions, it is not possible to monitor the stability of the beam with the movable detectors. Moreover, for the success of PRISM it is essential to have a stable beam configuration, or, at least, a quick assessment and modeling of the distortions.

The SAND detector is magnetised, and features an inner low density tracker, a LAr target with optical readout and a surrounding sampling calorimeter.

### 3.5 A More Capable Near Detector

In DUNE Phase II, a more capable near detector is needed to achieve the ultimate physics goals of the experiment. The current leading proposal for this detector is ND-GAr. As mentioned previously, it will fulfill the role of TMS, measuring the momentum and sign of the charged particles exiting ND-LAr. Additionally, it will be able to measure

### 3.5. A MORE CAPABLE NEAR DETECTOR

779 neutrino interactions inside the HPgTPC, achieving lower energy thresholds than those  
780 of the ND and FD LArTPCs. It will also provide a uniform event acceptance, similar  
781 to the FD, which could not be achieved by ND-LAr + TMS. By doing so, ND-GAr  
782 will allow to constrain the relevant systematic uncertainties for the LBL analysis even  
783 further. A detailed discussion on the requirements, design, performance and physics of  
784 ND-GAr can be found in the DUNE ND CDR [89] and the ND-GAr white paper [92].

#### 785 3.5.1 Requirements

786 The primary requirement for ND-GAr is to measure the momentum and charge of  
787 muons from  $\nu_\mu$  and  $\bar{\nu}_\mu$  CC interactions in ND-LAr, in order to measure their energy  
788 spectrum. To achieve the sensitivity to the neutrino oscillation parameters described  
789 in the DUNE FD TDR Volume II [83], ND-GAr should be able to constrain the muon  
790 energy within a 1% uncertainty or better.

791 Another requirement for ND-GAr is the precise measurement of neutrino interactions  
792 on argon for the energies relevant to the neutrino oscillation program. The goal is to  
793 constrain the cross section systematic uncertainties in the regions of phase space that  
794 are not accessible to ND-LAr. This requires the kinematic acceptance for muons in  
795 ND-GAr to exceed that of ND-LAr, being comparable to the one observed in the FD.

796 ND-GAr should also be able to help establishing the relationship between true and  
797 reconstructed energy from neutrino interactions on argon, being sensitive to particles  
798 that are not observed or may be misidentified in ND-LAr. In particular, ND-GAr needs  
799 to have low tracking thresholds in order to measure the spectrum of pions and protons  
800 produced in final-state interactions (FSI). It also must be able to accurately measure  
801 the pion multiplicity in 1, 2 and 3 pions final states, to inform the pion mass correction  
802 in the LArTPCs.

#### 803 3.5.2 Reference design

804 The final design of ND-GAr is still under preparation. However, a preliminary baseline  
805 design was in place at the time of the ND CDR. This section summarises the main

## CHAPTER 3. THE DEEP UNDERGROUND NEUTRINO EXPERIMENT

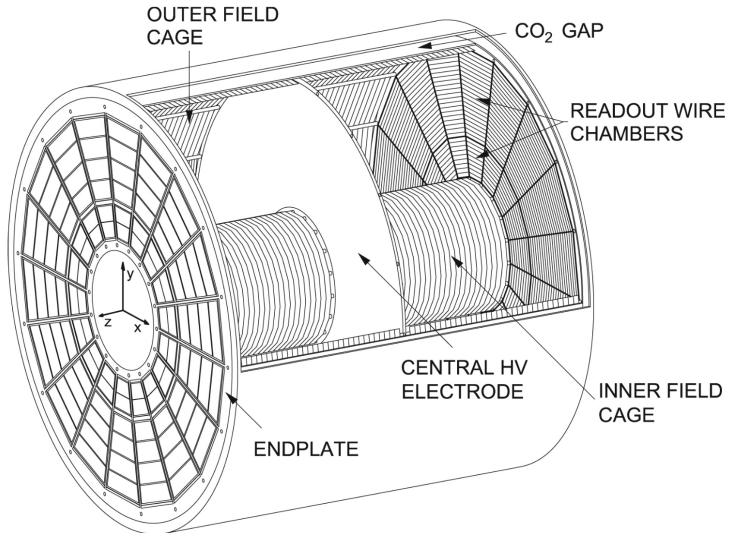


**Figure 3.9:** Diagram of the ALICE TPC, showing the two drift chambers, inner and outer field cages and readout chambers. Figure taken from Ref. [89].

806 features of that design, as it is also the one used by default in our simulation. The  
 807 different options under consideration for the ND-GAr design are further discussed in the  
 808 DUNE Phase II white paper [91].

### 809 HPgTPC

810 The reference design for the ND-GAr HPgTPC follows closely that of the ALICE TPC  
 811 [93]. It is a cylinder with a central high-voltage cathode, generating the electric field  
 812 for the two drift volumes, with a maximum drift distance of 2.5 m each. The anodes  
 813 will be instrumented with charge readout chambers. The original design repurposed  
 814 the multi-wire proportional readout chambers (MWPCs) of ALICE. However, some of  
 815 the current R&D efforts focus on a gas electron multiplier (GEM) [94] option instead.  
 816 Figure 3.9 shows a schematic diagram of the ALICE TPC design. The basic ND-GAr  
 817 geometry will resemble this, except for the inner field cage.

818 It will use a 90:10 molar fraction Ar:CH<sub>4</sub> mixture at 10 bar. With this baseline gas  
 819 mixture light collection is not possible, as the quenching gas absorbs most of the VUV  
 820 photons. Additional R&D efforts are underway, to understand if different mixtures allow  
 821 for the light signal to be used to provide a  $t_0$  while maintaining stable charge gain.

### 3.5. A MORE CAPABLE NEAR DETECTOR

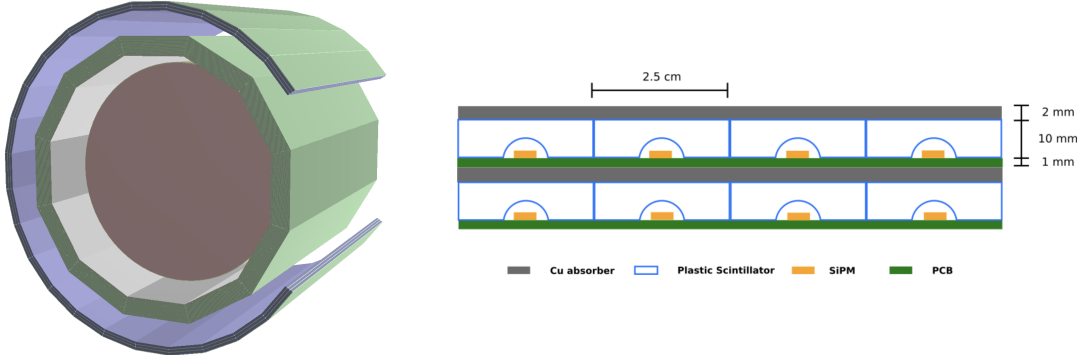


**Figure 3.10:** View of the 12-sided ECal barrel and outer muon tagger geometries (left) and layout of the ECal tile layers for the 2 mm Cu, 10 mm scintillator option (right). Figure adapted from Ref. [89].

#### 822    ECal

823    The main role of the ND-GAr ECal is the calorimetric measurement of the electron  
 824    energies and the reconstruction of photons, in particular those from neutral pion decays.  
 825    Also, the ECal is able to provide a  $t_0$  timestamp for neutrino interactions, by associating  
 826    its activity to the tracks in the HPgTPC. The ECal will also be able to perform neutron  
 827    reconstruction using time-of-flight measurements, and reject external backgrounds thanks  
 828    to its sub-nanosecond time resolution.

829       The ECal design features three independent subdetectors, two end caps at each side  
 830    and a barrel surrounding the HPgTPC. Each of the detectors is divided in modules,  
 831    which combine alternating layers of plastic scintillator and absorber material readout  
 832    by SiPMs. The inner scintillator layers consist of  $2.5 \times 2.5 \text{ cm}^2$  high-granularity tiles,  
 833    whereas the outer layers are made out of 4 cm wide cross-strips spanning the whole  
 834    module length. The current barrel geometry consists of 8 tile layers and 34 strip layers,  
 835    while the end caps feature 6 and 36 respectively. The thickness of the scintillator layers  
 836    is 7 mm and 5 mm for the Pb absorber layers. The 12-sided geometry of the ECal barrel  
 837    (left) and the layout of the tile layers (left)<sup>1</sup> can be seen in Fig. 3.10.

---

<sup>1</sup>The figure shows the layout of the tile layers for a previous design with 2 mm Cu absorber and 10 mm plastic scintillator. As mentioned in the text, the current choice is 5 mm Pb absorber and 7 mm scintillator.

## CHAPTER 3. THE DEEP UNDERGROUND NEUTRINO EXPERIMENT

### 838 Magnet

839 The ND-GAr magnet design, know as the Solenoid with Partial Yoke (SPY), consists  
840 of two coupled solenoids with an iron return yoke [95]. The idea behind the design is  
841 to have a solenoid as thin as possible, as well as a return yoke mass distribution that  
842 minimises the material budget between ND-LAr and ND-GAr. The magnet needs to  
843 provide a 0.5 T field in the direction perpendicular to the beam, parallel to the drift  
844 electric field. It needs to host the pressure vessel and the surrounding ECal, which points  
845 to a inner diameter of  $\sim 6.4$  m.

846 The solenoid is a single layer coil, based on niobium titanium superconducting  
847 Rutherford cable. The total length of the coil is 7.5 m. The bobbin will be split in four  
848 segments, grouped in pairs with two identical cryostats connected in series. The iron  
849 yoke features an aperture in the upstream side, to minimise the energy loss of the muons  
850 coming from ND-LAr. Still, its material will be enough to reduce the magnetic field  
851 reaching SAND, and also stop the charged pions produced inside the HPgTPC.

### 852 Muon system

853 The design of the ND-GAr muon system is still in a preliminary stage. Its role is to  
854 distinguish between muons and pions punching through the ECal. This is especially  
855 important for wrong-sign determination, to separate these from neutral current events.

856 In its current form, the muon system consists of three layers of longitudinal sampling  
857 structures. It alternates 10 cm Fe absorber slabs with 2 cm plastic scintillator strips.  
858 The transverse granularity required is still under study.

### 859 3.5.3 R&D efforts

860 There are several ND-GAr-related prototypes, mostly focused on the TPC charge  
861 readout and electronics. The priority is to test the full readout chain, in a high-pressure  
862 environment, using a gas mixture with high argon fraction. A detailed summary of these  
863 can be found in the DUNE Phase II white paper [91].

### 3.5. A MORE CAPABLE NEAR DETECTOR

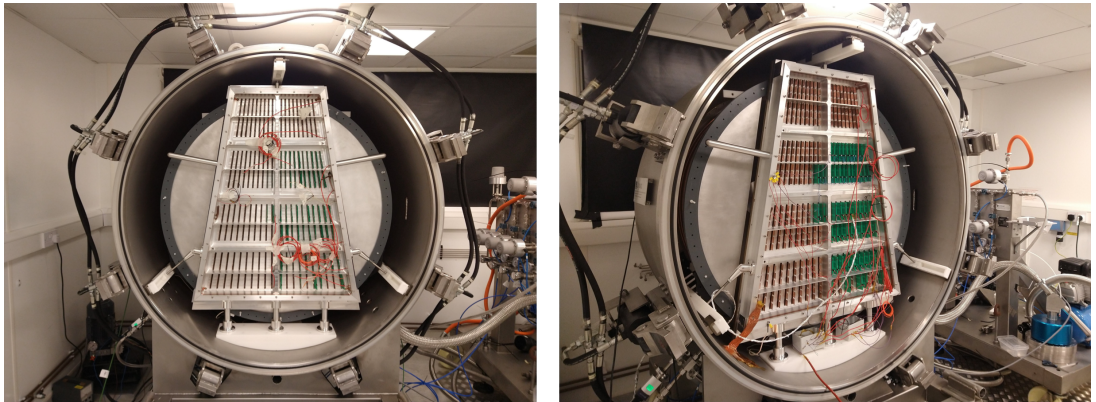


**Figure 3.11:** Photographs of the TOAD pressure vessel at RHUL. The TPC is mounted inside the vessel, and the OROC is supported by an aluminium frame. Figure taken from Ref. [96].

#### 864 Multi-Wire Proportional Chambers

865 As mentioned before, the original ND-GAr design repurposes the MWPCs of the ALICE  
866 TPC, which became available after the recent upgrade [97]. These were operated using  
867 a 90:10:5 Ne:CO<sub>2</sub>:N<sub>2</sub> gas mixture at 1 atm. Therefore, their performance needed to be  
868 studied in an argon gas environment at high pressure.

869 The Gas-argon Operation of ALICE TPC (GOAT) test stand tested the ALICE  
870 readout chambers at high pressure. In particular, it used one of the previously operated  
871 ALICE inner MWPCs, also known as IROCs, in a pressure vessel rated to 10 atm. It  
872 measured the gas gain at various pressure points, voltages and gas mixtures.

873 The Test stand of an Overpressure Argon Detector (TOAD) tested an ALICE outer  
874 MWPC, also known as OROC, up to 5 atm. During its time at RHUL, it was used to  
875 study the achievable gas gain of the OROC [96]. At the moment, it is being commissioned  
876 at Fermilab for a full detector test of the readout electronics and the DAQ.

877 Figure 3.11 shows the interior of the TOAD pressure vessel. The TPC is mounted  
878 inside the vessel on three rails. The back of the OROC, supported by an aluminium  
879 frame, can be seen at the front.

## CHAPTER 3. THE DEEP UNDERGROUND NEUTRINO EXPERIMENT

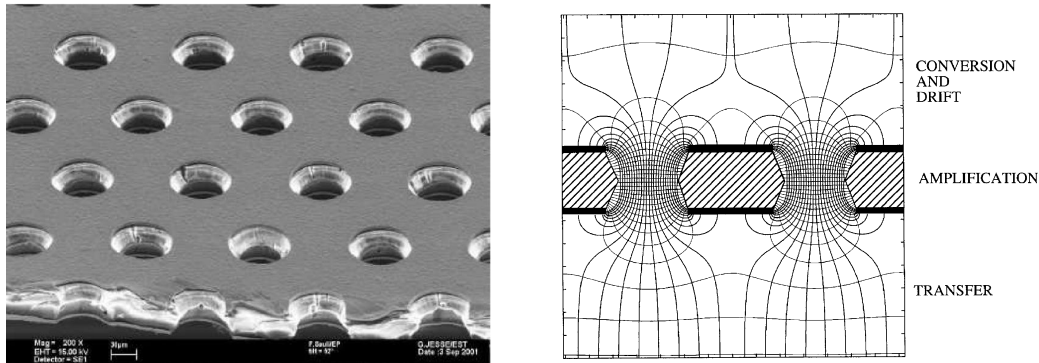


**Figure 3.12:** Left panel: electron microscope image of a 50  $\mu\text{m}$  thick GEM electrode, with hole pitch and diameter of 140 and 70  $\mu\text{m}$ , respectively. Right panel: Schematics of a GEM electrode cross section, showing the electric field lines around the holes. Figures taken from Ref. [98].

### 880 Gas Electron Multiplier

881 An alternative to the MWPC option is the use of GEMs. These are a type of micro-patter  
 882 detector, where the ionisation electrons passing through the holes in the GEM layers  
 883 are accelerated by a high intensity electric field. The acceleration causes the electrons  
 884 to ionise the medium, resulting in an avalanche which increase the signal exponentially  
 885 [94]. GEMs are used in numerous experiments that need a high spatial resolution, like  
 886 ALICE [99] and CMS [100] after their upgrades.

887 Figure 3.12 (left panel) shows an electron microscope picture of a 50  $\mu\text{m}$  thick GEM  
 888 electrode, with a pitch between neighbouring holes of 140  $\mu\text{m}$  and a hole diameter of  
 889 70  $\mu\text{m}$ . A schematic representation of the cross section of a GEM layer is shown in Fig.  
 890 3.12 (left panel).

891 The Gaseous Argon T0 (GAT0<sup>2</sup>) prototype studies the use of thick GEMs made out  
 892 of glass to achieve optical imaging of the primary ionisation. Using a 10 atm pressure  
 893 vessel, the goal is to study different argon-based mixtures that allow for a precise  $t_0$   
 894 determination.

895 The GEM Over-pressurized with Reference Gases (GORG<sup>3</sup>) test stand is currently  
 896 testing a GEM-based charge readout, using a triple-GEM stack.

---

<sup>2</sup>Spanish for cat.

<sup>3</sup>Persian for wolf.

### 3.6. FAR DETECTOR

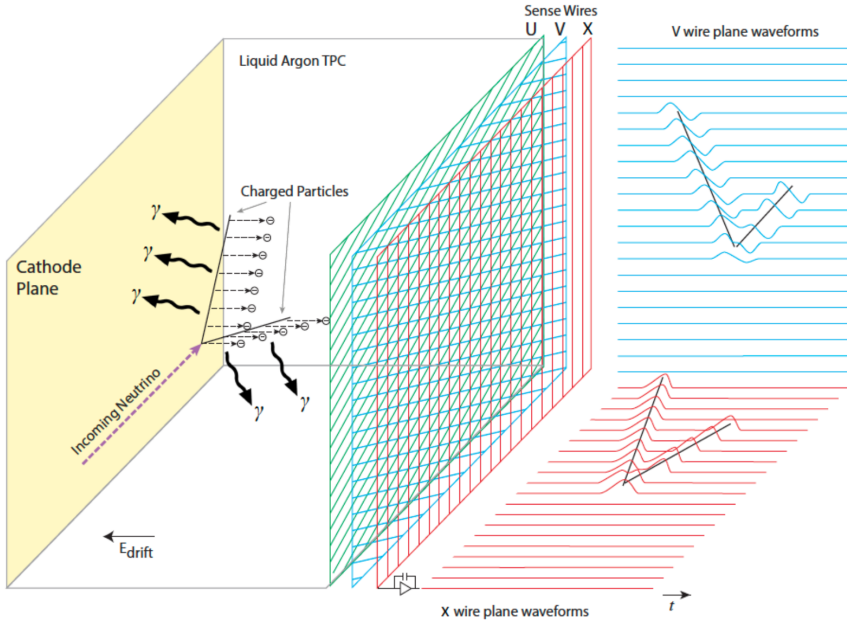


**Figure 3.13:** Schematic diagram showing the operating principle of a LArTPC with wire readout. Figure taken from Ref. [14].

## 897 3.6 Far Detector

898 The DUNE FD complex will sit 1300 km away from the beam target and 1.5 km  
 899 underground at SURF, South Dakota. Two caverns will host the four FD modules, two  
 900 of them per cavern, each embedded in cryostats of dimensions 18.9 m (w)  $\times$  17.8 m (h)  $\times$   
 901 65.8 m (l). A central, smaller cavern will host the cryogenic system.

902 Three out of the four modules are confirmed to be LArTPC detectors, with a LAr  
 903 fiducial mass of at least 10 kt each. The first and third FD modules, FD-1 and FD-3,  
 904 will use a Vertical Drift (VD) technology, whereas the second module, FD-2, will have  
 905 a Horizontal Drift (HD) direction. The technology for the fourth module is still to be  
 906 decided.

907 For each event, with energies ranging from a few MeV to several GeV, these detectors  
 908 collect both the scintillation light and the ionisation electrons created when the charged  
 909 particles produced in neutrino-nucleus interactions ionise the argon nuclei. In both HD  
 910 and VD designs the characteristic 128 nm scintillation light of argon is collected by a  
 911 photon detection system (PDS). This light will indicate the time at which electrons

## CHAPTER 3. THE DEEP UNDERGROUND NEUTRINO EXPERIMENT

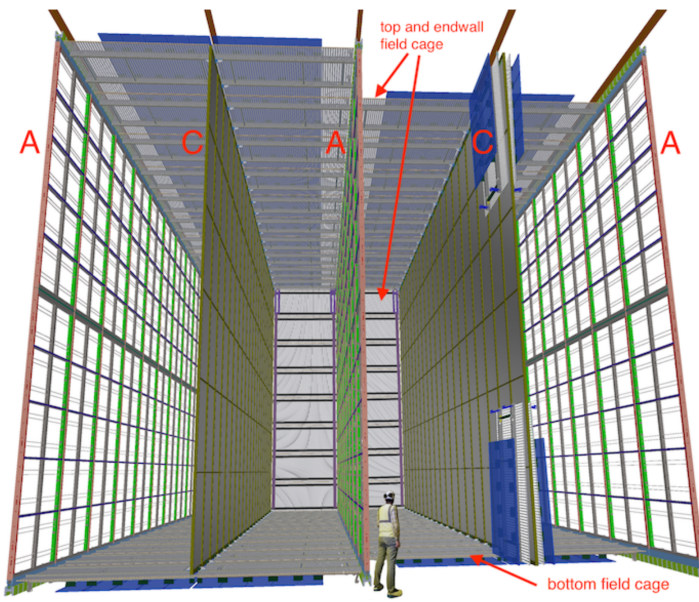


**Figure 3.14:** Proposed design for the FD-2 module following the HD principle. Figure taken from Ref. [14].

912 start to drift, thus enabling reconstruction over the drift coordinate when compared  
 913 to the time when the first ionisation electron arrives to the anode. Reconstruction of  
 914 the topology in the transverse direction is achieved using the charge readout. Fig. 3.13  
 915 illustrates the detection principle described, for the case of a HD detector with a wire  
 916 readout.

### 917 3.6.1 Horizontal Drift

918 In the HD design the ionisation electrons produced as charged particles traverse the  
 919 LAr drift horizontally towards the anode planes, due to the effect of an electric field.  
 920 These anode planes are made out of three layers of wire readout. This design, previously  
 921 known as single-phase (SP), was tested in the ProtoDUNE-SP detector at CERN. The  
 922 prototype collected data from a hadron beam and cosmic rays, providing high-quality  
 923 data sets for calibration and performance studies.

924 Each FD HD detector module is divided in four drift regions, with a maximum drift  
 925 length of 3.5 m, by alternating anode and cathode walls. The surrounding field cage  
 926 ensures the uniformity of the 500 V/cm horizontal electric field across the drift volumes.

### 3.6. FAR DETECTOR

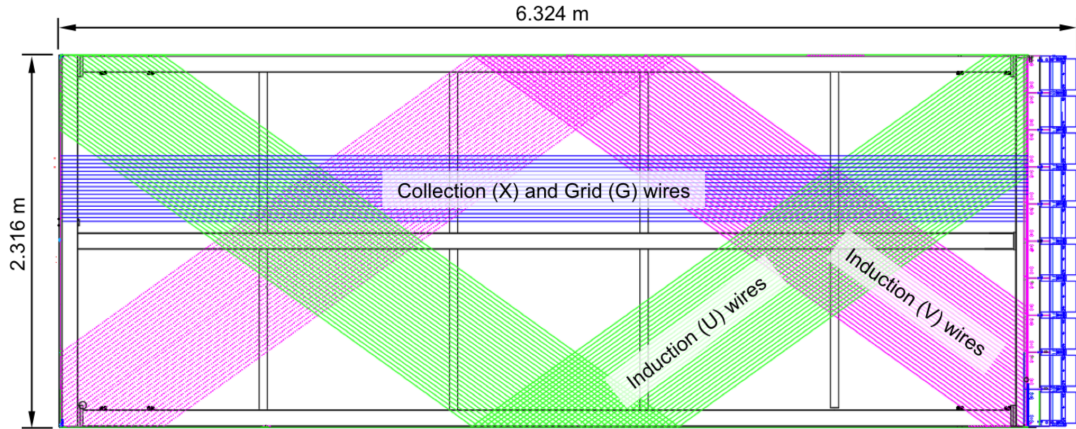


**Figure 3.15:** Schematic representation of an APA. The black lines represent the APA steel frame. The green and magenta lines correspond to the direction of the U and V induction wires respectively. The blue lines indicate the direction of the X collection wires and the wire shielding G. Figure taken from Ref. [14].

927 The three anode walls, which constitute the charge readout of the detector, are built by  
 928 stacking anode plane assemblies (APAs), 2 high times 25 wide. The design of the HD  
 929 modules is shown in Fig. 3.14.

930 Each APA is made of 2560 active wires arranged in three layers, plus an extra grid  
 931 layer, wrapped around a metal frame. The two induction wire planes, U and V, sit at  
 932  $\pm 35.7^\circ$  to the vertical on each side of the APA. The collection and shielding plane wires,  
 933 X and G, run parallel to the vertical direction. The ionisation electrons drift past the  
 934 induction planes, generating bipolar signals on those wires, and are collected by the  
 935 collection plane, producing a monopolar positive signal. The spacing between the wires  
 936 is  $\sim 5$  mm, and it defines the spatial resolution of the APA.

937 The front-end readout electronics, or cold electronics as they are immerse in the LAr,  
 938 are attached to the top of the up APAs and the bottom of the down APAs. Mounted on  
 939 the front-end mother boards we have a series of ASICs that digitise the signals from the  
 940 collection and induction planes. Each wire signal goes to a charge-sensitive amplifier,  
 941 then there is a pulse-shaping circuit and this is followed by the analogue-to-digital  
 942 converter. This part of the process happens inside the LAr to minimise the number of  
 943 cables penetrating the cryostat. The digitised signals come out finally via a series of

## CHAPTER 3. THE DEEP UNDERGROUND NEUTRINO EXPERIMENT

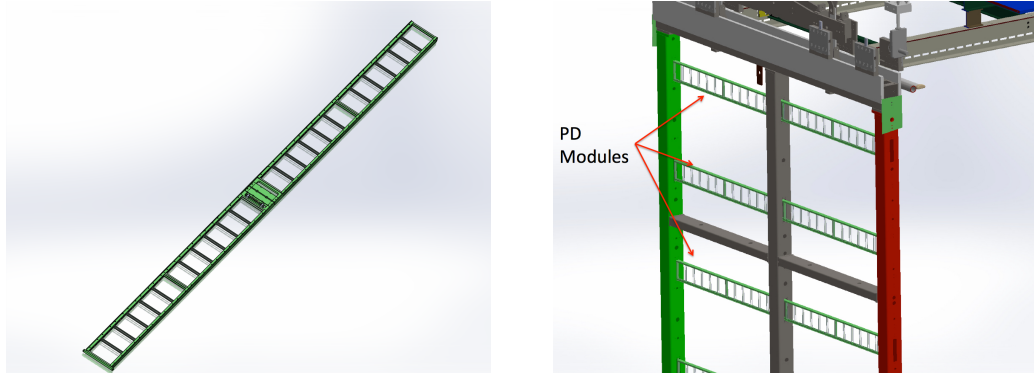


**Figure 3.16:** A PDS module containing 24 X-ARAPUCAs (left) and the location of the modules on the APAs (right). Figure taken from Ref. [14].

944 high-speed serial links to the warm interface boards (WIBs), from where the data is sent  
 945 to the back-end DAQ through optical fibers.

946 The PDS uses modules of X-ARAPUCA devices, mounted on the APA frames  
 947 between the wire planes. Each X-ARAPUCA consists of layers of dichroic filter and  
 948 wavelength-shifter. They shift the VUV scintillation light into the visible spectrum,  
 949 sending then the visible photons to silicon photomultiplier (SiPM) devices. The PDS  
 950 modules are 209 cm × 12 cm × 2 cm bars, containing 24 X-ARAPUCAs. There are 10  
 951 of these PDS modules per APA. Fig. 3.16 shows a PDS module (left) and the placement  
 952 of the modules on the APAs (right).

### 953 3.6.2 Vertical Drift

954 In the VD case the ionisation electrons will drift vertically until they meet a printed  
 955 circuit board-based (PCB) readout plane. It is based on the original dual-phase (DP)  
 956 design deployed at CERN, in the detector known as ProtoDUNE-DP, which used a  
 957 vertical drift design with an additional amplification of the ionisation electrons using a  
 958 GAr layer above the liquid phase. The VD module incorporates the positive features of  
 959 the DP design without the complications of having the LAr-GAr interface.

960 The current design of the FD VD module consists of two drift chambers with  
 961 a maximum drift distance of 6.5 m. A cathode plane splits the detector volume  
 962 perpendicular to the drift direction, while the two anode planes are connected to the

### 3.6. FAR DETECTOR

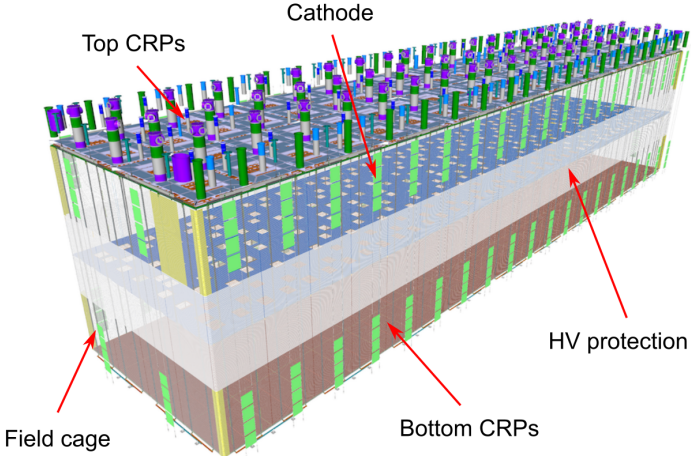


**Figure 3.17:** Proposed design for the FD-1 and FD-3 modules following the VD principle. Figure adapted from Ref. [101].

bottom and top walls of the detector. The layout of the VD module is shown in Fig. 3.17. Compared with the HD design, the VD option offers a slightly larger instrumented volume and a more cost-effective solution for the charge readout.

As in the HD design, each drift volume features a 500 V/cm electric field and a field cage that ensures its uniformity. The anode planes are arrays of  $3.4\text{ m} \times 3\text{ m}$  charge-readout planes (CRPs). These are formed by a pair of charge-readout units (CRUs), which are built from two double-sided perforated PCBs, with their perforations aligned. The perforations allow the drift electrons to pass between the layers.

The PCB face opposite to the cathode has a copper guard plane which acts as shielding, while its reverse face is etched with electrode strips forming the first induction plane. The outer PCB has electrode strips on both faces, the ones facing the inner PCB form the second induction plane while the outermost ones form the collection plane. Fig. 3.18 shows the layout of the electrode strips for the top (left) and bottom (right) CRUs. The magenta and blue lines represent the first and second induction planes respectively, and the green lines correspond to the collection plane.

The PDS in the VD module will use the same X-ARAPUCA technology developed for the HD design. The plan is to place the PDS modules on the cryostat walls and on

## CHAPTER 3. THE DEEP UNDERGROUND NEUTRINO EXPERIMENT

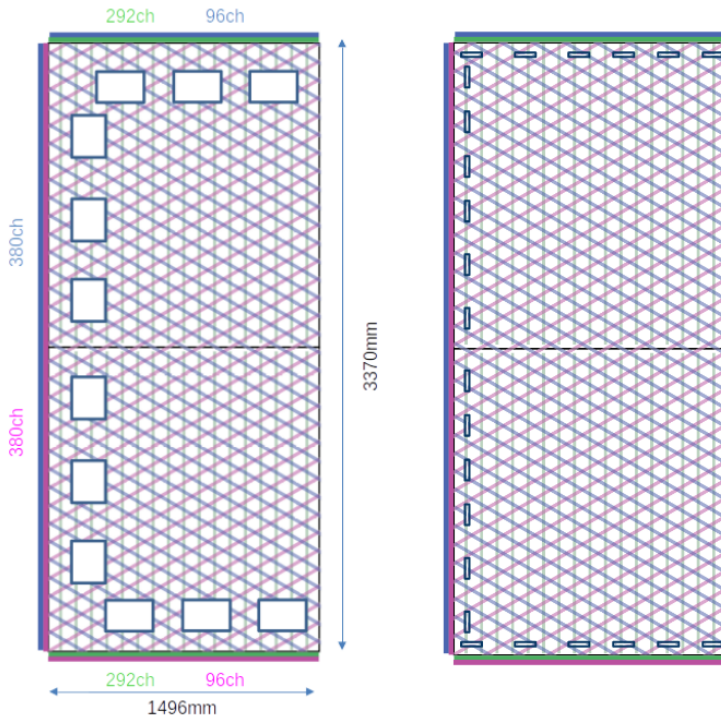


**Figure 3.18:** Schematic representation of the electrode strip configuration for a top (left) and bottom (right) CRU. Figure taken from Ref. [101].

980 the cathode, in order to maximise the photon yield.

981 **3.6.3 FD Data Acquisition System**

982 The data acquisition (DAQ) system receives, processes and stores data from the detector  
983 modules. In the case of DUNE, the DAQ architecture is designed to work for all FD  
984 modules interchangeably, except some aspects of the upstream part which may depend  
985 on the specific module technology.

986 The enormous sample rate and the number of channels in TPC and PD readouts  
987 will produce a very large volume of data. These pose really strong requirements and  
988 challenges to the DUNE FD DAQ architecture. It will be required to read out data of  
989 the order of ten thousand or more channels at rates of a few MHz. To cope with the  
990 huge data volume, segmented readouts and compression algorithms are used to reduce  
991 the data rate to manageable levels.

992 The DAQ system of the DUNE FD is composed of five different subsystems. The

### 3.6. FAR DETECTOR

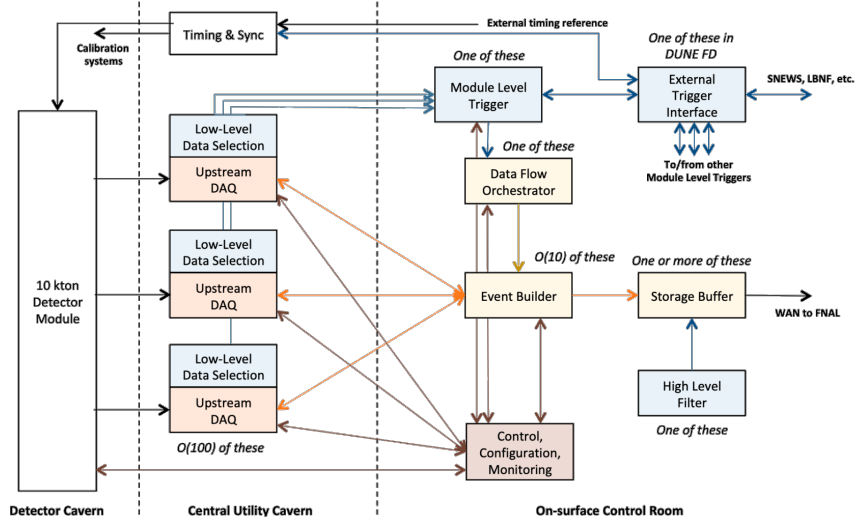


**Figure 3.19:** Detailed diagram of the DUNE FD DAQ system. Figure taken from Ref. [102].

993 first one is the upstream DAQ, which receives the raw data from the detector, buffers it  
994 and performs some low-level pre-processing. The minimally processed data is then fed  
995 into a hierarchical data selection system, which then performs a module level trigger  
996 decision. In case of a positive decision, a trigger command is produced and executed by  
997 the data flow orchestrator, located in the back-end (BE) DAQ subsystem. Subsequently  
998 the DAQ BE retrieves the relevant data from the buffers located in the upstream DAQ,  
999 adds all the data into a cohesive record and saves it to permanent storage. Watching  
1000 over all the other subsystems we also have the control, configuration and monitoring  
1001 subsystem and the time and synchronization subsystem. Figure 3.19 shows a schematic  
1002 diagram of the DAQ system, showing the different subsystems and their relations.

1003 A notorious challenge for the DUNE DAQ system comes from its broad physics goals.  
1004 We must be prepared to process events spanning a wide range of time windows from  
1005 5 ms in the case of beam and cosmic neutrinos and nucleon decay events, to 100 s in the  
1006 case of SNBs. This requires a continuous readout of the detector modules. Moreover,  
1007 because of the off-beam measurements, we need to ensure the capabilities of online data  
1008 processing and self-triggering. Having this into account, together with the technical  
1009 constraints, the DUNE FD DAQ faces a series of challenges: it needs to be fault tolerant

### CHAPTER 3. THE DEEP UNDERGROUND NEUTRINO EXPERIMENT

and redundant to reduce downtime, accommodate new components while it keeps serving the operational modules, have large upstream buffers to handle SNB physics, be able to support a wide range of readout windows, and reduce the throughput of data to permanent storage to be at most 30 PB/year.

1014

1015

## Matched Filter approach to Trigger

1016

## Primitives

1017

*It is a capital mistake to theorize before one has data. Insensibly one begins to twist facts to suit theories, instead of theories to suit facts.*

1019

– Arthur Conan Doyle, *A scandal in Bohemia*

1020

The DAQ system is responsible for the data that will be collected in the DUNE FD. Therefore, it has the capability of either expanding or limiting our physics reach, depending of its specifications. This is important for the low energy physics programme, as it requires more sensitive and reliable methods to pick up the relevant signals.

1024

In this Chapter, I present a novel method to improve the sensitivity of the DUNE FD by enhancing the production of hits in the online processing. This is possible thanks to a more efficient filtering strategy, the matched filter, which benefits the induction channels of the detector.

1028

### 4.1 Motivation

1029

The lowest-level objects that are formed within the DUNE FD DAQ system are the so-called trigger primitives (TPs) [103]. These represent the hits on a channel, and are used as input to the rest of the DAQ trigger chain. The TPs are formed in the hit finder chain. A schematic representation of it is shown in Fig. 4.1. This chain takes the raw ADC data from the detector, removes the constant pedestal of the signal using a

## CHAPTER 4. MATCHED FILTER APPROACH TO TRIGGER PRIMITIVES



**Figure 4.1:** Schematic representation of the Trigger Primitive Generation chain in the DUNE FD.

1034 dynamical median estimation method, applies a filter to the waveform, and tries to find  
 1035 peaks over a certain threshold. These peaks form the TPs, which contain information  
 1036 such as the start and end times over the threshold, the maximum ADC value and the  
 1037 corresponding ADC integral. Currently, there are two implementations of the hit finder  
 1038 chain, one firmware-based and other software-based.

1039 The filter implemented in the firmware of the upstream DUNE FD DAQ is a 32nd-  
 1040 order low-pass finite impulse-response (FIR) filter. The output of such filter for a discrete  
 1041 system can be written as:

$$y[i] = \sum_{j=0}^N h[i]x[i-j], \quad (4.1)$$

1042 where  $N$  is the order of the filter,  $y$  is the output sequence,  $x$  is the input sequence and  
 1043  $h$  is the set of filter coefficients. The current implementation within `dtp-firmware` [104]  
 1044 uses a set of 16 non-zero integer coefficients. For the software case, only a 5th-order  
 1045 filter is used, as the filtering is the most CPU-expensive part of the software hit finder.

1046 Filtering is a vital step in the hit finder chain. It helps suppressing the noise and  
 1047 enhances the signal peaks with respect to the noiseless baseline. A good filtering strategy  
 1048 allows us to use lower thresholds when forming the TPs, thus increasing the sensitivity  
 1049 of our detector to low energy physics events. In such events, the hits produced by the  
 1050 ionisation electrons tend to have lower amplitudes than those of interest to the LBL  
 1051 physics programme of the DUNE experiment.

1052 This is particularly important for the induction planes. In general, signal peaks in  
 1053 the induction channels have smaller amplitude than the ones in the collection plane.  
 1054 This, together with the fact that the pulse shapes are bipolar, reduces our capacity to

## 4.2. SIGNAL-TO-NOISE RATIO DEFINITION

1055 detect the hits on these channels. The inefficiency of detecting TPs in the induction  
1056 planes (denoted as U and V planes) leads trigger algorithms to focus mainly on the  
1057 TPs from the collection plane (so-called X plane). As a result, the possibility of making  
1058 trigger decisions based on the coincidence of TPs across the three wire planes remains  
1059 nowadays unexploited in DUNE. This will be beneficial for low energy events, as it  
1060 adds redundancy to the algorithms, as well as for other physics that requires online  
1061 directionality information, like the supernova pointing.

1062 A possible improvement of the current hit finder chain may require optimising the  
1063 existing or choosing a new filter implementation. A filter strategy which benefits the  
1064 induction signals may be able to enhance the detection efficiency of TPs from the  
1065 induction planes and ideally make it comparable to that of the collection plane.

1066 The goal is to implement a better finite-impulse response filter and to evaluate its  
1067 performance relative to the current filter. To do so, I need to take into account the  
1068 limitations of the firmware: the FIR filter shall have maximum 32 coefficients (so-called  
1069 taps) whose values are 12-bit unsigned integers. Although it is technically possible to  
1070 include non-integer coefficients, it would be a technical challenge. For instance, in the  
1071 HD design there are 40 FIR instances per APA, as there are 4 FIR blocks per optical  
1072 link and 10 optical links per APA. Therefore, the impact of increasing the complexity of  
1073 the filter will be amplified forty times in the FPGA load. With these restrictions, the  
1074 task is to provide a set of 32 coefficients which yield an optimal filter performance for the  
1075 induction channels. A solution compatible with the software hit finder implementation  
1076 is not considered, due to its current limitations concerning the filtering stage.

## 1077 4.2 Signal-to-noise ratio definition

1078 In the following, I use the signal to noise ratio (S/N) as a measure of the FIR filter  
1079 performance. The S/N metrics allow us to compare different filter implementations  
1080 and serve as a basis for more detailed studies presented later in this Chapter. Here,  
1081 I demonstrate how to extract its value for a set of ProtoDUNE-SP data. Specifically,

## CHAPTER 4. MATCHED FILTER APPROACH TO TRIGGER PRIMITIVES

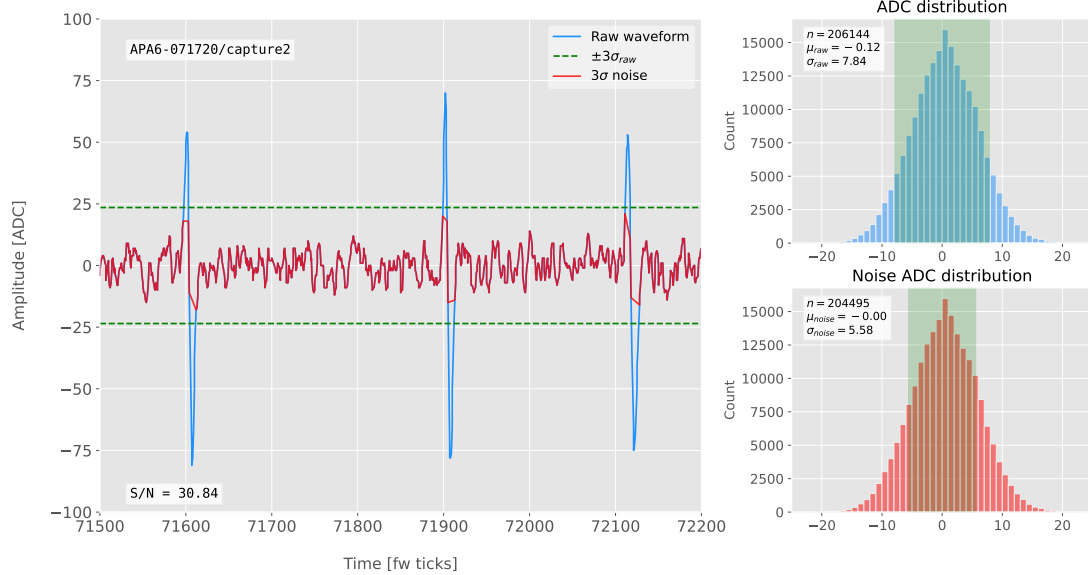


**Figure 4.2:** Left panel: Zoomed unfiltered waveform corresponding to channel 7840 from the ProtoDUNE-SP raw data capture `felix-2020-07-17-21:31:44` (blue line). The green dashed lines mark the region  $\pm 3\sigma_{\text{raw}}$ . The resulting noise waveform is also shown (red line). Top right panel: ADC distribution for channel 7840, where the green shaded region represents  $\pm \sigma_{\text{raw}}$ . Bottom right panel: noise ADC distribution for channel 7840, where the green shaded region represents  $\pm \sigma_{\text{noise}}$ .

1082 I use the ADC capture `felix-2020-07-17-21:31:44`, a raw data capture taken for  
 1083 firmware validation purposes. I define the S/N of a channel as the height of the signal  
 1084 peaks relative to the size of the noise. To quantify this, I first estimate the standard  
 1085 deviation of the ADC data for each channel,  $\sigma_{\text{ADC}}$ . Then, I define the corresponding  
 1086 noise waveform to be the ADC values in the range  $\pm 3 \sigma_{\text{ADC}}$ . From this new noise data  
 1087 I compute the mean and standard deviation,  $\mu_{\text{noise}}$  and  $\sigma_{\text{noise}}$ , so I can write the S/N  
 1088 for any given channel as:

$$\text{S/N} = \frac{\max [\text{ADC}] - \mu_{\text{noise}}}{\sigma_{\text{noise}}}, \quad (4.2)$$

1089 where  $\max [\text{ADC}]$  is simply the maximum ADC value found in the corresponding channel.

1090 As an example, I apply this definition of the S/N to a waveform from one of the  
 1091 channels of the data capture. Figure 4.2 shows a zoomed region of the waveform  
 1092 corresponding to channel 7840 (blue line), where one can clearly see three signal peaks

### 4.3. LOW-PASS FIR FILTER DESIGN

and continuous additive noise<sup>1</sup>. I estimated the standard deviation of this raw waveform to be  $\sigma_{raw} = 7.84$  ADC, and from this I am able to define the noise waveform (red line) as the ADC values in the range  $\pm 23.52$  ADC. This way, I obtain  $\mu_{noise} = 0.01$  ADC and  $\sigma_{noise} = 5.58$  ADC, which gives S/N = 30.84.

I repeat this calculation now for the corresponding filtered waveform, using the current firmware FIR filter. Figure 4.3 shows the same time window for the filtered waveform from channel 7840 (blue line). In this case, the standard deviation of the waveform is larger than before, giving  $\sigma_{raw} = 10.99$  ADC. The noise waveform (red line) is formed by selecting the ADC values in the  $\pm 32.91$  ADC range, which gives  $\mu_{noise} = -0.47$  ADC and  $\sigma_{noise} = 7.03$  ADC. Finally, one obtains S/N = 24.68. Notice that the value of S/N decreases after the filtering. Clearly, one can see that the noise baseline has increased by a factor of 1.35 when we applied the FIR filter, and at the same time the amplitude of the signal peaks has remained almost unchanged, leading to this poorer S/N value.

## 4.3 Low-pass FIR filter design

To optimise the frequency response of a digital filter, we can use the Parks-McClellan algorithm, where one finds a set of  $N$  real coefficients that give the best response for the specified pass-band and order of the filter [105].

Taking the detector ticks as the time unit, the Nyquist frequency will simply be  $1/2$  ticks<sup>-1</sup>. The current implementation of the filter seems to have as pass-band the range  $[0, 0.1]$  ticks<sup>-1</sup>. This can be seen in Fig. 4.4, where I show the power spectrum, in decibels, of that filter implementation (blue solid line). The Park-McClellan algorithm finds the optimal Chebyshev FIR filter [106] taking as input the boundaries of the target pass-band and stop-band, which can be written in the form:

$$\left\{ \begin{array}{l} [0, f_c] \\ [f_c + \delta f, f_N] \end{array} \right. , \quad (4.3)$$

---

<sup>1</sup>There are actually 6 peaks, 3 positive and 3 negative, but, because by design for induction channels the expected signal pulse shapes are bipolar, we treat them as a collection of 3 individual signals.

## CHAPTER 4. MATCHED FILTER APPROACH TO TRIGGER PRIMITIVES

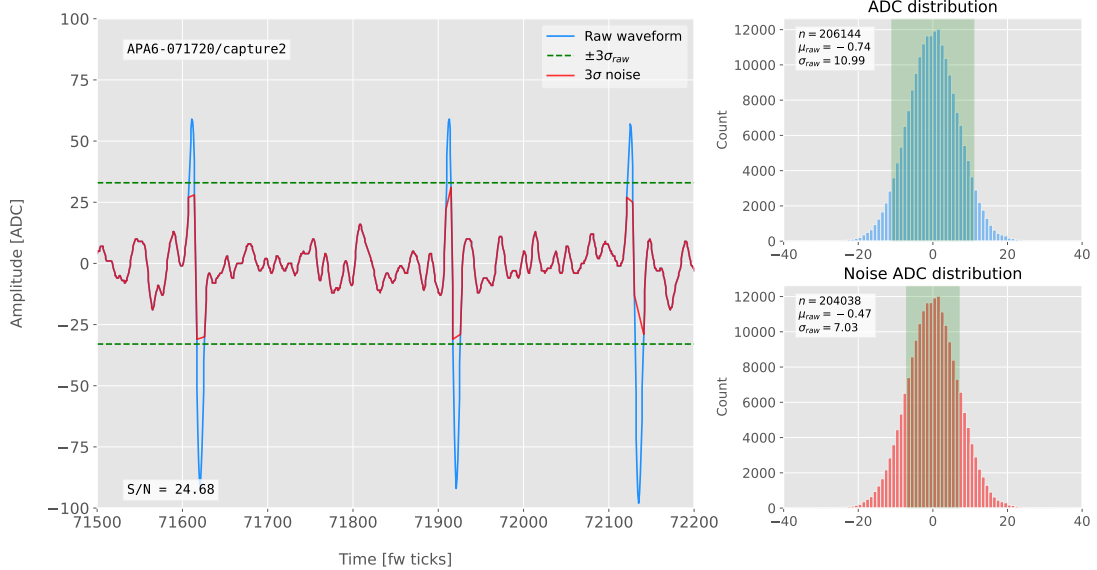


**Figure 4.3:** Left panel: Zoomed filtered waveform corresponding to channel 7840 from the ProtoDUNE-SP raw data capture `felix-2020-07-17-21:31:44` (blue line). The filter used was the current implementation of the low-pass FIR filter in `dtp-firmware`. The green dashed lines mark the region  $\pm 3\sigma_{raw}$ . The resulting noise waveform is also shown (red line). Top right panel: ADC distribution for channel 7840 after filtering, where the green shaded region represents  $\pm \sigma_{raw}$ . Bottom right panel: noise ADC distribution for channel 7840 after filtering, where the green shaded region represents  $\pm \sigma_{noise}$ .

where  $f_c$  is the cut-off frequency,  $\delta f$  is the transition width and  $f_N$  is the aforementioned Nyquist frequency. A filter with a similar behaviour to the previous one can be obtained by setting  $f_c = 0$  and  $\delta f = 0.1 \text{ ticks}^{-1}$ . The response of the resulting filter is also shown in Fig. 4.4 (blue solid line). Notice that the suppression of the stop-band is enhanced for this optimal filter. For comparison, I include the power response of the filter obtained by taking the integer part of the coefficients resulting from the Parks-McClellan method (red dashed line). One can see that it does not suppress that much the stop-band, in a similar way to the current implementation of the filter.

At this point, I tried to improve the performance of the FIR filter using the Parks-McClellan method, i.e. maximise the overall S/N, using the available data captures. I did so by varying the values of the two quantities that parametrise the pass-band and stop-band, the cut-off frequency  $f_c$  and the transition width  $\delta f$ .

### 4.3. LOW-PASS FIR FILTER DESIGN

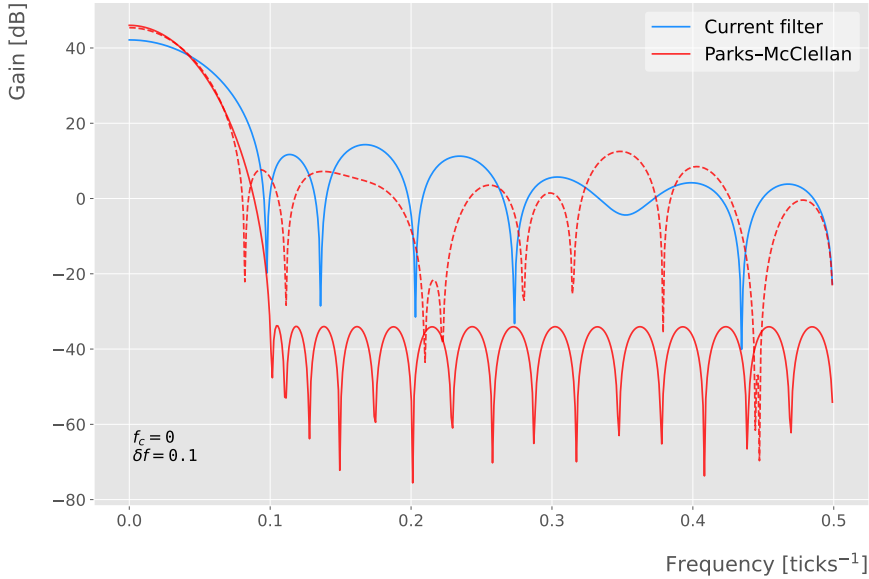


**Figure 4.4:** Power spectrum in decibels for the current implementation of the low-pass FIR filter in `dtp-firmware` (blue line), compared to the response of an optimal filter obtained using the Parks-McClellan algorithm for the same pass-band (red line). Also for comparison I include the spectrum of the optimal filter when taking only the integer part of the coefficients (red dashed line).

Figure 4.5 shows the average relative change in the S/N (i.e. the ratio between the value of the S/N after and before the filtering) for capture `felix-2020-07-17-21:31:44`, when using filters designed with the Parks-McClellan algorithm for the specified values of the cut-off frequency  $f_c$  and the transition width  $\delta f$ , restricted to integer values for the filter coefficients. One can clearly distinguish different regions where we get an improvement of up to a factor of 1.35 for the U plane. For large values of  $f_c + \delta f$  the ratio tends to 1, as expected. In that limit the width of the stop-band goes to 0, meaning that no frequencies are filtered out and thus the waveform remains the same.

As it can be seen in Fig. 4.5 (bottom right panel) the configuration which gives the best mean performance for the three planes is  $f_c = 0.068$  ticks<sup>-1</sup> and  $\delta f = 0.010$  ticks<sup>-1</sup>. We can use these to see how the filter affects the different channels. Figure 4.6 shows the distribution of the S/N improvement values for all the channels in the raw ADC capture `felix-2020-07-17-21:31:44`, separated by wire plane, after the optimal Chebyshev filter was applied. One can see that there is a clear improvement for both U and V

## CHAPTER 4. MATCHED FILTER APPROACH TO TRIGGER PRIMITIVES

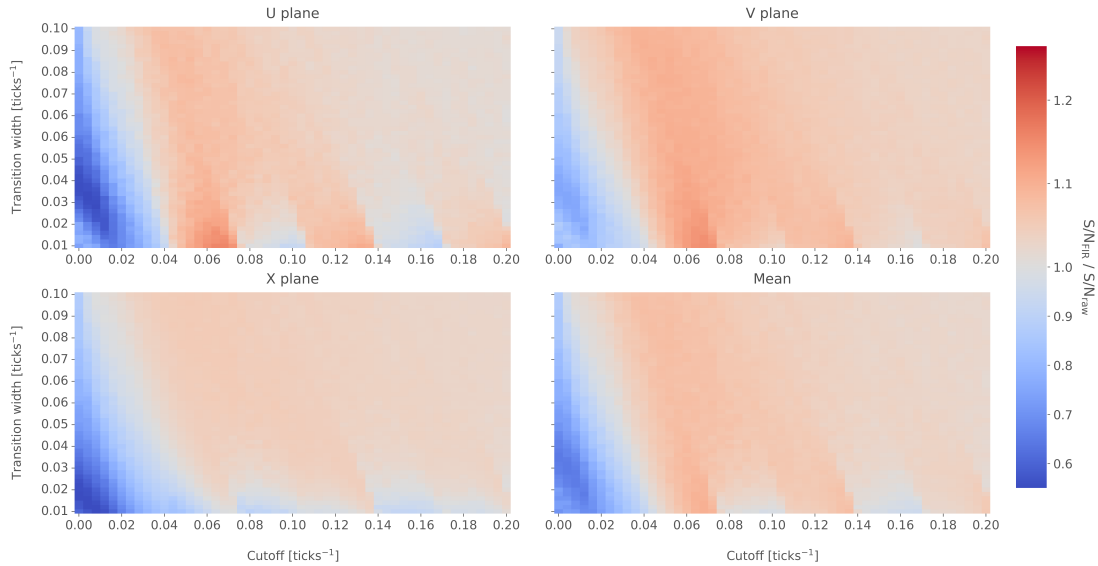


**Figure 4.5:** Relative change in the S/N for the ProtoDUNE-SP raw data capture `felix-2020-07-17-21:31:44`, using different values of the cutoff frequency  $f_c$  and the transition width  $\delta f$ . The optimal Chebyshev filters were applied using just the integer part of the coefficients given by the Parks-McClellan algorithm.

induction planes, obtaining a mean change of 1.25 and 1.30 for them, respectively. However, in the case of the X collection plane the distribution peaks around 1, meaning that an important fraction of channels in that plane get a slightly worse S/N after the filter is applied. This is not a big issue, as the S/N for collection channels is usually much higher than the one for induction channels.

The results I obtained optimising the low pass filter with the Parks-McClellan method are promising. Nonetheless, the improvement found is rather marginal. Thus, I explored alternative approaches to the filtering problem, which may yield better outputs. This way, I found a possible solution in matched filters. By construction, this kind of filters offer the best improvement on the S/N.

## 4.4 Matched filters

In the context of signal processing, a matched filter is the optimal linear filter for maximising the S/N in the presence of additive noise. It is obtained by convolving a conjugated time-reversed known template with an unknown signal to detect the presence

#### 4.4. MATCHED FILTERS

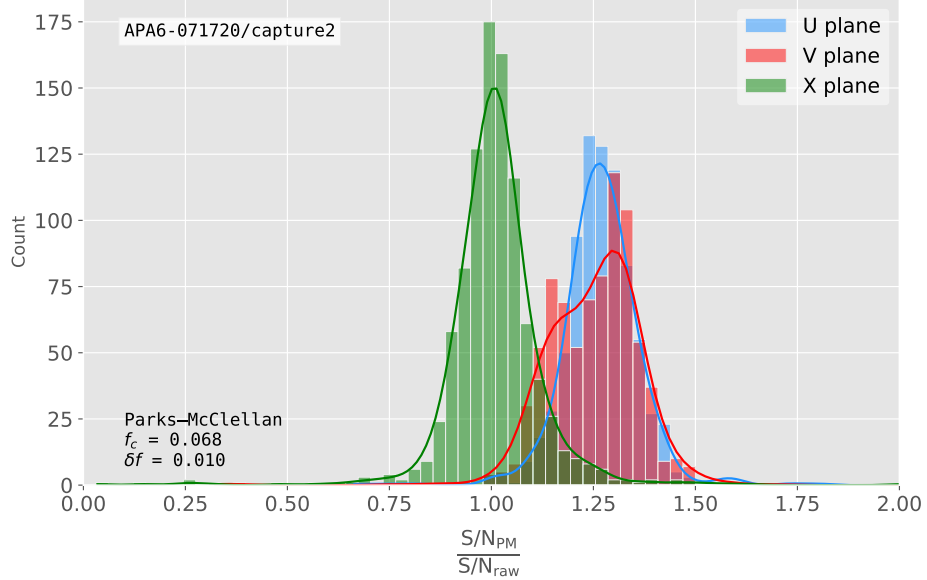


**Figure 4.6:** Distribution of the relative change of the S/N on the different wire planes from the ProtoDUNE-SP raw data capture `felix-2020-07-17-21:31:44` after the optimal Chebyshev filter was applied. The filter was computed with the Parks-McClellan algorithm using a cutoff of  $f_c = 0.068 \text{ ticks}^{-1}$  and a transition width  $\delta f = 0.010 \text{ ticks}^{-1}$ .

1157 of the template in the signal [107].

1158 Given a known signal sequence  $s(t)$  and another (a priori unknown) noise sequence  
1159  $n(t)$ , the input signal can be written as:

$$x(t) = s(t) + n(t). \quad (4.4)$$

1160 Now, considering a linear time-invariant filter, whose impulse-response function I  
1161 will refer to as  $h(t)$ , one can write the output signal as:

$$\begin{aligned} y(t) &= x(t) * h(t) \\ &= (s(t) + n(t)) * h(t) \\ &= y_s(t) + y_n(t), \end{aligned} \quad (4.5)$$

1162 where  $y_s(t)$  and  $y_n(t)$  are simply the outputs of the filter due to the signal and the noise  
1163 components respectively.

1164 The goal of the matched filter is to detect the presence of the signal  $s(t)$  in the input

## CHAPTER 4. MATCHED FILTER APPROACH TO TRIGGER PRIMITIVES

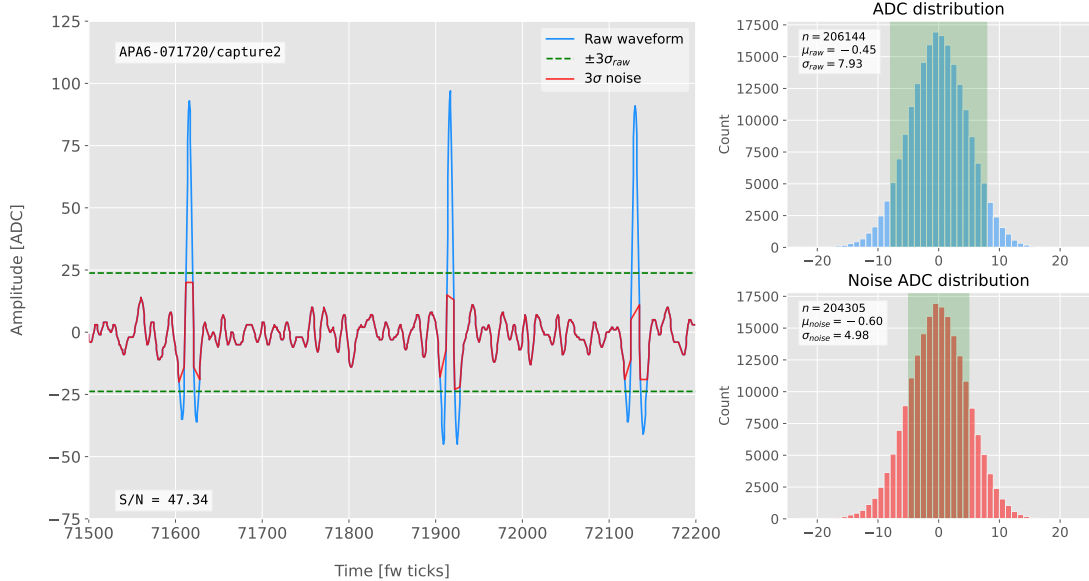


**Figure 4.7:** Left panel: Zoomed match filtered waveform corresponding to channel 7840 from the ProtoDUNE-SP raw data capture `felix-2020-07-17-21:31:44` (blue line). The filter used was directly extracted from the data, being the 32 values around the first peak in the original waveform. The green dashed lines mark the region  $\pm 3\sigma_{\text{raw}}$ . The resulting noise waveform is also shown (red line). Top right panel: ADC distribution for channel 7840 after match filtering, where the green shaded region represents  $\pm \sigma_{\text{raw}}$ . Bottom right panel: noise ADC distribution for channel 7840 after match filtering, where the green shaded region represents  $\pm \sigma_{\text{noise}}$

sample  $x(t)$  at a certain time  $t_0$ , which effectively means that we need to maximise the S/N at that given time. This way, what one wants is to have a filter which gives a much bigger output when the known signal is present than when it is not. Putting it in other words, the instantaneous power of the signal output  $y_s(t)$  should be much larger than the average power of the noise output  $y_n(t)$  at some time  $t_0$ .

For the case of the filtered signal, one can easily re-write it as an inverse Fourier transform:

$$y_s(t) = \frac{1}{2\pi} \int_{-\infty}^{\infty} d\omega H(\omega)S(\omega)e^{i\omega t}, \quad (4.6)$$

where  $H(\omega)$  and  $S(\omega)$  are the Fourier transforms of the impulse-response function (i.e. the transfer function of the filter) and of the input signal, respectively.

Now, focusing on the noise part, we can use the Wiener-Khinchin theorem [108] to

#### 4.4. MATCHED FILTERS

1175 write the mean power of the noise after filtering as:

$$E|y_n(t)|^2 = \frac{1}{2\pi} \int_{-\infty}^{\infty} d\omega |H(\omega)|^2 S_n(\omega), \quad (4.7)$$

1176 where  $S_n(\omega)$  is the power spectral density of the noise.

1177 Having these, one can write the instantaneous S/N at time  $t_0$  as:

$$\begin{aligned} \left( \frac{S}{N} \right)_{t_0} &= \frac{|y_s|^2}{E|y_n(t)|^2} \\ &= \frac{1}{2\pi} \frac{\left| \int_{-\infty}^{\infty} d\omega H(\omega) S(\omega) e^{i\omega t_0} \right|^2}{\int_{-\infty}^{\infty} d\omega |H(\omega)|^2 S_n(\omega)}. \end{aligned} \quad (4.8)$$

1178 Once we have this expression, we need to find its upper limit to determine what would  
1179 be the optimal choice for the transfer function. For this, we use the Cauchy-Schwarz  
1180 inequality, which in the present case takes the form:

$$\left| \int_{-\infty}^{\infty} dx f(x) g(x) \right|^2 \leq \int_{-\infty}^{\infty} dx |f(x)|^2 + \int_{-\infty}^{\infty} dx |g(x)|^2, \quad (4.9)$$

1181 for any two analytical functions  $f(x)$  and  $g(x)$ . One can prove that making the choice:

$$\begin{aligned} f(x) &= H(\omega) \sqrt{S_n(\omega)} e^{i\omega t_0}, \\ g(x) &= \frac{S(\omega)}{\sqrt{S_n(\omega)}}, \end{aligned} \quad (4.10)$$

1182 leads to the following upper bound for the S/N:

$$\left( \frac{S}{N} \right)_{t_0} \leq \frac{1}{2\pi} \int_{-\infty}^{\infty} d\omega \frac{|S(\omega)|^2}{S_n(\omega)}. \quad (4.11)$$

1183 From Eqs. (4.8), (4.9) and (4.10) one can also derive the form of the transfer function  
1184 such that the upper bound is exactly reached [109]:

$$H(\omega) \propto \frac{S^*(\omega) e^{-i\omega t_0}}{S_n(\omega)}. \quad (4.12)$$

## CHAPTER 4. MATCHED FILTER APPROACH TO TRIGGER PRIMITIVES

1185 From this last expression we can clearly see the way the matched filter acts. As the  
 1186 transfer function is proportional to the Fourier transform of the signal it will try to only  
 1187 pick the frequencies present in the signal [110].

1188 The matched filter transfer function can be greatly simplified if the input noise is  
 1189 Gaussian. In that case, the power spectral density of the noise is a constant, so it can be  
 1190 re-absorbed in the overall normalisation of the transfer function. Moreover, considering  
 1191 that the input signal is a real function, one can simply set  $S^*(\omega) = S(-\omega)$ , which gives:

$$H(\omega) \propto S(-\omega)e^{-i\omega t_0}. \quad (4.13)$$

1192 For a discrete signal, one can think of the input and impulse-response sequences  
 1193 as vectors. Then, the matched filter tries to maximise the inner product of the signal  
 1194 and the filter while minimising the output due to the noise by choosing a filter vector  
 1195 orthogonal to the latter. In the case of additive noise, that leads to the impulse-response  
 1196 vector:

$$h = \frac{1}{\sqrt{s^\dagger R_n^{-1} s}} R_n^{-1} s, \quad (4.14)$$

1197 where  $s$  is a reversed signal template sequence of length  $N$  equal to the order of the filter  
 1198 and  $R_n$  is the covariance matrix associated with the noise sequence  $n$ . For the Gaussian  
 1199 noise case, the covariance matrix is simply the unit matrix, so the above expression  
 1200 simplifies again to:

$$h = \frac{s}{|s|}. \quad (4.15)$$

1201 To test whether this choice of filter is appropriate one needs to choose a signal  
 1202 template. As an example of how a matched filter would affect our signal, I simply took  
 1203 the matched filter coefficients to be the 32 ADC values around a signal peak present in  
 1204 the data. In Fig. 4.7 (left panel) I plotted a zoomed region for channel 7840 in the raw  
 1205 data capture `felix-2020-07-17-21:31:44`, after applying the matched filter described  
 1206 before (blue line). When compared to the raw and FIR filtered case (see Figs. 4.2 and  
 1207 4.3), after applying the matched filter the standard deviation of the noise waveform (red

#### 4.4. MATCHED FILTERS

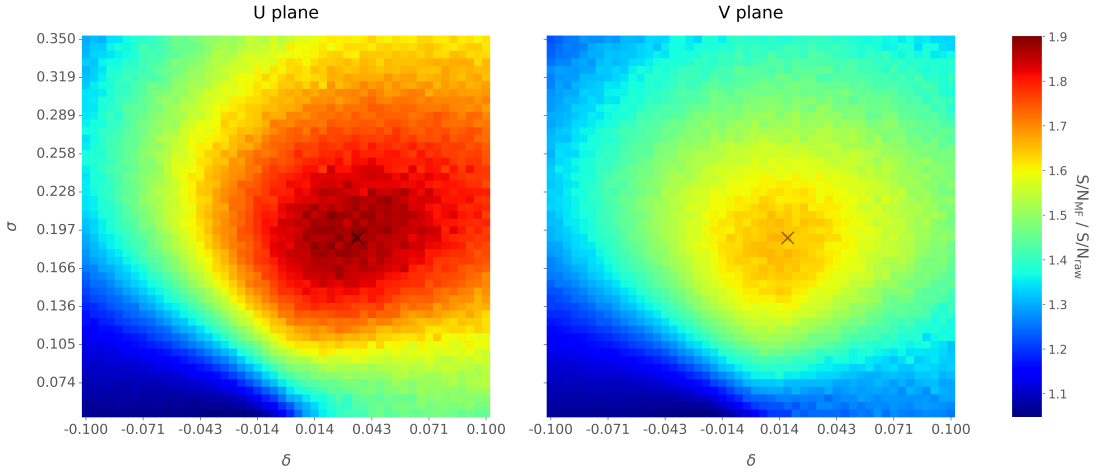


**Figure 4.8:** Relative change in the S/N for the ProtoDUNE-SP raw data capture `felix-2020-07-17-21:31:44` for different values of  $\delta$  and  $\sigma$  from the matched filter parametrisation in Eq. (4.16). The black crosses in both panels denote the location of the maximum ratio value.

line) decreases and at the same time the signal peaks are enhanced. This leads to an improvement of the S/N by a factor of 1.92 when compared to the raw waveform.

To obtain the matched filter that is more suitable for our data, I explored different configurations of signal templates. I parametrised the signal using the bipolar function:

$$f(x) = -A(x + \delta) e^{-x^2/\sigma^2}, \quad (4.16)$$

where the parameter  $\delta$  controls the asymmetry between the positive and negative peaks and  $\sigma$  controls their width. The amplitude parameter  $A$  is set such that it keeps the height of the biggest peak to be less than 200 ADC in absolute value.

As this parametrisation is only adequate for bipolar signals I will focus exclusively on the induction channels. Also, to achieve the best possible performance, I optimise the coefficients for the U and V planes separately. However, as I will discuss, the differences are not very pronounced. In case it is not technically possible to separate channels in the firmware according to the plane they are coming from and use different sets of filter coefficients for them, we can just find a common set of coefficients. In such case, I do not expect the results to change drastically.

## CHAPTER 4. MATCHED FILTER APPROACH TO TRIGGER PRIMITIVES

1222       Figure 4.8 presents the results of the parameter scan, for channels in the induction  
1223      planes U (left panel) and V (right panel). For each configuration of  $\sigma$  and  $\delta$  the resulting  
1224      matched filter was applied to all channels in the corresponding plane within the data  
1225      capture `felix-2020-07-17-21:31:44`. The change in S/N is computed with respect to  
1226      the raw waveforms, and then the mean value for all channels is kept as a score for each  
1227      filter. One can see that the improvements obtained for the U plane are in general higher  
1228      than the ones for the V plane. However, these ratios are substantially higher than the  
1229      ones obtained for the low-pass FIR filters. For the optimal configurations, I attained  
1230      improvements up to a factor of 1.85 for the U plane and 1.65 for the V plane.

1231       The sets of optimal matched filter coefficients were obtained for the parameters  
1232       $\delta = 0.035$ ,  $\sigma = 0.191$  for the U plane and  $\delta = 0.018$ ,  $\sigma = 0.191$  for the V plane. I  
1233      show these two sets of coefficients in Fig. 4.9 (left panel). Figure 4.9 (right panel)  
1234      shows the distribution of the S/N improvement after the optimal match filters for  
1235      the U and V were applied to the corresponding channels in the raw data capture  
1236      `felix-2020-07-17-21:31:44`. As mentioned before, the mean improvement achieved  
1237      for the U plane channels is slightly higher than the one for the V channels. Note, however,  
1238      that the spread of the distribution for the V plane is smaller than the one for the U  
1239      plane.

1240       Overall, one can see that the improvements on the S/N are much more significant in  
1241      the case of the matched filter than they were for the low-pass FIR filters. The analysis  
1242      of the raw data captures from ProtoDUNE-SP suggests that matched filters increase the  
1243      S/N of induction channels by a factor of 1.5 more than the optimal low-pass FIR filters.

1244       Although these results are by themselves great points in favour of the matched  
1245      filter, more studies are needed to completely assess the robustness of this approach. I  
1246      proceeded then to test the matched filter with simulated data samples.

## 4.5. MONTE CARLO STUDIES

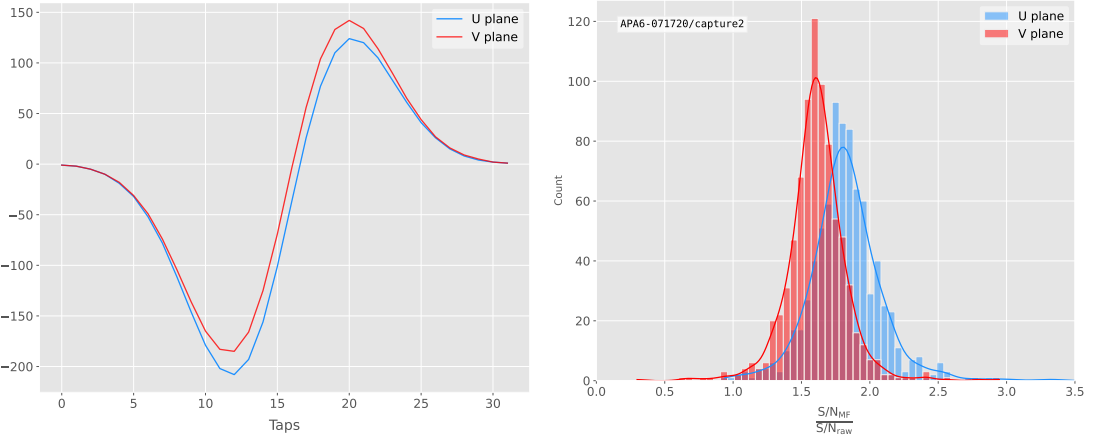


**Figure 4.9:** Left panel: Optimal matched filter coefficients for the U (blue line) and V (red line) planes. The filters were computed with our parametrisation in Eq. (4.16) for the parameter values  $\delta = 0.035$ ,  $\sigma = 0.191$  and  $\delta = 0.018$ ,  $\sigma = 0.191$  respectively. Right panel: Distribution of the relative change of the S/N on the two induction wire planes from the ProtoDUNE-SP raw data capture `felix-2020-07-17-21:31:44` after their respective optimal matched filters were applied.

## 1247 4.5 Monte Carlo studies

1248 To further test the matched filter, the next step is to generate and process data samples  
 1249 using LArSoft [111], the simulation and reconstruction software of the DUNE FD. In this  
 1250 way, one can control the particle content of the samples, the orientation of the tracks  
 1251 and their energy, and therefore see how the matched filter behaves in various situations.

1252 To begin with, I prepared different monoenergetic and isotropic samples containing  
 1253 a single particle per event. Each sample contains a different particle species, namely  
 1254 electrons, muons, protons and neutral pions, all with a kinetic energy of  $E_k = 100$  MeV.  
 1255 I chose these because of the fairly different topologies they generate in the liquid argon,  
 1256 ranging from shower-like to track-like.

1257 The event were generated with the single particle gun, and the Geant4 stage of the  
 1258 LArSoft simulation [111] was performed with the standard configuration for the DUNE  
 1259 FD HD design.

1260 For simplicity, I restricted the particles to start drifting in a single TPC volume<sup>2</sup>,

<sup>2</sup>A TPC volume is defined as the drift region between a single APA and the cathode. Therefore, for one drift volume of a HD module, there are twice as many TPC volumes as there are APAs in the

## CHAPTER 4. MATCHED FILTER APPROACH TO TRIGGER PRIMITIVES

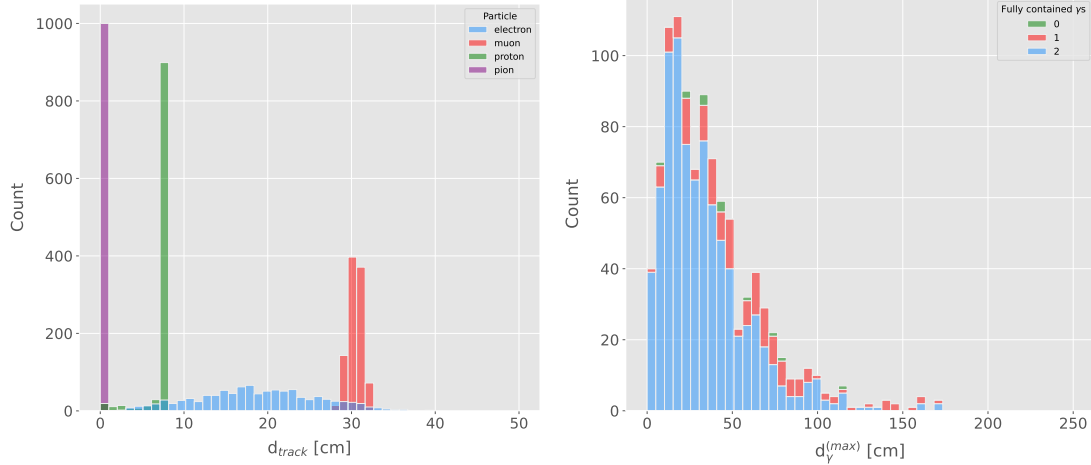


**Figure 4.10:** Left panel: distributions of the particles track length in the liquid argon for the generated  $E_k = 100$  MeV monoenergetic samples, electrons (blue), muons (red), protons (green) and neutral pions (purple). Right panel: distribution of the length of the longest photon in the neutral pion sample after the decay process  $\pi^0 \rightarrow \gamma\gamma$ .

so I can focus exclusively on the signals coming from one APA. The chosen kinetic energy for all the particles is  $E_k = 100$  MeV, as this produce tracks which are typically contained in one TPC volume. Figure 4.10 (left panel) shows the distributions of the track lengths in the liquid argon of all generated particles with  $E_k = 100$  MeV. One can see that, in the case of the track-like particles (i.e. muons and protons), their length distributions are quite sharp and centered at relatively low distances (30 and 8 cm, respectively). For electrons, the distribution is quite broad but it does not extend past  $\sim 30$  cm. The case of the neutral pions can be misleading. As they decay promptly, the track length associated to the true MC particle is always  $< 1$  cm. In Fig. 4.10 (right panel) I show the effective length distribution of the longest photon after the pion decays as  $\pi^0 \rightarrow \gamma\gamma$ , highlighting the number of fully contained photons in the TPC volume per event (either zero, one, or two). One can see that the vast majority of events have both photons contained in the TPC volume, whereas just a negligible fraction of them have none. However, for the sake of caution, I keep only the pion events with both photons contained.

The next step is to process the sample through the detector simulation. To make corresponding anode.

## 4.5. MONTE CARLO STUDIES

1277 adequate estimations of the noise levels, one needs to turn off the default zero-suppression  
1278 of the waveforms produced by the simulation. At this stage I am only interested int  
1279 the waveforms with noise added, so I keep the noise addition option as true in the  
1280 configuration. However, for studies related to the hit finder performance one also needs  
1281 to store the noiseless waveforms, to retrieve the truth information of the hits. I will  
1282 discuss this approach next.

1283 To reduce the amount of data that will go for processing, I used the information from  
1284 the Geant4 step of the simulation to select only the active channels, i.e. the channels  
1285 where some ionisation electrons arrived. Moreover, I only extract the waveforms from  
1286 one APA and exclusively the ones coming from induction channels. The resulting **ROOT**  
1287 file contains a **TTree** with two branches, one containing the waveforms for each event  
1288 and channel and the other with the corresponding offline channel numbers.

1289 Finally, I extract the truth values for the orientation of the tracks and the energies  
1290 of the particles to use them in the analysis. These are stored in a **ROOT** file with a single  
1291 **TTree**, containing several branches with information such as the components of the  
1292 initial momentum of the particles, initial and final positions, track length, etc.

1293 For the analysis of the resulting waveforms and truth values I used a custom analysis  
1294 code independent of LArSoft. Among other functionality, it allows the user to read the  
1295 **ROOT** files, export the raw data as **pandas** objects, apply the filters and compute the  
1296 S/N of both the raw and filtered signals. The default configuration for the filtering uses  
1297 the set of optimal matched filter coefficients that I found using the ProtoDUNE-SP data  
1298 samples.

1299 Additionally, for the analysis of the samples it was necessary to use two different  
1300 reference frames, to study separately the signals coming from the U and V induction  
1301 planes. Focussing on a single APA, the U and V channels have a different orientation in  
1302 the  $yz$  plane. In the case of U channels, these are tilted  $35.7^\circ$  clockwise from the vertical  
1303 ( $y$  direction), whereas the V channels are at the same angle but in the counter-clockwise  
1304 direction. Because of this, the best option is to deal with two new coordinate systems  
1305 rotated by  $\pm 35.7^\circ$  along the  $x$  axis, so the new  $y'$  and  $y''$  directions are aligned with the

## CHAPTER 4. MATCHED FILTER APPROACH TO TRIGGER PRIMITIVES

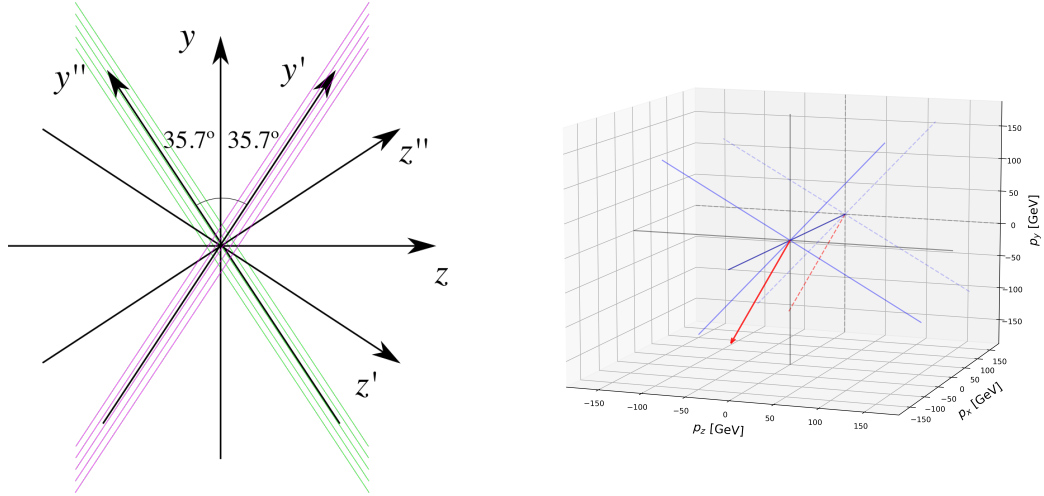


**Figure 4.11:** Left panel: schematic representation of the two new rotated reference frames used in this analysis (denoted as prime and double prime), viewed from the  $yz$  plane. The magenta stack of lines represent the wires in the U plane, whereas the green lines correspond to the wires in the V plane. Right panel: 3D representation of the momentum of one of the generated monoenergetic muons (red arrow) in the original reference frame (black lines), along with the new reference frame used for the U plane waveforms (blue lines). In the  $yz$  plane I added the projection of these three.

1306 U and V induction channels, respectively. Figure 4.11 (left panel) shows a schematic  
 1307 representation of the original reference frame together with the two rotated ones (denoted  
 1308 by primed and double primed). This way, one can easily understand how parallel was a  
 1309 track to the channels in the two induction planes. Figure 4.11 (right panel) shows a 3D  
 1310 representation of the momentum of a track (red arrow) in the original reference frame  
 1311 (black lines), along with the new reference frame for the U plane (blue lines). I added  
 1312 the projections onto the  $yz$  plane of these, to show the usefulness of the new reference  
 1313 frame to tell whether a track is parallel or perpendicular to the channels in a induction  
 1314 plane.

1315 Figure 4.12 shows the distribution of the average S/N change per event when I apply  
 1316 the optimised matched filters. I produce separate distributions for the channels in the U  
 1317 (red) and V (blue) induction planes. Notice that the S/N distributions for the track-like  
 1318 particles, i.e. muons (top left panel) and protons (bottom left panel), have significantly  
 1319 larger mean values than the distributions of the shower like particles, i.e. electrons (top

## 4.5. MONTE CARLO STUDIES

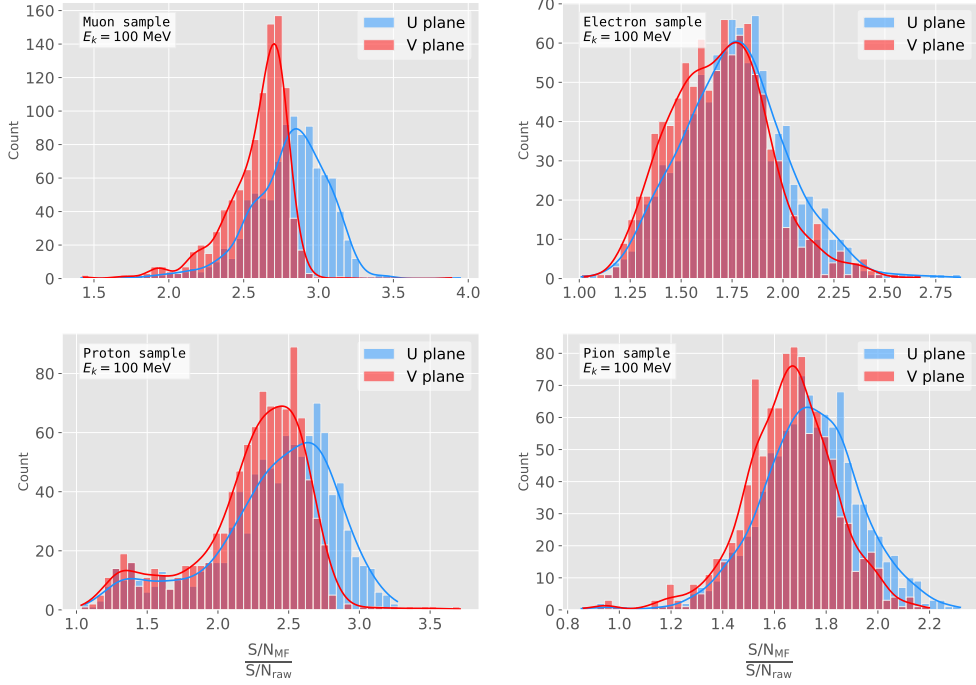


**Figure 4.12:** Distributions of the mean S/N change per event for the different MC samples after applying the matched filters. Here I separated the change in the U plane (blue) and the V plane (red) channels. From top left to the right: muon, electron, proton and neutral pion. All the events have a fixed kinetic energy of  $E_k = 100$  MeV.

right panel) and neutral pions (bottom right panel). An important difference between these results and the ones obtained before for the ProtoDUNE-SP data is that the overall improvements that I get with simulated data are more significant. This could be due to an underestimation of the noise levels in the LArSoft simulation. Nonetheless, the concluding message is that the previously optimised matched filters give an overall significant improvement of the S/N for the different samples.

About the convention I follow to present the results results, in the case of the raw and filtered S/N of each event I take the average of these quantities over all the active channels in the event. That is, if a certain event has  $N_{chan}$  active channels the two S/N values are computed as:

$$(S/N_{fir})_{event} = \frac{\sum_{i=0}^{N_{chan}} (S/N_{fir})_i}{N_{chan}}, \quad (4.17)$$

$$(S/N_{raw})_{event} = \frac{\sum_{i=0}^{N_{chan}} (S/N_{raw})_i}{N_{chan}}.$$

## CHAPTER 4. MATCHED FILTER APPROACH TO TRIGGER PRIMITIVES

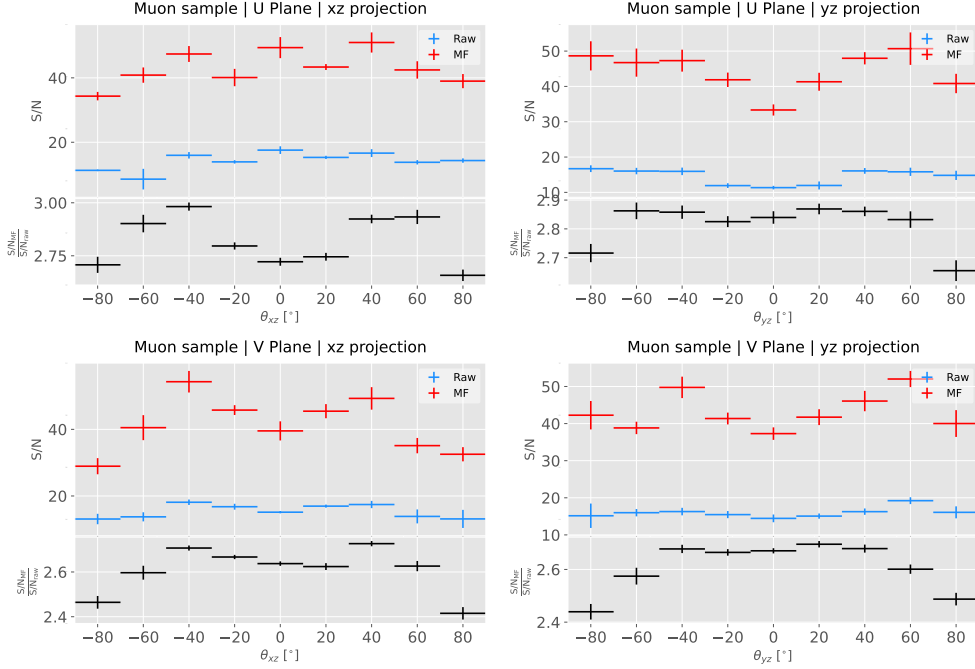


**Figure 4.13:** Angular dependence of the mean S/N and the S/N improvement for the monoenergetic muon sample. The top and bottom rows correspond to the U and V planes, respectively. The top subplots show the mean S/N for raw (blue) and filtered (red) waveforms whereas the bottom subplots depict the averaged S/N improvement (black).

1330 However, for the ratio of the raw and filtered S/N (what I call the S/N change) per  
 1331 event I do not take the ratio of the previous two quantities but compute the average of  
 1332 the individual ratios per channel in the event:

$$\left( \frac{S/N_{fir}}{S/N_{raw}} \right)_{event} = \frac{\sum_{i=0}^{N_{chan}} \left( \frac{S/N_{fir}}{S/N_{raw}} \right)_i}{N_{chan}}, \quad (4.18)$$

1333 therefore:

$$\left( \frac{S/N_{fir}}{S/N_{raw}} \right)_{event} \neq \frac{(S/N_{fir})_{event}}{(S/N_{raw})_{event}}. \quad (4.19)$$

### 1334 4.5.1 Angular dependence

1335 Having these monoenergetic samples, one can study the angular dependence of the  
 1336 matched filter performance. This is an important point, as it is a well established  
 1337 fact that for certain track configurations the S/N is much lower than average as the

## 4.5. MONTE CARLO STUDIES

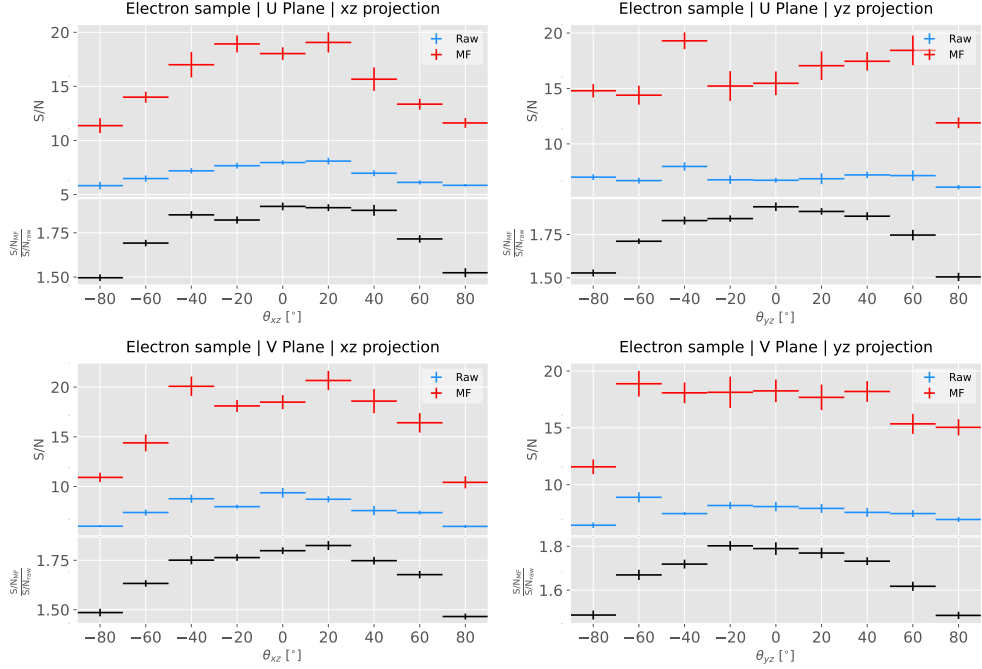


**Figure 4.14:** Angular dependence of the mean S/N and the S/N improvement for the monoenergetic electron sample. The top and bottom rows correspond to the U and V planes, respectively. The top subplots show the mean S/N for raw (blue) and filtered (red) waveforms whereas the bottom subplots depict the averaged S/N improvement (black).

corresponding waveforms are severely distorted. Therefore, I am interested in seeing how the matched filter behaves in different cases and how the S/N change for those compare to the average.

Figure 4.13 shows the angular dependence of the S/N for the monoenergetic  $E_k = 100$  MeV isotropic muons, for the different induction planes and projections. The angles for each event are given by the components of the initial value of the momentum of the particles, taking the angles of the projections on the  $xz$  and  $yz$  planes with respect to the  $z$  axis (more accurately, one needs to compute these angles twice for each event, a pair for the  $xy'z'$  coordinate system and the other for the  $xy''z''$ , as explained previously). The top row shows the dependence on the angles corresponding to the U plane, i.e.  $\theta_{xz'}$  and  $\theta_{y'z'}$ , whereas the bottom row shows the angular dependence viewed from the V plane,  $\theta_{xz''}$  and  $\theta_{y''z''}$ . In each panel, the top subplot represents the mean values of the S/N for the raw (blue) and matched filtered (red) signals, and the bottom subplot the

## CHAPTER 4. MATCHED FILTER APPROACH TO TRIGGER PRIMITIVES

averaged S/N change (black). The horizontal lines show the most probable value for the corresponding angular bin, obtained from a fit to a Landau distribution. The vertical lines represent the error in the parameter estimation.

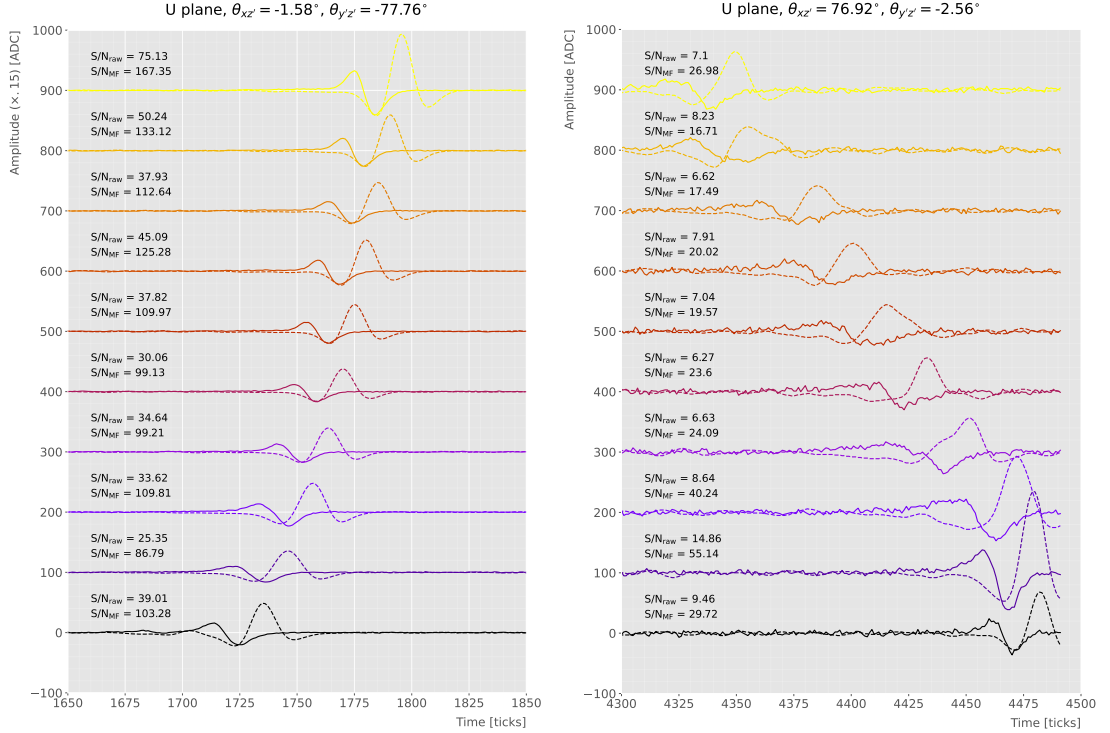
Both for the raw and matched filtered samples, the S/N is lower for tracks that are normal to the APA ( $\theta_{xz} \sim \pm 90^\circ$ ). Similarly, tracks parallel to the wires ( $\theta_{yz} \sim \pm 90^\circ$ ) tend to have higher S/N than those perpendicular to these ( $\theta_{yz} \sim 0$ ). The S/N improvement seems to follow similar trends for both projections in the two planes. In the  $xz$  plane there is a slight preference for tracks with  $\theta_{xz} \sim \pm 45^\circ$  (particularly in the U plane), whereas in  $yz$  the S/N change plateaus around the central region.

Figure 4.14 shows the corresponding angular dependence results for the  $E_k = 100$  MeV electrons sample. Although the S/N behaviour in this case is similar to what I observed for the muons, some differences are evident. A possible explanation can be that, because a significant fraction of the hits in these events are produced by the secondary particles generated in the EM shower, some of the S/N ratios do not correspond to the directional information of the primary electron. Even so, the S/N change distribution exhibits a consistent pattern and it is clear that the matched filter enhances the signal regardless of the electron direction.

### 4.5.2 Distortion and peak asymmetry

As a case study, I select two of the simulated  $E_k = 100$  MeV monoenergetic muon events. With respect to the U induction plane, one is parallel to the APA (low  $\theta_{xz'}$ ) and to the wires (high  $\theta_{y'z'}$ ) and the other is normal to the APA plane (high  $\theta_{xz'}$ ) and perpendicular to the wires (low  $\theta_{y'z'}$ ). As expected from the results on the angular dependence discussed above, the former has a higher S/N (both before and after the filtering) when compared to the latter. An interesting thing to notice about these two samples is that, even though one has a much larger S/N than the other, it is the one with the smallest S/N the one that gets a more significant averaged S/N improvement. In Tab. 4.1 I include all the relevant parameters of these two  $E_k = 100$  MeV muon events, namely the angles with respect to the  $xy'z'$  reference frame, the values of the

## 4.5. MONTE CARLO STUDIES



**Figure 4.15:** Selected consecutive waveforms corresponding to two monoenergetic  $E_k = 100$  MeV muon events, one is parallel to the APA and to the wires in the U plane (left panel) and the other is normal to the APA plane and perpendicular to the U plane wires (right panel). The solid lines represent the raw waveforms whereas the dashed lines correspond to the waveforms after the matched filter was applied. The waveforms on the left panel have been scaled by a factor of 0.15 to have similar amplitudes to the ones on the right panel.

1379 S/N, the S/N change and also the so-called peak asymmetry  $\Delta_{peak}$ , that I will define  
 1380 next.

**Table 4.1:** Characteristic parameters of the two monoenergetic muon events selected, relative to the U plane: projected angles in the  $xz'$  and  $y'z'$  planes, S/N values for the raw and filtered waveforms, mean improvement of the S/N and peak asymmetry.

	$\theta_{xz'} (\circ)$	$\theta_{y'z'} (\circ)$	S/N <sub>raw</sub>	S/N <sub>MF</sub>	$\frac{S/N_{MF}}{S/N_{raw}}$	$\Delta_{peak}$ (ADC)
High ("parallel")	-1.58	-77.76	41.65	112.44	2.83	-35.73
Low ("normal")	76.92	-2.56	8.07	25.46	3.12	-10.38

1381 One can try to understand better the nature of these two events by looking at the  
 1382 raw and filtered data from some of their active channels. Figure 4.15 shows a selection of  
 1383 consecutive raw and filtered U plane waveforms from the event with high S/N (left panel)

## CHAPTER 4. MATCHED FILTER APPROACH TO TRIGGER PRIMITIVES

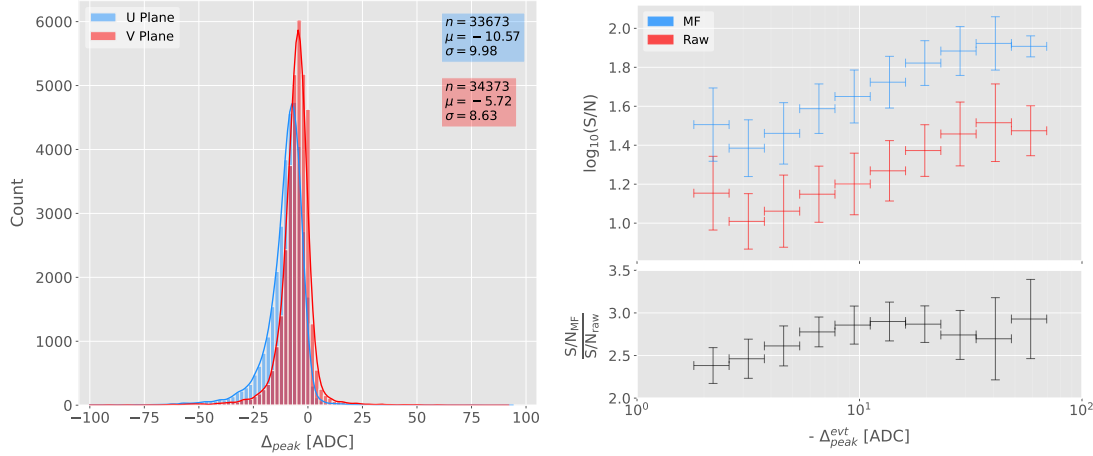


**Figure 4.16:** Left panel: peak asymmetry distribution for the case of the monoenergetic  $E_k = 100$  MeV muon sample. Each value corresponds to a single bipolar signal peak from a channel in any event. The blue distribution represents the peaks on U plane channels, whereas the red corresponds to signal peaks in V wires. Right panel: relation between the mean peak asymmetry per event with the S/N for U channel waveforms from the  $E_k = 100$  MeV muon sample. The top subplot shows the decimal logarithm of the mean S/N for the raw (red) and the matched filtered (blue) waveforms. The bottom subplot contains the mean S/N improvement ratio after the matched filter was applied.

1384 and the one with low S/N (right panel). To show both collections of waveforms at a  
 1385 similar scale I had to apply a factor of 0.15 to the waveforms with high S/N. Additionally,  
 1386 next to each waveform I include the values of the raw and matched filtered S/N for the  
 1387 corresponding channel. The first thing to notice is that the amplitude of the signal peaks  
 1388 from the normal track have a much smaller amplitude, and also appear quite distorted  
 1389 when compared to the others. On the other hand, although the matched filtered S/N for  
 1390 each channel are still smaller, the relative improvements are larger than in the parallel  
 1391 case.

1392 A way to quantify the difference between the shape of the waveforms of these two  
 1393 events is using their peak asymmetry. I define the peak asymmetry as the (signed)  
 1394 difference between the positive and the negative peaks of the bipolar shape, i.e.:

$$\Delta_{peak} \equiv h_+ - h_-, \quad (4.20)$$

1395 where both heights  $h_+$  and  $h_-$  are positive. Figure 4.16 (left panel) shows the distribution

## 4.5. MONTE CARLO STUDIES

of this peak asymmetry for all the waveforms corresponding to channels in the U (blue) and V (red) planes for the monoenergetic muon sample. One can see that these distributions are clearly shifted to negative values, with means  $\mu_{\Delta}^U = -10.57$  ADC and  $\mu_{\Delta}^V = -5.72$  ADC, respectively. Notice how the peak asymmetry value of the selected event with the high S/N sits at the left tail of the distribution, whereas the corresponding value of the sample with the low S/N lies around the mean.

It is possible to correlate the peak asymmetry with the S/N and the S/N change per event. Figure 4.16 (right panel) shows the result of comparing the mean peak asymmetry per event to the averaged raw (red) and matched filtered (blue) S/N per event (top subplot). The horizontal lines sit at the mean value obtained in the fit and represent the width of the  $-\Delta_{peak}$  bins used, while the vertical lines indicate one standard deviation around that mean value. Notice how there is an approximate linear relation between the peak asymmetry and the S/N, except for peak asymmetry values bigger than  $-5$  ADC where the S/N remains constant.

Also, in the bottom subplot of Fig. 4.16 (right panel) I show the relation between the peak asymmetry and the mean S/N change. In this case, one can see that there is a clear maximum at  $\Delta_{peak} \sim -10$  ADC. As mentioned previously, this is also the value of the mean of the peak asymmetry distribution. In fact, it is expected that our filter favours the signal peaks with the most common values of the peak asymmetry, as this was one of the features I target in our filter coefficient optimisation through the parameter  $\delta$ .

These results suggest that events with poorer values of the mean S/N, usually associated to non-favourable track orientations, tend to have smaller values of the mean peak asymmetry (in absolute value). Nonetheless, because our matched filters have been optimised to account for these asymmetries, the improvement on the S/N for these events is sizeable if not better than the one for events which already had a high S/N.

## CHAPTER 4. MATCHED FILTER APPROACH TO TRIGGER PRIMITIVES

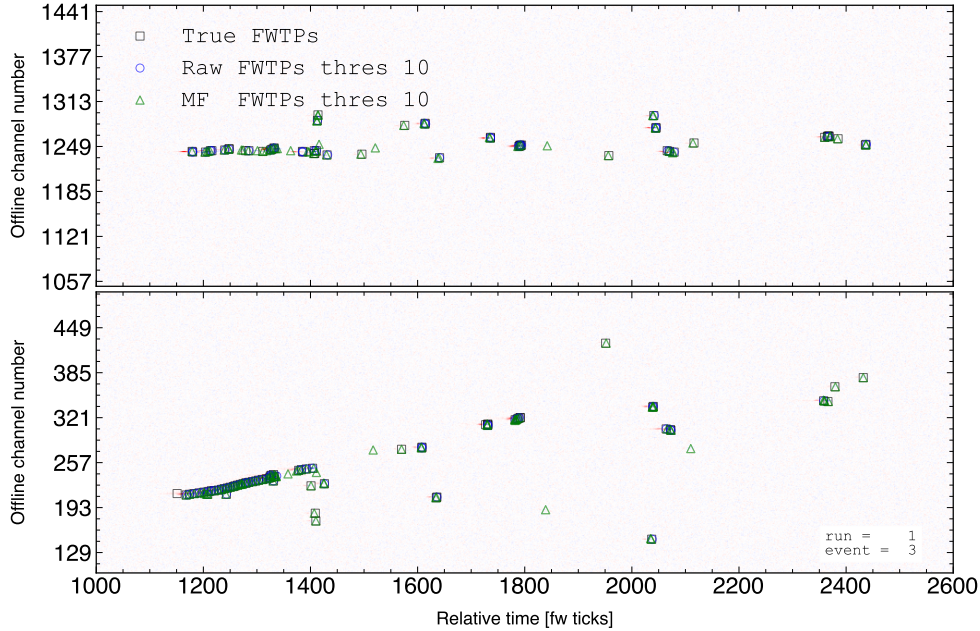


**Figure 4.17:** Raw event display showing the time (in firmware ticks) versus offline channel number for a  $E_k = 100$  MeV electron event. The produced true hits are superimposed (black boxes) as well as the hits coming from the standard hit finder chain (blue circles) and the hit finder using the matched filter (green triangles).

### 4.5.3 Hit sensitivity

One of the advantages of the matched filter, directly related to increasing the S/N, is the capability of forming TPs that before fell below the threshold. For instance, Fig. 4.17 shows the raw ADC data from an example electron event with the produced true hits superimposed (black boxes), together with the hits produced by the standard hit finder chain (blue circles), i.e. using the current FIR filter, and the hits obtained using the matched filters (green triangles). Both the standard and the matched filter hit finders run with a threshold of 10 ADC. Notice that the standard hits match well the true ones in the initial part of the event, where we have a track-like object. However, it misses most of the hits produced by the EM shower at later times. On the other hand, the hits produced with the matched filter have a better agreement with the true hits even for the more diffuse shower activity.

Even though the matched filter produces more hits as a results of the enhancement

## 4.5. MONTE CARLO STUDIES

1435 of the signal peaks relative to the noise level, it is also true that it may pick up some  
1436 spurious hits not related to any real activity if one lowers the thresholds too much.  
1437 Therefore, some optimisation of the threshold is needed, as there is a trade-off between  
1438 precision and sensitivity.

1439 Having this in mind, I compare the produced hits from both the standard and the  
1440 matched filter hit finders to the true hits. By running the hit finders on the samples  
1441 with different values of the threshold I can understand how low these can be pushed,  
1442 and then evaluate the gains obtained from this.

1443 To study how the hit formation depends on the energy, I prepared new isotropic  
1444 samples with the same types of particles as previously (muons, electrons, protons and  
1445 neutral pions) but with a flat kinetic energy distribution ranging from 5 to 100 MeV.

1446 To estimate the hit sensitivity for a certain sample, one needs to recover the set of  
1447 true hits to be able to compare these with the ones produced. To do so, I modify the  
1448 procedure I use to extract the raw waveforms. For this kind of study, I run the detector  
1449 simulation in two steps, first I produce the waveforms without noise and extract them  
1450 in the same format I used for the raw data. Then, the noise is added and the noisy  
1451 waveforms are similarly written to a file.

1452 To have a better comparison between the true hits and the ones produced from the  
1453 raw waveforms after applying the two filters, I apply the FIR filter and the matched  
1454 filters to the noiseless waveforms as well. I run the hit finder with a minimal threshold  
1455 (in this case I use 1 ADC) on the filtered noiseless waveforms, generating two sets of true  
1456 hits. I will refer to these as the standard true hits (with the default FIR filter) and the  
1457 matched filter true hits, respectively. This allows for a more precise matching between  
1458 the different groups of hits produced, as it will account for any delays and distortions  
1459 introduced by the filters.

1460 In the case of the raw waveforms (with noise added), I run the hit finder on them  
1461 with different values of the threshold, after applying either the FIR or the matched  
1462 filters. I name these simply standard and matched filter hits, respectively. Then, I  
1463 match the generated hits to the true hits, the standard hits to the standard true hits

## CHAPTER 4. MATCHED FILTER APPROACH TO TRIGGER PRIMITIVES

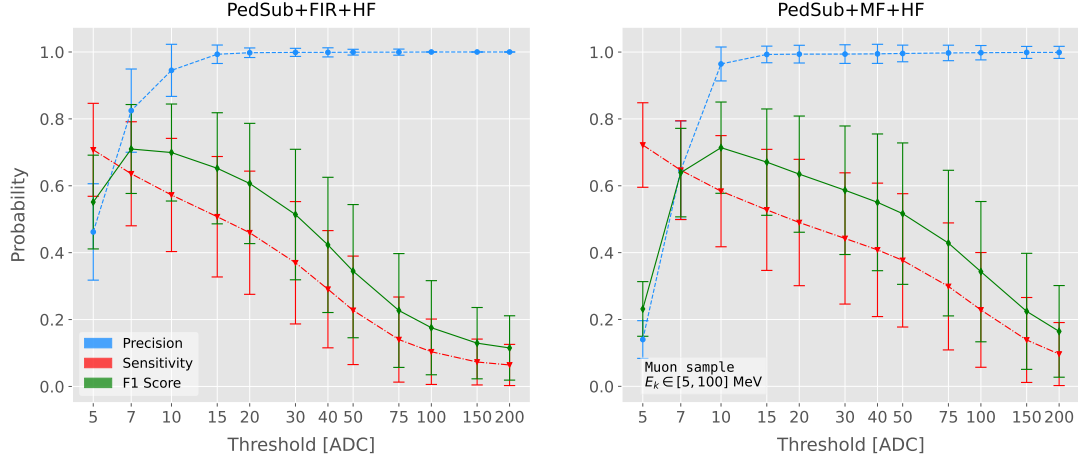


**Figure 4.18:** Dependence of the precision (blue), sensitivity (red), and  $F_1$  (green) scores on the threshold values used in the hit finder, for the FIR (left panel) and matched filter (right panel) cases. The results were obtained after matching the hits to the true hits in the case of the isotropic muon sample with kinetic energy in the range 5 to 100 MeV, taking only into account the induction plane channels. The points represent the mean value while the error bars indicate one standard deviation around that mean value.

and the matched filter hits to the matched filter true hits. The matching is performed by comparing the channel number and the timestamp of the hits. To count as a match, I require that all hits with the same channel number and timestamp have overlapping hit windows, i.e. the time windows between their hit end and hit start times need to overlap. If more than one hit in one of the groups have hit overlap with the same hit in the other group, I only count the match with the closest hit peak time value.

To quantify the performance of the two hit finder approaches, I use a classical method from statistical classification known as confusion matrix [112]. It divides the outputs in four categories: true positive (TP, both truth and predicted values are true), false negative (FN, truth value is true but predicted is false), false positive (FP, truth value is false but predicted is true) and true negative (TN, both truth and predicted values are false).

The contents of the confusion matrix allow us to compute other derived scores to assess the performance of our classification. In this study, I make use of three of these

## 4.5. MONTE CARLO STUDIES

1478 metrics, namely the precision or positive predictive value:

$$\text{PPV} = \frac{\text{TP}}{\text{TP} + \text{FP}}, \quad (4.21)$$

1479 the sensitivity or true positive rate:

$$\text{TPR} = \frac{\text{TP}}{\text{TP} + \text{FN}}, \quad (4.22)$$

1480 and the  $F_1$  score [113]:

$$F_1 = \frac{2\text{TP}}{2\text{TP} + \text{FP} + \text{FN}}, \quad (4.23)$$

1481 which is the harmonic mean of the precision and the sensitivity.

1482 For this specific case I am not going to make use of the true negative category, as its  
1483 definition in this context can be ambiguous because one does not have clear instances in  
1484 the classification process. This way, I only count the number of true positives as the  
1485 total amount of hits I can match between true and raw populations, the number of false  
1486 negatives will be the number of missing true hits, and the false positives the number of  
1487 hits which do not match any true hit.

1488 In Fig. 4.18 I show the precision (blue), sensitivity (red) and  $F_1$ -score (green) I  
1489 obtain as a function of the threshold used in the hit finder for the muon sample. Because  
1490 the matched filters are only applied to induction channels, I consider exclusively the hits  
1491 coming from the U and V planes. The panel on the left corresponds to the results I  
1492 get when running the hit finder on the FIR filtered waveforms, whereas the right panel  
1493 contains the scores for the matched filter case. The points are centered at the threshold  
1494 value used and represent the mean value obtained for each score using all the generated  
1495 events, while the error bars indicate one standard deviation around the mean value.

1496 One can see that the precision for the matched filter case is lower when the thresholds  
1497 are very low, as the noise baseline is slightly amplified, but then rises to high values  
1498 quicker than for the FIR case. The other difference one can spot is that the sensitivity  
1499 in the FIR case starts dropping faster at around the same threshold values where the

## CHAPTER 4. MATCHED FILTER APPROACH TO TRIGGER PRIMITIVES

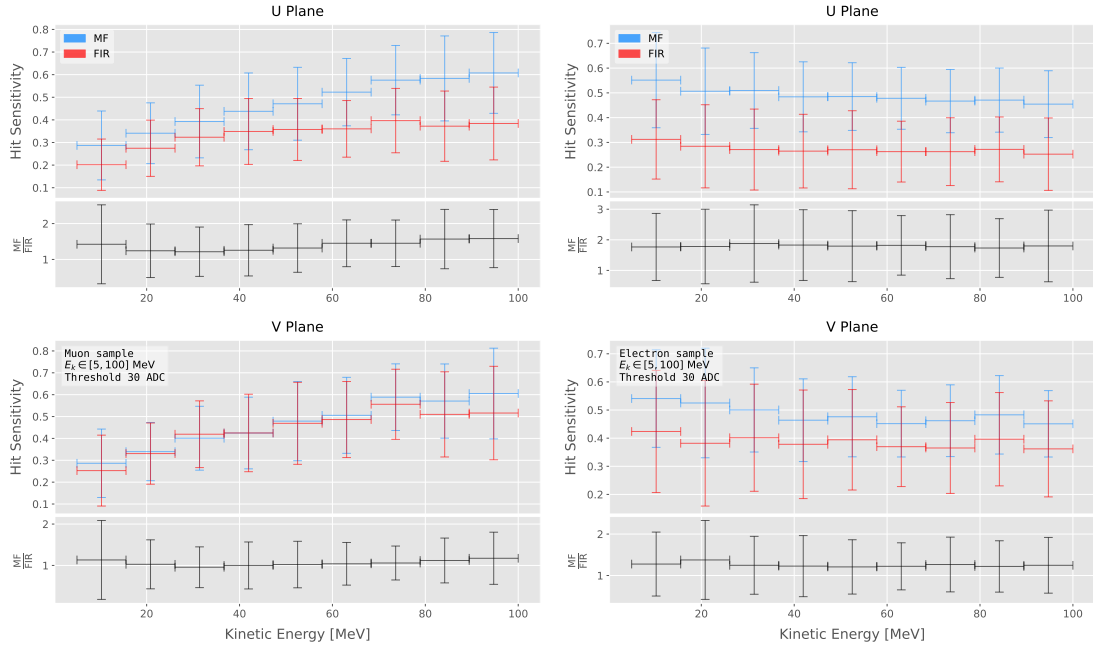


**Figure 4.19:** Dependence of the averaged hit sensitivity on the kinetic energy of the events for the matched filter (blue) and standard (red) hits, for the case of the muon (left panel) and electron (right panel) samples, separated between U (top plots) and V (bottom plots) induction wire planes. The top subplots contain the hit sensitivities for the two hit finder alternatives, while the bottom subplots show the ratio between the two. The horizontal lines sit at the mean value and represent the size of the energy bins, while the vertical error bars indicate one standard deviation around that mean value.

precision stabilises around 1, while in contrast for the matched filter this rapid decrease starts at higher threshold values. A similar scan for the same thresholds was performed for the electron sample in the same energy range, yielding similar results.

In Fig. 4.19 I show the average hit sensitivity versus the kinetic energy of the events, both for the matched filter hits (blue) and the standard hits (red). The left panel corresponds to the muon sample, whereas the one on the right corresponds to the electron sample, both with kinetic energies between 5 and 100 MeV. In each panel, the top plot corresponds to hits in the U plane, while the bottom plot contains the same information for the V plane. Each plot contains two subplots, the one on the top shows the hit sensitivity values for the matched filter and standard hits separate, while the bottom subplot depicts the ratio between the matched filter and standard sensitivities. The horizontal lines are placed at the mean value obtained in the fit and represent the

## 4.5. MONTE CARLO STUDIES

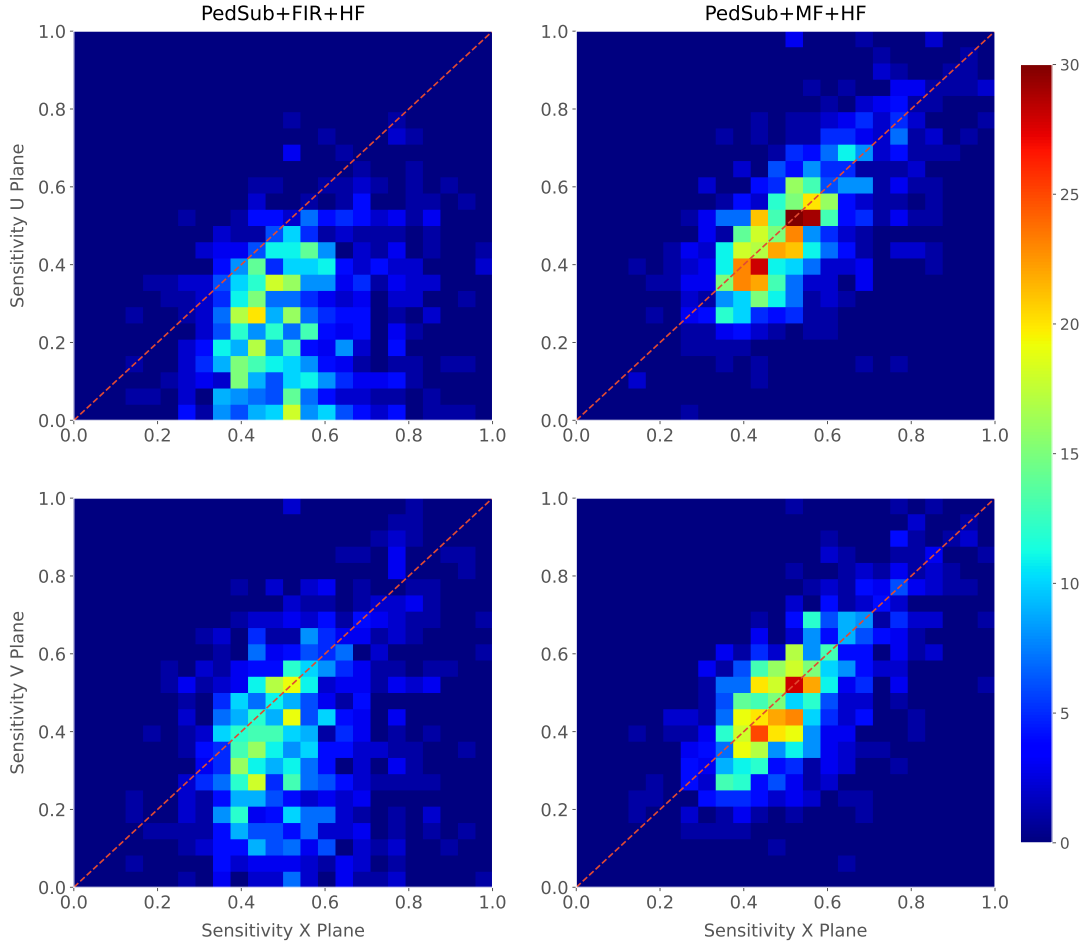


**Figure 4.20:** Distributions of the hit sensitivity in the U (top panels) and V (bottom panels) planes versus the hit sensitivity in the X plane, both for the standard hits (left panels) and the matched filter hits (right panels), in the case of the electron sample and a threshold of 30 ADC.

width of the  $E_k$  bins used, while the vertical error bars indicate one standard deviation around that mean. In both cases, the threshold used was 30 ADC, as I require the precision to be higher than 0.99 for both matched filter and standard cases.

In general, the improvements are better for the U than for the V plane. While for the U channels I achieve a mean improvement of 50% and 80% for muons and electrons, respectively, the improvement in the V plane is stalled at 10% and 25%. Nevertheless, looking at the sensitivities for the matched filter hits in both planes, one can see these have similar mean values for each energy bin. On the other hand, for the standard hits the sensitivity remains higher for the V plane. This way, it looks there is a less

## CHAPTER 4. MATCHED FILTER APPROACH TO TRIGGER PRIMITIVES



**Figure 4.21:** Top panels: standard residual plots of the hit sensitivities between the X and U planes. Bottom panels: quantile-quantile plots of the hit sensitivity standard residuals between the X and U planes. In all cases, the left panel corresponds to the standard hits while the right panel represents the matched filter case, all from the electron sample with a 30 ADC threshold.

1521 significant gain because the hit sensitivity was already high.

1522 Another interesting observation is the different behaviors for muons and electrons.

1523 While hit sensitivity for muons grows significantly with energy, in the case of electrons it

1524 slightly decreases the higher the kinetic energy of the event is. However, when it comes

1525 to the improvement on the sensitivities, this remains almost constant in all cases.

1526 Furthermore, we can look at how the concurrence of hits between the different wire

1527 planes has changed. For any given event, I expect to have a similar number of hits in

1528 the three planes. As the ionisation electrons need to cross the U and V planes prior

1529 to reach the collection plane X, they will induce current in those wire planes. A way

1530 to check the concurrence of hits across planes is comparing the hit sensitivities in the

1531 different planes for each individual event. Although the sensitivities will not be exactly

1532 equal across planes, ideally they should be normally distributed around the diagonal.

## 4.6. VD COLDBOX DATA TAKING

1533       Figure 4.20 shows the hit sensitivity in the U (top panels) and V (bottom panels)  
1534      planes versus the hit sensitivity in the X plane, for the case of the standard hits (left  
1535      panels) and the matched filter hits (right panels). All plots were generated for the  
1536      electron sample and a threshold of 30 ADC. From these, one can see a clear trend.  
1537      The standard hit finder chain produces hit sensitivities in the induction planes that are  
1538      systematically lower than the sensitivity in the X plane, i.e. most of the points sit below  
1539      the diagonal (red dashed line). In contrast, when the matched filters are applied, the  
1540      majority of the events are distributed around the diagonal. This points out that the  
1541      concurrence of hits across planes has improved.

1542       To exemplify the improvement I obtain, I take the residuals of the hit sensitivities  
1543      for the X and U planes. Assuming the diagonal hypothesis, i.e. given a dataset of the  
1544      form  $(x, y)$  for any  $x$  I take the predicted  $y$  value to be equal to the value of  $x$ , I can  
1545      compute the standard residuals for the hit sensitivities in U given the sensitivities for  
1546      X. In Fig. 4.21 (top panels) I show these standard residuals against the corresponding  
1547      values of the hit sensitivity in the U plane, for the electron sample with kinetic energy  
1548      between 5 and 100 MeV. Comparing the scatter points in the case of the standard hits  
1549      (left panel) and the matched filter hits (right panel), it can be seen that the residuals for  
1550      the standard hit finder follow a certain pattern and their mean deviates from 0.

1551       To see clearly if the residuals are normally distributed, in Fig. 4.21 (bottom panels)  
1552      I plot the corresponding quantile-quantile plot for both the standard (left panel) and  
1553      matched filter (right panel) residuals. One can clearly see that the points for the standard  
1554      hit finder case follow a strongly non-linear pattern, suggesting that the residuals do not  
1555      follow a normal distribution. In contrast, for the matched filter hits the points conform  
1556      to a roughly linear path, implying that in this case the normality condition is fulfilled.

1557       All these results hint at the fact that the concurrence of hits across the wire planes  
1558      can be strengthened by applying the matched filters.

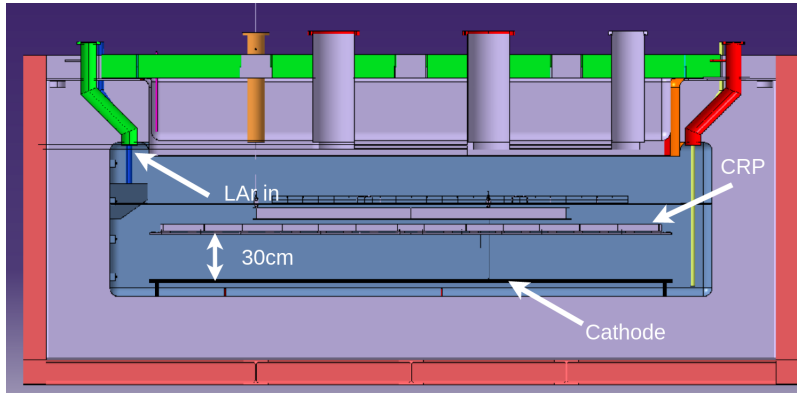


**Figure 4.22:** Schematic diagram of the vertical drift ColdBox setup at CERN.

## 1559 4.6 VD ColdBox data taking

1560 Between February and April 2023 the vertical drift (VD) ColdBox setup at CERN,  
 1561 shown in Fig. 4.22, was recommissioned for cold electronics testing with CRP5. That  
 1562 provided an opportunity for testing the firmware TP generation in a real LArTPC.  
 1563 However, during the two run periods new software-related complications that were not  
 1564 observed in previous running conditions arose.

1565 These prevented us from taking data with the whole system. As a palliative measure,  
 1566 new configurations were developed that allowed to run with TP generation enabled for a  
 1567 subset of the ADC links. With these workarounds, we managed to run with up to three  
 1568 out of twelve ADC links and the horizontal muon trigger algorithm (HMA).

1569 Additionally, an alternative firmware version was prepared featuring the matched  
 1570 filter coefficients optimised for the induction plane hit finding. The version of the filter  
 1571 we used for the data taking is slightly different from the one of the previous studies, as  
 1572 in this case we needed to apply the same filter coefficients to all channels irrespective  
 1573 of the readout plane they come from. With this, we also managed to run with three  
 1574 ADC links and the HMA trigger. Figure 4.23 shows an example event display from the  
 1575 longest run we recorded with the matched filter firmware.

1576 We used the recorded data, together with our standalone TPG simulation tool, to  
 1577 perform comparisons between the firmware and simulated TPs. One such comparison

## 4.6. VD COLDBOX DATA TAKING

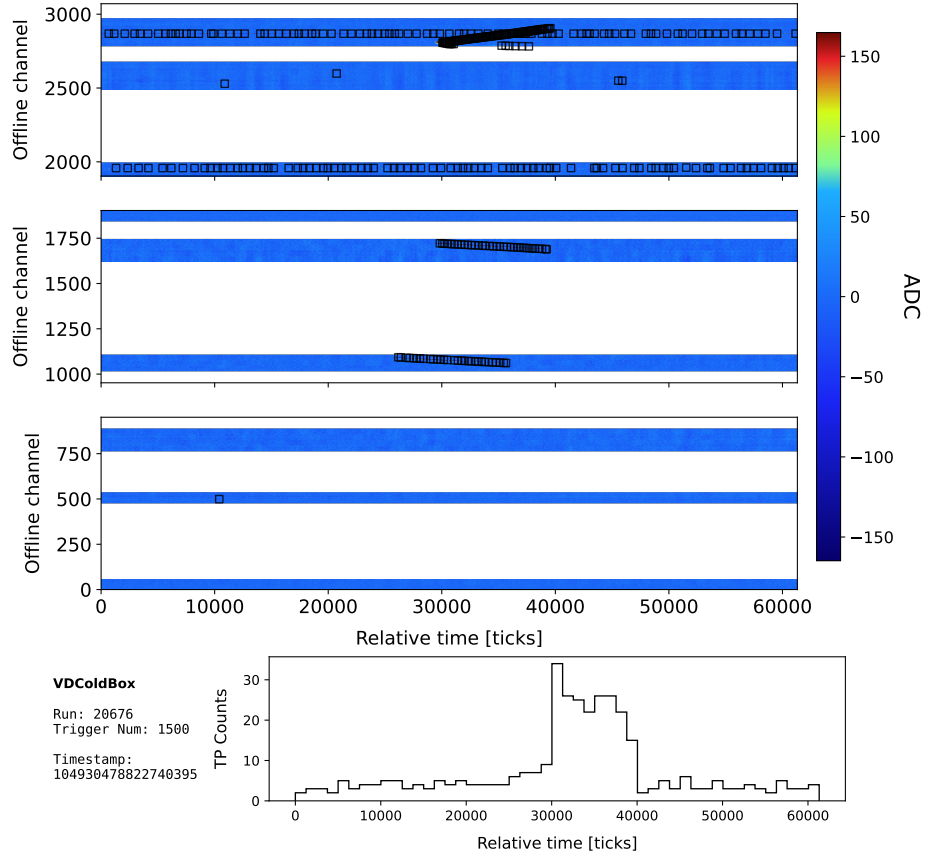


**Figure 4.23:** Event display of the data taken with the matched filter and HMA trigger at the VD ColdBox. The display shows the data from 3 ADC links for the full trigger window, with the black squares representing the produced TPs. The bottom panel represents the TP counts as a function of time in the trigger window.

for a matched filter run can be seen in Fig. 4.24. The agreement achieved is within the expectation, from what we have seen in previous samples.

All the studies presented demonstrate the robustness of the matched filter approach to form TPs. I have used both ProtoDUNE-SP data and MC samples to assess its impact on the S/N and TP production of the induction channels. Additionally, I have shown that it is possible to run with it in a real detector environment, after the tests at the VD ColdBox setup.

CHAPTER 4. MATCHED FILTER APPROACH TO TRIGGER PRIMITIVES

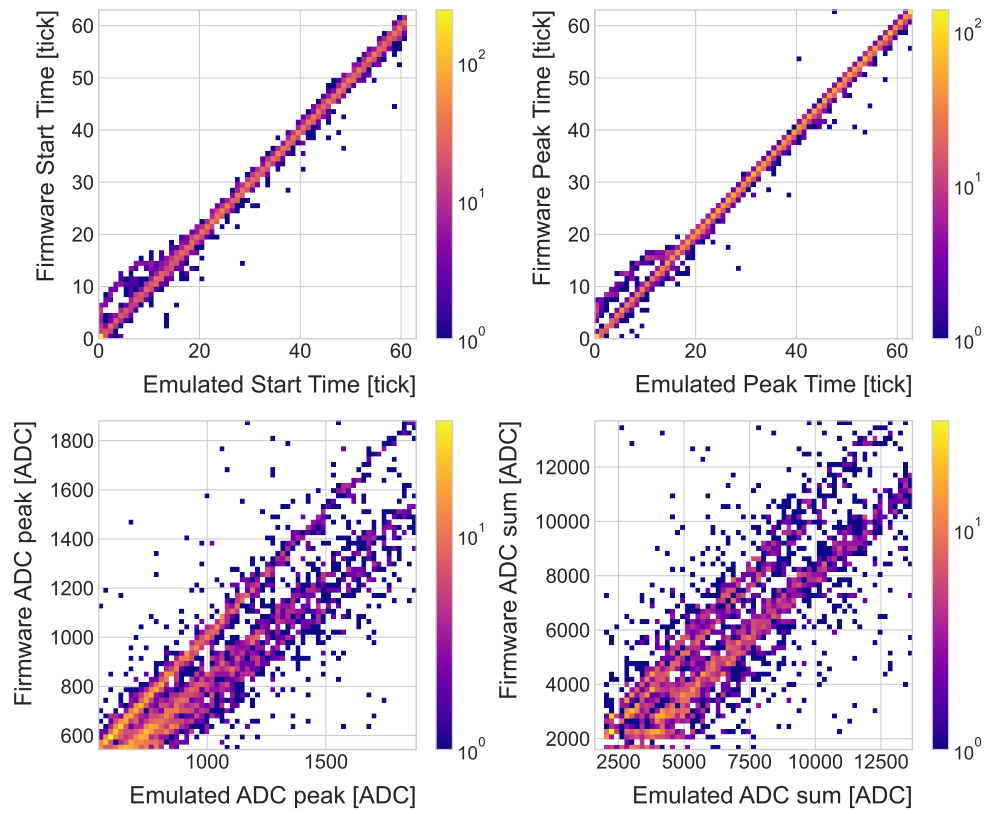


**Figure 4.24:** Comparison between firmware-produced and simulated TP quantities for a matched filter run at the VD ColdBox.

## Dark Matter searches

### with neutrinos from the Sun

1588       *He stepped down, trying not to look long at her, as if she were the Sun, yet he  
1589        saw her, like the Sun, even without looking.*

1590                          – Leo Tolstoy, *Anna Karenina*

1591       The idea of detecting neutrino signals coming from the core of the Sun to probe DM  
1592       is not new. The main focus of these searches has usually been high-energy neutrinos  
1593       originated from DM annihilations into heavy particles [114–117]. However, recent studies  
1594       have proposed to look at the low-energy neutrino flux arising from the decay of light  
1595       mesons at rest in the Sun [118–121], previously thought undetectable.

1596       In this Chapter, I try to demonstrate the capability of DUNE to constrain different  
1597       DM scenarios. I use the neutrino fluxes arising from DM annihilations in the core of the  
1598       Sun to compute the projected limits that DUNE would be able to set on the annihilation  
1599       rates of DM particles in the Sun and the DM scattering cross sections.

#### 1600 5.1 Gravitational capture of DM by the Sun

1601       The Sun and the centre of the Earth are possible sources of DM annihilations, specially  
1602       interesting because of their proximity. Their gravitational attraction ensures the capture  
1603       of DM from the local halo through repeated scatterings of DM particles crossing them.  
1604       Only neutrinos produced from DM annihilations can escape the dense interior of these

## CHAPTER 5. DARK MATTER SEARCHES WITH NEUTRINOS FROM THE SUN

1605 objects. Therefore, neutrino telescopes are the most useful experimental layouts to  
 1606 pursue DM searches from their cores.

1607 The neutrino flux from DM annihilations inside the Sun depends on the DM capture  
 1608 rate, which is proportional to the DM scattering cross section, and the annihilation rate,  
 1609 which is proportional to the velocity-averaged DM annihilation cross section. The total  
 1610 number of DM particles inside the Sun follows the Boltzmann equation [118]:

$$\frac{dN_{DM}}{dt} = C_{\odot} - A_{\odot}N_{DM}^2, \quad (5.1)$$

1611 where  $C_{\odot}$  and  $A_{\odot}$  are the total Sun DM capture and annihilation rates respectively.  
 1612 In this expression I neglected the evaporation term, proportional to  $N_{DM}$ , which only  
 1613 contribute for  $m_{DM} \lesssim 4$  GeV [122]. As the current threshold of neutrino telescopes  
 1614 is a few GeV, this region falls below the probed range but can be important in future  
 1615 low-energy projects like DUNE.

1616 This equation has an equilibrium solution:

$$N_{DM}^{eq} = \sqrt{\frac{C_{\odot}}{A_{\odot}}}, \quad (5.2)$$

1617 which represents the amount of DM inside the Sun if the capture and annihilation have  
 1618 reached equilibrium. As the Sun is approximately 4.6 Gyr old [123], it is usually assumed  
 1619 that equilibrium has been achieved. Therefore, the anomalous neutrino flux from the  
 1620 Sun would only depend on the DM scattering cross section, enabling us to set limits  
 1621 on this quantity. If one does not assume equilibrium, some assumptions on the DM  
 1622 annihilation cross section are necessary to extract predictions from neutrino signals.

1623 Here, I am going to consider three possible scenarios for the DM interactions: DM  
 1624 scattering off electrons, spin-dependent (SD) and spin-independent (SI) interactions  
 1625 with nuclei. For these last two, the cross sections will be given in terms of the SD and  
 1626 SI elastic scattering DM cross section off protons (assuming that the DM interactions

## 5.1. GRAVITATIONAL CAPTURE OF DM BY THE SUN

1627 with protons and neutrons are identical),  $\sigma_p^{\text{SD}}$  and  $\sigma_p^{\text{SI}}$ , as [118, 124]:

$$\sigma_i^{\text{SD}} = \left( \frac{\tilde{\mu}_{A_i}}{\tilde{\mu}_p} \right)^2 \frac{4(J_i + 1)}{3J_i} |\langle S_{p,i} \rangle + \langle S_{n,i} \rangle|^2 \sigma_p^{\text{SD}}, \quad (5.3)$$

$$\sigma_i^{\text{SI}} = \left( \frac{\tilde{\mu}_{A_i}}{\tilde{\mu}_p} \right)^2 A_i^2 \sigma_p^{\text{SI}}, \quad (5.4)$$

1628 where  $\tilde{\mu}_{A_i}$  is the reduced mass of the DM-nucleus  $i$  system,  $\tilde{\mu}_p$  is the reduced mass  
 1629 of the DM-proton system,  $A_i$  and  $J_i$  the mass number and total angular momentum  
 1630 of nucleus  $i$ , and  $\langle S_{p,i} \rangle$  and  $\langle S_{n,i} \rangle$  the expectation value of the spins of protons and  
 1631 neutrons averaged over all nucleons, respectively (see Ref. [125] for a review on spin  
 1632 expectation values).

1633 Since the Sun is mainly composed of hydrogen, the capture of DM from the halo is  
 1634 expected to occur mainly through SD scattering. However, since the SI cross section is  
 1635 proportional to the square of the atomic mass, heavy elements can contribute to the  
 1636 capture rate (even though they constitute less than 2% of the mass of the Sun). Heavy  
 1637 elements can also contribute to the SD cross section if the DM also has momentum-  
 1638 dependent interactions [126].

1639 DM particles can get captured by the Sun if after repeated scatterings off solar  
 1640 targets their final velocity is lower than the escape velocity of the Sun. In the limit of  
 1641 weak cross sections, this capture rate can be approximately written as [127]:

$$C_{\odot}^{\text{weak}} = \sum_i \int_0^{R_{\odot}} dr 4\pi r^2 \int_0^{\infty} du_{\chi} \frac{\rho_{\chi}}{m_{\chi}} \frac{f_{v_{\odot}}(u_{\chi})}{u_{\chi}} \omega(r) \int_0^{v_e(r)} dv R_i^-(\omega \rightarrow v) |F_i(q)|^2, \quad (5.5)$$

1642 where the summation extends over all possible solar targets. In this expression,  $R_{\odot}$   
 1643 is the radius of the Sun,  $\rho_{\chi}$  is the local DM density,  $m_{\chi}$  the mass of the DM particle,  
 1644  $f_{v_{\odot}}(u_{\chi})$  the DM velocity distribution seen from the Sun's reference frame,  $R_i^-(\omega \rightarrow v)$   
 1645 is the differential rate at which a DM particle with velocity  $v$  scatters a solar target of  
 1646 mass  $m_i$  to end up with a velocity  $\omega$  and  $|F_i(q)|$  is the nuclear form factor of target  $i$ .

1647 The differential scattering rate takes a rather simple form when considering velocity-

## CHAPTER 5. DARK MATTER SEARCHES WITH NEUTRINOS FROM THE SUN

<sup>1648</sup> independent and isotropic cross sections. In that case, this quantity is given by [124, 127]:

$$R_i^-(\omega \rightarrow v) = \frac{2}{\sqrt{\pi}} \frac{\mu_{i,+}^2}{\mu_i} \frac{v}{\omega} n_i(r) \sigma_i \left[ \chi(-\alpha_-, \alpha_+) + \chi(-\beta_-, \beta_+) e^{\mu_i(\omega^2 - v^2)/u_i^2(r)} \right], \quad (5.6)$$

<sup>1649</sup> where  $\mu_i$  is the ratio between the DM mass and the mass of target  $i$ ,  $\mu_{i,\pm}$  is defined as:

$$\mu_{i,\pm} \equiv \frac{\mu_i \pm 1}{2}, \quad (5.7)$$

<sup>1650</sup>  $n_i(r)$  is the density profile of target  $i$  in the solar medium,  $u_i(r)$  is the most probable

<sup>1651</sup> velocity of target  $i$  given by:

$$u_i(r) = \sqrt{\frac{2T_\odot(r)}{m_i}}, \quad (5.8)$$

<sup>1652</sup> where  $T_\odot(r)$  is the temperature of the Sun, the quantities  $\alpha_\pm$  and  $\beta_\pm$  are defined as:

$$\alpha_\pm \equiv \frac{\mu_{i,+}v \pm \mu_{i,-}\omega}{u_i(r)}, \quad (5.9)$$

$$\beta_\pm \equiv \frac{\mu_{i,-}v \pm \mu_{i,+}\omega}{u_i(r)}, \quad (5.10)$$

<sup>1653</sup> and the function  $\chi(a, b)$  is a Gaussian integral of the form:

$$\chi(a, b) \equiv \int_a^b dx e^{-x^2}. \quad (5.11)$$

<sup>1654</sup> Finally, if one assumes the DM halo velocity distribution in the galactic rest frame

<sup>1655</sup> to be a Maxwell-Boltzmann distribution, one can write the halo velocity distribution for

<sup>1656</sup> an observer moving at the speed of the Sun with respect to the DM rest frame as:

$$f_{v_\odot}(u_\chi) = \sqrt{\frac{3}{2\pi}} \frac{u_\chi}{v_\odot v_d} \left( e^{-\frac{3(u_\chi - v_\odot)^2}{2v_d^2}} - e^{-\frac{3(u_\chi + v_\odot)^2}{2v_d^2}} \right), \quad (5.12)$$

<sup>1657</sup> where:

$$\omega^2(r) = u_\chi^2 + v_e^2(r), \quad (5.13)$$

<sup>1658</sup> is the DM velocity squared,  $v_\odot$  the relative velocity of the Sun from the DM rest frame

## 5.1. GRAVITATIONAL CAPTURE OF DM BY THE SUN

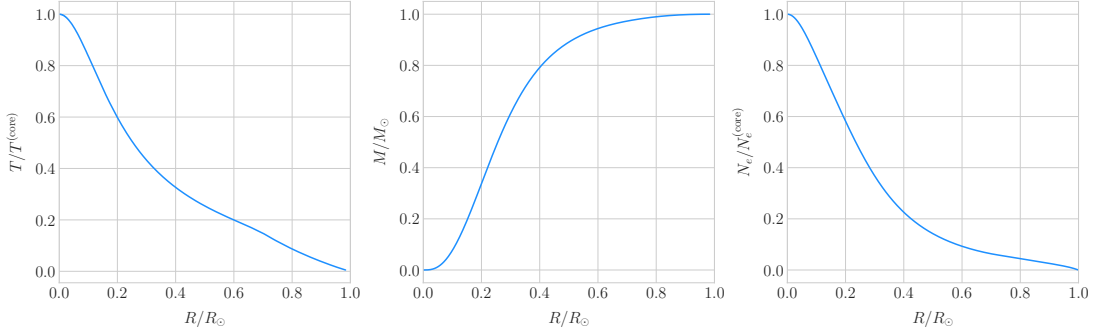


**Figure 5.1:** Input solar parameters used in the capture rate computation as a function of the solar radius, from left to right: temperature (with respect to the temperature at the core), mass (in solar masses) and electron number density (with respect to the electron density at the core). All quantities shown correspond to the standard solar model BS2005-OP [20].

and  $v_d \simeq \sqrt{3/2}v_\odot$  the velocity dispersion.

For the case of strong scattering cross sections, Eq. (5.5) ceases to be valid, as it escalates indefinitely with the cross section. In that limit, the capture rate saturates to the case where the probability of interaction is equal to one, which can be written as [128]:

$$C_\odot^{\text{geom}} = \pi R_\odot^2 \left( \frac{\rho_\chi}{m_\chi} \right) \langle v \rangle \left( 1 + \frac{3}{2} \frac{v_e^2(R_\odot)}{v_d^2} \right) \xi(v_\odot, v_d), \quad (5.14)$$

where  $\langle v \rangle = \sqrt{8/3\pi}v_d$  is the mean velocity in the DM rest frame and the factor  $\xi(v_\odot, v_d)$  accounts for the suppression due to the motion of the Sun:

$$\xi(v_\odot, v_d) = \frac{v_d^2 e^{-\frac{3v_\odot^2}{2v_d^2}} + \sqrt{\frac{\pi}{6}} \frac{v_d}{v_\odot} (v_d^2 + 3v_e^2(R_\odot) + 3v_\odot^2) \operatorname{Erf} \left( \sqrt{\frac{3}{2}} \frac{v_\odot}{v_d} \right)}{2v_d^2 + 3v_e^2(R_\odot)}. \quad (5.15)$$

Having these into account, one can write the total capture rate as a combination of both contributions, allowing a smooth transition between the two, as [118]:

$$C_\odot = C_\odot^{\text{weak}} \left( 1 - e^{C_\odot^{\text{geom}}/C_\odot^{\text{weak}}} \right). \quad (5.16)$$

I computed the capture rate from Eq. (5.16) in the case of interactions with electrons. To do so, I used the standard solar model BS2005-OP [20]. Fig. 5.1 shows the

## CHAPTER 5. DARK MATTER SEARCHES WITH NEUTRINOS FROM THE SUN

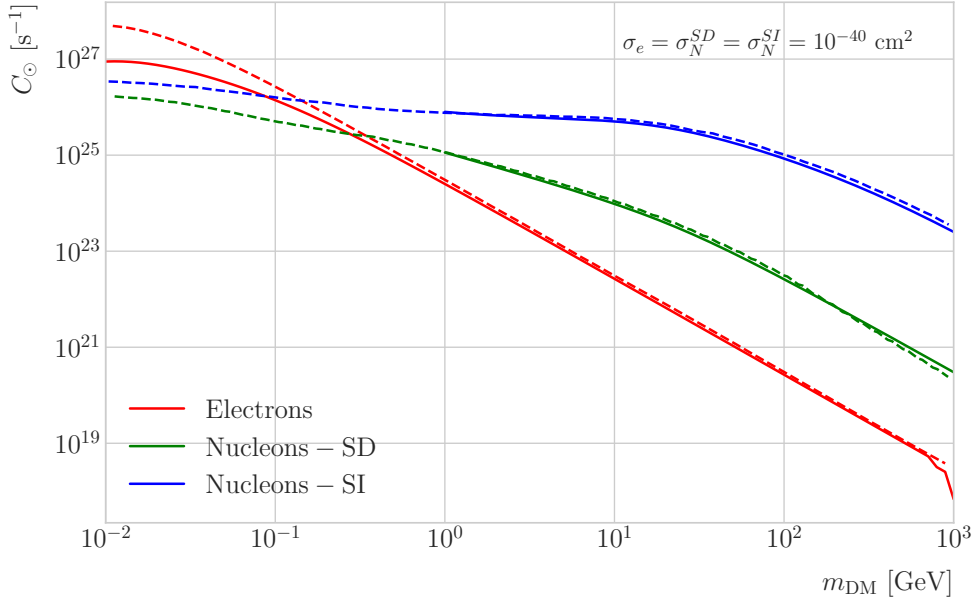


**Figure 5.2:** Capture rates as a function of the DM mass for the DM-electron interactions (red lines), SD DM-nucleons interactions (green lines), and SI DM-nucleons interactions (blue lines). Solid lines represent the values computed in this work while the dashed lines are the one given in Ref. [124]. All the rates are shown for a choice of scattering cross section of  $\sigma_i = 10^{-40} \text{ cm}^2$ .

1670 three parameters from the solar model that are needed for the computation, the solar  
 1671 temperature (left panel), mass (central panel) and electron density (right panel) profiles.

1672 For the case of the interactions off nuclei, the computations are more convoluted  
 1673 as one needs to add up the contributions of the different most abundant nuclei in  
 1674 the Sun. Also, in contrast to the electron scenario where the form factor is trivially  
 1675  $|F_e(q)|^2 = 1$ , for any nucleus  $i$  one would need to consider some appropriate nuclear  
 1676 density distribution (either a Gaussian approximation, a Woods-Saxon distribution, etc)  
 1677 which would complicate the calculations even further.

1678 That is the reason why, at this stage of the study, I decided to take an alternative  
 1679 approach to the computation of the DM-nucleus capture rates. I used the **DarkSUSY**  
 1680 software, that allows us to compute these quantities performing a full numerical  
 1681 integration over the momentum transfer of the form factors [129]. The default standard  
 1682 solar model used by **DarkSUSY** is BP2000<sup>1</sup> [130].

---

<sup>1</sup>This is what they say in their manual, but I fear it is somewhat outdated. It appears to me

## 5.1. GRAVITATIONAL CAPTURE OF DM BY THE SUN

1683 In Fig. 5.2 I show the results I obtain for the capture rates, for the case of interactions  
 1684 off electrons (red solid line), SD (green solid line) and SI (blue solid line) interactions of  
 1685 nucleons. In all cases I use a value of the scattering cross sections of  $\sigma_i = 10^{-40} \text{ cm}^2$ .  
 1686 Note here one of the limitations of the **DarkSUSY** approach, one can not extend the  
 1687 computation below  $m_{\text{DM}} = 1 \text{ GeV}$ . Nevertheless, this is not something to worry about in  
 1688 this case, as I will discuss next. As a comparison, I added also the values computed in Ref.  
 1689 [124] (same color scheme, dashed lines). One can see there is good agreement between  
 1690 these and the **DarkSUSY** computation of the SD and SI interactions for  $m_{\text{DM}} \geq 1 \text{ GeV}$ .  
 1691 In this regime their computations also matches quite well the results for the electron  
 1692 capture rate. However, these start to differ significantly below  $m_{\text{DM}} = 1 \text{ GeV}$ , being  
 1693 their estimate up to a factor of 5 bigger than ours for low masses. This could be due to  
 1694 the use of a different solar model in the calculation.

1695 Let me comment briefly about the assumption I made before about not including  
 1696 an evaporation term in the Boltzmann equation. If I include this term in the equation,  
 1697 which is proportional to the number of DM particles, the equilibrium solution takes the  
 1698 form:

$$N_{\text{DM}}^{eq} = \sqrt{\frac{C_{\odot}}{A_{\odot}}} \frac{1}{\kappa + \frac{1}{2} E_{\odot} \tau_{eq}}, \quad (5.17)$$

1699 where  $E_{\odot}$  is the total evaporation rate,  $\tau_{eq}$  is the equilibrium time in the absence of  
 1700 evaporation:

$$\tau_{eq} = \frac{1}{\sqrt{C_{\odot} A_{\odot}}}, \quad (5.18)$$

1701 and  $\kappa$  is defined as:

$$\kappa \equiv \sqrt{1 + \left( \frac{E_{\odot} \tau_{eq}}{2} \right)^2}. \quad (5.19)$$

1702 Now, it is easy to proof that in the case evaporation dominates  $\kappa \gg 1$  and therefore:

$$N_{\text{DM}}^{eq} \simeq \frac{C_{\odot}}{E_{\odot}}. \quad (5.20)$$

---

this model is relatively old and do not see why they are not using others like [20]. Maybe one can double-check in the code to make sure.

## CHAPTER 5. DARK MATTER SEARCHES WITH NEUTRINOS FROM THE SUN

1703 In contrast, if evaporation is irrelevant  $\kappa \simeq 1$  and one recovers Eq. (5.2).  
1704 In this way, one can define the evaporation mass as the mass for which the number  
1705 of DM particles in equilibrium approaches Eq. (5.20) at 10% level:

$$\left| N_{DM}^{eq}(m_{\text{evap}}) - \frac{C_{\odot}(m_{\text{evap}})}{E_{\odot}(m_{\text{evap}})} \right| = 0.1 N_{DM}^{eq}(m_{\text{evap}}). \quad (5.21)$$

1706 This can be regarded as the minimum testable mass one can reach using the annihilation  
1707 products of the DM in the Sun.

1708 It was reported in Ref. [124] that, in the case of both SD and SI DM interactions  
1709 off nuclei, this value ranges from 2 to 4 GeV depending on the specific scattering  
1710 cross section value, compatible with the usual assumptions in the literature. What is  
1711 interesting is the case of the electron capture. It was found that, when one applies a  
1712 cutoff in the velocity distribution of the DM trapped in the Sun slightly below the escape  
1713 velocity, the evaporation mass for the DM-electron interaction decreases remarkably. For  
1714 a moderate choice of  $v_c(r) = 0.9v_e(r)$  one gets an evaporation mass of around 200 to  
1715 600 MeV. This possibility opens a region of the parameter space that could be tested  
1716 with the next generation of neutrino detectors.

## 1717 5.2 Neutrino flux from DM annihilations

1718 When WIMPs annihilate inside the Sun a flux of high-energy neutrinos is expected  
1719 from heavy quarks, gauge bosons and  $\tau^+\tau^-$  final states, which decay before losing  
1720 energy in the dense solar medium [119]. These produce a continuous neutrino spectra  
1721 up to  $E_{\nu} \sim m_{\chi}$ . In the case of direct annihilation into neutrinos, one would have a  
1722 monochromatic flux with  $E_{\nu} = m_{\chi}$ . This kind of signal has been extensively studied in  
1723 the literature, allowing to put strong limits on the SD WIMP-proton cross section for  
1724 large  $m_{\chi}$ . However, the number of high-energy neutrinos per WIMP annihilation is small  
1725 and the spectrum depends on the unknown final state. Moreover, although background  
1726 rejection is easier for large  $m_{\chi}$ , neutrinos with  $E_{\nu} \gtrsim 100$  GeV are significantly attenuated  
1727 by interactions in the Sun.

### 5.3. COMPUTING LIMITS FROM SOLAR NEUTRINO FLUXES

1728        Nevertheless, most WIMP annihilation final states eventually produce a low-energy  
 1729        neutrino spectrum. In this case one does not just consider the more massive final states  
 1730        but also annihilations into  $e^+e^-$ ,  $\mu^+\mu^-$  and light quarks [118]. In particular, light  
 1731        mesons would be produced and stopped in the dense medium, thus decaying at rest and  
 1732        producing a monoenergetic neutrino signal. The decay-at-rest of kaons will produce a  $\nu_\mu$   
 1733        flux with  $E_\nu = 236$  MeV, while in the case of pions one would have  $E_\nu = 29.8$  MeV. In  
 1734        practice, only the  $K^+$  and  $\pi^+$  contribute to these signals, as the  $K^-$  and  $\pi^-$  are usually  
 1735        Coulomb-captured in an atomic orbit and get absorbed by the nucleus. There is also a  
 1736        low-energy neutrino signal coming from muon decays, which are produced in kaon or  
 1737        pion decays, leptonic decays of other hadrons and heavy leptons or even directly from  
 1738        WIMP annihilations. These can decay at rest and contribute to the previous low-energy  
 1739        neutrino flux with a well known spectrum below 52.8 MeV.

1740        These monoenergetic MeV neutrinos were previously considered undetectable but,  
 1741        due to the large yield, the known spectra and the modern advances in the detector  
 1742        technology, these low-energy neutrino flux can be a good probe of the SD WIMP-proton  
 1743        cross section in standard solar WIMP capture scenario, as it is sensitive to low WIMP  
 1744        masses and insensitive to the particular final state. A good place to look for these signals  
 1745        are next-generation neutrino experiments such as DUNE.

#### 1746        5.3 Computing limits from solar neutrino fluxes

1747        The first step to use these fluxes to search for DM in the Sun is to determine the expected  
 1748        number of atmospheric background events. For a given exposure, after directionality  
 1749        selection has been applied, this can be written as:

$$N_B = \eta_B \int d\Omega \int_{E_{min}}^{E_{max}} dE_\nu \frac{d^2\Phi_{atm}^\mu}{dE_\nu d\Omega} \times \left( A_{eff}^{(\mu)}(E_\nu) T \right), \quad (5.22)$$

1750        where  $\eta_B$  is the background efficiency,  $E_{min}$  and  $E_{max}$  the minimum and maximum  
 1751        energies to integrate over,  $d^2\Phi_{atm}^\mu/dE_\nu d\Omega$  the differential flux of atmospheric muon  
 1752        neutrinos,  $A_{eff}^{(\mu)}$  is the effective area of DUNE to muon neutrinos, and  $T$  is the exposure

## CHAPTER 5. DARK MATTER SEARCHES WITH NEUTRINOS FROM THE SUN

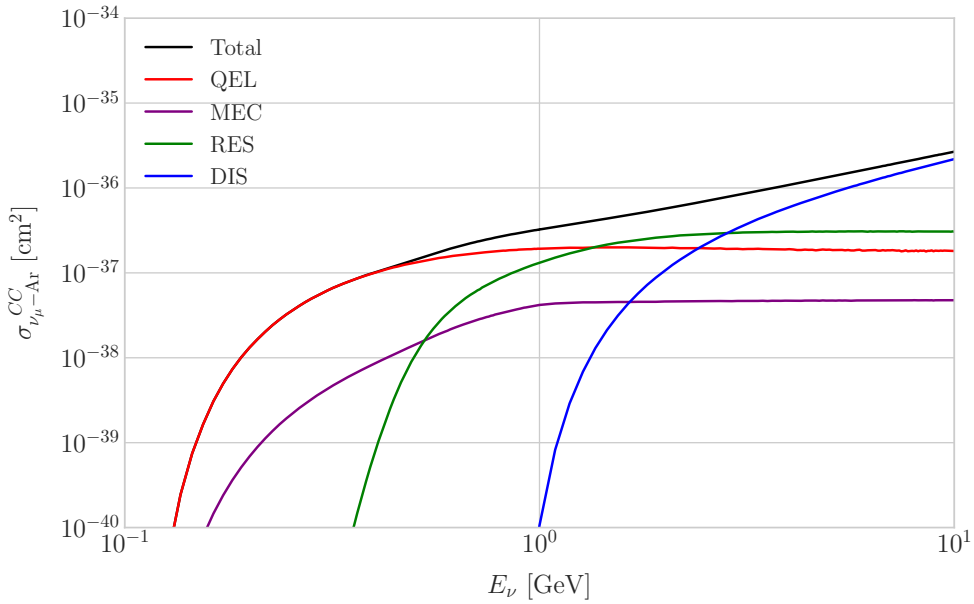


**Figure 5.3:** NuWro computed  $\nu_\mu - {}^{40}\text{Ar}$  charged-current scattering cross section as a function of the neutrino energy. The black line shows to the total cross section, whereas the others correspond to the different contributions (in red quasi-elastic scattering, in green resonant pion exchange, in blue deep inelastic scattering and in purple meson exchange current).

time. The effective area can be expressed as the product of the neutrino-nucleus scattering cross section and the number of nuclei in the fiducial volume of the detector. This way, for DUNE we have:

$$A_{eff}^{(\mu)}(E_\nu) = (6.0 \times 10^{-10} \text{ m}^2) \left( \frac{\sigma_{\nu-\text{Ar}}^{(\mu)}(E_\nu)}{10^{-38} \text{ cm}^2} \right) \left( \frac{M_{target}}{40 \text{ kT}} \right), \quad (5.23)$$

where  $\sigma_{\nu-\text{Ar}}^{(\mu)}$  is the  $\nu_\mu - {}^{40}\text{Ar}$  charged-current scattering cross section. In Fig. 5.3 I show the computed value of the cross section as a function of the neutrino energy  $E_\nu$ , in the range of interest both for the atmospheric background and signal events. It was computed using the NuWro Monte Carlo neutrino event generator [131], including the CC contributions of the quasi-elastic scattering (red line), resonant pion exchange (green line), deep inelastic scattering (blue line) and meson exchange current (purple line).

The background rejection will depend on the resolution of the detector and the selection one applies on the events. A geometry argument can be used to estimate

### 5.3. COMPUTING LIMITS FROM SOLAR NEUTRINO FLUXES

the maximum background rejection one can achieve in this case, considering one can efficiently discriminate all events coming from a direction different from that of the Sun. In that case, the optimal background efficiency will simply be the relative angular coverage of the Sun. Taking the angular diameter of the Sun as seen from the Earth to be  $0.5^\circ$ , I have:

$$\eta_B^{(opt)} \approx \frac{\pi \left(\frac{0.5}{2}\right)^2}{360 \times 180} \simeq 3.03 \times 10^{-6}. \quad (5.24)$$

This value gives an optimistic estimate of the number of background events. However, it can be regarded as an upper limit, as it represents the best case scenario.

In Fig. 5.4 I show the fluxes of atmospheric neutrinos at the Homestake mine during solar minimum, taken from Ref. [132]. The values are averaged over the two angular directions. In blue I have the flux of muon neutrinos while in red I indicate the flux of electron neutrinos. Additionally, the dashed lines correspond to both antineutrino species.

Using these values for the muon neutrino and the corresponding total CC cross section, one can compute the total number of expected background events by integrating over the given energy range. For this I choose the range for DUNE specified in [83],  $E_{min} = 10^{-1}$  GeV and  $E_{max} = 10$  GeV. Taking all these into account, I find the total number of background events to be:

$$N_B \simeq \eta_B \times (3.827 \times 10^4) \times \left( \frac{\text{exposure}}{400 \text{ kT yr}} \right). \quad (5.25)$$

To estimate the sensitivity of DUNE to this kind of signals, one can consider a hypothetical data set where the number of observed neutrinos is taken to be the expected number of background events rounded to the nearest integer,  $N_{obs} = \text{round}(N_B)$  [133]. Now, if I assume that the number of signal and background events seen by DUNE are given by Poisson distributions with means equal to the expected number of signal and background events,  $N_S$  and  $N_B$ , one can denote by  $N_S^{90}$  to the number of expected signal events such that the probability of having an experimental run with a number of events greater than  $N_{obs}$  is 90%. This number can be obtained as the numerical solution

## CHAPTER 5. DARK MATTER SEARCHES WITH NEUTRINOS FROM THE SUN

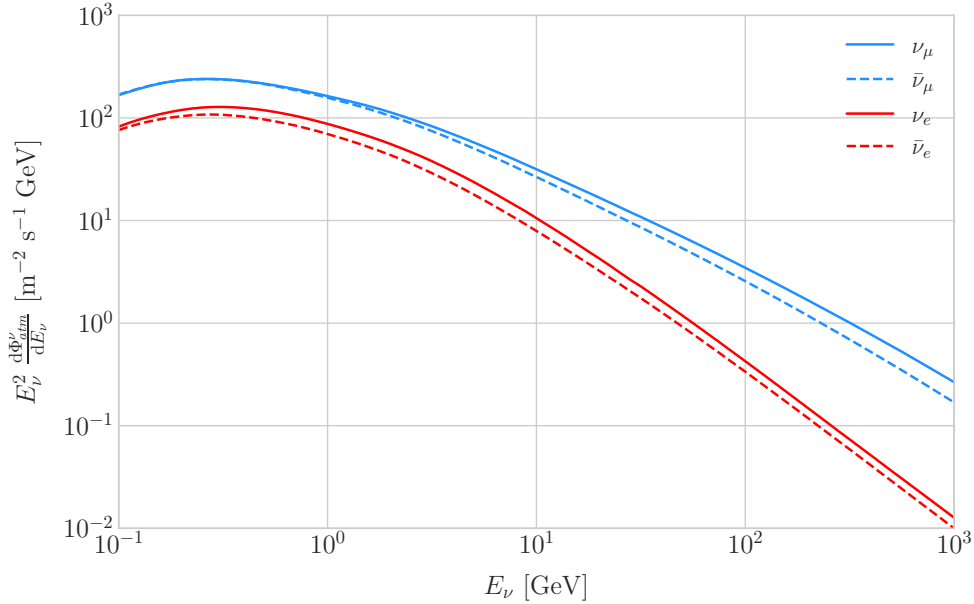


**Figure 5.4:** Expected atmospheric neutrino flux as a function of the neutrino energy  $E_\nu$  at Homestake at solar minimum, taken from Ref. [132]. The blue solid (dashed) line correspond to muon neutrinos (antineutrinos) and the red solid (dashed) line correspond to electron neutrinos (antineutrinos).

1789 to the equation:

$$1 - \frac{\Gamma(N_{obs} + 1, N_S^{90} + N_B)}{N_{obs}!} = 0.9, \quad (5.26)$$

1790 where  $\Gamma(x, y)$  is the upper incomplete gamma function.

1791 The number of signal events is related to the neutrino flux from DM annihilations in  
1792 a similar way as the background events to the atmospheric neutrino flux. In this case I  
1793 have:

$$N_S = \eta_S \Gamma_A^{eq} \int_{z_{min}}^{z_{max}} dz \frac{dN_\nu}{dAdN_A dz} \times (A_{eff}^\mu(z)T), \quad (5.27)$$

1794 where  $\eta_S$  is the signal efficiency,  $\Gamma_A^{eq}$  is the total annihilation rate of DM particles at  
1795 equilibrium,  $\Gamma_A^{eq} = A_\odot (N_{DM}^{eq})^2$ ,  $z_{min}$  and  $z_{max}$  the minimum and maximum relative  
1796 energies to integrate over (given by  $z_{min,max} = E_{min,max}/m_{DM}$  for each  $m_{DM}$ ) and  
1797  $dN_\nu/dAdN_A dz$  the muon neutrino flux per DM annihilation in the Sun.

1798 Having obtained  $N_S^{90}$  one can use the relation in Eq. (5.27) to compute  $\Gamma_A^{eq,90}$  for  
1799 different values of the DM mass. Then, I can directly translate those values into the

## 5.4. EXAMPLE: KALUZA-KLEIN DARK MATTER

1800 projected sensitivities for DUNE to the DM scattering cross sections, for a given exposure.  
1801 The relation between the annihilation rate and the DM-nucleon cross section comes from  
1802 the equilibrium condition through the solar DM capture rate, discussed above.

### 1803 5.4 Example: Kaluza-Klein Dark Matter

1804 Even though there are plenty of BSM theories which provide viable dark matter  
1805 candidates, Kaluza-Klein type of models [134, 135] within the universal extra dimensions  
1806 (UED) paradigm naturally predict the existence of a massive, stable particle that can  
1807 play the role of the dark matter. In the UED scenario all the SM fields can propagate  
1808 in one or more compact extra dimensions [136], as opposed to the idea of brane worlds  
1809 [137, 138], where just gravity can propagate in the bulk while SM particles live at fixed  
1810 points.

1811 Furthermore, in UED there is no violation of the translational invariance along the  
1812 extra dimensions, thus leading to degenerate KK modes masses and also the conservation  
1813 of the KK number in the effective four dimensional theory. At loop level, radiative  
1814 corrections and boundary terms shift the masses of the KK modes and break KK  
1815 number conservation into a KK parity. As a result, this theory only contains interactions  
1816 between an even number of odd KK modes and therefore the lightest among the first KK  
1817 excitations will be stable. This particle is usually denoted as the lightest Kaluza-Klein  
1818 particle (LKP) and its mass is proportional to  $1/R$ , being  $R$  the size of the extra  
1819 dimension.

1820 A viable DM candidate needs to be electrically neutral and non-baryonic, therefore  
1821 good candidates among the first Kaluza-Klein excitations would be the KK neutral  
1822 gauge bosons and the KK neutrinos [139]. Another possible candidate is the first KK  
1823 excitation of the graviton, which receives negligible radiate contributions and therefore  
1824 has a mass almost equal to  $1/R$ , but it has been shown that the lightest eigenstate from  
1825 the mixing of the gauge mass states  $(B^1, W_3^1)$  would be lighter, as  $B^1$  and  $W_3^1$  receive  
1826 negative radiate corrections [140]. It is also understood that, when these corrections

CHAPTER 5. DARK MATTER SEARCHES WITH NEUTRINOS FROM THE SUN

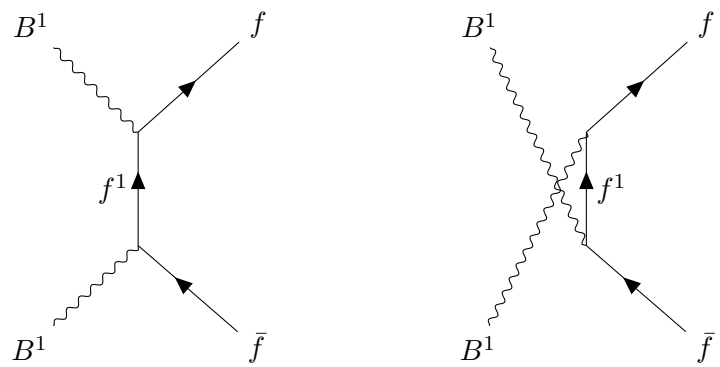


**Figure 5.5:** Feynman diagrams for  $B^1B^1$  annihilation into SM fermions.

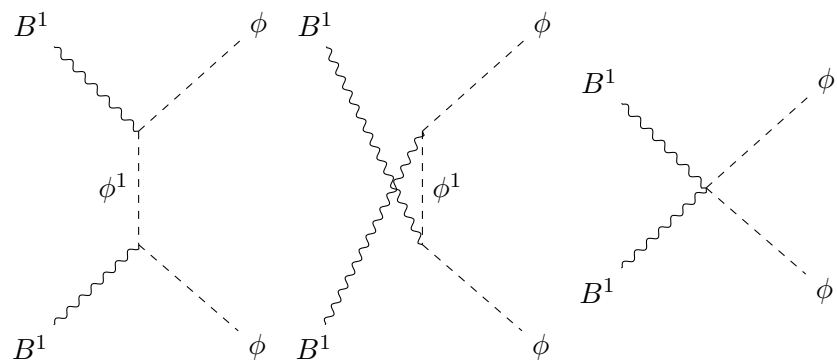


**Figure 5.6:** Feynman diagrams for  $B^1B^1$  annihilation into a Higgs boson pair.

#### 5.4. EXAMPLE: KALUZA-KLEIN DARK MATTER

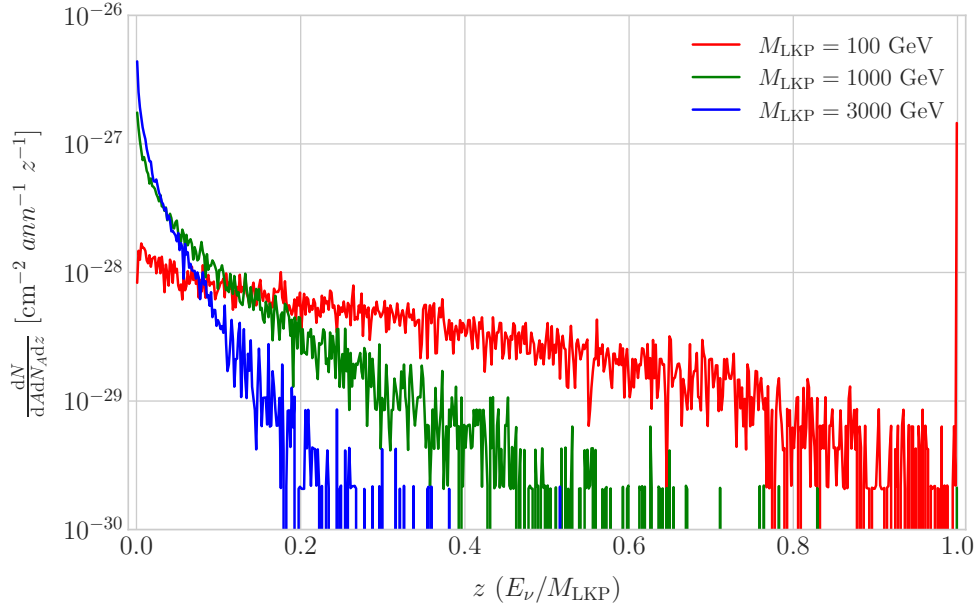


**Figure 5.7:** Computed spectra of muon neutrinos at the DUNE FD site from  $B^1$  annihilations in the Sun for three different values of  $M_{\text{LKP}}$ , plotted in relative energy units for legibility.

1827 become sizeable, the eigenstates become approximately pure  $B^1$  and  $W_3^1$  states as the  
 1828 Weinberg mixing angle grows small with the KK number [140]. In that case, the LKP  
 1829 can be well-approximated as being entirely  $B^1$ .

1830 I need to compute the neutrino flux produced by the annihilations of the LKP in  
 1831 the core of the Sun, taking into account their propagation in the solar medium, as  
 1832 well as neutrino oscillations. To this end I used `WimpSim` [141, 142] to generate one  
 1833 million annihilation events in the Sun over a time span of four years and propagate  
 1834 them to the DUNE FD location ( $44^\circ 20' \text{ N}, 103^\circ 45' \text{ W}$ ), for different values of  $M_{\text{LKP}}$ .  
 1835 In Fig. 5.7 I show the obtained muon neutrino spectra arriving to the detector from  
 1836 LKP annihilations in the Sun, per unit area and per annihilation, plotted in relative  
 1837 energy units for different values of the mass. As one could expect the spectra get  
 1838 steeper the higher is the mass, due to the absorption of high-energy neutrinos in the  
 1839 solar medium. Also, one can see the peak at  $z = 1$  due to the direct annihilation into  
 1840 neutrinos  $\chi\chi \rightarrow \nu\bar{\nu}$ .

1841 Now, one can estimate the sensitivity of DUNE to this particular model by using

## CHAPTER 5. DARK MATTER SEARCHES WITH NEUTRINOS FROM THE SUN

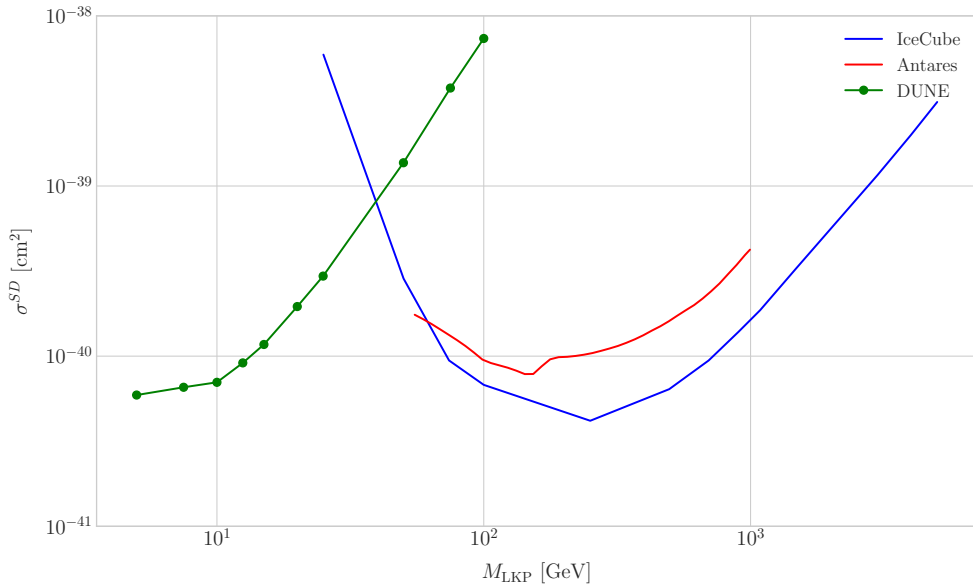


**Figure 5.8:** Projected 90% confidence level upper limit for DUNE (400 kT yr) on the spin-dependent  $B^1$ -proton scattering cross section as a function of  $M_{\text{LKP}}$  (green dots). I also show the previous limits from IceCube [143] (blue line) and Antares [144] (red line) on the LKP cross section. The shaded area represents the disfavoured region (at 95% confidence level) on the mass of the LKP from LHC data [145].

the methods I previously discussed. To begin with, I will use the optimistic estimation of the background efficiency in Eq. (5.24) to get an upper bound. Using it, one can directly compute the number of expected background events to be  $N_B = 0.11$  for an exposure of 400 kT yr. Then, Eq. (5.26) give us a value of  $N_S^{90} = 2.20$  for the 90% exclusion number of expected signal events. By using the NuWro generated cross sections and the computed neutrino fluxes from  $B^1$  annihilations in the Sun I can estimate the limits on the SD and SI DM-nucleus cross section using the relation in Eq. (5.2) and the capture rates I computed with DarkSUSY.

In Fig. 5.8 I show the projected sensitivity for DUNE on the spin-dependent  $B^1$ -proton scattering cross section versus the mass of the DM particle, for a exposure of 400 kT yr (green dots). I also include the previous results from IceCube [143] (blue line) and Antares [144] (red line). The shaded area represents the disfavoured region from combined searches for UED by ATLAS and CMS [145].

From the experimental point of view, this estimation lacked a detailed simulation of

## 5.5. HIGH ENERGY DM NEUTRINO SIGNALS

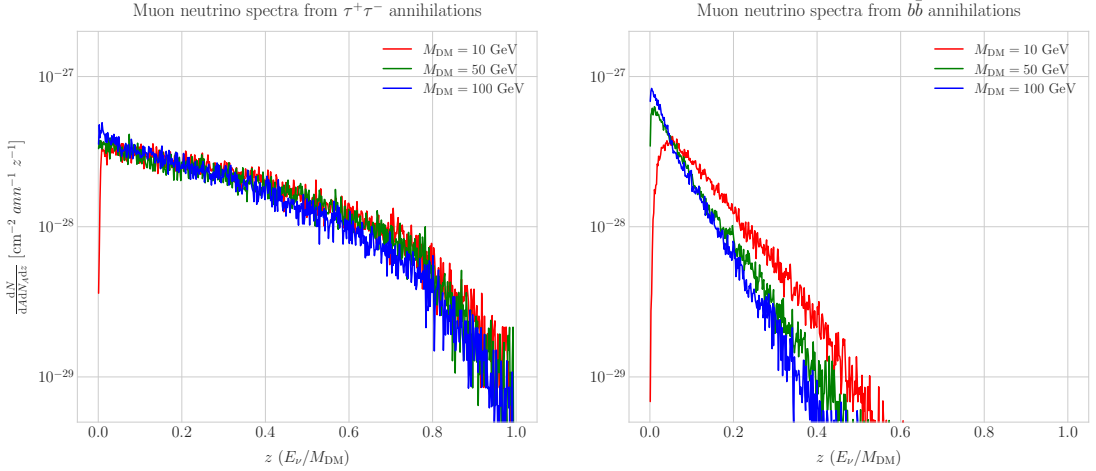


**Figure 5.9:** Computed spectra of muon neutrinos at the DUNE FD site from  $\tau^+\tau^-$  (left panel) and  $b\bar{b}$  (right panel) annihilations in the Sun for the DM masses  $m_{DM} = 10$  GeV (red line), 50 GeV (green line) and 100 GeV (blue line), plotted in relative energy units.

1856 the detector response and thus this must be consider as a mere optimistic sensitivity  
 1857 computation. However, it shows the potential of DUNE to constrain this kind of exotic  
 1858 scenarios, showing the region where it will be in a position to compete with other neutrino  
 1859 telescopes. A more detailed analysis is needed if I am to make a realistic estimation.  
 1860 Even though the region of the parameter space where DUNE would be sensitive to this  
 1861 particular model is quite constrained by collider searches [145] and other rare decay  
 1862 measurements [146, 147], it still constitutes an alternative indirect probe.

## 1863 5.5 High energy DM neutrino signals

1864 To have better estimates on the capability of the DUNE FD to constrain the parameter  
 1865 space of DM using solar neutrino fluxes, I need to start accounting for the detector  
 1866 resolution effects and the topologies of the different signatures. As a starting point, I  
 1867 will focus on specific annihilation channels. For the case of DUNE, the relevant ones  
 1868 are mainly the hard channels  $\tau^+\tau^-$  and  $\nu\bar{\nu}$  and the soft channel  $b\bar{b}$ . These are the open  
 1869 annihilation channels for relatively low mass WIMPs that will actually give neutrino  
 1870 fluxes. Other channels, like  $W^+W^-$  and  $ZZ$ , are open for more massive WIMPs, but  
 1871 those will produce usually a higher energy neutrino flux that will be out of reach for

## CHAPTER 5. DARK MATTER SEARCHES WITH NEUTRINOS FROM THE SUN

1872 DUNE (usually the maximum neutrino energy is taken to be  $E_{max} = 10$  GeV).

1873 In Fig. 5.9 I show the `WimpSim` [141, 142] generated muon neutrino spectra at the  
1874 DUNE FD location ( $44^\circ 20' N$ ,  $103^\circ 45' W$ ) from  $\tau^+\tau^-$  (left panel) and  $b\bar{b}$  (right panel)  
1875 annihilations in the core of the Sun, for different DM masses. Here, one can clearly see  
1876 the meaning of the previous distinction between hard and soft channels. For the same  
1877 DM mass value, the muon neutrino spectrum from the  $\tau^+\tau^-$  channel is more flat and  
1878 reaches higher energies than the one from the  $b\bar{b}$  channel, which drops faster.

1879 In this case, I prepared two sets of files, one for  $\tau^+\tau^-$  and the other for  $b\bar{b}$ , for DM  
1880 masses in the range from 5 to 100 GeV (for  $b\bar{b}$  the first mass point I take is 7.5 GeV, as  
1881 this annihilation channel is not kinematically allowed for a WIMP with  $m_{DM} = 5$  GeV).  
1882 Then, I prepared the `WimpSim` output fluxes in a specific way to use them as inputs to  
1883 `NuWro`, which simulates the neutrino interaction with the argon.

1884 Because `WimpSim` outputs an event list together with the fluxes, I can use the former  
1885 to generate the events. The direction of these is given in terms of the azimuth and  
1886 altitude angles viewed from the specified location, so first I need to convert these into the  
1887 DUNE FD coordinates. Once I have done it, each event can be processed with `NuWro`.  
1888 To increase the number of samples and optimise the computation time, I generate 100  
1889 interactions (i.e. `NuWro` events) for each `WimpSim` event<sup>2</sup>. I restrict the event generation  
1890 to charged current interactions, but I allow all the different contributions to the CC  
1891 cross section, i.e. quasielastic scattering (QE), meson exchange current process (MEC),  
1892 resonant pion production (RES) and deep inelastic scattering (DIS). I just take into  
1893 account the CC contribution because I am only interested in final states with charged  
1894 leptons, as we have better chances of reconstructing the kinematics of CC events.

1895 For the atmospheric fluxes I follow a similar procedure, only that this time I do not  
1896 have a set of events but the fluxes binned in azimuth and altitude angles. This way, I  
1897 transform these to DUNE coordinates and process the fluxes for each bin separated with  
1898 `NuWro`.

---

<sup>2</sup>This also solves a problem related with the generation of the neutrino interactions in `NuWro`, as if you only produce one event each time you launch `NuWro` it will always produce an interaction of the dominant interaction type for that particular energy.

## 5.5. HIGH ENERGY DM NEUTRINO SIGNALS

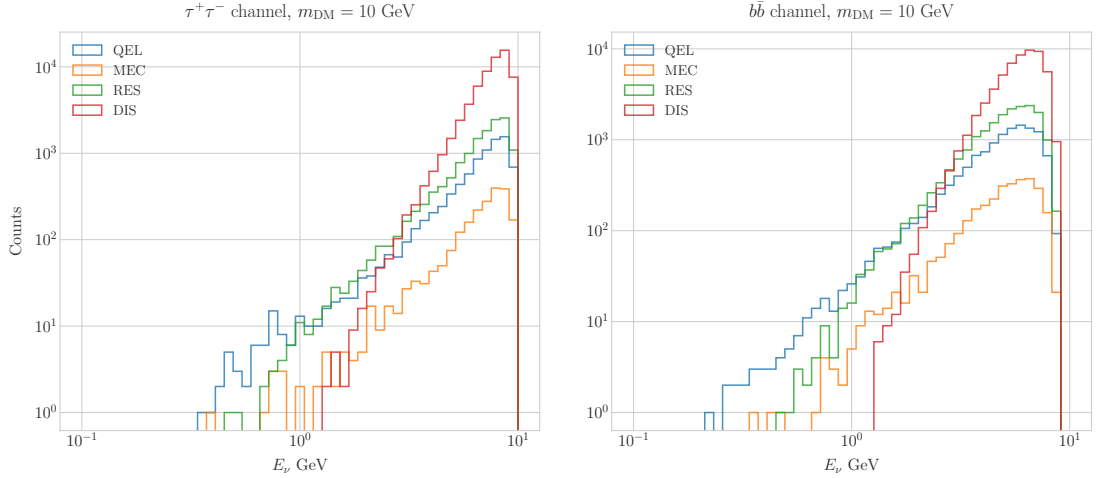


**Figure 5.10:** Distribution of the muon neutrino energies from the  $\tau^+\tau^-$  (left panel) and  $b\bar{b}$  (right panel) annihilation channels, for  $m_{\text{DM}} = 10 \text{ GeV}$ , separated by CC interaction type: QE (blue), MEC (orange), RES (green) and DIS (red).

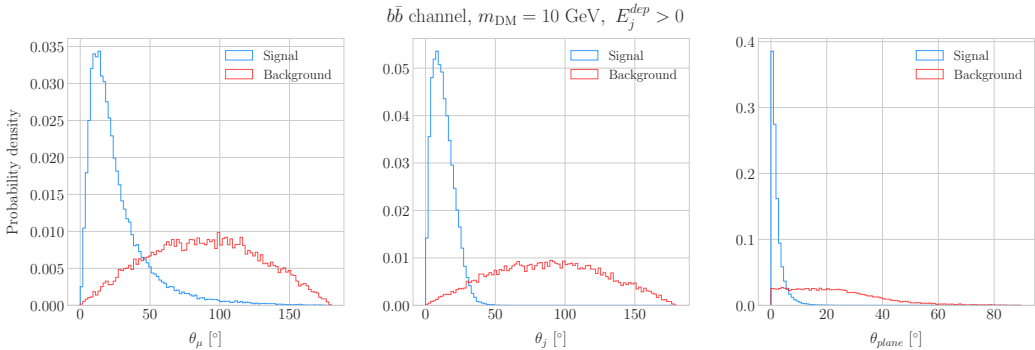


**Figure 5.11:** Distributions of  $\theta_\mu$  (left panel),  $\theta_j$  (central panel) and  $\theta_{\text{plane}}$  (right panel) for the  $b\bar{b}$  sample with  $m_{\text{DM}} = 10 \text{ GeV}$  (blue) and the atmospheric background (red).

1899 At this point, I have two sets of events with different energies and final states.  
 1900 In Fig. 5.10 one can see the distribution of the muon neutrino energies for the case  
 1901  $m_{\text{DM}} = 10 \text{ GeV}$ , both for the  $\tau^+\tau^-$  (left panel) and  $b\bar{b}$  (right panel) channels, separated  
 1902 by interaction. One can clearly see that there are different energy regimes where the  
 1903 primary interaction type is different. This leads to a plurality of event topologies,  
 1904 therefore making it difficult to implement a general approach to the selection of events  
 1905 in detriment of the background. As a way to proceed, I decided to focus on a subset of  
 1906 the samples, based on the different interaction modes and contents of the final state.  
 1907 Thus, I consider a CC DIS sample and a single proton CC QE sample.

## CHAPTER 5. DARK MATTER SEARCHES WITH NEUTRINOS FROM THE SUN

### 1908 5.5.1 DIS-like events

1909 To begin with, I consider the high energy part of the spectrum. In this region DIS events  
1910 dominate, i.e. interactions of the form  $\nu_\mu + q_d(\bar{q}_u) \rightarrow \mu^- + q_u(\bar{q}_d)$ . Therefore, our final  
1911 estates will contain a muon and a hadronic jet from the fragmentation of the outgoing  
1912 quark. As all these events have  $E_\nu \gtrsim 1$  GeV the momentum transfer to the remnant  
1913 nucleus is negligible, for this reason the neutrino energy can be effectively reconstructed  
1914 just taking into account the momenta of the muon and the jet. This technique was  
1915 successfully used in Ref. [148] to select monoenergetic DM solar neutrino events from  
1916  $\nu\bar{\nu}$  annihilation channels.

1917 Using momentum conservation one sees that the plane generated by the momenta  
1918 of the muon and the jet needs to also contain the momentum of the neutrino. As we  
1919 are interested in neutrinos coming from the Sun, the momentum of the neutrino can be  
1920 regarded as known beforehand. This will allow us to define the angle of the outgoing  
1921 muon and jet with respect to the incoming neutrino. Moreover, one can also use that  
1922 information to reject poorly reconstructed jets, checking for deviations of these from the  
1923 momentum conservation plane.

1924 To account for the limited angular resolution of the detector, I smeared the momenta  
1925 of the muons and hadrons. In a LArTPC muons are expected to be tracked with high  
1926 precision, therefore I take the associated angular resolution to be  $1^\circ$ . In the case of  
1927 jets, it is expected that for the hadrons dominating the cascade a detector like DUNE  
1928 has an angular resolution between  $1^\circ$  to  $5^\circ$  [83], so I take the latter, more conservative,  
1929 estimate.

1930 As a first selection step, I will just take into account particles with kinetic energies  
1931 above the detection threshold of DUNE. For muons and photons the specified threshold  
1932 energy is 30 MeV, for charged pions 100 MeV and for other hadrons 50 MeV [83]. This  
1933 way, if the outgoing muon in a certain event has an energy lower than the required  
1934 threshold I will drop such event. For the case of hadrons and photons, I will only require  
1935 to have at least one particle above the energy threshold, so then one can compute the

## 5.5. HIGH ENERGY DM NEUTRINO SIGNALS

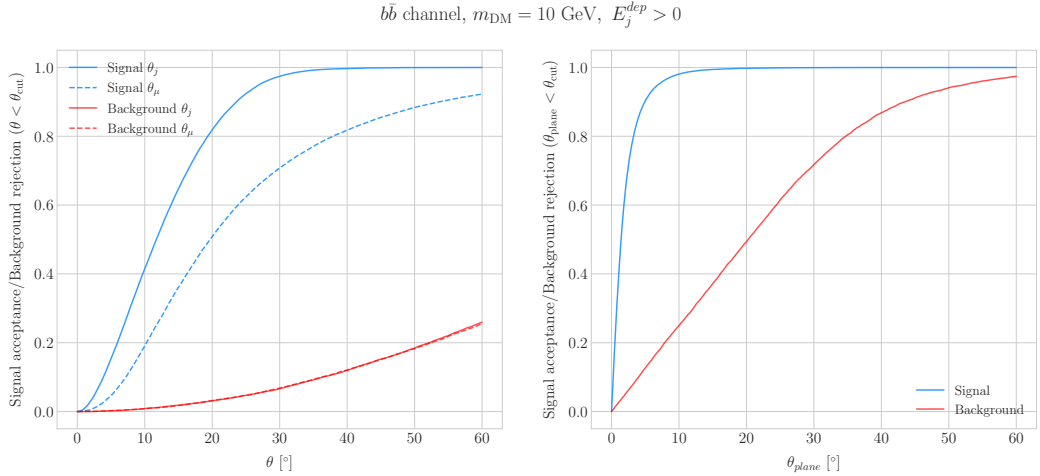


**Figure 5.12:** Left panel: signal efficiencies (blue lines) and background rejections (red lines) for events passing the cuts  $\theta < \theta_{cut}$  for the jet (solid lines) and muon (dashed lines) angles. Right panel: signal efficiency (blue line) and background rejection (red line) for events passing the cut  $\theta_{plane} < \theta_{cut}$  for the momentum conservation plane deviation.

1936 jet momentum using the (smeared) momenta of the  $N$  particles above threshold as:

$$\vec{p}_j = \sum_{i=1}^N \vec{p}_i. \quad (5.28)$$

1937 Additionally, I will also define an estimation of the deposited hadronic energy as:

$$E_j^{dep} = m_{39\text{Ar}} - m_{40\text{Ar}} + \sum_{i=1}^N \sqrt{|\vec{p}_i|^2 + m_i^2}. \quad (5.29)$$

1938 This quantity is useful to select events with enough hadronic visible energy in the  
 1939 detector. For events where most of the hadronic energy is scattered across plenty of  
 1940 hadrons with individual energies below the detection threshold, this estimation will  
 1941 give  $E_j^{dep} \leq 0$ . In these cases it could be expected that the jet momentum is poorly  
 1942 reconstructed, and therefore I require events to pass the cut  $E_j^{dep} > 0$ .

1943 For the events I can compute the angles for the muon and jet with respect to the  
 1944 incoming neutrino as:

$$\cos \theta_\mu = \hat{p}_\nu \cdot \hat{p}_\mu, \quad (5.30)$$

## CHAPTER 5. DARK MATTER SEARCHES WITH NEUTRINOS FROM THE SUN

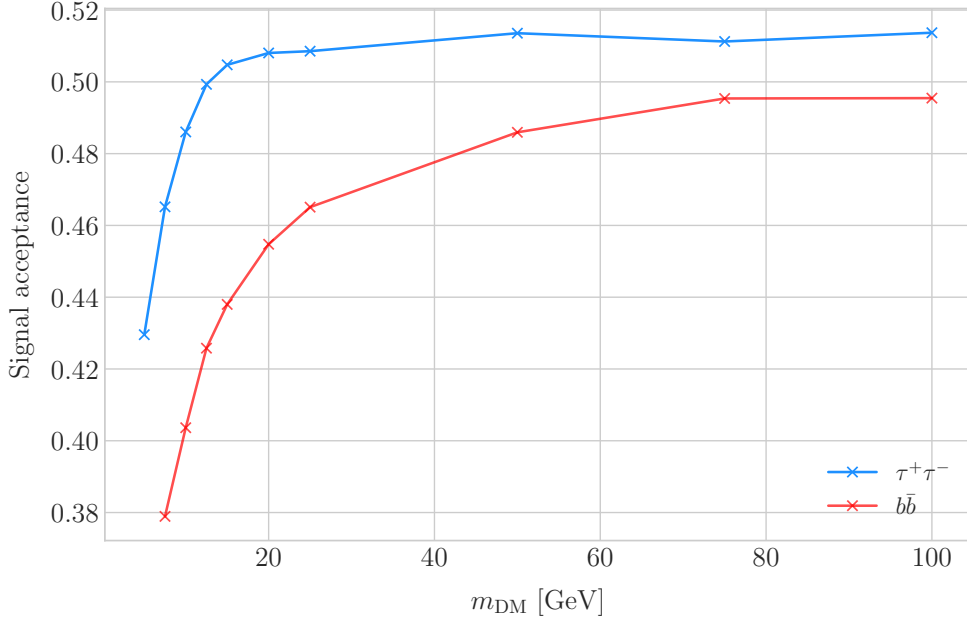


**Figure 5.13:** Signal efficiencies for the  $\tau^+\tau^-$  (blue line) and  $b\bar{b}$  (red line) DIS samples as functions of the DM mass,  $m_{\text{DM}}$ , obtained by applying the optimal angular cuts  $\theta_\mu < 27^\circ$ ,  $4^\circ < \theta_j < 26^\circ$  and  $\theta_{\text{plane}} < 3.5^\circ$ .

$$\cos \theta_j = \hat{p}_\nu \cdot \hat{p}_j, \quad (5.31)$$

and the deviation from the momentum conservation plane as:

$$\sin \theta_{\text{plane}} = \left| \frac{\hat{p}_\mu \times \hat{p}_\nu}{|\hat{p}_\mu \times \hat{p}_\nu|} \cdot \hat{p}_j \right|. \quad (5.32)$$

In Fig. 5.11 I show some distributions of these quantities for the case of the  $b\bar{b}$  sample with  $m_{\text{DM}} = 10$  GeV (blue histograms) and for the atmospheric backgrounds (red). In order to select the atmospheric events I followed the same criteria as for the signal events. However, because in the signal case I used the true direction of the neutrino as input, as it should be that of the Sun at that time and therefore known, in the atmospheric case I used a set of solar positions as our ansatz for the neutrino direction. From the distributions, one can see that the muon and the jet for the signal events are predominantly forward and also that the deviations from the momentum conservation plane are peaked at zero, as one should expect.

## 5.5. HIGH ENERGY DM NEUTRINO SIGNALS

Now, I can start applying cuts to maximise our signal selection efficiency while at the same time I try to minimise the amount of atmospheric background events passing the selection. To this end, I will need to find some lower and upper cuts for  $\theta_j$  and  $\theta_\mu$  and an upper bound for  $\theta_{plane}$ . In Fig. 5.12 I show how upper bound cuts in the different angular variables affect the signal efficiency (blue lines) and the background rejection (red lines). Notice that the signal efficiency behaves in a quite different way when I apply cuts in the jet and the muon angles. On the contrary, the cuts on both variables have a similar effect on the background rejection.

In order to obtain the optimal set of cuts, I perform a multidimensional scan. I do this separately for the  $\tau^+\tau^-$  and the  $b\bar{b}$  samples. For each case, I scan the possible cuts for each mass point and then I take the mean value of the signal efficiency for each configuration, to get the mean efficiency for each set of cuts. I do a similar scan for the atmospheric sample independently. Then, I take the sets of cuts such that the background rejection achieved is greater than 99.8% and search for the one which maximises the  $\tau^+\tau^-$  and  $b\bar{b}$  sample mean efficiencies. I found that with the cuts  $\theta_\mu < 27^\circ$ ,  $4^\circ < \theta_j < 26^\circ$  and  $\theta_{plane} < 3.5^\circ$  I get a background rejection of 99.80% while achieving a 49.40% and 44.92% mean signal efficiencies for the  $\tau^+\tau^-$  and  $b\bar{b}$  signals respectively.

In Fig. 5.13 I show the signal efficiencies as a function of the DM mass for the  $\tau^+\tau^-$  (blue line) and the  $b\bar{b}$  (red line) DIS events, after applying the cuts discussed above, as well as the energy threshold and hadronic visible energy selections. One can see that the efficiency grows with the mass, as annihilations of more massive DM particles will produce a neutrino spectrum centered at higher energies, where DIS events dominate. Notice also that the efficiency is higher for the  $\tau^+\tau^-$  case at every mass point, as in general this channel produces neutrinos at higher energies than the corresponding  $b\bar{b}$  channel.

### 5.5.2 Single proton QE-like events

Now, one can try to explore the low energy tail of the neutrino energy distributions. This regime is dominated by the QE interactions, i.e. events of the type  $\nu_\mu + n \rightarrow \mu^- + p$ .

## CHAPTER 5. DARK MATTER SEARCHES WITH NEUTRINOS FROM THE SUN

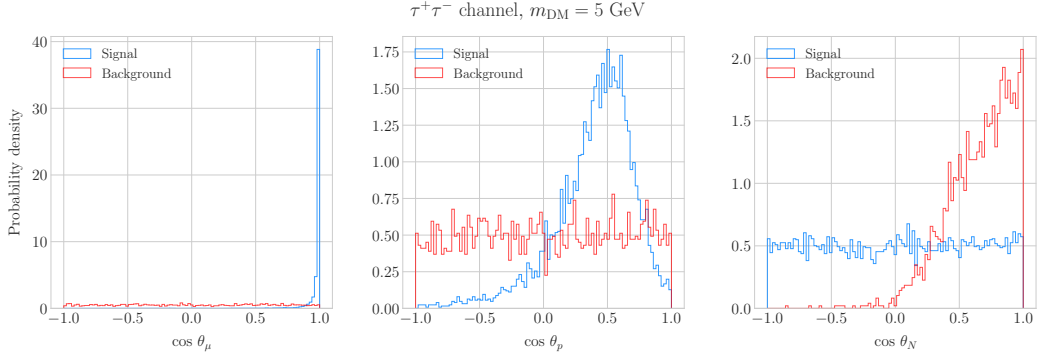


**Figure 5.14:** Distributions of  $\cos \theta_\mu$  (left panel),  $\cos \theta_p$  (central panel) and  $\cos \theta_N$  (right panel) for the  $\tau^+\tau^-$  QE sample with  $m_{\text{DM}} = 5 \text{ GeV}$  (blue) and the atmospheric background (red).

1983 In this case, as the typical energies are  $E_\nu \lesssim 1 \text{ GeV}$ , the momentum transfer to the  
 1984 remnant nucleus is sizeable. Therefore, I can not make the approximation I did before  
 1985 and assume that the momentum of the muon and the proton will give an adequate  
 1986 estimation of the reconstructed neutrino energy.

1987 In any case, as before, I can take the direction of the incoming neutrino as known.  
 1988 That way, one can estimate the energy of the neutrino as:

$$E_\nu^{reco} = E_\mu + E_p + m_{^{39}\text{Ar}} - m_{^{40}\text{Ar}}, \quad (5.33)$$

1989 and using momentum conservation I can write the momentum of the remnant nucleus  
 1990 as:

$$\vec{p}_N = \hat{p}_\nu (E_\mu + E_p + m_{^{39}\text{Ar}} - m_{^{40}\text{Ar}}) - \vec{p}_\mu - \vec{p}_p. \quad (5.34)$$

1991 As in the previous case, I need to drop the events where the muon or the proton fall  
 1992 below the kinetic energy detection threshold [83]. Also, I again apply a smearing to the  
 1993 momenta of the particles, a 1% for muons and 5% for protons.

1994 Having done that, one can compute the following angular variables for our selected  
 1995 events:

$$\cos \theta_\mu = \hat{p}_\nu \cdot \hat{p}_\mu, \quad (5.35)$$

## 5.5. HIGH ENERGY DM NEUTRINO SIGNALS

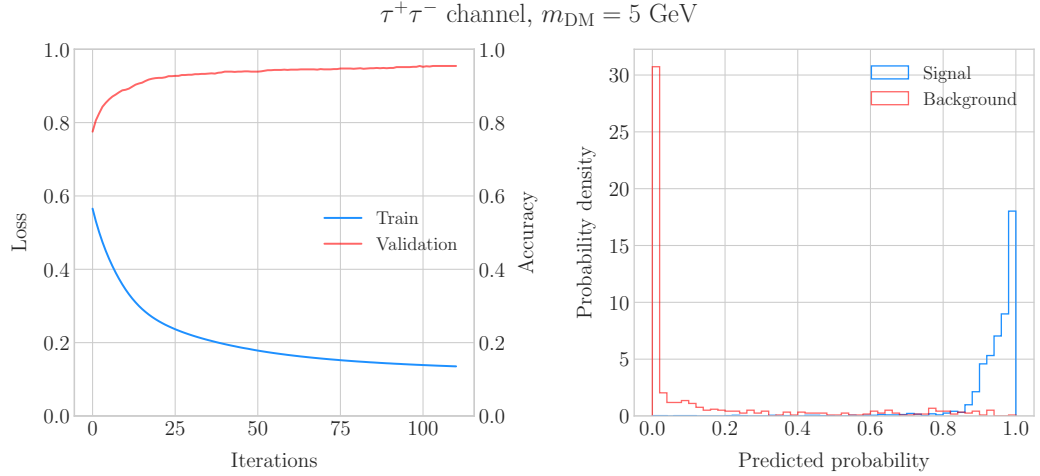


**Figure 5.15:** Left panel: value of the loss function for the training sample (blue line) and accuracy for the validation sample (red line) versus the number of iterations for the MLP classifier training. Right panel: distributions of the predicted probabilities assigned by the MLP classifier to the test sample for the  $\tau^+\tau^-$  QE signal with  $m_{\text{DM}} = 5 \text{ GeV}$  (blue) and the atmospheric background (red).

$$\cos \theta_p = \hat{p}_\nu \cdot \hat{p}_p, \quad (5.36)$$

$$\cos \theta_N = \hat{p}_\nu \cdot \hat{p}_N. \quad (5.37)$$

1996 Fig. 5.14 shows the distributions of these angular variables for the  $\tau^+\tau^-$  QE sample  
 1997 with  $m_{\text{DM}} = 5 \text{ GeV}$  (blue) and the atmospheric background (red). Again, for the  
 1998 atmospheric events I used a random solar position as the ansatz for the incoming  
 1999 neutrino direction. Notice that now, opposed to the DIS case where the signal had very  
 2000 sharp distributions for the variables considered, the shapes of the angular distributions  
 2001 for signal and background are not that much different.

2002 This effectively means that the usual approach of applying simple angular cuts would  
 2003 not work as well as in the previous situation. Therefore, as a possible solution, I tried to  
 2004 use a multilayer perceptron (MLP) classifier to separate between signal and background  
 2005 events. Thus, the power of the hypothesis test will serve as an estimate of the signal  
 2006 efficiency, and in the same way one can take the size of the test to be our background  
 2007 rejection.

2008 For each DM mass value and channel, as well as for the background sample, I divide

## CHAPTER 5. DARK MATTER SEARCHES WITH NEUTRINOS FROM THE SUN

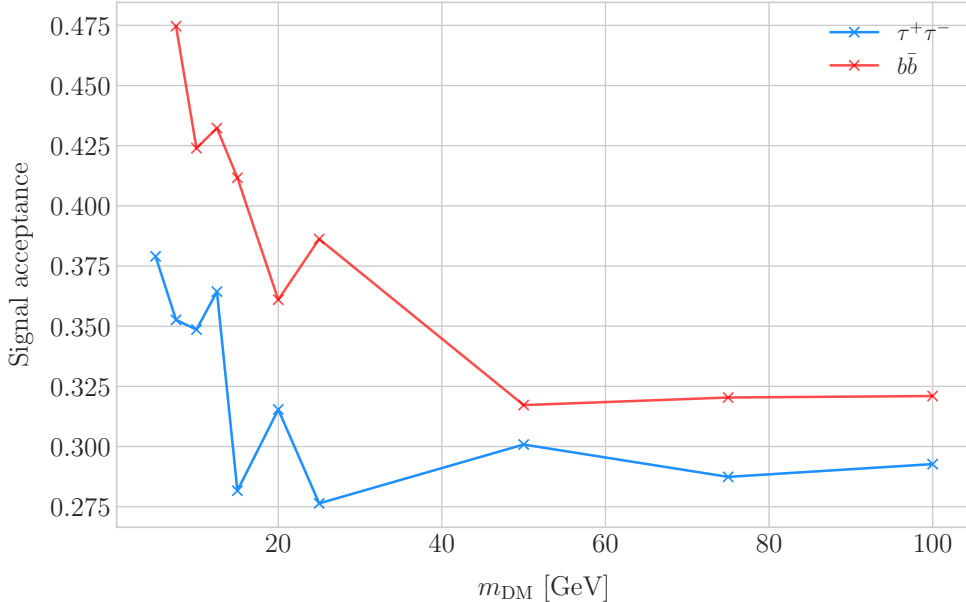


**Figure 5.16:** Signal efficiencies for the  $\tau^+\tau^-$  (blue line) and  $b\bar{b}$  (red line) single proton QE samples as functions of the DM mass,  $m_{\text{DM}}$ , obtained by requiring a minimum predicted probability from the MLP classifier of 0.97 in order to achieve a background rejection greater than 99.8%.

2009 our events into training, validation and test samples. The input variables for the classifier  
 2010 were the reconstructed neutrino energy from Eq. (5.33) and the angular variables defined  
 2011 in Eqs. (5.35 - 5.37). I used the MLP classifier implemented in `scikit-learn` [149], with  
 2012 a total of five hidden layers, the rectified linear unit activation function and adaptive  
 2013 learning rate. In order to account for fluctuations due to artifacts in the training process I  
 2014 repeated the training a thousand times for each sample, redefining each time the training,  
 2015 validation and test subsets, so one can take as our signal efficiency and background  
 2016 rejection the mean values of the powers and sizes of the tests.

2017 The results of one of these training processes for the  $\tau^+\tau^-$  QE signal with  $m_{\text{DM}} =$   
 2018 5 GeV is shown in Fig. 5.15. On the left panel I show the loss function values (blue) and  
 2019 accuracy (red) at each iteration for the training and the validation samples respectively.  
 2020 The training stops either when the maximum number of iterations is reached (1000 in  
 2021 this case) or when the accuracy for the validation sample reaches a certain tolerance  
 2022 (I chose  $10^{-4}$  as our tolerance). On the right panel I have the distributions for the

## 5.5. HIGH ENERGY DM NEUTRINO SIGNALS

predicted probability by the model, separated in true signal (blue) and background (red) events, for the test sample. One can see that both populations are well separated, obtaining a power of 44.97% and a size of 0.17% when I require a predicted probability greater than 0.97.

Applying this criteria for each sample, I obtain the mean signal efficiencies shown in Fig. 5.16. Notice that the efficiencies for the channel  $\tau^+\tau^-$  (blue line) are consistently lower than the ones for the  $b\bar{b}$  channel (red line). This can be due to the fact that, for each DM mass point, the neutrino spectrum coming from the  $b\bar{b}$  annihilation channel is centered at lower energies when compared to the  $\tau^+\tau^-$  spectrum. This directly translates into more low energy neutrinos undergoing QE interactions, which give signals that can be easily separated from the atmospheric background. This explanation also help us understand why in both cases the signal acceptance drops when the DM mass increases. In all cases, the background rejection took values between 99.8% to 99.9%. I will assume a 99.8% background rejection value in all cases to keep our estimation conservative.

### 5.5.3 Results

In order to estimate the DM-nucleon cross section sensitivities in the present case I need again to compute the expected number of background events. As I am now separating events by interaction type Eq. (5.25) does not hold anymore, as in that case I integrated over the total neutrino-argon cross section. In this instance, the expected background events for DIS events is approximately given by:

$$N_B^{DIS} \simeq \eta_B^{DIS} \times (4.655 \times 10^3) \times \left( \frac{\text{exposure}}{400 \text{ kT yr}} \right), \quad (5.38)$$

whereas for QE events we have:

$$N_B^{QE} \simeq \eta_B^{QE} \times (2.248 \times 10^4) \times \left( \frac{\text{exposure}}{400 \text{ kT yr}} \right). \quad (5.39)$$

Now, using these together with Eqs. (5.26) and (5.27) one can obtain the 90% C.L.

## CHAPTER 5. DARK MATTER SEARCHES WITH NEUTRINOS FROM THE SUN

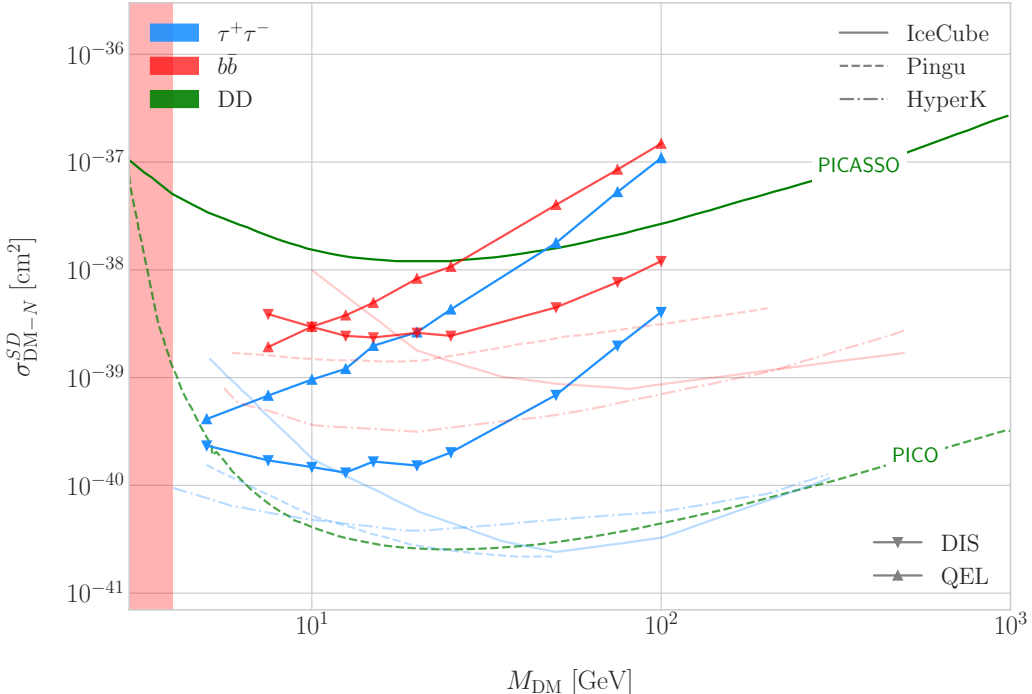


**Figure 5.17:** Projected 90% confidence level upper limit for DUNE (400 kT yr) on the spin-dependent DM-nucleon scattering cross section as a function of  $m_{\text{DM}}$ , for the annihilation channels  $\tau^+\tau^-$  (blue) and  $b\bar{b}$  (red) separated by interaction mode (up triangles denote DIS interactions whereas down triangles represent QE interactions). I also show the previous limits from IceCube [150] (solid lines) and the projected sensitivities for Pingu [151] (dashed lines) and Hyper-Kamiokande [152] (dash-dotted lines), as well as the direct detection limits from PICASSO [153] (solid green line) and PICO-60 C<sub>3</sub>F<sub>8</sub> [154] (dashed green line).

2045 upper limit on the total annihilation rate at equilibrium for both kind of events. Then,  
 2046 applying the computed DM-nucleons capture rates I can translate these into limits on  
 2047 the DM-nucleon cross section by means of Eqs. (5.2), (5.5) and (5.6).

2048 Fig. 5.17 shows the obtained limits on the SD DM-nucleon cross section for DUNE,  
 2049 using the DIS (up triangles) and QE (down triangles) events both for the  $\tau^+\tau^-$  (blue)  
 2050 and the  $b\bar{b}$  (red) samples, for an exposure of 400 kT yr. I also include the corresponding  
 2051 current limits from IceCube [150] (solid lines), as well as the projected sensitivities  
 2052 of Pingu [151] (dashed lines) and Hyper-Kamiokande [152] (dash-dotted lines). For  
 2053 comparison, I also show the reported direct detection limits from PICASSO [153] (solid  
 2054 green line) and PICO-60 C<sub>3</sub>F<sub>8</sub> [154] (dashed green line).

## 5.6. EXAMPLE: LEPTOPHILIC DARK MATTER

2055 Notice that, for most of the mass range, the limits one can set by using the DIS  
 2056 events are stronger than those of the QE interactions, except for the low mass part  
 2057 of both the  $\tau^+\tau^-$  and the  $b\bar{b}$  curves where the QE events dominate. In general, the  
 2058 expected sensitivity of DUNE for DM masses  $\lesssim 25$  GeV surpasses the stronger current  
 2059 indirect limits. However, experiments like Hyper-Kamiokande are foreseen to have an  
 2060 overall better sensitivity in this kind of searches, as they have a bigger active volume  
 2061 and accept a broader energy range.

2062 A pending question is what happens when we add the RES and MEC charged-current  
 2063 interaction contributions. In that case it would probably be more convenient to split  
 2064 the samples by final state interaction topologies. Also, another necessary improvement  
 2065 would be adding a full detector simulation and reconstructions. This will also require  
 2066 considering the effect of poorly reconstructed events or final states containing neutral  
 2067 particles such that they mimic the desired topology at the reconstruction level.

### 2068 5.6 Example: Leptophilic Dark Matter

2069 In general, the capture rate of DM particles by the Sun via interactions with electrons is  
 2070 several orders of magnitude smaller than the capture via DM-nucleus scattering. Thus,  
 2071 it would be sub-leading even when nucleon capture is loop suppressed. As I showed in  
 2072 Fig. 5.2, the capture rate via scattering off electrons only surpasses the capture rates  
 2073 via DM-nucleons interactions for DM masses  $\lesssim 100 - 500$  MeV.

2074 However, if one considers a model where DM-nucleon interactions are forbidden even  
 2075 at loop level, then electron interactions will be the sole contributor to DM capture in  
 2076 the Sun. One can describe such scenario where the DM particles couple to leptons but  
 2077 not to the quark sector using effective operators.

2078 In general, assuming that the DM particle is a Dirac fermion, the dimension six  
 2079 operators describing the interaction between two DM particles and two leptons can be  
 2080 written as:

$$\mathcal{L}_{eff} = G \sum_i (\bar{\chi} \Gamma_x^i \chi) (\bar{\ell} \Gamma_\ell^i \ell), \quad (5.40)$$

## CHAPTER 5. DARK MATTER SEARCHES WITH NEUTRINOS FROM THE SUN

where  $G = 1/\Lambda^2$  is the effective coupling strength,  $\Lambda$  the cut-off of the effective field theory and  $\ell$  denotes any lepton. In principle, one should consider all the possible Lorentz structures  $\Gamma_f^i$  in order to have a complete set of effective operators.

However, some combinations will induce interactions with nucleons at loop level. As we are specifically interested in interactions which forbid any communication with the quark sector, I will not consider those [155]. In addition, some of the effective operators give rise to velocity-suppressed scattering cross sections between DM particles and leptons. I will also neglect those, as the suppression goes with the square of the DM halo velocity which in units of the speed of light is  $\sim 10^{-6}$ .

This way, the only Lorentz tensor structure that do not induce interactions with quarks at loop level and gives a contribution to the scattering cross section that is not velocity suppress is the axial-axial interaction. The effective Lagrangian is then given by:

$$\mathcal{L}_{eff} = \frac{c_A^\chi c_A^\ell}{\Lambda^2} (\bar{\chi} \gamma^\mu \gamma^5 \chi) (\bar{\ell} \gamma_\mu \gamma^5 \ell), \quad (5.41)$$

where  $c_A^\chi$  and  $c_A^\ell$  are the couplings for the different species. As the DM coupling appears as a common factor for any lepton choice, I will redefine the corresponding coupling  $c_A^\ell$  to absorb  $c_A^\chi$ . Also, for simplicity, I will assume that the couplings between the DM particles and the leptons are flavour independent, i.e. I have just two couplings,  $c_A^e$  for charged leptons and  $c_A^v$  for neutrinos.

In the case of a scalar DM particle, the lowest order effective interaction with leptons happens through a dimension five operator, generating scalar and pseudoscalar interactions. However, the former induces interactions with quarks at two loop level whereas the latter gives a velocity suppressed scattering cross section.

From the effective Lagrangian in Eq. (5.41) it can be shown that the axial-axial contribution to the scattering cross section for the fermionic DM and a charged lepton is given by:

$$\sigma_{DM-e}^{AA} = 3 (c_A^e)^2 \frac{m_e^2}{\pi \Lambda^4}. \quad (5.42)$$

If the DM interacts exclusively with fermions, then the only annihilation channels

## 5.6. EXAMPLE: LEPTOPHILIC DARK MATTER

that will give us a measurable neutrino flux coming out of the Sun are  $\tau^+\tau^-$  and  $\nu\bar{\nu}$ . The former channel, already explored previously in the more mainstream scenario of the DM capture via scattering off nucleons, is open only for  $m_{\text{DM}} > m_\tau \simeq 1776.86 \pm 0.12$  MeV [156], a mass region where the solar DM capture by electrons is at least one order of magnitude smaller than the capture via interactions with nucleons. On the contrary, the latter allows us to explore a region where the capture rate via scattering off electrons dominates over the rest.

One downside of focusing in such low mass range is that it falls below the usual limit of  $m_{\text{evap}} \sim 4$  GeV usually explored in the literature. The pretext to explore this region is the result discussed previously reported in Ref. [124], where DM evaporation in the Sun for the case of capture via electron scattering could be negligible for masses as low as  $m_{\text{evap}} \sim 200$  MeV. This result is quite sensitive to the high velocity tail of the DM velocity distribution in equilibrium inside the Sun, and therefore full numerical simulations would be needed to assess the impact of this effect. However, this falls out of the scope of our work.

In this case, as I have a specific realisation of the interaction between the DM and leptons, one can estimate the relic density of our DM for different values of the couplings and the effective field theory scale  $\Lambda$ . The first step to do so is compute the self-annihilation cross section. Because I consider cold relics, at the freeze-out time our DM particles were non-relativistic and so one can expand the annihilation cross section in terms of the relative velocity  $v$  between two annihilating DM particles as [157]:

$$\sigma_{\text{ann}}^{AA}|v| \approx \frac{1}{2\pi\Lambda^4} \sum_\ell \left( c_A^\ell \right)^2 m_\chi^2 \sqrt{1 - \frac{m_\ell^2}{m_\chi^2} \left[ \frac{m_\ell^2}{m_\chi^2} + \frac{1}{12} \left( 2 - \frac{m_\ell^2}{m_\chi^2} \right) v^2 \right]}, \quad (5.43)$$

where the sum includes all the possible lepton final states with mass  $m_\ell$ .

Solving the Boltzmann equation for the evolution of the DM density gives as a solution a relic density of:

$$\Omega_\chi h^2 \approx \frac{(1.04 \times 10^9) x_F}{M_{Pl} \sqrt{g_*} (a + 3b/x_F)}, \quad (5.44)$$

## CHAPTER 5. DARK MATTER SEARCHES WITH NEUTRINOS FROM THE SUN

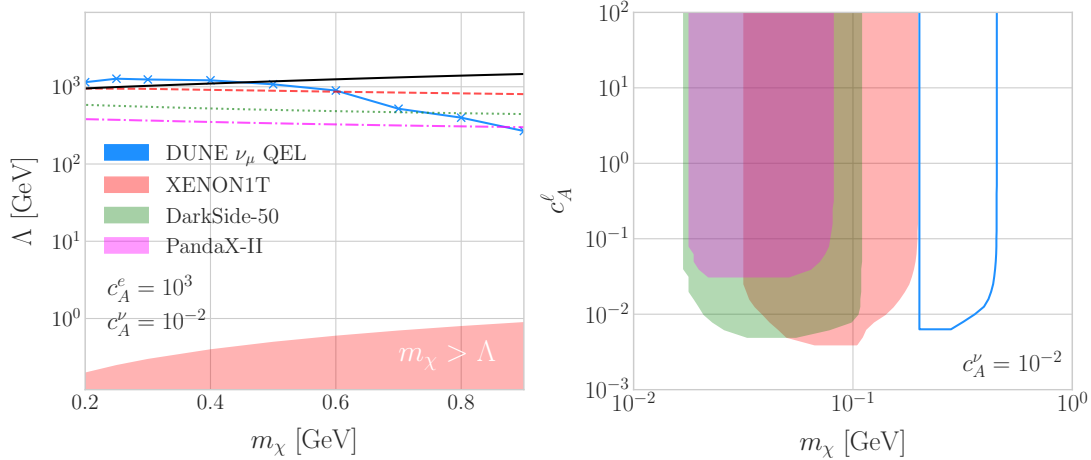


**Figure 5.18:** Left panel: Projected 90% confidence level sensitivity of DUNE (400 kT yr) to the scale  $\Lambda$  of an EFT containing only leptophilic DM axial-axial interactions (blue line), for the coupling values  $c_A^e = 10^3$  and  $c_A^\nu = 10^{-2}$ . The black line represents the values for which the correct relic density is achieved. Right panel: Excluded values of  $c_A^\ell$  as a function of the DM mass, for a fixed value  $c_A^\nu = 10^{-2}$ . In both cases the corresponding limits from XENON1T [159] (red), DarkSide-50 [160] (green) and PandaX-II [161] (magenta) are also shown.

where  $x_F = m_\chi/T_F$  being  $T_F$  the freeze-out temperature,  $g_*$  the number of relativistic degrees of freedom at freeze-out and  $a$  and  $b$  the terms in the annihilation cross section expansion  $\sigma_{ann}|v| \approx a + bv^2 + \mathcal{O}(v^4)$ . Using the current best fit for the relic DM density  $\Omega_\chi h^2 = 0.1198 \pm 0.0012$  [158] one can use these relations to compute the required effective theory scale  $\Lambda$  at which the correct density is achieved for any combinations of  $m_\chi$  and  $c_A^\ell$ .

As discussed before, in the low DM mass region QE interactions dominate. Moreover, if I focus on direct annihilation to neutrinos, the energy of the muon neutrino flux is known as it must be equal to the mass of the DM particle,  $E_\nu = m_\chi$ . That way, now I do not need to use Eq. (5.33) in order to estimate the momentum transfer to the remnant nucleus, I can simply take:

$$\vec{p}_N = \hat{p}_\nu m_\chi - \vec{p}_\mu - \vec{p}_p. \quad (5.45)$$

To estimate the signal efficiency and background rejection for this case I used again

## 5.6. EXAMPLE: LEPTOPHILIC DARK MATTER

the MLP classifier from `scikit-learn`, using the same specifications as before. The only difference now is that I add also the reconstructed neutrino energy as one of the features to train the classifier with, because the characteristic monoenergetic flux for each  $m_\chi$  value will help to distinguish between signal and background events.

In this case, for masses below  $\sim 500$  MeV I obtain a signal efficiency close to unity while keeping a background rejection of 99.9%. For bigger values of the mass, the signal efficiency drops significantly if I require to keep the background acceptance under 0.01%. However, because this kind of search is dominated by the background, sacrificing the signal acceptance to keep the background rejection to a minimum enhances the reach of the analysis. This way, for DM masses of the order of  $m_\chi \sim 1$  GeV I end up with efficiencies as low as 1%.

Now, estimating the number of background events using Eq. (5.39) one can go on and apply Eqs. (5.26) and (5.27) together with Eq. (5.42) to derive the sensitivity of DUNE to this kind of model. Fig. 5.18 (left panel) shows the potential reach of DUNE to constrain the EFT scale  $\Lambda$  this model containing only leptophilic DM axial-axial interactions (blue line), for a choice of couplings  $c_A^e = 10^3$  and  $c_A^\nu = 10^{-2}$ . I also included the current limits on the DM-electron scattering cross section from XENON1T [159] (dashed red line), DarkSide-50 [160] (dotted green line) and PandaX-II [161] (dash-dotted magenta line), reworked with Eq. (5.42) to show their implications for the EFT scale. The values of  $\Lambda$  for which the correct DM relic density value is achieved for each mass are also shown (black line). This tells us that, for that specific choice of couplings, DUNE would be sensitive to DM configurations allowed by the relic density constraint up to a mass of  $m_\chi \sim 400$  MeV.

In Fig. 5.18 (right panel) I show similar limits for the excluded values of  $c_A^\ell$  as a function of the DM mass, for a fixed  $c_A^\nu = 10^{-2}$ . I do not show the limits for other values of  $c_A^\nu$ , as this parameter has little effect on the phenomenology at hand. From this view one can see that DUNE would be able to offer complementary information to the low energy DM-electron interaction searches performed by direct detection experiments, in a slightly higher mass range.

## CHAPTER 5. DARK MATTER SEARCHES WITH NEUTRINOS FROM THE SUN

**Table 5.1:** Systematic uncertainties for the solar WIMP signal events. Table adapted from Ref. [162].

Systematic	Value
Form factor	Does not apply to SD [163]
Solar model	3% [163]
Local DM density	Not relevant for relative interpretations [163, 164]
Dynamics of solar system	Negligible [165]
Velocity distributions	20% at 20 GeV [163, 164]
Oscillation parameters	8% for $\tau^+\tau^-$ , 5% for $b\bar{b}$ [166]
Neutrino interactions in the Sun	10%
Matter effects in the Earth	10%

2172 With the present example, although it focuses on a very specific realisation of the DM  
 2173 interactions, I show the potential of DUNE to constrain exotic DM scenarios. Thanks  
 2174 to its low backgrounds and superb angular resolution DUNE will be able to help with  
 2175 the systematic searches for dark sectors physics.

## 2176 5.7 Systematic uncertainties

2177 The estimation of the DM cross sections using neutrinos from WIMP annihilations  
 2178 inside the Sun is affected by systematic uncertainties from different sources. Surely, the  
 2179 atmospheric background estimation is also affected by systematic uncertainties. There  
 2180 are uncertainties common to both types of events, as well as others specific to each. In  
 2181 this section, I try to provide a comprehensive summary of the main sources of uncertainty  
 2182 for this analysis, which should be taken into account in any future extensions of the  
 2183 same.

### 2184 5.7.1 Systematic uncertainties in the solar WIMP signal

2185 The systematic uncertainties affecting the solar WIMP neutrino signal can be divided in  
 2186 two categories. On the one hand, we have those affecting the solar WIMP annihilation  
 2187 rate. On the other hand, there are the ones which modify the neutrino flux resulting

## 5.7. SYSTEMATIC UNCERTAINTIES

**Table 5.2:** Systematic uncertainties for the solar WIMP atmospheric background events. Table adapted from Ref. [49].

Systematic	Value
Flux normalisation	25 – 7% for $0.1 < E_\nu \leq 1$ GeV (linear in $\log E_\nu$ ) 7% up to 10 GeV
$(\nu_\mu + \bar{\nu}_\mu)/(\nu_e + \bar{\nu}_e)$	2% for $E_\nu \leq 1$ GeV 3% for $1 < E_\nu \leq 10$ GeV
$\bar{\nu}_\mu/\nu_\mu$	2% for $E_\nu \leq 1$ GeV 6% for $1 < E_\nu \leq 10$ GeV
K/ $\pi$ ratio	5% $E_\nu \leq 100$ GeV

2188 from the annihilations reaching our detector.

2189 • **Uncertainties on the annihilation rate.** These include the astrophysical effects  
 2190 that affect the normalisation of the solar DM neutrino flux. The main contributions  
 2191 are the solar model choice, the form factor uncertainties (only for SI searches), the  
 2192 gravitational effect of other planets, the local DM density (not relevant for relative  
 2193 comparisons, as it affects direct detection experiments in the same way), and the  
 2194 DM halo and dispersion velocities.

2195 • **Uncertainties on the neutrino flux.** These are related to the oscillation effects,  
 2196 as well as the absorption and regeneration of neutrinos in the Sun. Matter effects  
 2197 inside the Earth also affect the neutrino flux the measured at the detectors.

2198 Table 5.1 summarises the contributions of the different sources of uncertainty for the  
 2199 signal events. These are the signal systematic uncertainties that have been taken into  
 2200 account in previous solar DM searches with neutrinos [162, 164, 166].

### 2201 5.7.2 Systematic uncertainties in the atmospheric background

2202 For the atmospheric background events, one needs to take into account the systematic  
 2203 uncertainties affecting the atmospheric  $\nu_\mu$  flux. These have been extensively studied  
 2204 in the context of atmospheric neutrino oscillation measurements. Among these, the  
 2205 energy-dependent flux normalisation uncertainty is the in the low energy regime. Other

## CHAPTER 5. DARK MATTER SEARCHES WITH NEUTRINOS FROM THE SUN

2206 important contributions to the uncertainty come from the ratios between the muon to  
2207 electron neutrino and the muon to anti-muon neutrino components of the flux. Additional  
2208 uncertainty is introduced by the errors in the pion and kaon production rates calculated  
2209 for the hadronic interactions of cosmic rays in the atmosphere [167].

2210 Table 5.2 shows a summary of the leading contributions to the uncertainty on the  
2211 atmospheric muon neutrino flux, in the energy range relevant for this analysis.

### 2212 5.7.3 Common systematic uncertainties

2213 Finally, there are sources of uncertainty common to both signal and backgrounds. These  
2214 have two different origins:

2215 • **Uncertainties on the neutrino cross section.** These are introduced by the  
2216 modelling of the neutrino-nucleus interactions. In the context of the solar WIMP  
2217 analysis, these have been estimated to be 10% for DM masses around 10 GeV  
2218 [166].

2219 • **Uncertainties related to the detector.** They affect the measurement of the  
2220 neutrino interaction and the final state particles produced. The main detector  
2221 uncertainties relevant to this analysis are those of the energy and angular resolutions  
2222 of the DUNE FD. Other effects, like the timing and triggering efficiencies, will  
2223 also contribute to the uncertainties. The particular values these will take for this  
2224 analysis need to be worked out in the context of DUNE.

2225

2226

# Particle identification in ND-GAr

2227        *I am no bird; and no net ensnares me; I am a free human being with an  
2228        independent will.*

2229                          – Charlotte Brontë, *Jane Eyre*

2230        In DUNE Phase II, ND-GAr will fulfill the role of TMS measuring the momentum  
2231        and sign of the charged particles exiting ND-LAr. Additionally, it will measure neutrino  
2232        interactions inside the HPgTPC. This way, ND-GAr will allow to constrain certain cross  
2233        section systematic uncertainties and study the effect of FSI in CC interactions. To  
2234        do so, it needs to measure the spectrum of protons and charged pions at low energies,  
2235        as well as measure the pion multiplicity. This puts strong requirements to the ~~the~~  
2236        particle identification (PID) capabilities of the detector, as well as stimulates the relevant  
2237        developments in the reconstruction.

2238        The goal of the present Chapter is to review the status and design of the GArSoft  
2239        package, the simulation and reconstruction software of ND-GAr, and present the different  
2240        additions and upgrades that I have added to the reconstruction with the PID in mind.

## 2241        6.1      GArSoft

2242        GArSoft is a software package developed for the simulation and reconstruction of events  
2243        in ND-GAr. It is inspired by the LArSoft tool  used for the simulation of LArTPC  
2244        experiments, like the DUNE FD modules. It is based on `art`, the framework for event  
2245        processing in particle physics experiments [168]. Other of its main dependencies are

## CHAPTER 6. PARTICLE IDENTIFICATION IN ND-GAr

2246 ROOT, NuTools, GENIE and Geant<sup>1</sup>. It allows the user to run all the steps of a generation-  
2247 simulation-reconstruction workflow using FHiCL configuration files.

### 2248 6.1.1 Event generation

2249 The standard generator FHiCLs in GArSoft run the event generation and particle  
2250 propagation simulation (i.e. Geant4) in the same job by default. However, it is possible  
2251 to split them up if needed. The current version of GArSoft provides five different event  
2252 generators, each of them producing `simb::MCTruth` products defined in NuTools. The  
2253 available modules are:

- 2254 • **SingleGen**: particle gun generator. It produces the specified particles with a given  
2255 distribution of momenta, initial positions and angles.
- 2256 • **TextGen**: text file generator. The input file must follow the `hepevt` format<sup>1</sup>, the  
2257 module simply copies this to `simb::MCTruth` data products.
- 2258 • **GENIEGen**: GENIE neutrino event generator. The module runs the neutrino-nucleus  
2259 interaction generator using the options specified in the driver FHiCL file (flux file,  
2260 flavour composition, number of interactions per event,  $t_0$  distribution, ...). Current  
2261 default version is v3\_04\_00.
- 2262 • **RadioGen**: radiological generator. It produces a set list of particles to model  
2263 radiological decays. Not tested.
- 2264 • **CRYGen**: cosmic ray generator. The module runs the CRY event generator with a  
2265 configuration specified in the FHiCL file (`latitude` and altitude of detector, energy  
2266 threshold, ...). Not tested.

---

<sup>1</sup>In brief, each event contains at least two lines. The first line contains two entries, the event number and the number of particles in the event. Each following line contains 15 entries to describe each particle. The entries are: status code, pdg code for the particle, entry of the first mother for this particle, entry of the second mother for this particle, entry of the first daughter for this particle, entry of the second daughter for this particle, x component of the particle momentum, y component of the particle momentum, z component of the particle momentum, energy of the particle, mass of the particle, x component of the particle initial position, y component of the particle initial position, z component of the particle initial position and time of the particle production.

## 6.1. GArSOFT

2267        The module **GArG4** searches for all the generated **simb::MCTruth** data products, using  
2268        them as inputs to the Geant4 simulation with the specified detector geometry. A constant  
2269        0.5 T magnetic field along the drift coordinate is assumed. The main outputs of this step  
2270        are **simb::MCParticle** objects for the generated Geant4 particles, **gar::EnergyDeposit**  
2271        data products for the energy deposits in the HPgTPC and **gar::CaloDeposit** data  
2272        products for the energy deposits in the ECal and muon system.

### 2273        6.1.2    Detector simulation

2274        The standard detector simulation step in GArSoft is all run with a single FHiCL, but  
2275        the different modules can be run independently as well. First the **IonizationReadout**  
2276        module simulates the charge readout of the HPgTPC, and later the **SiPMReadout** module  
2277        runs twice, once for the ECal and then for the muon system, with different configurations.

2278        The **IonizationAndScintillation** module collects all the **gar::EnergyDeposit**  
2279        data products, to compute the equivalent number of ionization electrons for each energy  
2280        deposit. The **ElectronDriftAlg** module simulates the electron diffusion numerically  
2281        both in the longitudinal and transverse directions and applies an electron lifetime  
2282        correction factor. The induced charge on the nearest and neighbouring readout pads  
2283        is modeled using the provided pad response functions. The digitisation of the data is  
2284        then simulated with the **TPCReadoutSimAlg** module. By default, the ADC sampling  
2285        rate used is 50.505 MHz. The resulting raw waveforms for each channel are stored with  
2286        zero-suppression, in order to save memory and CPU time. The algorithms keep blocks  
2287        of ADC values above a certain threshold, plus some adjustable additional early and late  
2288        tick counts. The results of these three steps are **gar::raw::RawDigit** data products.

2289        For the ECal and the muon system the **SiPMReadout** module calls either the  
2290        **ECALReadoutSimStandardAlg** or **MuIDReadoutSimStandardAlg** modules. These take  
2291        all the **gar::CaloDeposit** data products in the corresponding detector and do the  
2292        digitisation depending on whether the hit was in a tile or strip layer. They include single  
2293        photon statistics, electronic noise, SiPM saturation and time smearing. The resulting  
2294        objects are **gar::raw::CaloRawDigit** data products.

## CHAPTER 6. PARTICLE IDENTIFICATION IN ND-GAr

### 2295 6.1.3 Reconstruction

2296 The reconstruction in GArSoft is also run as a single job by default. It first runs the hit  
2297 finding, clustering, track fitting and vertex identification in the HPgTPC, followed by  
2298 the hit finding and clustering in the ECal and muon system. After those it produces the  
2299 associations between ~~the associations between~~ the tracks and the ECal clusters.

2300 Focusing first on the HPgTPC reconstruction, the `CompressedHitFinder` module  
2301 takes the zero-suppressed ADCs from the `gar::raw::RawDigit` data products. The  
2302 reconstructed hits largely correspond to the above threshold blocks, however the hit  
2303 finder identifies waveforms with more than one maximum, diving them in multiple hits  
2304 if they dip below a certain threshold. The data products produced are of the form  
2305 `gar::rec::Hit`. These are the inputs to the clustering of hits in the `TPCHitCluster`  
2306 module. Hits close in space and time are merged, and the resulting centroids are found.  
2307 This module outputs `gar::rec::TPCClusters` objects and associations to the input  
2308 hits.

2309 The following step prior to the track fitting is pattern recognition. The module  
2310 called `tpcvechitfinder2` uses the `gar::rec::TPCClusters` data products to find track  
2311 segments, typically called vector hits. They are identified by performing linear 2D fits  
2312 to the positions of the clusters in a 10 cm radius, one fit for each coordinate pair. A  
2313 3D fit defines the line segment of the vector hit, using as independent variable the one  
2314 whose sum of (absolute value) slopes in the 2D fits is the smallest. The clusters are  
2315 merged to a given vector hit if they are less than 2 cm away from the line segment. The  
2316 outputs are `gar::rec::VecHit` data products, as well as associations to the clusters. The  
2317 `tpcpatrec2` module takes the `gar::rec::VecHit` objects to form the track candidates.  
2318 The vector hits are merged together if their direction matches, their centers are within  
2319 60 cm and their direction vectors point roughly to their respective centers. Once  
2320 the clusters of vector hits are formed they are used to make a first estimation of the  
2321 track parameters, simply taking three clusters along the track. The module produces  
2322 `gar::rec::Track` data products and associations between these tracks and the clusters

## 6.1. GArSOFT

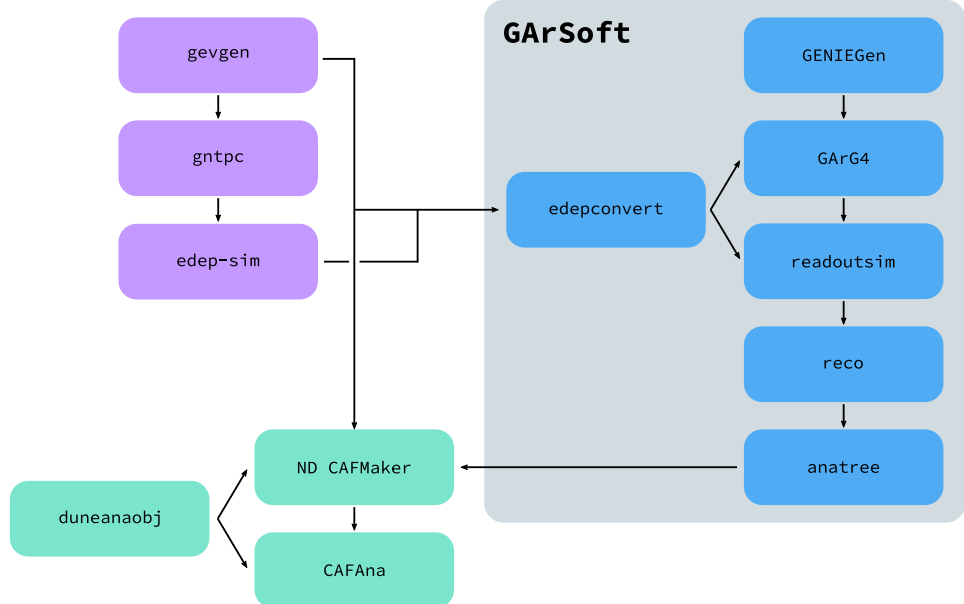


**Figure 6.1:** Schematic diagram showing the different modules involved in the ND-GAr production.

and vector hits.

The track is fitted by means of a Kalman filter in the `tpctrackfit2` module, using the position along the drift direction as the independent variable. Two different fits are performed per track, a forward and a backwards fit, each starting from one of the track ends. The Kalman filter state vector ( $y, z, R, \phi, \tan\lambda$ ) is estimated at each point along the track using a Bayesian update. The track parameters reported in the forward and backwards fits are the ones computed at the opposite end where the fit started. The main outputs of the track fit are the `gar::rec::Track` objects. Additionally, the module stores the fitted 3D positions along the track in the `gar::rec::TrackTrajectory` data products and the total charge and step sizes for each point also get stored in the form of `gar::rec::TrackIonization` objects.

After the tracking step, the `vertexfinder1` module looks at the reconstructed `gar::rec::Track` products, creating vertex candidates with the track ends that are within 12 cm of each other. The vertices are then fitted using linear extrapolations from the different track ends associated. The results are `gar::rec::Vertex` data products,

## CHAPTER 6. PARTICLE IDENTIFICATION IN ND-GAr

2338 and associations to the tracks and corresponding track ends.

2339 For the ECal and muon tagger, the `SiPMHitFinder` module runs twice with different  
2340 configurations, adapted to the particular capabilities of both. The module simply takes  
2341 the `gar::raw::CaloRawDigit` products, applies a calibration factor to convert the ADC  
2342 counts to MeV and for the strip layer hits it calculates the position along the strip using  
2343 the times recorded of both SiPMs. This module produces `gar::rec::CaloHit` data  
2344 products. Next, these objects are used as inputs to the `CaloClustering` module. It  
2345 merges the hits based on a simple nearest neighbours (NN) algorithm. For the resulting  
2346 clusters it also computes the total energy and position of the centroid. The results are  
2347 stored as `gar::rec::Cluster` data products, with associations to the hits.

2348 The last step in the reconstruction is associating the reconstructed tracks in the  
2349 HPgTPC to the clusters formed in the ECal and muon system. The `TPCECALAssociation`  
2350 module checks first the position of the track end points, considering only the points  
2351 that are at least 215 cm away from the cathode or have a radial distance to the center  
2352 greater than 230 cm. The candidates are propagated up to the radial position, in the  
2353 case of clusters in the barrel, or the drift coordinate position, for the end cap cluster, of  
2354 the different clusters in the collection using the track parameters computed at the end  
2355 point. The end point is associated to the cluster if certain proximity criteria are met.  
2356 This module creates associations between the tracks, the end points and the clusters.  
2357 The criteria for the associations are slightly different for the ECal and the muon tagger.

## 2358 6.2 $dE/dx$ measurement in the TPC

2359 Among the parameters extracted from the track fitting, ionisation is particularly useful  
2360 for particle identification, as it is a function of the particle velocity. Although for the  
2361 case of relativistic particles this dependence is not very strong, measuring the track on  
2362 a large number of points may allow us to estimate the amount of ionisation accuratel.  
2363 This, paired with a measurement of the momentum, may allow us to identify the particle  
2364 type.

## 6.2. $dE/dx$ MEASUREMENT IN THE TPC

2365 The first calculation of the energy loss per unit length of relativistic particles using a  
 2366 quantum-mechanical treatment is due to Bethe [169]. Using this approach, the mean  
 2367 ionisation rate of a charged particle traveling through a material medium is (using  
 2368 natural units  $G = \hbar = c = 1$ ):

$$\left\langle \frac{dE}{dx} \right\rangle = \frac{4\pi Ne^4}{m_e \beta^2} z^2 \left( \log \frac{2m_e \beta^2 \gamma^2}{I} - \beta^2 \right), \quad (6.1)$$

2369 where  $N$  is the number density of electrons in the medium,  $e$  the elementary charge,  $m_e$   
 2370 is the electron mass,  $z$  the charge of the particle in units of  $e$ ,  $\beta$  is the velocity of the  
 2371 particle,  $\gamma = (1 - \beta^2)^{-1}$  and  $I$  denotes the effective ionisation potential averaged over  
 2372 all electrons. This relation is known as the Bethe-Bloch formula.

2373 From Eq. (6.1) one can see that the ionisation loss does not depend explicitly on  
 2374 the mass of the charged particle, that for non-relativistic velocities it falls as  $\beta^{-2}$ , then  
 2375 goes through a minimum and increases as the logarithm of  $\gamma$ . This behaviour at high  
 2376 velocities is commonly known as the relativistic rise. The physical origin of this effect  
 2377 is partly due to the fact that the transverse electromagnetic field of the particle is  
 2378 proportional to  $\gamma$ , therefore as it increases so does the cross section.

2379 It was later understood that the relativistic rise could not grow indefinitely with  $\gamma$ .  
 2380 A way to add this feature in the Bethe-Bloch formula is by introducing the so-called  
 2381 density effect term. It accounts for the polarisation effect of the atoms in the medium,  
 2382 which effectively shield the electromagnetic field of the charged particle halting any  
 2383 further increase of the energy loss [170]. Denoting the correction as  $\delta(\beta)$ , one can rewrite  
 2384 Eq. (6.1) as:

$$\left\langle \frac{dE}{dx} \right\rangle = \frac{4\pi Ne^4}{m_e \beta^2} z^2 \left( \log \frac{2m_e \beta^2 \gamma^2}{I} - \beta^2 - \frac{\delta(\beta)}{2} \right). \quad (6.2)$$

2385 In general, the form of  $\delta(\beta)$  depends on the medium and its state of aggregation,  
 2386 involving the usage of tabulated parameters and implicit relations [171].

2387 Another standard method to compute the amount of ionisation a charged particle  
 2388 produces is the so-called photo-absorption ionisation (PAI) model proposed by Allison  
 2389 and Cobb [172]. Within their approach, the mean ionisation is evaluated using a

## CHAPTER 6. PARTICLE IDENTIFICATION IN ND-GAR

2390 semiclassical calculation in which one characterises the continuum material medium by  
2391 means of a complex dielectric constant  $\varepsilon(k, \omega)$ . However, in order to model the dielectric  
2392 constant they rely on the quantum-mechanical picture of photon absorption and collision.  
2393 Therefore, in the PAI model the computation of the ionisation loss involves a numerical  
2394 integration of the measured photo-absorption cross-section  for the relevant material.

2395 In a particle physics experiment, the typical way of determining the energy loss  
2396 per unit length as a function of the particle velocity is studying identified particles  
2397 over a range of momenta. Once we have established this relation we can use it for  
2398 other, unknown particles. In this sense, it makes sense to have a regular mathematical  
2399 expression for this relation that one can use.

2400 It happens that neither the Bethe-Bloch theory nor the PAI model from Allison and  
2401 Cobb offer a close mathematical form for the ionisation curve. This is the reason why a  
2402 full parametrisation of the ionisation curves can be useful. A parametrisation originally  
2403 proposed for the ALEPH TPC [173] and later used by the ALICE TPC [174] group that  
2404 manages to capture the features of the ionisation energy loss is:

$$f(\beta\gamma) = \frac{P_1}{\beta^{P_4}} \left( P_2 - \beta^{P_4} - \log \left[ P_3 + \frac{1}{(\beta\gamma)^{P_5}} \right] \right), \quad (6.3)$$

2405 where  $P_i$  are five free parameters. Hereafter, we will refer to Eq. (6.3) as the ALEPH  
2406  $dE/dx$  parametrisation.

### 2407 6.2.1 Energy calibration

2408 In order to obtain the amount of energy loss by a charged particle due to ionisation  
2409 in our TPC we need to determine the conversion between the charge deposited in our  
2410 readout planes and the actual energy depositions. This procedure is known as energy  
2411 calibration.

2412 In general, the first step of the calibration involves a non-uniformity correction,  
2413 to make sure that the detector response is uniform throughout the TPC. These are  
2414 typically divided into three categories, non-uniformities in the transverse  $YZ$  plane,

## 6.2. $dE/dx$ MEASUREMENT IN THE TPC

2415 non-uniformities along the drift direction  $X$  and variations of the detector response  
2416 over time (would not apply to us as the detector is not built yet). These would correct  
2417 for effects such as electron diffusion and attenuation, space charge effects or channel  
2418 misconfiguration. However, because at the moment I am only interested in making sure  
2419 we recover a sensible result from our simulation, I will not apply uniformity corrections  
2420 to our charge deposits.

2421 Other effects, like electron-ion recombination or ADC saturation, lead to a non-linear  
2422 relation between the observed charge and the deposited energy in the detector, with the  
2423 observed readout charge saturating at high ionisation energies. In this case, because we  
2424 are dealing with gaseous argon and therefore recombination is not as important as in  
2425 liquid, we do not simulate recombination effects in the TPC. Even so, the simulation of  
2426 the electronic response will still introduce charge saturation, and one needs to correct  
2427 for it in order to obtain the exact amount of energy loss due to ionisation.

2428 By default, the track fitting algorithm in GArSoft provides a `TrackIonization`  
2429 object associated to each reconstructed track. It contains two collections of charge  
2430 deposits, one for each fitting direction, consisting on pairs of charge values ( $dQ$ , in ADC)  
2431 and step sizes ( $dx$ , in cm).

2432 In order to estimate the ionisation loss in the ND-GAr TPC, I ~~have used~~ an MC  
2433 sample consisting of single, isotropic protons propagating in the TPC. The starting points  
2434 of the protons were sampled inside a  $50 \times 50 \times 25$  cm box centered at  $(100, -150, 1250)$ ,  
2435 and their momenta are uniformly distributed in the range  $0.25 - 1.75$  GeV. I ran the  
2436 simulated sample through GArSoft's default detector simulation and reconstruction, and  
2437 then a custom analyser module that extracts the ionisation data together with other  
2438 reconstructed track information from the Kalman fit.

2439 For studying the energy loss of the protons I select the reconstructed tracks that  
2440 range out (i.e. slow down to rest) inside the TPC. A characteristic feature of the energy  
2441 loss profile of any stopping ionising particle is the so-called Bragg peak, a pronounced  
2442 peak that occurs immediately before the particle comes to rest. From Eq. (6.1) we can  
2443 see that this behaviour is expected, as the energy loss for non-relativistic particles is

## CHAPTER 6. PARTICLE IDENTIFICATION IN ND-GAR

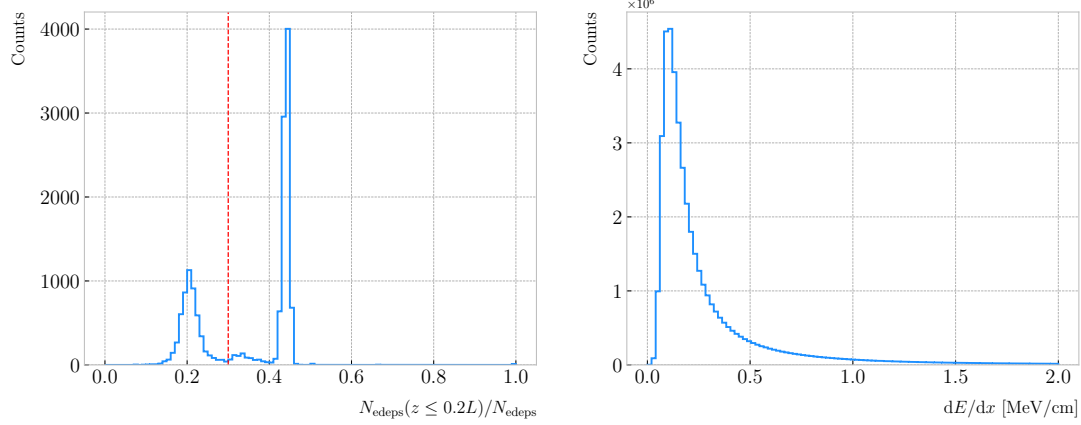


**Figure 6.2:** Left panel: distribution of the fraction of Geant4-level energy deposits per track with residual range less than 20% of the total track length, for the isotropic proton sample. Right panel: distribution of the ionisation per unit length of the energy deposits in the proton sample after removing the tracks with less than 30% of their energy deposits in the last 20% of the track.

2444 inversely proportional to  $\beta^2$ . In data, a way of identifying the Bragg peak, and thus  
 2445 select the stopping particles, is checking the number of energy deposits towards the  
 2446 end of the track. In this case, I count the fraction of the Geant4 simulated energy  
 2447 deposits with a residual range value (the distance from a given energy deposit to the  
 2448 last deposit in the track trajectory) less than a 20% of the corresponding track length<sup>2</sup>.  
 2449 The distribution of this fraction of energy deposits for our proton sample is shown in  
 2450 Fig. 6.2 (left panel). We can clearly see two well separated peaks in this distribution,  
 2451 one centered at 0.2 and another, narrower, one centered at a higher value. The first  
 2452 one corresponds to non-stopping protons, as in that case the number of energy deposits  
 2453 towards the end of the track is uniformly distributed due to the absence of the Bragg  
 2454 peak. In that way, I apply a cut in this distribution, requiring that at least 30% of the  
 2455 simulated energy deposits sit in the last 20% of the tracks, to ensure that the Bragg  
 2456 peak is present.

2457 Figure 6.2 (right panel) shows the distribution of the energy loss per unit length for  
 2458 the Geant4 simulated energy deposits of the selected stopping protons. We can see that

<sup>2</sup>As we are applying this selection at the Geant4 level we could have simply selected the stopping protons using the `EndProcess` labels from the simulation. However, the Bragg peak identification method displayed here could serve as a starting point for a selection of stopping protons in real data.

## 6.2. $dE/dx$ MEASUREMENT IN THE TPC

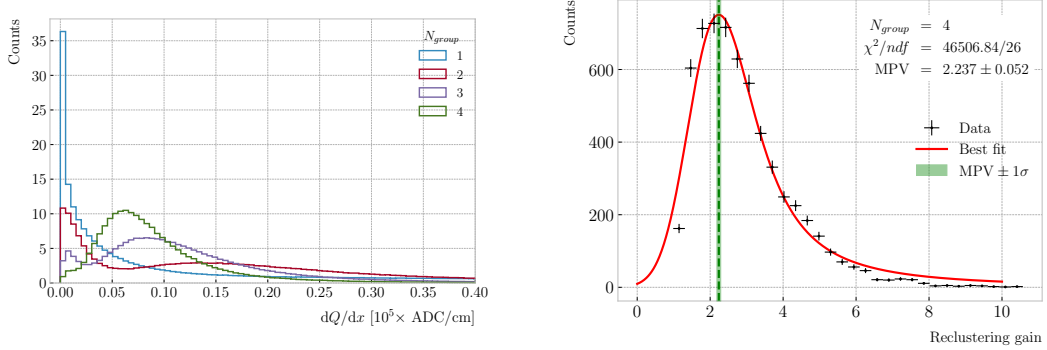


**Figure 6.3:** Left panel: distribution of the reconstructed ionisation charge per unit length for our MC stopping proton sample. The different colors indicate how many consecutive  $dQ/dx$  pairs were grouped together. Right panel: distribution of the median change in  $dQ/dx$  per track after  $N_{group} = 4$  clusters were reclustered together.

it follows the expected shape of a Landau distribution, which describes the fluctuations of the ionisation energy losses [175]. This distribution has a characteristic asymmetric PDF, with a long right tail that translates into a high probability for high-energy ionisation losses. The origin of these fluctuations is mainly the possibility of transferring a high enough energy to an electron, so it becomes a ionising particle itself.

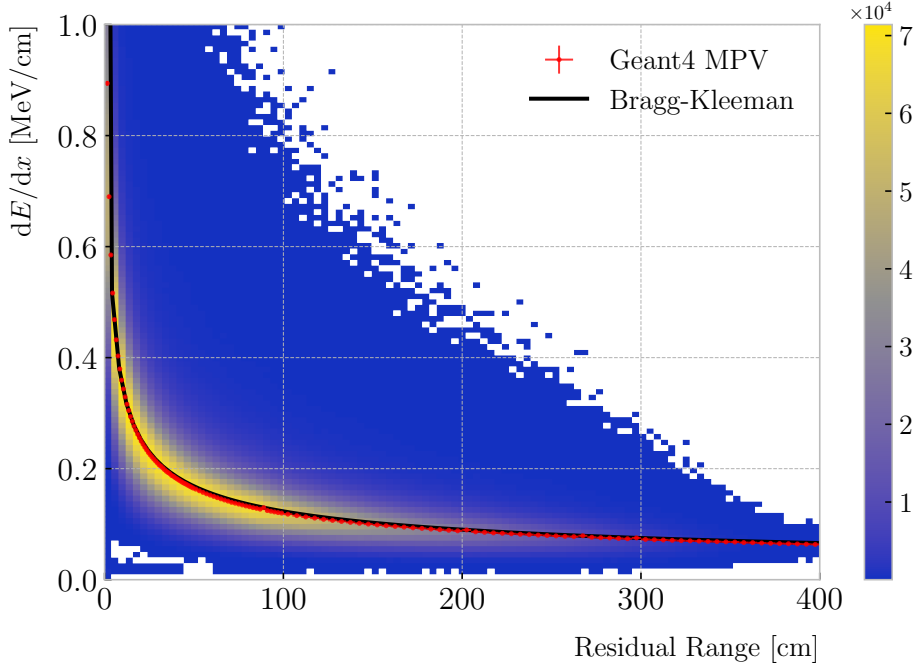
Now, from the point of view of the reconstruction, the objects that we have available to extract the ionisation information for the different reconstructed tracks are the collections of  $dQ$  and  $dx$  pairs, as stated before. The  $dQ$  values come from adding up the amplitude of all the reconstructed hits in a cluster, which is the input object to the Kalman fit.

Figure 6.3 (left panel) shows the distribution of the ionisation charge deposits per unit length for the track in the stopping proton sample (blue line). As one can notice, this distribution does not resemble the expected shape of the Landau PDF. This distribution peaks sharply at 0 and has a heavy tailed behaviour. Notice, however, how the distribution changes its shape as we group together  $N_{group}$  consecutive charge deposit pairs (red, purple and green lines). The distribution in the  $N_{group} = 4$  case already has a shape which resembles that of the Geant4-level ionisation per unit length, so I will proceed using this amount of reclustering for the reconstruction-level depositions.

An extra factor I need to account for, when reclustering is applied, is how the overall



## CHAPTER 6. PARTICLE IDENTIFICATION IN ND-GAR



**Figure 6.4:** Distribution of the Geant4-simulated energy losses per unit length versus residual range for the stopping proton sample. The overlaid points represent the fitted most probable value of the  $dE/dx$  distribution in each residual range bin, whereas the curve is their best fit to the Bragg-Kleeman formula from Eq. (6.4).

2478  $dQ/dx$  per track changes. To do so, we can look at the ratio between the median  $dQ/dx$   
 2479 after and before the reclustering. Figure 6.3 (right panel) shows the median enhancement  
 2480 in  $dQ/dx$  per track for the stopping proton sample in the case  $N_{group} = 4$ . Fitting a  
 2481 Landau distribution convolved with a Gaussian<sup>3</sup>, I estimate the most probable value of  
 2482 this ratio to be  $G_{group} = 2.24 \pm 0.05$ .

2483 At this point, I am left with determining the conversion between the charge deposits  
 2484 per unit length  $dQ/dx$  and the energy deposits per unit length  $dE/dx$ . To this end, we  
 2485 need a way of comparing the two. I can use the residual range  $z$  to get a prediction of  
 2486 the most probable  $dE/dx$  by using the following empirical parametrisation [176]:

$$\frac{dE}{dx}(z) = \frac{z^{\frac{1}{p}-1}}{p\Lambda^{\frac{1}{p}}}, \quad (6.4)$$

---

<sup>3</sup>In the literature, this distribution is often referred to as Landau+Gaussian or langau. In the following, I will use LanGauss to refer to such PDF.

## 6.2. $dE/dx$ MEASUREMENT IN THE TPC

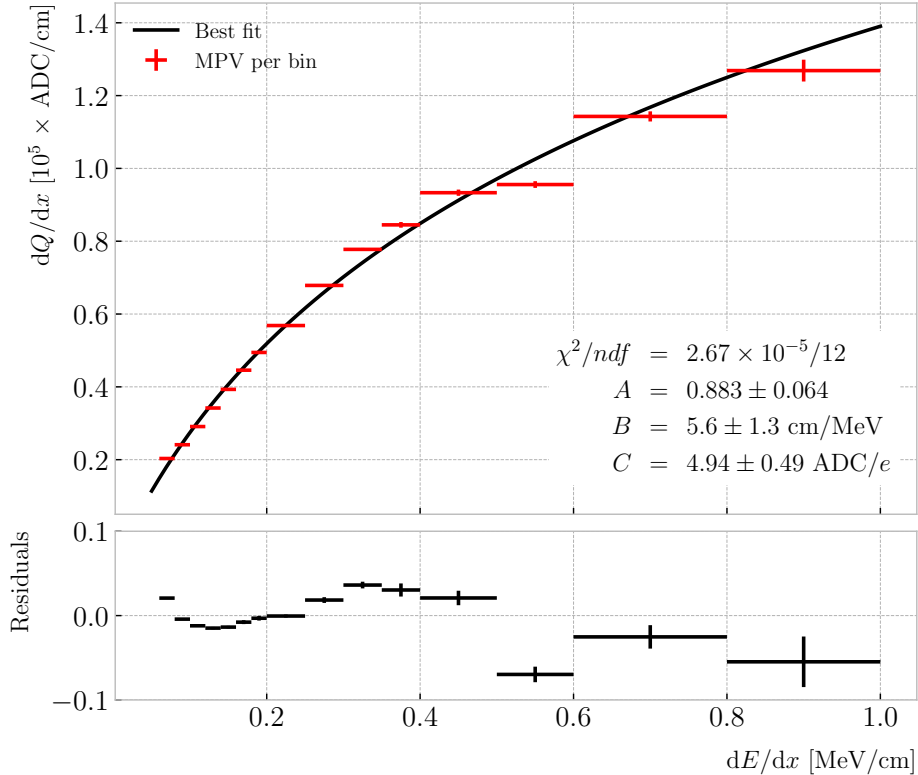


**Figure 6.5:** Fitted most probable  $dQ/dx$  values for each  $dE/dx$  bin (red points), obtained from the stopping proton sample. The overlaid curve (black line) represents the best fit to the logarithmic calibration function from Eq. (6.5).

which is quoted in the literature as the Bragg-Kleeman formula. In order to obtain the  $p$  and  $\Lambda$  parameters I perform a fit using the energy losses and the residual ranges given by the Geant4 stage of our proton sample.

Within our simulation, the residual range is sampled with a maximum size of 5 mm. Therefore, to perform the fit to the Bragg-Kleeman formula, we can use a fine-grained residual range binning. For each of the residual range bins I extract the  $dE/dx$  distribution and fit it to a LanGauss distribution, to obtain the value of the most probable  $dE/dx$  in the bin together with a statistical uncertainty. I then fit Eq. (6.4) to these most probable values and the centres of the residual range bins. This procedure is depicted in Fig. 6.4, where I show the distribution of the energy loss per unit length versus the residual range, together with the most probable  $dE/dx$  values and their uncertainty in each bin (red points) and the curve with the best fit of the

## CHAPTER 6. PARTICLE IDENTIFICATION IN ND-GAr

2499 Bragg-Kleeman relation to those values (black line). The best fit is obtained for the  
 2500 parameter values  $p = 1.8192 \pm 0.0005$  and  $\Lambda = 0.3497 \pm 0.0008 \text{ cm}/\text{MeV}^p$ <sup>4</sup>.

2501 Having an analytical expression that relates the residual range to  $dE/dx$ , I can take  
 2502 our reconstruction-level residual ranges from the stopping proton sample and compute  
 2503 the most probable energy loss associated.

2504 In order to parametrise the charge saturation, we can use the following logarithmic  
 2505 function inspired by the modified box model for recombination:

$$\frac{dE}{dx} = \frac{e^{\frac{dQ}{dx}B\frac{W_{ion}}{G_{group}C}} - A}{B}, \quad (6.5)$$

2506 where  $A$  and  $B$  are the calibration parameters we need to determine,  $W_{ion}$  is the average  
 2507 energy to produce an electron-ion pair,  $G_{group}$  is the gain from the reclustering discussed  
 2508 above and  $C$  is the calibration constant to convert number of electrons to ADC counts,  
 2509 commonly refer to as gain (also to be obtained in the fit). In this case, I use a value  
 2510 for the electron-ion production energy of  $W_{ion} = 26.4 \text{ eV}$  [177]. This value, used in our  
 2511 simulation as well, was measured for gaseous argon in normal conditions, and therefore  
 2512 should be checked in the future to describe correctly the high-pressure argon-CH<sub>4</sub> mixture  
 2513 of ND-GAr.

2514 For the calibration fit I follow a procedure similar to the previous one for Eq. (6.4).  
 2515 Binning the  $dE/dx$  range, I fit a LanGauss distribution to the corresponding  $dQ/dx$   
 2516 distribution to obtain the most probable value. The resulting data points (red bars) are  
 2517 shown in Fig. 6.5 (top panel), the horizontal error bars depict the width of the  $dE/dx$   
 2518 bin whereas the vertical bars represent the error associated to the most probable value  
 2519 estimation. A fit to the logarithmic function in Eq. (6.5) is also shown (black line).  
 2520 For this I weighted the data points using the inverse of their relative error, obtaining  
 2521 a reduced chi-square value of  $\chi^2/ndf = 2.22 \times 10^{-6}$ . The best fit parameters I found  
 2522 from this fit are  $A = 0.883 \pm 0.064$ ,  $B = 5.6 \pm 1.3 \text{ cm}/\text{MeV}$  and  $C = 4.94 \pm 0.49 \text{ ADC}/e$ .  
 2523 Figure 6.5 (bottom panel) shows the residuals between the data points and the fit.

---

<sup>4</sup>These strange units for  $\Lambda$  come from dimensional analysis, just to keep the Bragg-Kleeman formula (6.4) consistent.

## 6.2. $dE/dx$ MEASUREMENT IN THE TPC

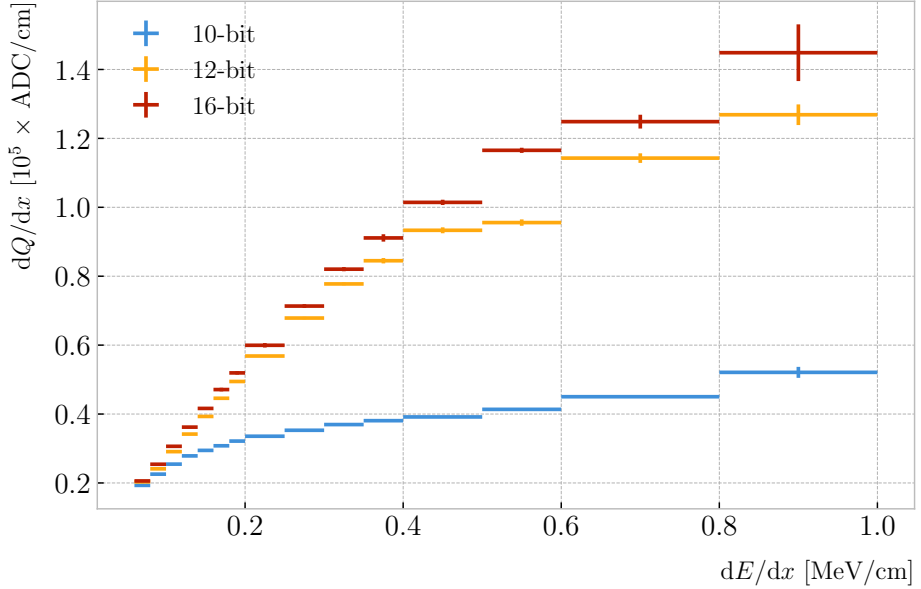


**Figure 6.6:** Fitted most probable  $dQ/dx$  values for each  $dE/dx$  bin for three different ADC bit limits, 10 (blue points), 12 (default, yellow points) and 16-bit (red points).

**Table 6.1:** Calibration parameters obtained from the fit of the ND-GAr simulated stopping proton sample to the calibration function from Eq. (6.5). The fits were performed for the 10, 12, and 16-bit ADC limits.

	$\chi^2/ndf$	Best fit $\pm 1\sigma$			
		$A$	$B$ (cm/MeV)	$C$ (ADC/e)	
10-bit	$1.83 \times 10^{-6}/12$	$-9.3 \pm 3.9$	$270 \pm 69$	$27.1 \pm 5.4$	
12-bit	$2.67 \times 10^{-5}/12$	$0.883 \pm 0.064$	$5.6 \pm 1.3$	$4.94 \pm 0.49$	
16-bit	$1.44 \times 10^{-5}/12$	$0.949 \pm 0.024$	$3.53 \pm 0.58$	$4.52 \pm 0.29$	

2524     The value for the gain I obtained from the fit is in reasonable agreement with our  
2525     expectation. This value is set in GArSoft to 5 ADC/e by default.

2526     One interesting thing to check is what induces this non-linear relation between charge  
2527     and energy. The only effects that modify the amount of electrons reaching the readout  
2528     planes in the simulation are the transverse diffusion and the finite electron lifetime  
2529     Once the electrons reach the readout chambers, the pad response functions are applied,  
2530     together with an electrons-to-ADC conversion and the ADC saturation limit.

2531     By default, GArSoft applies a 12-bit ADC limit, which can be changed in the  
2532     simulation configuration. However, it can only be increased up to 16-bit, as we represent

## CHAPTER 6. PARTICLE IDENTIFICATION IN ND-GAr

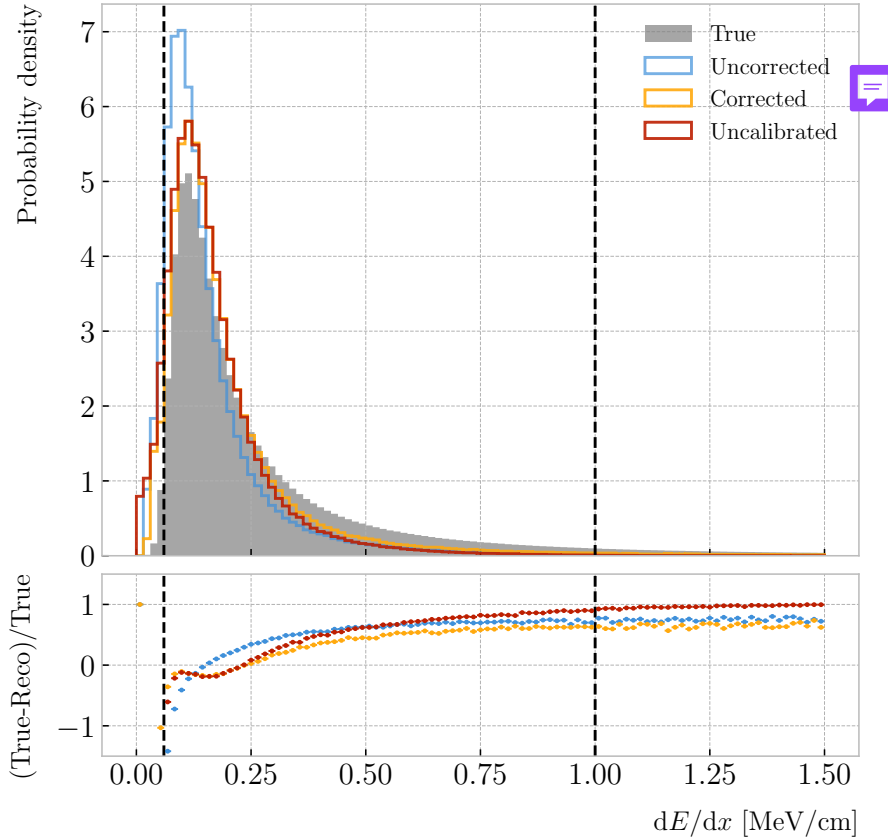


**Figure 6.7:** Top panel: area normalised  $dE/dx$  distributions for the true (solid grey) and the reconstructed energy deposits in the stopping proton sample, both after applying the calibration (blue) and the calibration and the normalisation correction (yellow). Also shown is the distribution obtained by applying a correction factor to the  $dQ/dx$  values but not the calibration (red). Bottom panel: fractional residuals for the uncorrected (blue), corrected (yellow) and uncalibrated (red) samples.

2533 the ADC collection as a `std::vector<short>`. This way, I tried to change the saturation  
 2534 parameter to see how it affects the relation between reconstructed charge and energy.  
 2535 Figure 6.6 shows a comparison between the most probable  $dQ/dx$  for 10, 12 and 16-  
 2536 bit ADC limits. As expected, the lower the limit is the sooner the charge saturates.  
 2537 For higher ADC limits the relation between energy and charge remains linear up to  
 2538 higher  $dE/dx$  values, but even for the 16-bit limit the saturation is noticeable for values  
 2539  $\gtrsim 0.5$  MeV/cm.

2540 Table 6.1 shows the results of fitting the samples with 10 and 16-bits ADC limits to  
 2541 the calibration function from Eq. (6.5), using the weights based on their relative error

## 6.2. $dE/dx$ MEASUREMENT IN THE TPC

as described previously. One interesting feature to notice is how different the best fit points look for the 10-bit ADC saturation when compared to the other two, which are consistent with each other.

At this point we can compare the  $dE/dx$  distribution one gets from Geant4, i.e. the true energy loss distribution, and the distribution I found by applying the calibration function to our collection of reconstructed  $dQ/dx$  values. Figure 6.7 (top panel) shows the true (solid grey) and reconstructed (blue, labeled as uncorrected) distributions together. The dashed vertical lines indicate the region of validity of the calibration fit, i.e. the left and right edges of the first and last  $dE/dx$  bin respectively. Notice that these histograms are area-normalised, as the total number of true energy deposits is much higher than the number of reconstructed charge deposits. This is due to a combination of effects, like the finite spatial resolution of the detector, the hit clustering used in the track fitting and the reclustering we have applied here.

The two distributions are significantly different. That can be seen clearly when looking at the fractional residuals, shown in Fig. 6.7 (bottom panel). In particular, the position of the peak is off, which could bias the mean energy loss predictions. It seems like the difference between these may be due to an overall scaling factor. One possibility is to scale the most probable value of the reconstructed distribution to the most probable value predicted by Geant4. I do this by fitting both distributions using a LanGauss function, obtaining  $dE/dx_{MPV, true} = 0.1145 \pm 0.0005$  MeV/cm and  $dE/dx_{MPV, reco} = 0.0928 \pm 0.0005$  MeV/cm for the true and reconstructed most probable values respectively. These can be translated into a scaling factor  $S = 0.579 \pm 0.006$ .

The result of applying the scaling correction can be seen in Fig. 6.7 (top panel). The corrected  $dE/dx$  distribution (yellow, labeled as corrected) peaks around the same value the true distribution does, as expected. Moreover, the high energy region is also slightly better described. For low ionisations, below the lower limit of the calibration fit, the differences between true and reconstructed are still significant. This low energy excess may be migration of some events from the peak region. The overall effect of the correction can be seen in the fractional residual plot in Fig. 6.7 (bottom panel).

## CHAPTER 6. PARTICLE IDENTIFICATION IN ND-GAr

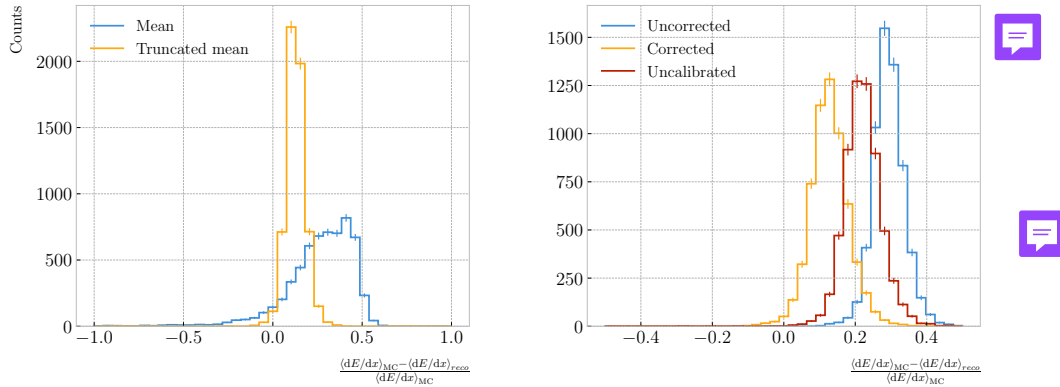


**Figure 6.8:** Left panel: fractional residuals between the true and the corrected  $dE/dx$  means (blue) and the 60% truncated means (yellow), for each event in the stopping proton sample. Right panel: fractional residuals between the true and the uncorrected (blue), corrected (yellow) and uncalibrated (red)  $dE/dx$  60% truncated means, for each event in the stopping proton sample.

2571 One can also check what happens if instead of applying the logarithmic calibration we  
 2572 simply scale the  $dQ/dx$  distribution (post reclustering) to have the same most probable  
 2573 value as the true  $dE/dx$  distribution. In this case, following an analogous procedure to the  
 2574 one described earlier, I found the scaling factor  $S_{uncalibrated} = 0.414 \pm 0.002$  MeV/ADC<sup>5</sup>.  
 2575 The resulting distribution (red, labeled as uncalibrated) is also shown in Fig. 6.7 (top  
 2576 panel). The behaviour of the new distribution is similar to the corrected case at low  
 2577 energy losses, around the peak of the true distribution, but it is worse at describing the  
 2578 high energy tail. This is expected, it is in the high ionisation regime where saturation  
 2579 effects apply and therefore calibration is needed.

### 2580 6.2.2 Truncated $dE/dx$ mean

2581 Once we have a collection of  $dE/dx$  values for each reconstructed track, we can compute  
 2582 the corresponding most probable ionisation loss per unit length of the particle. This  
 2583 is the value predicted by the Bethe-Bloch or the PAI models, and together with a  
 2584 measurement of the momentum it allows for particle identification.

2585 However, estimating the most probable  $dE/dx$  value for each reconstructed track  
 2586 is not a trivial task. As mentioned before, the  $dE/dx$  distributions follow Landau-like

<sup>5</sup>Notice that now the scaling factor is not dimensionless, as it acts more like a conversion factor here.

## 6.2. $dE/dx$ MEASUREMENT IN THE TPC

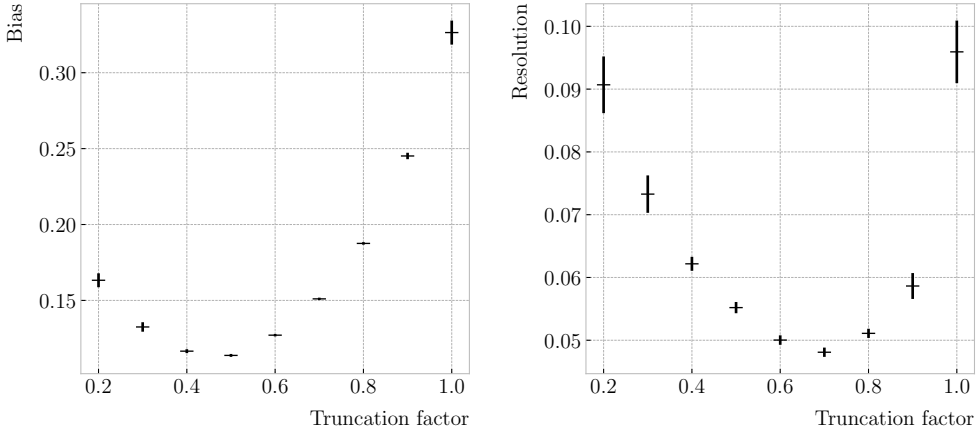


**Figure 6.9:** Estimated values of the mean  $dE/dx$  bias (left panel) and resolution (right panel) obtained using the corrected data from the stopping proton sample, for different values of the truncation factor.

2587 distributions. Therefore, one should perform e.g. a LanGauss fit to correctly estimate  
 2588 the most probable values. Automating this kind of fits is often problematic, as they  
 2589 usually incur in convergence problems. Moreover, the reconstructed  $dE/dx$  distributions  
 2590 we obtain tend to have relatively small statistics, which may also produce poor fits. In  
 2591 practice, doing these unsupervised fits may degrade our performance, and a more robust  
 2592 method is preferred.

2593 A possibility could be taking the mean of the reconstructed  $dE/dx$  distribution for  
 2594 each particle. The problem with this approach is that the high energy Landau tail,  
 2595 combined with our limited statistics, can induce large fluctuations in the computation  
 2596 of the mean. Imagine you have two protons with the same kinetic energy, but due to  
 2597 reconstruction problems in one case you did not get as many charge deposits reconstructed  
 2598 in its high ionisation loss region. If you do not remove the tails the computed  $dE/dx$   
 2599 means will be significantly different.

2600 In order to avoid those fluctuations, one can compute the mean of a truncated  $dE/dx$   
 2601 distribution instead. By keeping only a given fraction of the lowest energy deposits  
 2602 we obtain an estimate of the mean energy loss that is more resilient to reconstruction  
 2603 inefficiencies and statistical effects. Figure 6.8 (left panel) shows a comparison between  
 2604 the  $\langle dE/dx \rangle$  computed by taking the mean of the full distribution (blue line) and the

## CHAPTER 6. PARTICLE IDENTIFICATION IN ND-GAR

2605 60% lowest energy clusters (yellow line), for the stopping proton sample. The fractional  
 2606 residuals are computed for each proton, taking the corresponding means using their  
 2607 collections of true and reconstructed energy deposits. One can see that using the simple  
 2608 mean translates into a high bias and uncertainty in the  $\langle dE/dx \rangle$  estimation, whereas  
 2609 applying the truncation reduces both significantly.

2610 Additionally, I performed a comparison between the 60% truncated mean  $dE/dx$   
 2611 obtained using the different calibration methods discussed earlier, namely the uncorrected  
 2612 (blue), corrected (yellow) and uncalibrated (red) distributions. The results are shown  
 2613 in Fig. 6.8 (right panel). While the widths of these distributions are similar, the bias  
 2614 obtained for the corrected sample, i.e. calibration function and correction factor applied,  
 2615 is a factor of  $\sim 2$  lower than in the uncalibrated case and almost three times smaller  
 2616 than for the uncorrected sample.

2617 The next step is to optimise the level of truncation we are going to apply to our  
 2618 data. To do so, I used different truncation factors, i.e. the percentage of energy-ordered  
 2619 reconstructed energy deposits we keep to compute the mean, on the corrected  $dE/dx$   
 2620 sample of the stopping protons. Then, following the same procedure of computing the  
 2621 fractional residuals as before, I fitted the resulting histograms using a double Gaussian  
 2622 function. This is simply the sum of two Gaussian functions of the type:

$$g(x; \mu, \sigma, A) = A e^{-\frac{(x-\mu)^2}{2\sigma^2}}. \quad (6.6)$$

2623 I do not add the classical normalisation factor of the Gaussian,  $1/\sqrt{2\pi}\sigma$ , therefore  
 2624 the amplitude  $A$  simply represents the maximum of the function. One of the two  
 2625 Gaussian functions describes the core part of the distribution, while the other captures  
 2626 the behaviour of the tails.

2627 For each truncation factor, I look at the bias and the resolution I obtain. I define  
 2628 these as the weighted means of the corresponding parameters in the fits:

$$\bar{x} = \frac{A_{core} x_{core} + A_{tail} x_{tail}}{A_{core} + A_{tail}}, \quad (6.7)$$

## 6.2. $dE/dx$ MEASUREMENT IN THE TPC

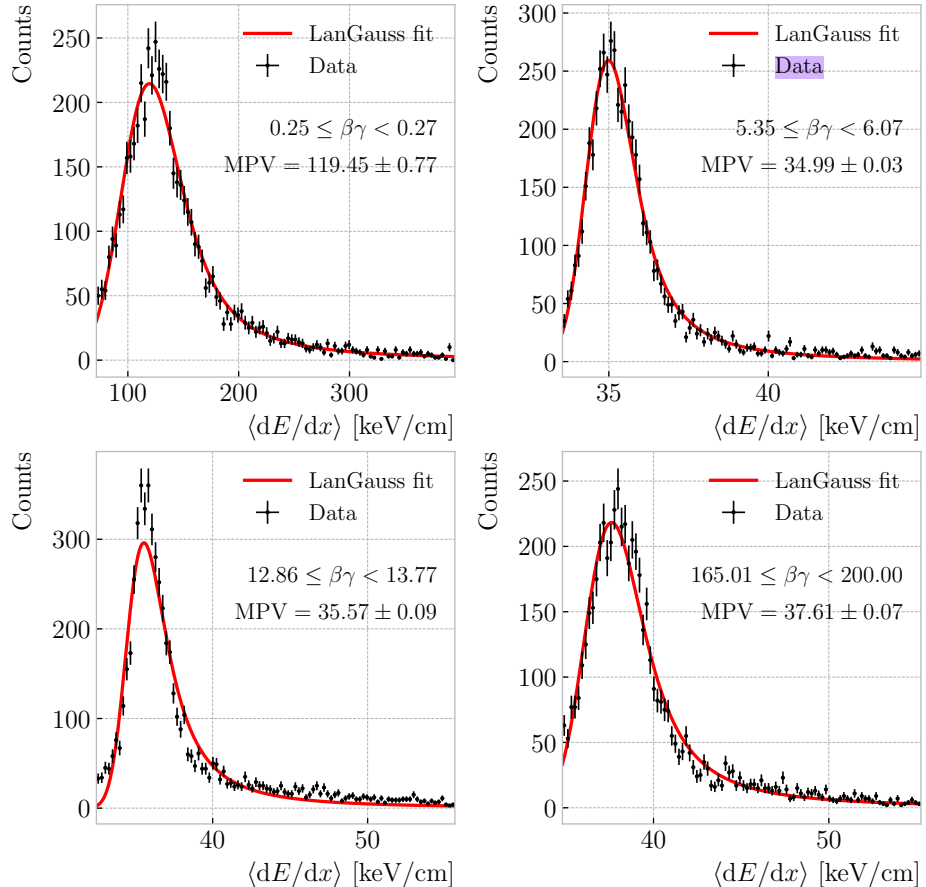


**Figure 6.10:** Examples of the truncated mean  $dE/dx$  LanGauss fits for various  $\beta\gamma$  bins, from a simulated FHC neutrino sample.

where  $A_{core}$  and  $A_{tail}$  are the amplitudes of the core and tail distributions respectively and  $x$  is either the mean  $\mu$  or the width  $\sigma$  of said distributions.

Figure 6.9 shows the bias (left panel) and the resolution (right panel) I obtained for the stopping proton sample, using different values of the truncation. From these, it can be seen that a truncation factor of 50% minimises the bias in the estimation, while 70% gives the best resolution. That way, I settled on the intermediate value of 60% truncation, which yields a  $\langle dE/dx \rangle$  resolution of  $5.00 \pm 0.08$  % for stopping protons 

### 6.2.3 Mean $dE/dx$ parametrisation

Now that we have a way to estimate the mean energy loss of a particle in the HPgTPC, we can determine the value of the free parameters in the ALEPH formula, Eq. (6.3).

## CHAPTER 6. PARTICLE IDENTIFICATION IN ND-GAr

2639 For this, I used a sample of  $10^5$  reconstructed FHC neutrino events inside ND-GAr. In  
2640 this case I cannot use the stopping proton sample, as we need to cover the full kinematic  
2641 range of interest for the neutrino interactions in our detector.

2642 The original **data** does not contain an estimation of the velocity of the tracks, instead  
2643 the tracks have a value for the reconstructed momentum and the associated PDG code  
2644 of the Geant4-level particle that created the track. Therefore, one can select some of the  
2645 particles in the **data**, in this case I selected electrons, muons, pions and protons, and  
2646 compute  $\beta$  and  $\gamma$  using the reconstructed momentum and their mass. In terms of  $\beta\gamma$   
2647 the mean  $dE/dx$  does not depend on the particle species, so one can consider **all** the  
2648 dataset as a whole. For this fit, I will express  $\beta$  in terms of the  $\beta\gamma$  product as:

$$\beta = \frac{\beta\gamma}{\sqrt{1 + (\beta\gamma)^2}}, \quad (6.8)$$

2649 which can be easily proven from the definition of  $\gamma$ .

2650 Next, I bin the **data** in  $\beta\gamma$ . I chose a fine binning so as to capture the different  
2651 features of the ionisation curve. Instead of fixing the bin width, I select them so each one  
2652 has approximately the same statistics. Then, for each  $\beta\gamma$  slice, I compute the median  
2653 and the interquartile range (IQR) of the  $\langle dE/dx \rangle$  distribution. Using these, I make a  
2654 histogram in the range [median - IQR, median + 5 IQR], which I fit to a LanGauss  
2655 function in order to extract the MPV. Using this range accounts for the asymmetric  
2656 nature of the distributions, while also helps avoiding a second, lower maximum present  
2657 at low  $\beta\gamma$ , probably a result of reconstruction failures.

2658 A few examples of these fits are shown in Fig. 6.10. The chosen values of  $\beta\gamma$  sit in  
2659 very distinct points along the  $\langle dE/dx \rangle$  curve, going from the high ionisation region at  
2660 low velocities (top left panel), to the minimum point (top right panel), the beginning of  
2661 the relativistic rise (bottom left panel), and the plateau produced by the density effect  
2662 (bottom right panel).

2663 I used the resulting most probable  $\langle dE/dx \rangle$  values and the centres of the  $\beta\gamma$  bins as  
2664 the points to fit to the ALEPH formula. For this particular fit I used the least-squares

## 6.2. $dE/dx$ MEASUREMENT IN THE TPC

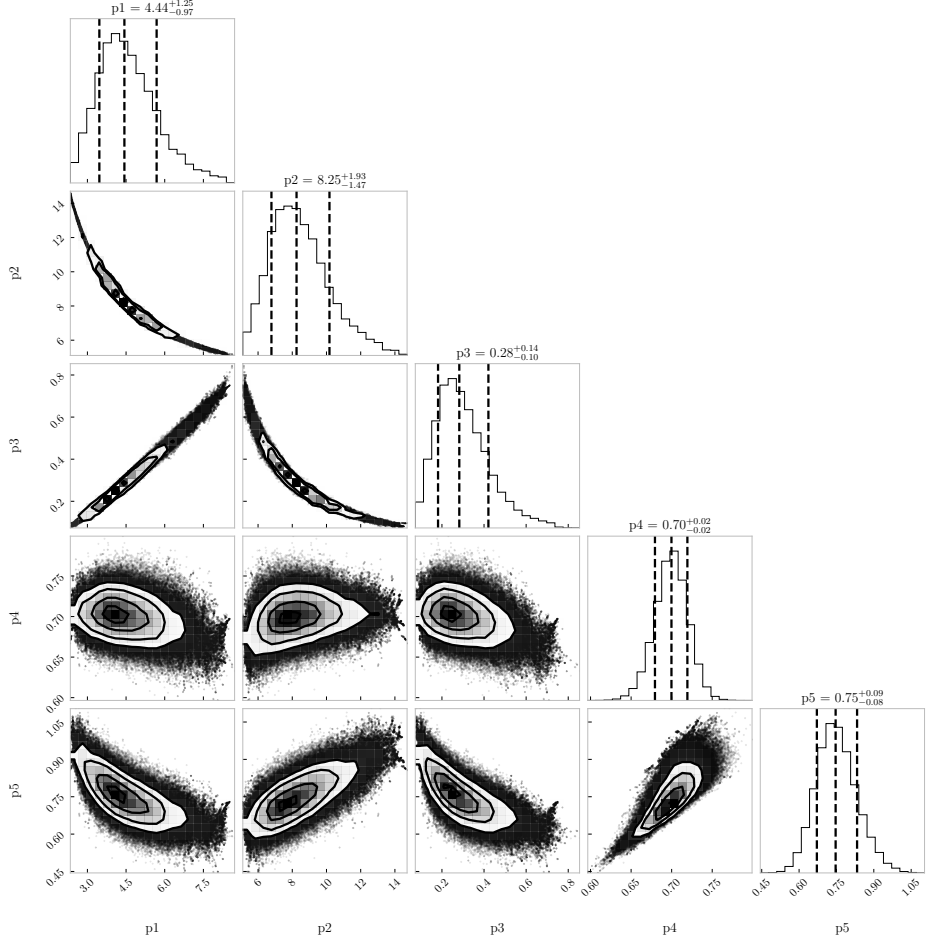


**Figure 6.11:** Resulting one and two dimensional projections of the posterior probability distributions of the ALEPH  $\langle dE/dx \rangle$  parameters obtained by fitting the 60% truncated mean  $dE/dx$  values from a FHC neutrino sample in ND-GAr. The vertical dashed lines in the 1D distributions represent the 16th, 50th and 84th percentiles.

method to get a first estimation of the ALEPH parameters. Applying some uniform priors, I then used these values as the starting point of a 100000 steps MCMC. Figure 6.11 shows the posterior probability distributions I obtain for each parameter. The reported best fit points are based on the 16th, 50th, and 84th percentiles in the marginalised distributions.

The resulting fit (black line), compared to the data points (red points) and the underlying distribution is shown in Fig. 6.12 (top panel). The overall fit is good, with a reduced chi-squared of  $\chi^2/ndf = 1.02$ . However, there are some regions where the fit does not describe the data correctly, like the very low  $\beta\gamma$  regime, where the fit severely

## CHAPTER 6. PARTICLE IDENTIFICATION IN ND-GAR

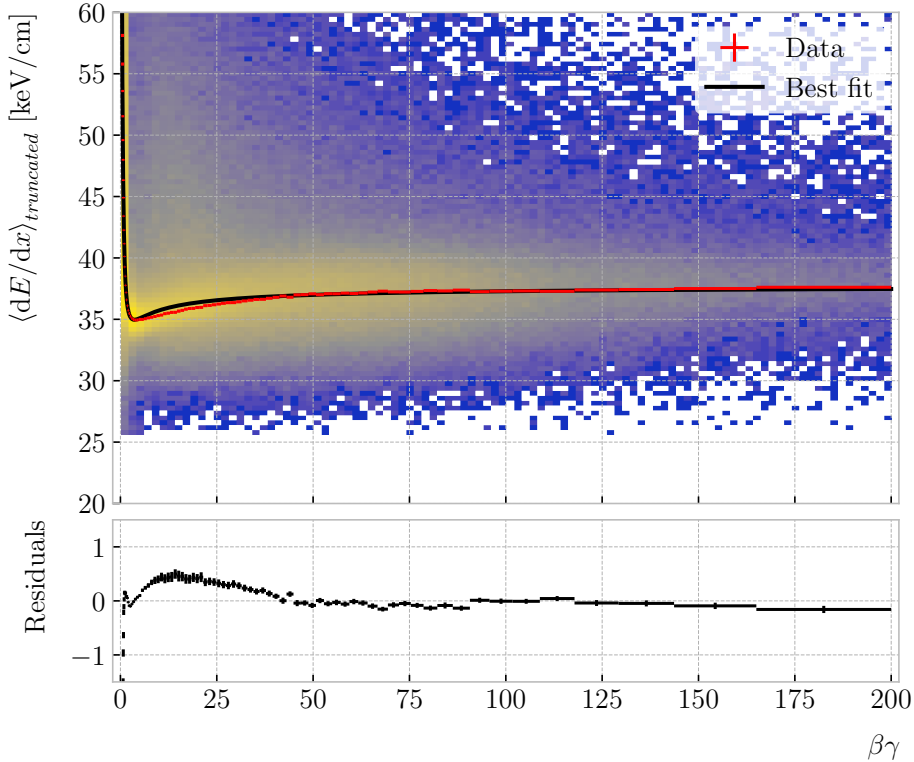


**Figure 6.12:** Truncated mean  $dE/dx$  obtained for the FHC neutrino sample as a function of the  $\beta\gamma$  product (upper panel). Also shown are the fitted most probable values for each  $\beta\gamma$  bin (red points) and the best fit obtained using the ALEPH parametrisation (black line). The residuals resulting from the fit are shown in the lower panel.

underestimates for energy losses  $\gtrsim 50$  keV/cm, and the start of the relativistic raise, where we have a slight overestimation. This is a result of those points having a larger uncertainty when compared to the ones around the dip or the plateau areas. These differences can be better seen in the residual plot, Fig. 6.12 (bottom panel).

It is interesting to look at the results of the fit in momentum space, for the different particle species. Figure 6.13 shows the truncated mean  $dE/dx$  values versus the reconstructed momentum for the neutrino sample. Using a logarithmic scale for the momentum helps visualising the curves corresponding to the various particles. The resulting fits for electrons, muons, pions and protons are also shown (solid black lines). Notice that each curve stops at different momentum values, as the fits only extend up to  $\beta\gamma = 200$  and translating this limit into momentum depends on the particle.

## 6.2. $dE/dx$ MEASUREMENT IN THE TPC

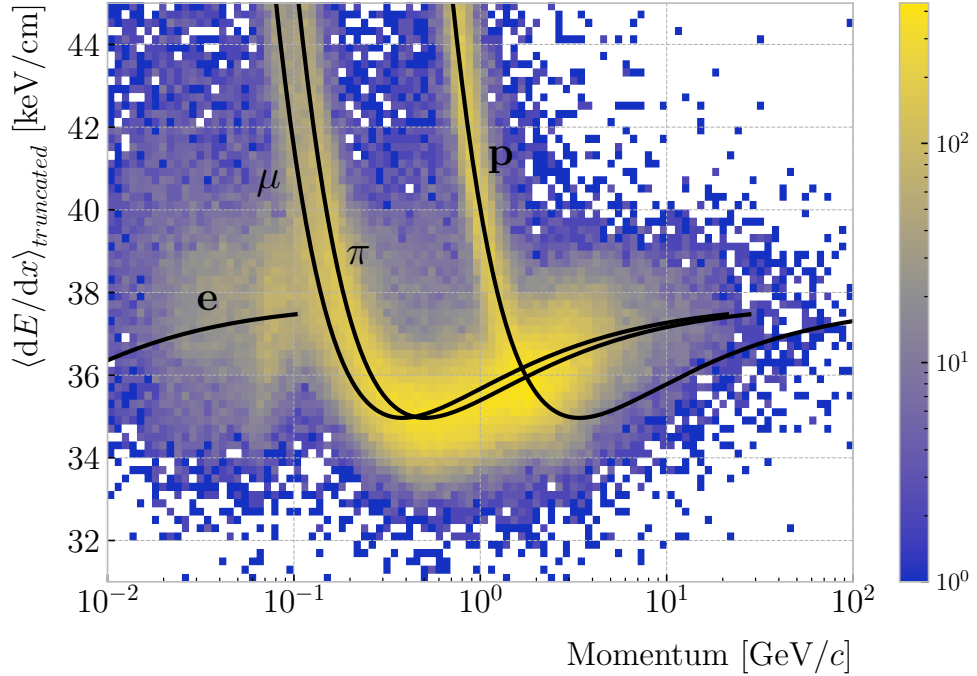


**Figure 6.13:** Distribution of the 60% truncated mean  $\langle dE/dx \rangle$  versus reconstructed momentum for the FHC neutrino sample. The black lines indicate the predictions of the ALEPH parametrisation for electrons, muons, charged pions and protons.

- From this plot, the particle separation power of the  $\langle dE/dx \rangle$  measurement is evident. In the low momentum regime separating electrons, muons and pions is possible, while protons can be reliably identified up to  $1.5 \text{ GeV}/c$ . Relevant to the separating power is the  $\langle dE/dx \rangle$  resolution. This can be obtained from the fit, by taking the ratio of the difference between the expected energy loss for a given particle type and momentum and the measured value over the expectation. Then, performing a double Gaussian fit we can extract the bias and the resolution by means of Eq. (6.7). Figure 6.14 presents the values of the  $\langle dE/dx \rangle$  bias (left panel) and resolution (right panel) as a function of the momentum for the true protons in the neutrino sample. When compared to the values for the resolution obtained for the stopping proton sample (see e.g. Fig. 6.9), it appears that the performance now is much lower. For that low energy sample the resolution obtained was 5%, whereas now we only achieve those numbers for momenta  $\geq 0.75 \text{ GeV}/c$ . However, there are several differences between these two cases. The former was obtained for a single proton sample, with tracks are fully

## CHAPTER 6. PARTICLE IDENTIFICATION IN ND-GAr

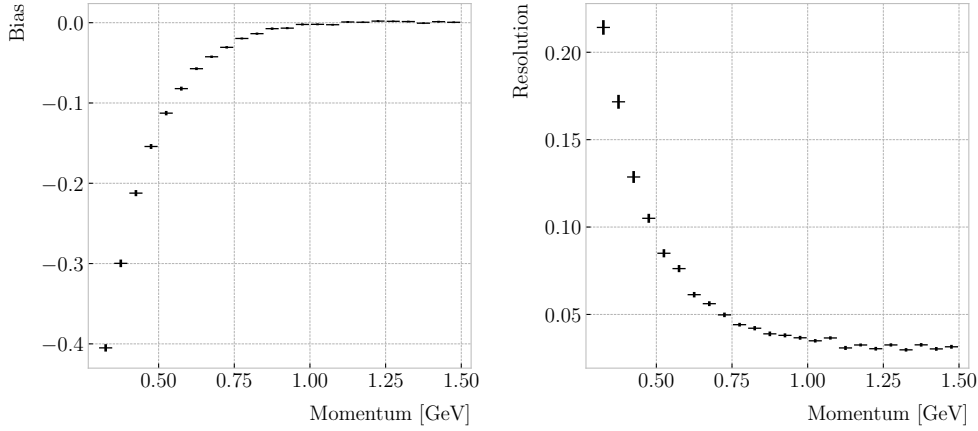


**Figure 6.14:** Estimated values of the mean  $dE/dx$  bias (left panel) and resolution (right panel) obtained for the true protons in the FHC neutrino sample.

2699 contained in the detector volume. On top of that, I refined the selection requiring a single  
 2700 reconstructed track per event, which eliminates any misreconstruction effects. In this  
 2701 case, we are dealing with tracks that may have fragmented, or even have contributions  
 2702 from different true particles. Also, note that at low energies the  $\langle dE/dx \rangle$  for protons is  
 2703 much higher than it is for other particles. Therefore, having a poor resolution in that  
 2704 range does not have an impact on the proton separation.

### 2705 6.3 Muon and pion separation in the ECal and MuID

2706 As it could be seen from Fig. 6.13, it is not possible to separate muons and charged pions  
 2707 in the HPgTPC using  $dE/dx$  for momenta  $\gtrsim 300$  MeV/ $c$ . In ND-GAr, approximately  
 2708 70% of the interactions in FHC mode will be  $\nu_\mu$  CC (compared to the 47% of  $\bar{\nu}_\mu$  CC  
 2709 interactions when operating in RHC mode), while 24% are neutral currents. Out of  
 2710 these, around 53% and 47% of them will produce at least one charged pion in the final  
 2711 state, respectively. Figure 6.15 shows a comparison between the spectra of the primary  
 2712 muons and the charged pions for  $\nu_\mu$  CC interactions in ND-GAr producing one or more  
 2713 charged pions. From this, one can see that (i) the majority of muons and charged pions  
 2714 are not going to be distinguishable with a  $\langle dE/dx \rangle$  measurement, and that (ii) particle  
 2715 identification is necessary both to classify correctly the  $\nu_\mu$  CC events and identify the

### 6.3. MUON AND PION SEPARATION IN THE ECAL AND MUID

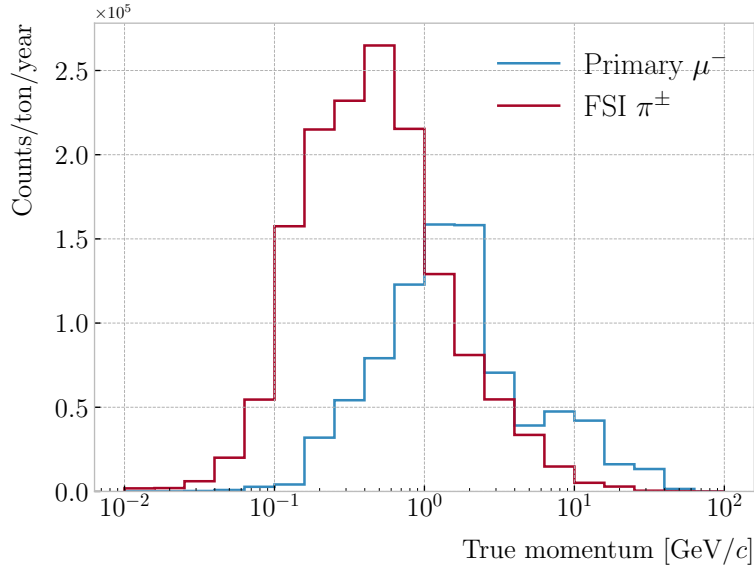


**Figure 6.15:** True momentum distribution for the primary muon in  $\nu_\mu$  CC  $N\pi^\pm$  interactions inside the fiducial volume of ND-GAr (blue line), compared to the post FSI charged pion spectrum (red line).

2716 primary muon within them.

2717 ND-GAr features two other subdetectors which can provide additional information  
 2718 for this task, namely the ECal and MuID. The current ECal design, described in (ref  
 2719 section), consists of 42 layers, made of 5 mm of Pb, 7 mm of plastic scintillator and a  
 2720 1 mm PCB board. The total thickness of this calorimeter is 1.66 nuclear interaction  
 2721 lengths or 1.39 pion interaction lengths. The MuID design is in a more conceptual  
 2722 stage, however it is envisioned to feature layers with 10 cm of Fe and 2 cm of plastic  
 2723 scintillator<sup>6</sup>. With its three layers, it will have a thickness of 1.87 or 1.53 nuclear or pion  
 2724 interaction lengths, respectively.

2725 Because pion showers are dominated by inelastic nuclear interactions, the signatures  
 2726 of these particles in the calorimeter will look significantly different from those of muons.  
 2727 Although our ECal is not thick enough to fully contain the hadronic showers of the  
 2728 charged pions at their typical energies in FHC neutrino interactions, they can still be  
 2729 used to understand whether the original particle was more hadron-like or MIP-like. In

<sup>6</sup>It is not mentioned anywhere, but I assume that there should also be another layer of PCB board of 1 mm. However, in this case its contribution to the total thickness of the sampling calorimeter would be negligible.

## CHAPTER 6. PARTICLE IDENTIFICATION IN ND-GAr

2730 Fig. 6.16 I show two examples of energy distributions created by a muon (left panel)  
2731 and a charged pion (right panel) of similar momenta interacting in the ECal. These  
2732 figures represent the transverse development of the interactions. For each of them, I  
2733 computed the principal component and centre of mass of the interaction, projecting  
2734 the position of the hits onto the plane perpendicular to that direction, and taking the  
2735 distances relative to the centre. It can be seen that the muon follows an almost MIP-like  
2736 behaviour, being the central bin in the histogram the one with the highest deposited  
2737 energy. On the other hand, the pion not only deposits more energy overall, but also this  
2738 energy is more spread-out among the different hits. It is this kind of information that  
2739 would allow us to tell apart muons from pions.

2740 This way, I identify three main action points that need to be addressed if one wants  
2741 to use these detectors to distinguish between muons and charged pions. These are:

- 2742 1. the way we make the associations between tracks in the HPgTPC to the activities  
2743 (what in GArSoft we call clusters) in the ECal and the MuID,
- 2744 2. what variables or features one can extract from the calorimeters that encapsulate  
2745 the information we are interested about,
- 2746 3. and how to carry out the classification problem.

### 2747 6.3.1 Track-ECal matching

2748 One of the main players in the muon and pion separation is the way we associate clusters  
2749 in the ECal to reconstructed tracks in the TPC. Missing some associations or making  
2750 wrong ones can bias the ECal quantities that we can use for classifying particles. The  
2751 current algorithm in GArSoft provides precise associations, i.e. most of the associations  
2752 that it produces are correct, but it appears to miss an important number of associations  
2753 (at least when using the default configuration).

2754 The current TPC track-ECal cluster association algorithm is divided in four parts.  
2755 It first checks whether the track end point fulfils certain conditions to be extrapolated.  
2756 There are two cut values in this step, one for the drift direction and other radial.

### 6.3. MUON AND PION SEPARATION IN THE ECAL AND MUID

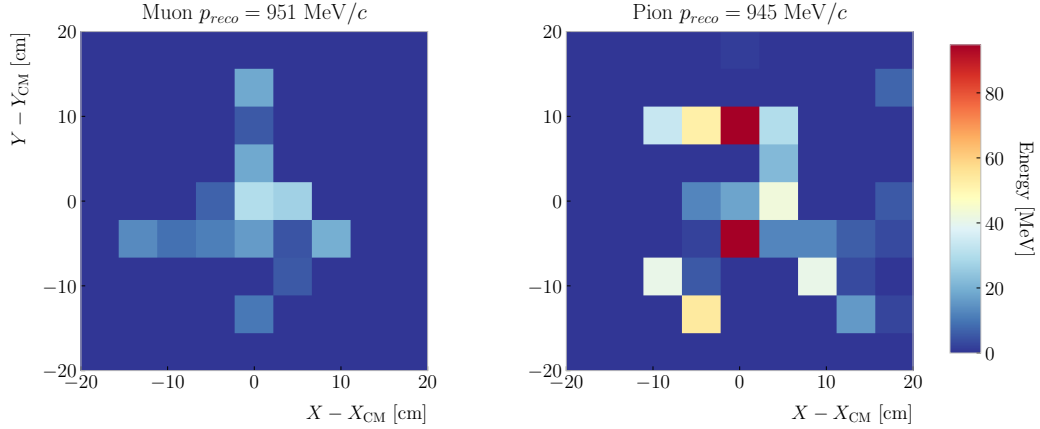


**Figure 6.16:** Distributions of energy deposits in the ECal for a muon (left panel) and a charged pion (right panel) with similar momenta. The energy is projected onto the plane perpendicular to the principal component of the hits, and the positions are relative to the center of the interaction.

If the point can be extrapolated, the code computes the coordinates of the centre of curvature using the Kalman fit estimates at the track end ( $y$ ,  $z$ ,  $1/R$ ,  $\phi$ ,  $\tan\lambda$ ). It then compares the distance between this and the cluster in the  $(z, y)$  plane with  $R$ . This introduces another cut in the perpendicular direction.

The next step is different for clusters ~~is~~ in the barrel or in one of the end caps. If it is a barrel cluster the algorithm extrapolates the track up to the radial distance of the cluster. There are three possible outcomes, the extrapolated helix can cut the cylinder of radius  $r_{clus}$  two, one or zero times. I get the cut point that is closer to the cluster and check that it is either in the barrel or the end caps. Computing the difference between the  $x$  coordinates of the cluster and the extrapolated point, the module checks that this is not greater than a certain cut. If the cluster is in an end cap, I propagate the track up to the  $x$  position of the cluster. Then, the algorithm computes the angle in the  $(z, y)$  plane between the centre of curvature and the cluster,  $\alpha$ , and the centre of curvature and the propagated point,  $\alpha'$ . A cut is applied to the quantity  $(\alpha - \alpha')R$ .

If the cluster contains more than a certain number  $N$  of hits, I apply an extra cut to the dot product of the direction of the track at the propagated  $x$  value and the cluster direction.

## CHAPTER 6. PARTICLE IDENTIFICATION IN ND-GAR

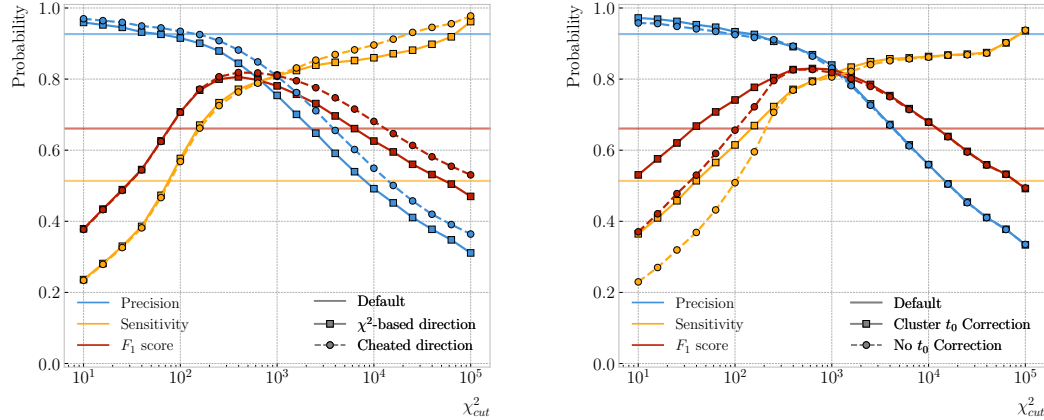


**Figure 6.17:** Left panel: comparison between the precision (blue), sensitivity (yellow) and  $F_1$  score (red) obtained for the default (horizontal lines) and new algorithms, both with the  $\chi^2$ -based direction estimator (squares) and cheating the directions (circles), for different values of the  $\chi^2_{cut}$ . Right panel: comparison of the performance of the new algorithm when applying the cluster  $t_0$  correction (squares) and when (circles).

2774     The code makes sure to only associate one end of the track (if any) to a cluster.  
2775     However, it can associate more than one track to the same cluster. This makes sense,  
2776     as different particles can contribute to the same cluster in the ECal, but it makes it  
2777     difficult to quantify the relative contributions of the tracks to a certain cluster.

2778     As a way of comparing the performance of this algorithm, a new, simpler association  
2779     module was written. The goal was to have a simple and robust algorithm, which depends  
2780     on as few parameters as possible and that can produce a one-to-one matching between  
2781     tracks and ECal clusters.

2782     For each reconstructed track, the new algorithms applies the same procedure to the  
2783     forward and the backward fits irrespective of their end point positions. It first gets the  
2784     Kalman fit parameters at the corresponding end point together with the  $X$  position,  $x_0$ ,  
2785      $(y_0, z_0, 1/R, \phi_0, \tan\lambda)$ .

2786     For each ECal cluster, I compute the radial distance to the centre of the TPC and  
2787     find the  $\phi$  value in the range  $[\phi_0, \phi_0 + \text{sign}(R)\phi_{max}]$  that makes the propagated helix  
2788     intersect with the circle defined with such radius. The  $(x, y, z)$  position of the helix for  
2789     the  $\phi$  value found (if any) is then computed. In case there are two intersections, I keep  
2790     the one that minimises the distance between  $(y, z)$  and  $(y_c, z_c)$ .

### 6.3. MUON AND PION SEPARATION IN THE ECAL AND MUID

2791 I then calculate  $\chi^2$  value based on the Euclidean distance between the propagated  
2792 point and the cluster:

$$\chi^2/ndf = \frac{\sum_{n=0}^2 (x^{(n)} - x_c^{(n)})^2}{3}. \quad (6.9)$$

2793 If there was no intersection I store a  $-1$  instead. In the end, for each reconstructed track  
2794 in the event one ends up with two collections of  $\chi^2$  values, one for each ECal cluster  
2795 and fit directions.

2796 The current code only supports having ECal clusters associated to one end of each  
2797 track. We have two options to decide what track end to keep. The first one tries to  
2798 cheat the selection, looking at the distance between the two track ends and the true  
2799 start position of the associated MC particle. The second one keeps the track end with  
2800 more  $\chi^2$  entries below the cut.

2801 This feature of only considering one track end limits the algorithm, making it not  
2802 suitable for reconstructing events with particles originating outside the TPC. However,  
2803 as for the moment the main concern of the group is the study of neutrino interactions  
2804 off the gaseous argon, this is an acceptable assumption.

2805 In order to associate a cluster to a track, I take all clusters with a  $\chi^2$  value in the  
2806 range  $[0, \chi_{cut}^2]$ . If a cluster has been assigned to more than one track we leave it with  
2807 the one with the lowest  $\chi^2$ .

2808 This default behaviour of the algorithm can be modified to associate more than one  
2809 track to each cluster. Not only that, but the  $\chi^2$  values can be used to assign relative  
2810 weights to the different contributions.

2811 To evaluate the performance of the association method, I use a binary classification  
2812 approach. In this case, I check the leading MC Track IDs associated to the reconstructed  
2813 tracks and ECal clusters. I count an association as true positive (TP) if both Track  
2814 IDs coincide. An association is considered false positive (FP) when the Track IDs are  
2815 different. If a cluster has not been associated to any track but it shares the Track ID  
2816 with a reconstructed track it is counted as a false negative (FN).

2817 For the testing, I used a sample of 10000 FHC neutrino events inside the HPgTPC.

## CHAPTER 6. PARTICLE IDENTIFICATION IN ND-GAr

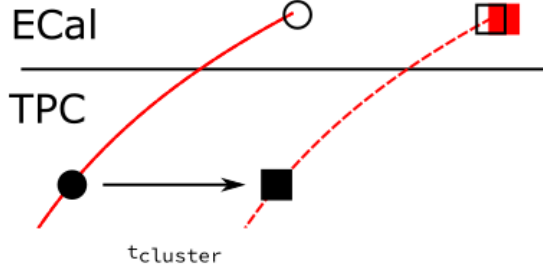


**Figure 6.18:** Schematics of a possible option to deal with track-ECal associations in non-zero  $t_0$  neutrino interaction events, trying to correct for the drift direction uncertainty in a cluster-by-cluster basis using the cluster time,  $t_{cluster}$ .

2818 Figure 6.17 (left panel) shows the precision (blue line), sensitivity (yellow line), and  $F_1$   
 2819 score (red line) I obtained for different values of  $\chi^2_{cut}$ . For comparison, the same metrics  
 2820 computed for the default algorithm with the current configuration are also shown (dashed  
 2821 lines). In the case of the new algorithm, I used both the  $\chi^2$ -based method to estimate  
 2822 the track direction described earlier (square markers) and the cheated direction from the  
 2823 Geant-level information (circle markers). For either of these we achieve similar values of  
 2824 the precision compared to the old code, while having a considerably higher sensitivity.  
 2825 It can be seen that cheating the direction of the tracks only makes a difference at high  
 2826  $\chi^2_{cut}$ , past the optimal value of the cut around the  $F_1$  score maximum. Therefore, I set  
 2827 the  $\chi^2$  method as the default.

2828 One of the possible weak points of this approach is that it relies on the position along  
 2829 the drift direction to make the decisions. Within the current ND-GAr design implemented  
 2830 in GArSoft, the timing information is provided by the ECal. That effectively means  
 2831 that prior to make the track-ECal associations the reconstructed  $x$  positions of the track  
 2832 trajectories differ from the simulated ones by an amount:

$$x_{reco}^{(n)} - x_{sim}^{(n)} = v_{drift} t_0, \quad (6.10)$$

2833 where  $v_{drift}$  is the mean drift velocity in our medium and the initial time is in the range  
 2834  $t_0 \in [0, t_{spill}]$  where  $t_{spill}$  is the spill length. For a  $10 \mu\text{s}$  spill this translates into a  
 2835 maximum 30 cm uncertainty on the drift direction position.

### 6.3. MUON AND PION SEPARATION IN THE ECAL AND MUID

2836        The current default in GArSoft sets  $t_0 = 0$ , but the functionality to randomly sample  
2837        this within the spill time is in place. Therefore, we need to understand what is the impact  
2838        of a non-zero  $t_0$  on the associations algorithm and foresee possible ways of minimising a  
2839        loss in performance.

2840        Figure 6.18 represents a possible option to tackle the association problem when  
2841        having events with a non-zero initial time  $t_0$ . The black and white circles represent the  
2842        original points, whereas the squares indicate the corrected positions. The end points of  
2843        the track and the propagated points up to the cluster radius are indicated using filled  
2844        and unfilled markers respectively. The red square represents the position of the cluster.

2845        Here I try to correct for the drift coordinate position using the time associated to the  
2846        cluster. Assuming that the drift time is much larger than the propagation time,  $t_{cluster}$   
2847        could be used as a good estimation of the  $t_0$ . An alternative can be using the earliest  
2848        time associated to a hit in said cluster. Doing this for each cluster before computing  
2849        the  $\chi^2$  value could be used as an alternative to knowing the specific value of the  $t_0$ , as  
2850        when the association is correct this will provide the right correction but its impact is  
2851        small enough to not change the position significantly in the case the cluster does not  
2852        correspond to a given track.

2853        I tested the effect of this correction again using a sample of 10000 FHC neutrino  
2854        events. Figure 6.17 (right panel) shows the precision (blue line), sensitivity (yellow line),  
2855        and  $F_1$  score (red line) for the case the cluster  $t_0$  correction is applied (square markers)  
2856        and for the no correction case (circle markers), as a function of  $\chi^2_{cut}$ . In this case, the  
2857        differences are particularly notorious at low values of the cut. It makes sense, as the  $t_0$   
2858        effect becomes subdominant when the distance we consider grows large. Overall, the  
2859        correction increases the sensitivity while keeping the precision almost unchanged. As a  
2860        result, I apply the  $t_0$  correction to the generated samples as the default.



#### 2861        6.3.2 Classification strategy

2862        The problem of the muon and charged pion separation has to be viewed in the broader  
2863        context of the particle identification in our detector. Focusing on the beam neutrino

## CHAPTER 6. PARTICLE IDENTIFICATION IN ND-GAR

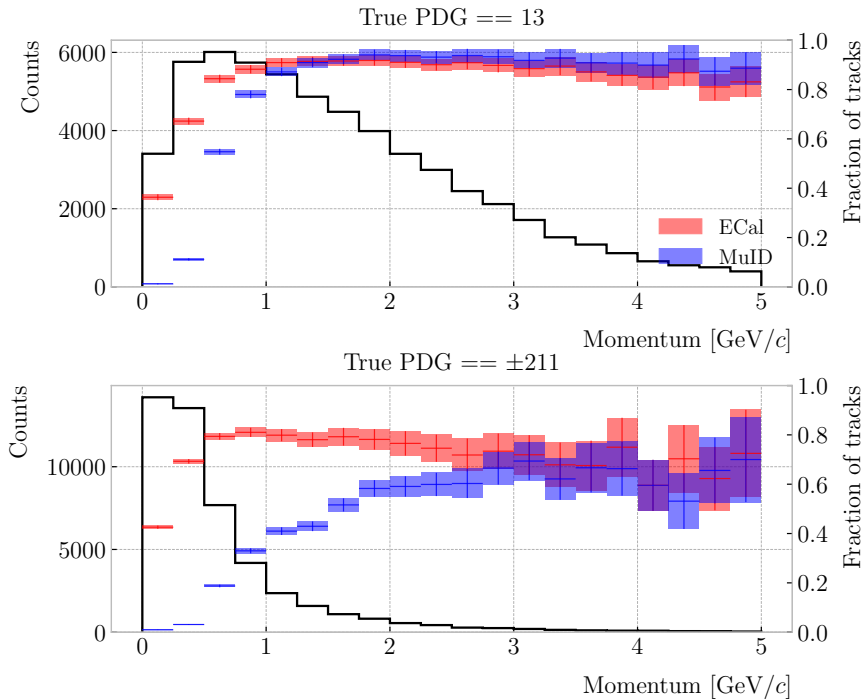


**Figure 6.19:** Momentum distribution for the reconstructed muons (top panel) and charged pions (bottom panel) in a FHC neutrino sample, together with the fraction of them reaching the ECal (red) and MuID (blue). Each entry corresponds to a reconstructed track, backtracked to a true muon or pion which has not produced any other reconstructed track.

2864 interactions, it is clear that we are going to have muons and pions spanning a broad  
2865 momentum range. Not only that, but we will also have other particles with similar  
2866 characteristics that will make the classification even more challenging. Therefore, we are  
2867 presented with a task that will depend heavily on the kinematic range we are looking at  
2868 each time, as both the available information and the possible impurities of other particle  
2869 species vary.

2870 For instance, distinguishing muons from pions could be difficult at low momenta, as  
2871 a great number of them do not reach the ECal. Therefore, we could think of tailoring a  
2872 version of the classification for that particular case, which could be complemented with  
2873 a  $dE/dx$  measurement. Likewise, for momenta  $\gtrsim 1$  GeV muons and pions reach the  
2874 calorimeters efficiently, but so do protons. Because of this, one can try to train another  
2875 classifier for this energy range, and rely on other methods to remove as many of the

### 6.3. MUON AND PION SEPARATION IN THE ECAL AND MUID

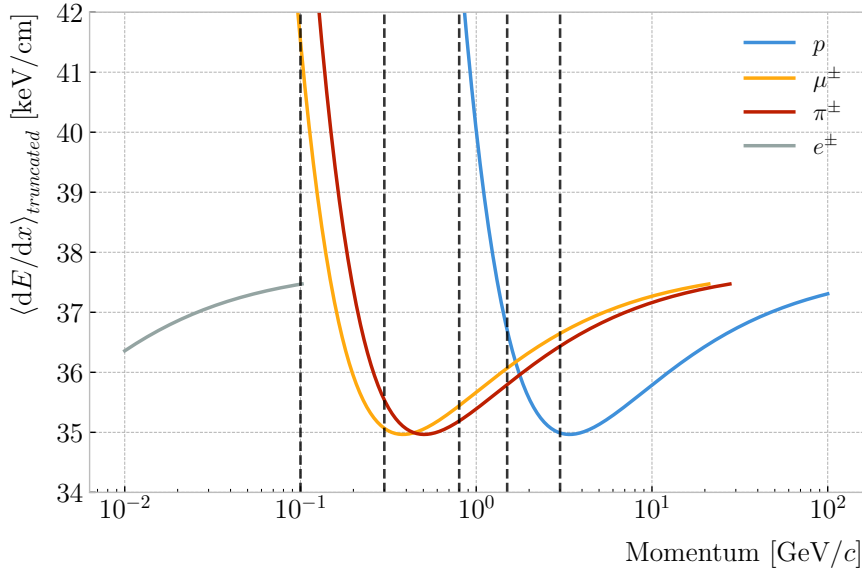


**Figure 6.20:** Predicted truncated mean  $dE/dx$  versus momentum, for electrons, muons, charged pions and protons, obtained using the ALEPH parametrisation. The vertical dashed lines represent the boundaries of the six regions used for the muon and pion classification training.

2876 protons as possible.

2877 Figure 6.19 shows the momentum distribution of the reconstructed muons (top) and  
 2878 pions (bottom) in a FHC sample. It also contains the fraction of particles reaching the  
 2879 ECal (red) and MuID (blue), for the different momentum bins. In Fig. 6.20 I show the  
 2880 mean  $dE/dx$  of different particles as a function of the momentum, computed using the  
 2881 ALEPH parametrisation with the best fit parameters found in Subsec. 6.2.2.

2882 Using these two figures as references, I decided to approach the classification by  
 2883 dividing the problem into six different momentum regions. A summary of these can be  
 2884 found in Tab. 6.2. The basic idea is to exploit all the information that is available in  
 2885 each region and . For the problem at hand, I prepared separated samples of isotropic  
 2886 single muons and pions, with momenta uniformly distributed along the corresponding  
 2887 momentum range. Each sample contains 50000 events of the corresponding particle  
 2888 species. I did not generate samples for the first region, as it is assumed that the separation  
 2889 can be achieved using  $dE/dx$  only. For the last region, I generated particles up to a  
 2890 momentum of 10  $\text{GeV}/c$ , as that is well above the typical energies of muons and pions

## CHAPTER 6. PARTICLE IDENTIFICATION IN ND-GAr

**Table 6.2:** Momentum ranges and description of the PID approach assumed for the muon and pion classification task.

Momentum range	Description
$< 0.1$ GeV/c	All tracks can be separated with $dE/dx$
[0.1, 0.3) GeV/c	Use ECal for reaching muons and pions, $dE/dx$ for the rest
[0.3, 0.8) GeV/c	Use ECal for muons and pions, $dE/dx$ for protons
[0.8, 1.5) GeV/c	Use ECal and MuID for muons and pions, $dE/dx$ for protons
[1.5, 3.0) GeV/c	Use ECal and MuID for muons and pions, ToF for protons
$\geq 3.0$ GeV/c	Use ECal and MuID for muons and pions, $dE/dx$ and ToF for protons

2891 from FHC neutrino interactions in ND-GAr.

2892 Additionally, I prepared another sample of 100000 FHC neutrino events. For each  
 2893 interaction, I select the reconstructed particles which were backtracked to true muons or   
 2894 charged pions. I use this dataset to perform validation checks, to see how the models  
 2895 trained with the single particle data generalise to a more realistic scenario.

2896 To tackle this classification problem, I make use of Boosted Decision Trees (BDT). A  
 2897 decision tree uses a flowchart-like structure to make decisions based on some input data.  
 2898 It starts from a root node, which represents the complete dataset, and then it splits  
 2899 this based on the variable or feature which gives the best separation between classes,  
 2900 creating two new nodes. The process repeats for each node until it reaches a certain  
 2901 limit, like a maximum number of splits or some tolerance criteria. The last set of nodes  
 2902 are often called leave nodes, and represent the final prediction of the classifier.

2903 Boosting refers to a family of methods to combine the predictions from multiple  
 2904 classifiers, following a sequential approach where each new model learns from the errors  
 2905 of the previous one. The process starts with a simple decision tree, which is used to  
 2906 make predictions on the training data. Then, the data points misclassified by the first  
 2907 model are assigned higher weights, and another decision tree is trained on the data with  
 2908 adjusted weights. The predictions of the two trees are then combined, and the cycle  
 2909 repeats for a predefined number of iterations. Gradient boosting uses the direction of  
 2910 the steepest error descent to guide the learning process and improve the accuracy with

### 6.3. MUON AND PION SEPARATION IN THE ECAL AND MUID

2911 each iteration.

#### 2912 6.3.3 Feature selection and importance

2913 Using the reconstructed tracks as a starting point, I compute a number of ECal and  
2914 MuID variables for each of them. As there can be more than one cluster associated to a  
2915 track, what I do is collect all associated clusters and compute these variables from the  
2916 complete collection of associated hits. For the MuID, because it only features three layers  
2917 and typically there will be less hits, I also allow single hits to be associated with tracks<sup>7</sup>.  
2918 I can roughly divide the variables in three types: energy-related, geometry-related and  
2919 statistical. In the following, I briefly describe the variables related exclusively to the  
2920 ECal:

2921 • Energy-related ECal

- 2922 – ECal total energy (ClusterTotalEnergy): sum of the energy of all the ECal  
2923 hits.
- 2924 – Mean ECal hit energy (HitMeanEnergy): mean of the hit energy distribution.
- 2925 – Standard deviation ECal hit energy (HitStdEnergy): standard deviation of  
2926 the hit energy distribution.
- 2927 – Maximum ECal hit energy (HitMaxEnergy): maximum of the hit energy  
2928 distribution.

2929 • Geometry-related ECal

- 2930 – Mean distance hit-to-cluster (DistHitClusterMean): mean of the distance  
2931 distribution between the hits and the corresponding cluster's main axis.
- 2932 – RMS distance hit-to-cluster (DistHitClusterRMS): root mean square of the  
2933 distance distribution between the hits and the corresponding cluster's main  
2934 axis.

---

<sup>7</sup>At the reconstruction level what happens is that non-clustered hits are put into single hit clusters, instead of being thrown away. This is necessary to keep the consistency of the track-cluster association code.

## CHAPTER 6. PARTICLE IDENTIFICATION IN ND-GAR

- 2935        – Maximum distance hit-to-centre (DistHitCenterMax): maximum of the  
2936                  distance distribution between the hits and the centre of the TPC.
- 2937        – Time-of-Flight velocity (TOFVelocity): slope obtained when fitting a straight  
2938                  line to the hit time versus hit distance to the centre (i.e.  $d = v \times t$ ).

### 2939        • Energy and geometry ECal

- 2940        – Radius 90% energy (Radius90E): distance in the hit-to-cluster distribution  
2941                  for which 90% of the total energy is contained in the hits that are closer to  
2942                  the axis (i.e. radius that contains 90% of the energy).

### 2943        • Statistical ECal

- 2944        – Number of hits (NHits): total number of hits associated to the track.
- 2945        – Number of layers with hits (NLayers): not really a count of all layers with  
2946                  hits but the difference between the last and the first layer with hits.

2947        Figure 6.21 shows the distributions of three different ECal variables, separating true  
2948        muons (blue) and charged pions (red), for the five momentum ranges considered. I chose  
2949        to show one feature from each category, namely the mean energy per hit (left column),  
2950        the mean distance between the hits and the centre of the cluster (middle column), and  
2951        the number of ECal layers with hits (right column). These give an idea of the separating  
2952        power of the different features, and how it changes considerably with the energy. In  
2953        the number of layers with hits distributions, the peak at 6 is due to the fact that the  
2954        first six ECal layers sit inside the pressure vessel<sup>8</sup>. Therefore, some of the particles get  
2955        stopped crossing it, never making it to the seventh layer.

2956        In the case of the MuID, because at low momenta a significant fraction of the particles  
2957        do not make it past the ECal, I only consider the information coming from this detector  
2958        for momenta  $\geq 0.8$  GeV/ $c$ , i.e. for the last three momentum regions. The variables I  
2959        extract from it are the following:

<sup>8</sup>Note to self: check this. I thought the ECal barrel had 8 layers of tiles, and that all of them were inside the pressure vessel.

### 6.3. MUON AND PION SEPARATION IN THE ECAL AND MUID

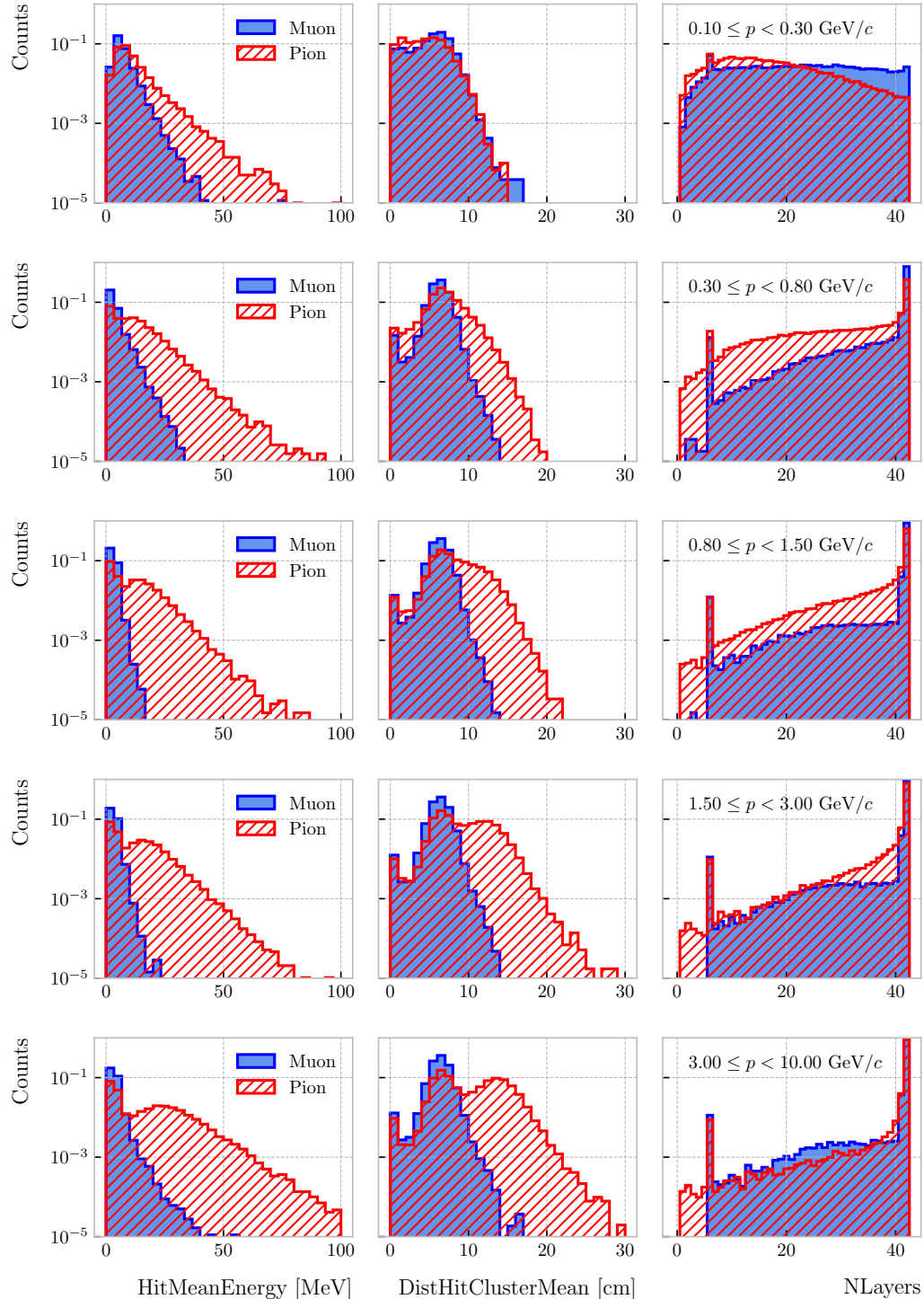


**Figure 6.21:** Example ECal feature distributions for muons (blue) and charged pions (red) in the five different momentum ranges considered (from top to bottom, in ascending momentum order). From left to right: mean hit energy, mean distance hit-to-cluster, and number of layers with hits.

## CHAPTER 6. PARTICLE IDENTIFICATION IN ND-GAR

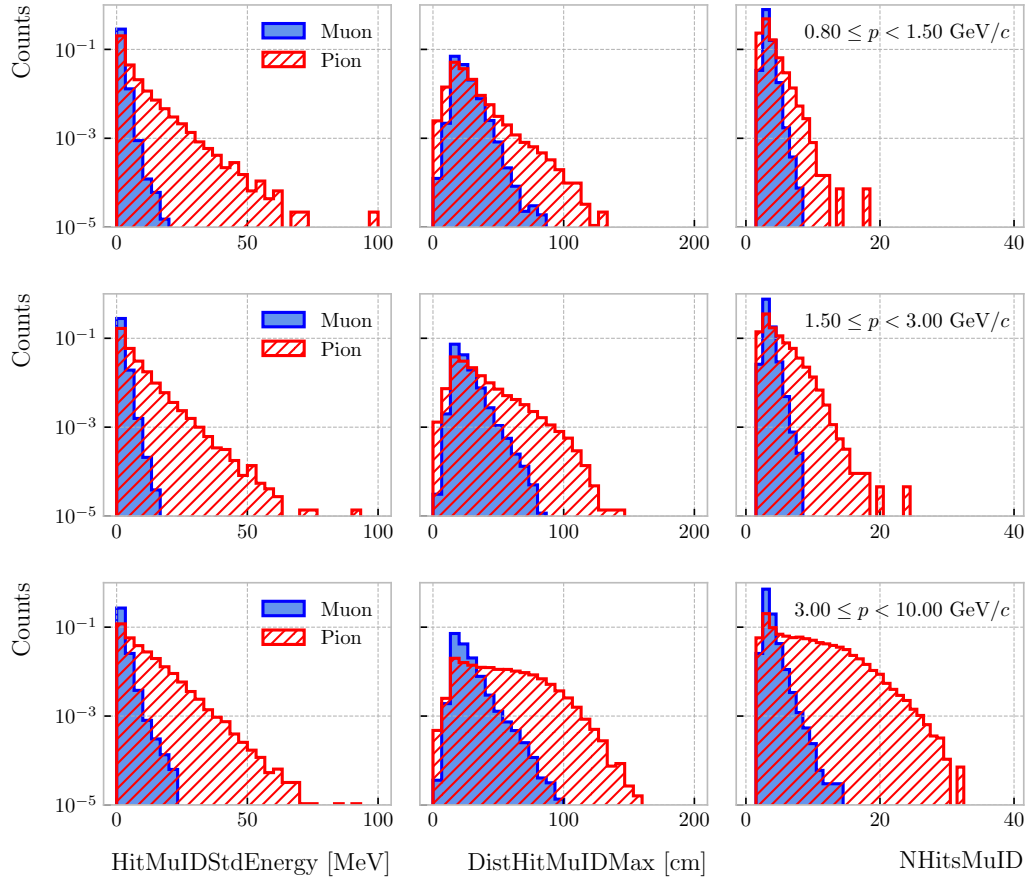


**Figure 6.22:** Example MuID feature distributions for muons (blue) and charged pions (red) in the three different momentum ranges considered (from top to bottom, in ascending momentum order). From left to right: standard deviation hit energy, maximum distance hit-to-hit, and number of hits.

### • Energy-related MuID

- MuID total energy (ClusterMuIDTotalEnergy): sum of the energy of all the MuID hits.
- Mean MuID hit energy (HitMuIDMeanEnergy): mean of the MuID hit energy distribution.
- Standard deviation MuID hit energy (HitMuIDStdEnergy): standard deviation of the MuID hit energy distribution.
- Maximum MuID hit energy (HitMuIDMaxEnergy): maximum of the MuID hit energy distribution.

### 6.3. MUON AND PION SEPARATION IN THE ECAL AND MUID

#### • Geometry-related MuID

- 2969 – Maximum distance MuID hit-to-hit (DistHitMuIDMax): maximum distance
- 2970        between pairs of MuID hits (not sure this is a good variable, distribution
- 2971        looks nuts).
- 2973 – Maximum distance MuID hit-to-centre (DistHitCenterMuIDMax): maximum
- 2974        of the distance distribution between the MuID hits and the centre of the
- 2975        TPC.

#### • Statistical MuID

- 2977 – Number of hits (NHitsMuID): total number of MuID hits associated to the
- 2978        track.
- 2979 – Number of layers with hits (NLayersMuID): not really a count of all layers
- 2980        with MuID hits but the difference between the last and the first layer with
- 2981        MuIDhits.

2982        Figure 6.22 shows the distributions of three different MuID variables, separating true  
2983        muons (blue) and charged pions (red), for the three momentum ranges which use the  
2984        muon tagger information. In this case I decided to standard deviation of the MuID hit  
2985        energy distribution (left column), the maximum distance between the MuID hit pairs  
2986        (middle column), and the number of MuID hits (right column). These variables are used  
2987        together with the ECal features at high momenta, providing additional disambiguation  
2988        power.

2989        Once our features have been defined, one can do some exploratory analysis to  
2990        understand how well the variables describe the target class, and avoid the black-box  
2991        approach by what features are most relevant for the learning process. This way, I  
2992        performed a feature analysis for each of the momentum ranges I divided this classification  
2993        problem into. It follows three steps: first a principal component analysis (PCA), followed  
2994        by a feature importance study using Gini and Shapley values, and finally a feature  
2995        permutation importance analysis.

## CHAPTER 6. PARTICLE IDENTIFICATION IN ND-GAR

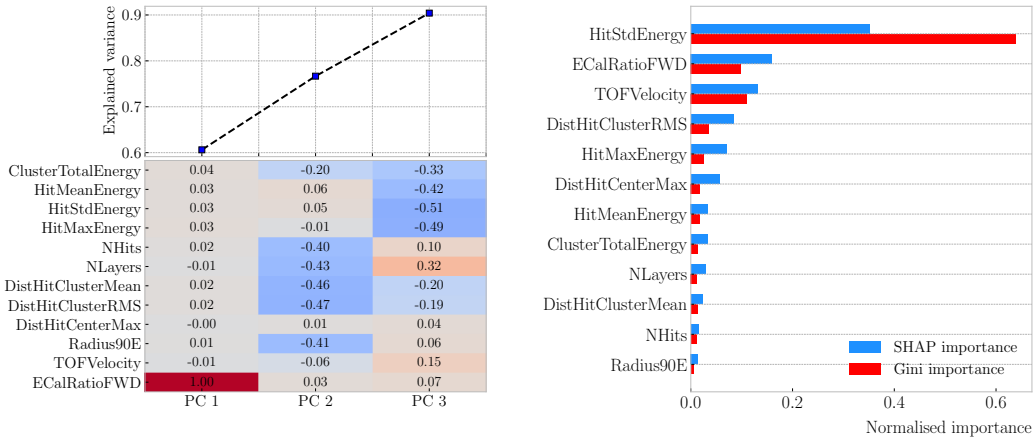


**Figure 6.23:** Left panel: cumulative explained variance for the first three principal components (top panel) and contribution of the different features to the principal axes in feature space (bottom panel). Right panel: Shapley (blue) and Gini (red) feature importances for the different input features. Both figures correspond to the samples in the momentum range  $0.3 \leq p < 0.8 \text{ GeV}/c$ .

2996     The PCA is useful to understand the variance of the feature space. It is an  
 2997     unsupervised machine learning technique that allows the user to perform a dimensionality  
 2998     reduction. It uses a singular value decomposition of the input features to project them  
 2999     into a lower dimensional space. The idea is to find the matrix  $\mathbf{C}_m$ , whose columns are  
 3000     the first  $m$  orthonormal eigenvectors of the input covariance matrix. Consider the  $n \times p$   
 3001     real matrix of input data  $\mathbf{X}$ , where  $n$  is the number of samples and  $p$  the number of  
 3002     features. If  $\mathbf{X}$  is centred, i.e. the means of its columns are equal to zero, we can write the  
 3003     covariance matrix of  $\mathbf{X}$  as  $\mathbf{C} = \mathbf{X}^\top \mathbf{X} / (n - 1)$ . This matrix can be diagonalised, yielding:

$$\mathbf{C} = \mathbf{V} \mathbf{L} \mathbf{V}^\top, \quad (6.11)$$

3004     where  $\mathbf{V}$  is a matrix of eigenvectors and  $\mathbf{L}$  a diagonal matrix with eigenvalues  $\lambda_i$ . Then,  
 3005     performing SVD on  $\mathbf{X}$  gives us:

$$\mathbf{X} = \mathbf{U} \mathbf{S} \mathbf{W}^\top, \quad (6.12)$$

3006     where  $\mathbf{U}$  is a unitary matrix, whose columns are called left singular vectors,  $\mathbf{S}$  is a  
 3007     diagonal matrix of single values  $s_i$ , and  $\mathbf{W}$  is another unitary matrix, its columns known

### 6.3. MUON AND PION SEPARATION IN THE ECAL AND MUID

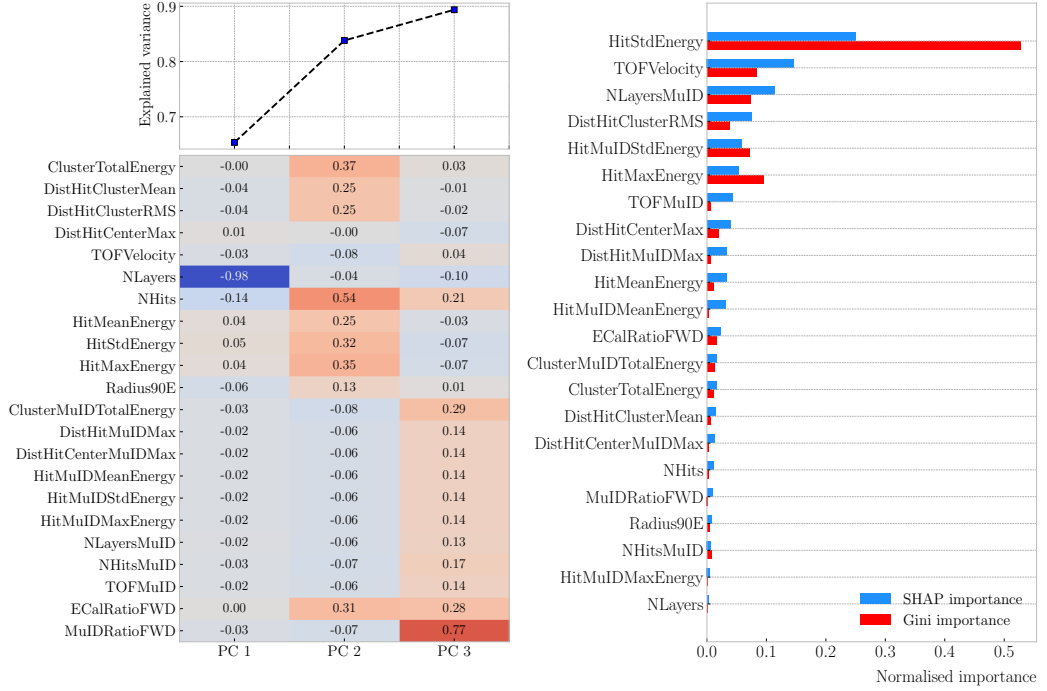


**Figure 6.24:** Left panel: cumulative explained variance for the first three principal components (top panel) and contribution of the different features to the principal axes in feature space (bottom panel). Right panel: Shapley (blue) and Gini (red) feature importances for the different input features. Both figures correspond to the samples in the momentum range  $0.8 \leq p < 1.5$  GeV/c.

as right singular vectors. This way, we can write:

$$\mathbf{C} = \mathbf{W}\mathbf{S}\mathbf{U}^\top\mathbf{U}\mathbf{S}\mathbf{W}^\top/(n-1) = \mathbf{W}\frac{\mathbf{S}^2}{n-1}\mathbf{W}^\top. \quad (6.13)$$

meaning that the right singular vectors are also the eigenvectors of the covariance matrix.

The SVD can be computed numerically following an iterative approach.

This way, taking an input data vector  $X \in \mathbb{R}^n$ , the resulting feature vector  $Y \in \mathbb{R}^m$

is given by:

$$Y = \mathbf{C}_m^\top X. \quad (6.14)$$

The new features capture most of the variance of the original sample, while being lower dimensional, as  $m < n$ .

Before applying the PCA reduction one needs to centre and scale the input data.

## CHAPTER 6. PARTICLE IDENTIFICATION IN ND-GAR

3016 Centring is necessary when using SVD to obtain the eigenvectors of the covariance  
3017 matrix, as only in that case we can do the identification with the right singular vectors  
3018 from the input data. Scaling is needed when variables are on different scales, as some  
3019 can then dominate the PCA procedure.

3020 I used the PCA module of `scikit-learn`, together with the `RobustScaler`, which  
3021 centres the data and scales it based on the interquartile range. In Fig. 6.23 (left panel)  
3022 and Fig. 6.24 (left panel) I show the results I obtained from the PCA for the momentum  
3023 ranges  $0.3 \leq p < 0.8 \text{ GeV}/c$  and  $0.8 \leq p < 1.5 \text{ GeV}/c$ , respectively. Notice that in  
3024 the second case the number of features increases considerably, as this is the first region  
3025 which uses the MuID variables. I found that, in all the cases, adding a fourth PC does  
3026 not add additional information. As it can be seen in the top panels of the figures, the  
3027 cumulative explained variance is already over 80% with three PCs.

3028 The bottom panels show the contribution of the variables to the principal axes. For  
3029 the two first momentum regions, I observe a tendency of the energy-related and the  
3030 geometry-related ECal variables to be clustered together. For the other ranges, when  
3031 I include the MuID variables, there seems to be a division between ECal and MuID  
3032 variables. For these, it seems like the number of ECal layers with hits also plays an  
3033 important role.

3034 The next step in the analysis is to quantify the importance of the features based on  
3035 two additional metrics, namely the Gini and the Shapley values. The Gini importance,  
3036 often called mean decrease impurity, is based on how much a feature contributes to the  
3037 purity improvement at the splits in each decision tree. The purity is measured in terms  
3038 of the Gini impurity index, defined as:

$$I_G = 1 - \sum_i f_i, \quad (6.15)$$

3039 where  $f_i$  is the fractional abundance of the  $i$ -th class. Then, for each split one can

### 6.3. MUON AND PION SEPARATION IN THE ECAL AND MUID

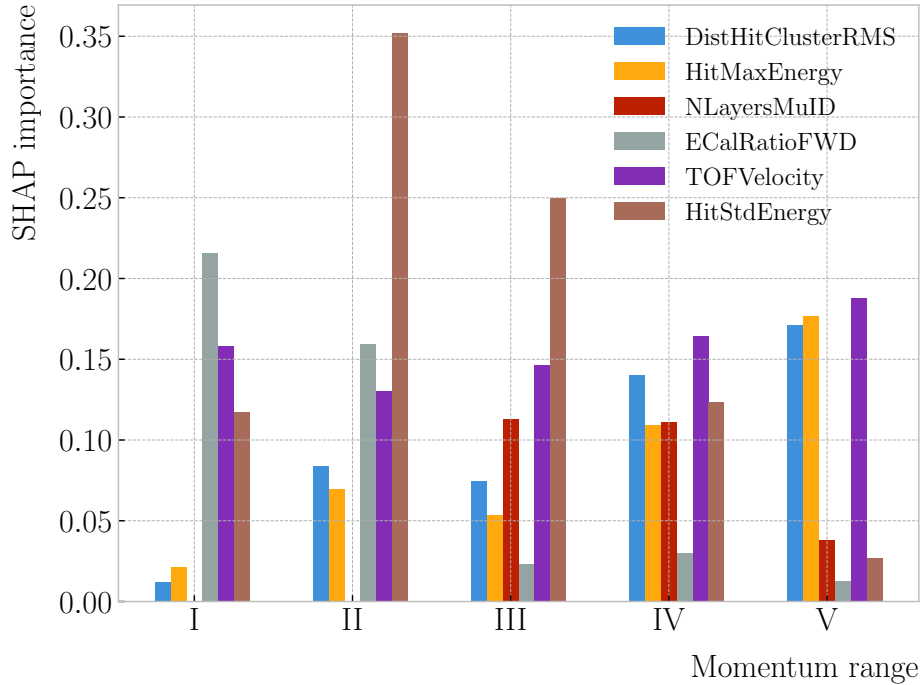


**Figure 6.25:** Evolution of the SHAP importance for the top six most important features across all five momentum ranges.

3040 compute the weighted decrease in impurity as:

$$\Delta_G = \frac{N_t}{N} \left( I_G - \frac{N_t^R}{N_t} I_G^R - \frac{N_t^L}{N_t} I_G^L \right), \quad (6.16)$$

3041 where  $N$  represents the total number of samples,  $N_t$  the number of samples at the current  
 3042 node,  $N_t^R$  and  $N_t^L$  the number of samples in the right and left children respectively,  
 3043  $I_G$  is the Gini impurity at the current node, and  $I_G^R$  and  $I_G^L$  the Gini impurities of the  
 3044 resulting right and left children.

3045 For each decision tree, one will have a normalised vector with the accumulated  
 3046 decrease in Gini impurity for each feature. In the case of a BDT, the feature importances  
 3047 are simply the mean for all the estimators in the ensemble<sup>9</sup>.

3048 The concept of Shapley values originated in the context of game theory, and it  
 3049 measures the marginal contribution of a feature in enhancing the accuracy of a classifier.

---

<sup>9</sup>Note to self: this appears not to be the case. If you get the `feature_importance` for each tree in the BDT and take the average, the result is not the same to be one reported in the `feature_importance` attribute of the BDT.

## CHAPTER 6. PARTICLE IDENTIFICATION IN ND-GAR

3050 Take  $F$  to be the set of all features in a problem, and  $S \subseteq F$  the subset of features. To  
 3051 compute the Shapley value of the  $i$ -th feature, one has to train a model with that feature  
 3052 present,  $f_{S \cup \{i\}}$ , and another model trained without it,  $f_S$ . This has to be repeated for  
 3053 all possible combinations of subsets  $S \subset F \setminus \{i\}$ , and evaluating the models predictions  
 3054 on the appropriate sets of data  $x_S$ . This way, the Shapley value results:

$$\varphi_i = \sum_{S \subset F \setminus \{i\}} \frac{|S|! (|F| - |S| - 1)!}{|F|!} [f_{S \cup \{i\}}(x_{S \cup \{i\}}) - f_S(x_S)]. \quad (6.17)$$

3055 I trained the `GradientBoostingClassifier` from `scikit-learn` with the default  configuration in order to evaluate both the Gini and Shapley importances. The Gini  
 3056 scores are automatically computed by `scikit-learn`, using the training data. For the  
 3057 Shapley importance, I used the implementation from the `SHAP` package, computing  
 3058 it using the test sample. The results can be seen in Fig. 6.23 (right panel) and  
 3059 Fig. 6.24 (right panel), again for the momentum ranges  $0.3 \leq p < 0.8 \text{ GeV}/c$  and  
 3060  $0.8 \leq p < 1.5 \text{ GeV}/c$ . The length of the bars denote either the SHAP (blue) or the Gini  
 3061 (red) importance of the feature. One interesting thing to notice is that, when looking at  
 3062 the Gini importance, there is always one feature that dominates over the rest. This is  
 3063 not the case for the SHAP importance, where importances tend to be more balanced.

3065 Across all momentum ranges, I observe that the most important features  are. For  
 3066 the five momentum ranges considered, only six variables sit in the top five at least once.  
 3067 Figure 6.25 shows the evolution of the SHAP importance of these six features. It is  
 3068 interesting to see that the time-of-flight variable keeps its importance almost unchanged  
 3069 for all momenta. Also, it looks like the ECal energy ratio gets less relevant the higher the  
 3070 momentum is, but the RMS of the hit-to-cluster distance distribution and the maximum  
 3071 ECal hit energy become more important in the last momentum ranges.

3072 The last step in the feature selection analysis is the feature permutation. This  
 3073 technique measures the contribution of each feature to the performance of a model by  
 3074 randomly shuffling its values and checking how some scores degrade. For the present  
 3075 case, I am interested in the precision or purity, and the sensitivity or efficiency, as these

### 6.3. MUON AND PION SEPARATION IN THE ECAL AND MUID

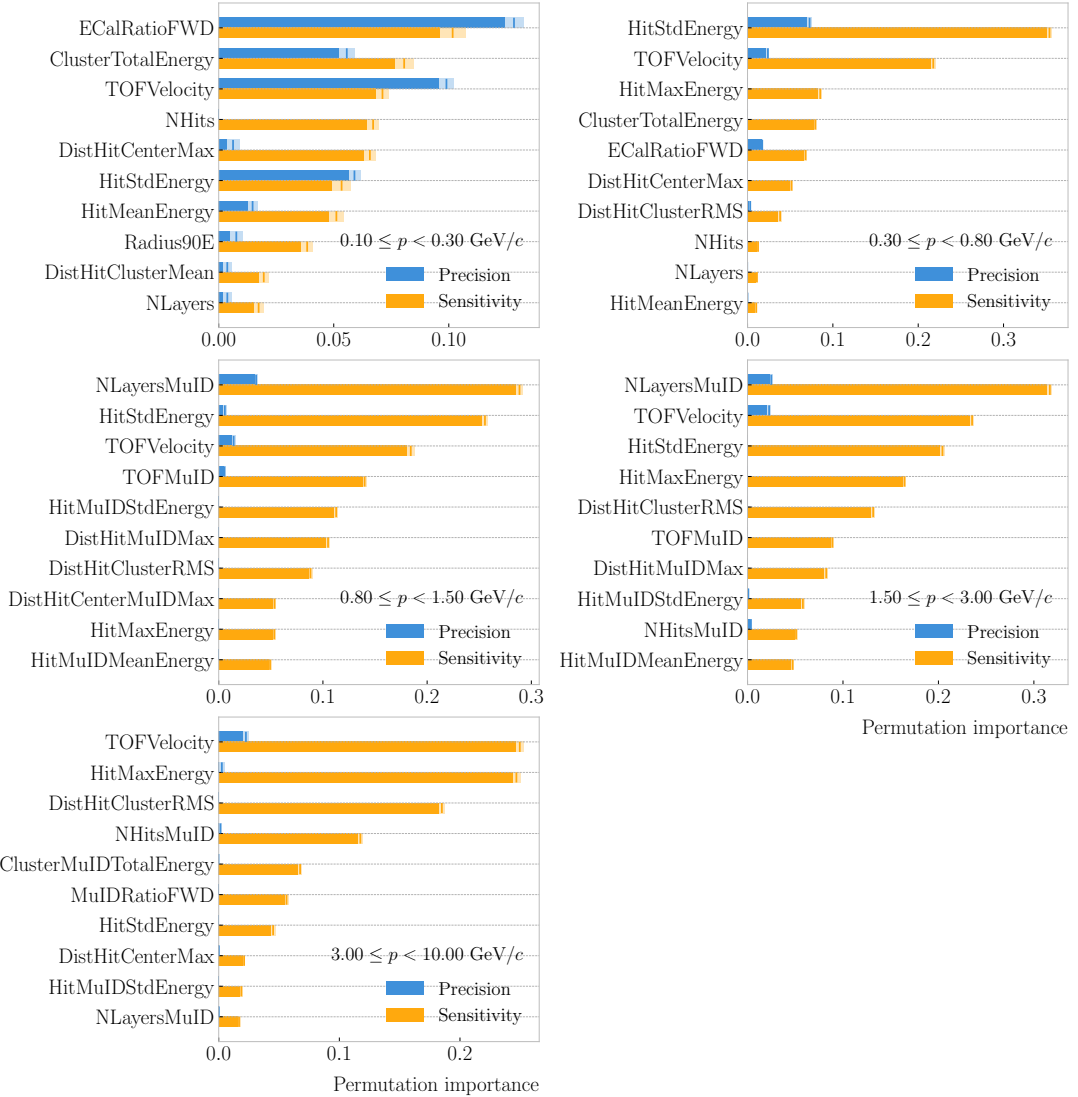


**Figure 6.26:** Permutation importances for the ten most important features in the different momentum ranges (from left to right, top to bottom, in increasing momentum order). The bars indicate the effect that permutations of each feature have on the purity (blue) and the sensitivity (yellow), the translucent regions representing one standard deviation around the central value.

## CHAPTER 6. PARTICLE IDENTIFICATION IN ND-GAR

3076 two are the most relevant metrics from a physics point of view. The `scikit-learn`  
3077 module provides the user with a method to perform the permutation scans.

3078 The results of these are shown in Fig. 6.26. For the different momentum ranges  
3079 I show the permutation importances for the ten most important features. For each  
3080 of the variables I report the effect the permutations have on the precision (blue) and  
3081 sensitivity (yellow) of the models. The bars indicate the importance value, with the  
3082 lighter part representing one standard deviation around the mean (hinted as an additional  
3083 vertical line). Something to notice is that, in the first momentum region, the feature  
3084 permutations have an effect on both the precision and the sensitivity. However, for the  
3085 rest the precision is almost unaffected, while the sensitivity changes are considerably  
3086 larger.

3087 It is also interesting to see that most of the variables identified as important here  
3088 are the same I found when looking at the Shapley values. The behaviour of these across  
3089 the momentum ranges is also similar, with the same patterns of some features being  
3090 important at low momenta and then dropping in importance for the high momentum  
3091 ranges.

3092 **With** this, I conclude the study of the features. I have prepared the training and  
3093 testing datasets and understood what features are likely to have the largest impact on  
3094 the performance of the classifiers.

### 3095 6.3.4 Hyperparameter optimisation

3096 Any BDT requires the user to specify a number of parameters that will dictate its  
3097 behaviour. They can be divided into two categories: (i) tree-specific parameters, which  
3098 affect each individual tree in the model, and (ii) boosting parameters, which control the  
3099 boosting operation in the model. The value of these so-called hyperparameters affect the  
3100 performance and predictive power of the models. Therefore, one needs to carefully select  
3101 their optimal values in order to extract as much information as possible from the data.

3102 From all the parameters used to define a tree in the `scikit-learn` implementation  
3103 of the BDT classifier, I only consider a subset of them. This is due to the fact that some

### 6.3. MUON AND PION SEPARATION IN THE ECAL AND MUID

3104 are mutually exclusive, but also because I noticed that others have little effect on the  
3105 problem at hand. Therefore, the parameters I investigate are the following:

- 3106 • `min_samples_split`: defines the minimum number of samples required in a node  
3107 to be considered for splitting. Higher values prevent a model from learning relations  
3108 which might be highly specific to the particular sample, but may lead to under-fitting  
3109 if the value is too low.
- 3110 • `min_samples_leaf`: defines the minimum samples required in a leaf node. For  
3111 imbalanced problems it should take a low value, as there will not be many cases  
3112 where the minority class dominates.
- 3113 • `max_depth`: maximum depth of a tree. Useful to prevent over-fitting, as higher  
3114 depth will allow a model to learn relations specific to the training sample.

3115 In the case of the boosting parameters, the ones I look at are:

- 3116 • `learning_rate`: determines the impact of each tree on the final outcome. Low  
3117 values make the model robust to the specific characteristics of a tree, and thus  
3118 allow it to generalise well. However, that usually requires a large number of trees  
3119 to model the data properly.
- 3120 • `n_estimators`: number of sequential trees to be trained. In general, BDTs are  
3121 fairly robust at higher number of trees but it can still overfit at a point.
- 3122 • `subsample`: fraction of observations to be selected for each tree. Values slightly  
3123 less than 1 make the model robust by reducing the variance.

3124 In general, hyperparameters depend on each other. Thus, it is not possible to  
3125 optimise them independently. In the literature, we find two main strategies to explore  
3126 the hyperparameter space. We could use a grid search, in which one discretises a  
3127 portion of the space of hyperparameters and evaluates the model at each point. Another  
3128 approach is the randomised search, where a certain number of random configurations of  
3129 hyperparameters are explored.

## CHAPTER 6. PARTICLE IDENTIFICATION IN ND-GAR

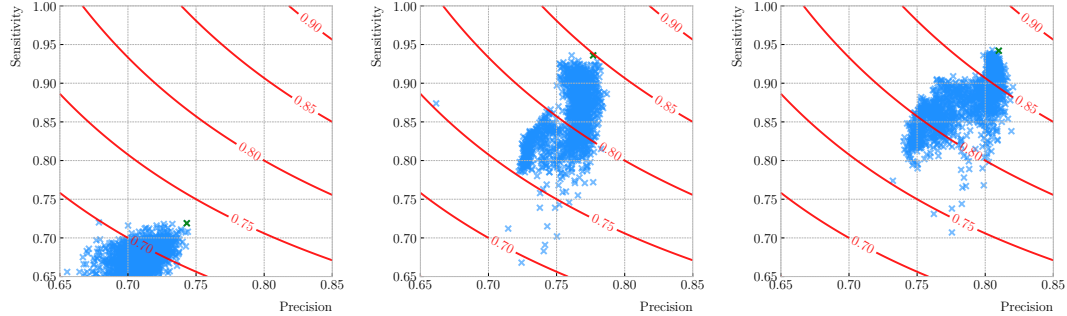


**Figure 6.27:** Values of the precision and sensitivity obtained for 10000 BDT hyperparameter configurations, for the momentum regions I, III and V. The red contours indicate the curves of equal  $F_1$ -score, while the green crosses are the selected configurations.

3130 In this case, I used the random search to scan the hyperparameter space. Also,  
 3131 because it is not guaranteed that a set of hyperparameters can be efficiently applied  
 3132 across different datasets, I perform the optimisation for each of the momentum ranges  
 3133 considered. Table 6.3 shows the list of hyperparameters considered, and the range within  
 3134 which I let them vary. I decided to fix the number of estimators to 400 in all cases, as  
 3135 its value is correlated with that of the learning rate.

3136 I evaluate 10000 different hyperparameter configurations for each momentum range.  
 3137 For the hyperparameter tuning, I used subsamples containing 10% of the full datasets,  
 3138 keeping the original proportions between classes, in order to reduce the computational  
 3139 load. The performance of the models was assessed using a stratified 3-fold cross-validation  
 3140 with replacement. Cross-validation involves dividing the data in a number of subsets,  
 3141 training the model using some of them, and testing it with the rest. In our case, I  
 3142 divide the data in 3 equal-sized subsets, maintaining the class proportions of the original  
 3143 dataset. Then, for 3 consecutive iterations, I train the models using 2 of the subsets  
 3144 while I compute the precision and sensitivity scores with the other. This approach  
 3145 provides a more robust estimate of the performance on unseen data.

3146 Figure 6.27 shows the results in the precision versus sensitivity plane, for the  
 3147 momentum regions I, III and V (from left to right). The contours represent the curves  
 3148 of equal  $F_1$ -score, i.e. the harmonic mean of the precision and the sensitivity. In order

### 6.3. MUON AND PION SEPARATION IN THE ECAL AND MUID

**Table 6.3:** Optimal values of the hyperparameters used by the BDT, for each momentum range.

Hyperparameter	Range	Best value				
		I	II	III	IV	V
<code>min_samples_split</code>	[0.001, 1]	0.10	0.06	0.05	0.27	0.06
<code>min_samples_leaf</code>	[0.001, 1]	0.02	0.03	0.01	0.02	0.07
<code>max_depth</code>	{2, 3, ..., 8}	8	2	4	2	7
<code>learning_rate</code>	[0.05, 1]	0.10	0.23	0.07	0.13	0.09
<code>subsample</code>	[0.01, 1]	0.75	0.65	0.79	0.86	0.95

**Table 6.4:** Performance metrics of the BDTs with optimal hyperparameters, for the different momentum ranges.

Metric	Value $\pm 1\sigma$				
	I	II	III	IV	V
Accuracy	$0.779 \pm 0.003$	$0.812 \pm 0.003$	$0.846 \pm 0.002$	$0.861 \pm 0.003$	$0.874 \pm 0.002$
Precision	$0.769 \pm 0.003$	$0.752 \pm 0.005$	$0.788 \pm 0.002$	$0.805 \pm 0.003$	$0.815 \pm 0.003$
Sensitivity	$0.745 \pm 0.009$	$0.921 \pm 0.006$	$0.965 \pm 0.002$	$0.967 \pm 0.002$	$0.976 \pm 0.001$
$F_1$ -score	$0.757 \pm 0.004$	$0.828 \pm 0.003$	$0.867 \pm 0.002$	$0.879 \pm 0.002$	$0.889 \pm 0.002$
ROC AUC	$0.868 \pm 0.003$	$0.865 \pm 0.003$	$0.899 \pm 0.002$	$0.902 \pm 0.002$	$0.911 \pm 0.001$

3149 to select the optimal configurations (indicated in the plots with a green cross), I chose  
 3150 the point with the highest  $F_1$ -score.

3151 The results for the different momentum ranges are summarised in Tab. 6.3. One  
 3152 can see some consistency in hyperparameter choices, with models generally preferring  
 3153 small values for the tree-specific parameters, small learning rate, and relatively large  
 3154 subsample sizes.

3155 Now that I have obtained the optimal values of the hyperparameters, I can train  
 3156 the different BDTs. In this case I use the complete datasets, keeping 20% of the data  
 3157 for testing. Table 6.4 shows the values of the different performance metrics obtained  
 3158 using the selected hyperparameters and 5-fold cross-validation. The last row indicates  
 3159 the value of the area under the receiver operating characteristic (ROC) curve. This  
 3160 represents the sensitivity of a model as a function of the false positive rate. I have

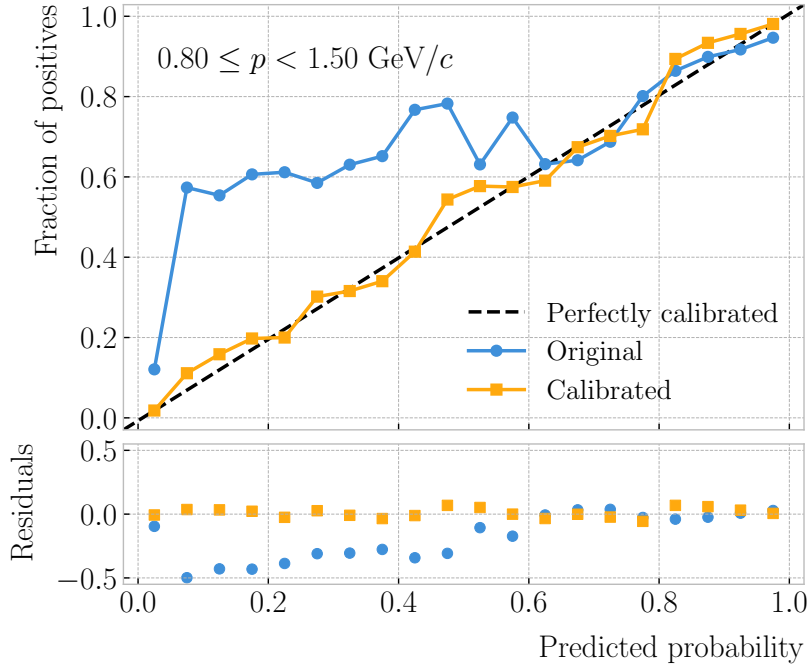


**Figure 6.28:** Reliability diagrams for the BDT classifier used in the momentum range  $0.3 \leq p < 0.8 \text{ GeV}/c$ , both for the original (blue circles) and calibrated (yellow squares) responses. For reference, the response of a perfectly calibrated classifier is also shown (black dashed line).

3161 included it here as it is a classic model metric used in the machine learning community.

3162 Overall, there is a clear trend of models performing better at higher momentum.

### 3163 6.3.5 Probability calibration

3164 So far, the trained BDTs are able to provide predictions of the class labels. Ideally,  
3165 one would like the output of a classifier to give a confidence level about the prediction.  
3166 However, it is not straightforward to interpret the outputs of our BDTs in terms of  
3167 probabilities.

3168 A way to visualise how well the predictions of a classifier are calibrated is using  
3169 reliability diagrams [178]. They represent the probability of the positive label versus the  
3170 probability predicted by the classifier. These can be obtained by binning the predicted  
3171 probabilities, and then compute the conditional probability  $P(y_{true} = 1 | y_i \leq y_{pred} <$   
3172  $y_{i+1})$  by checking the fraction of true positive instances in each bin. The reliability

### 6.3. MUON AND PION SEPARATION IN THE ECAL AND MUID

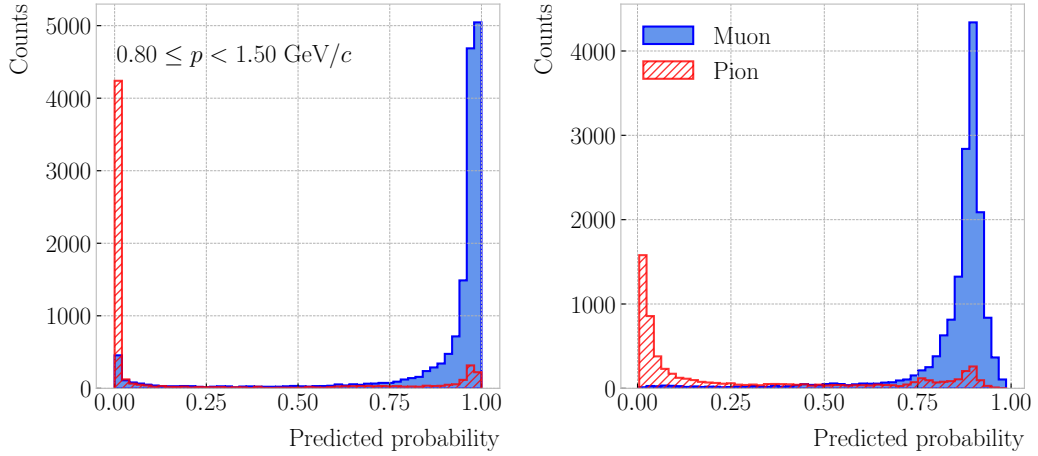


**Figure 6.29:** Uncalibrated (left panel) and calibrated (right panel) predicted probabilities assigned by the BDT classifiers for true muons (blue) and charged pions (red) in the momentum range  $0.3 \leq p < 0.8 \text{ GeV}/c$ .

3173 diagram of a perfectly calibrated classifier would be a diagonal line.

3174 In this case, I try to correct the raw response of the classifiers by applying a sigmoid  
3175 function:

$$\sigma(x; A, B) = \frac{1}{1 + e^{Ax+B}}, \quad (6.18)$$

3176 where the parameters  $A$  and  $B$  are real numbers determined using the method of least  
3177 squares.

3178 For each classifier, I perform a grid search to obtain the optimal values of  $A$  and  $B$ .  
3179 For any pair, I compute the predicted probabilities as  $y_{pred} = \sigma(y_{raw}; A, B)$ , where  $y_{raw}$   
3180 are the raw predictions of the classifier<sup>10</sup>. Then, I calculate the corresponding reliability  
3181 curve, and take the sum of the squared residuals between it and the response of the  
3182 perfectly calibrated classifier.

3183 Figure 6.28 shows the reliability diagrams for the original (blue) and calibrated  
3184 (yellow) probability predictions of the classifier for the III momentum range,  $0.3 \leq p <$   
3185  $0.8 \text{ GeV}/c$ . The original response of the classifier is given by  $y_{pred} = \sigma(y_{raw}; -2, 0)$ ,  
3186 which is the transformation applied by `scikit-learn` to produce the probability estimate.  
3187 Notice how the calibrated prediction matches the ideal response much better than the

---

<sup>10</sup>In `scikit-learn` these correspond to the outputs of the `decision_function` method.

## CHAPTER 6. PARTICLE IDENTIFICATION IN ND-GAR

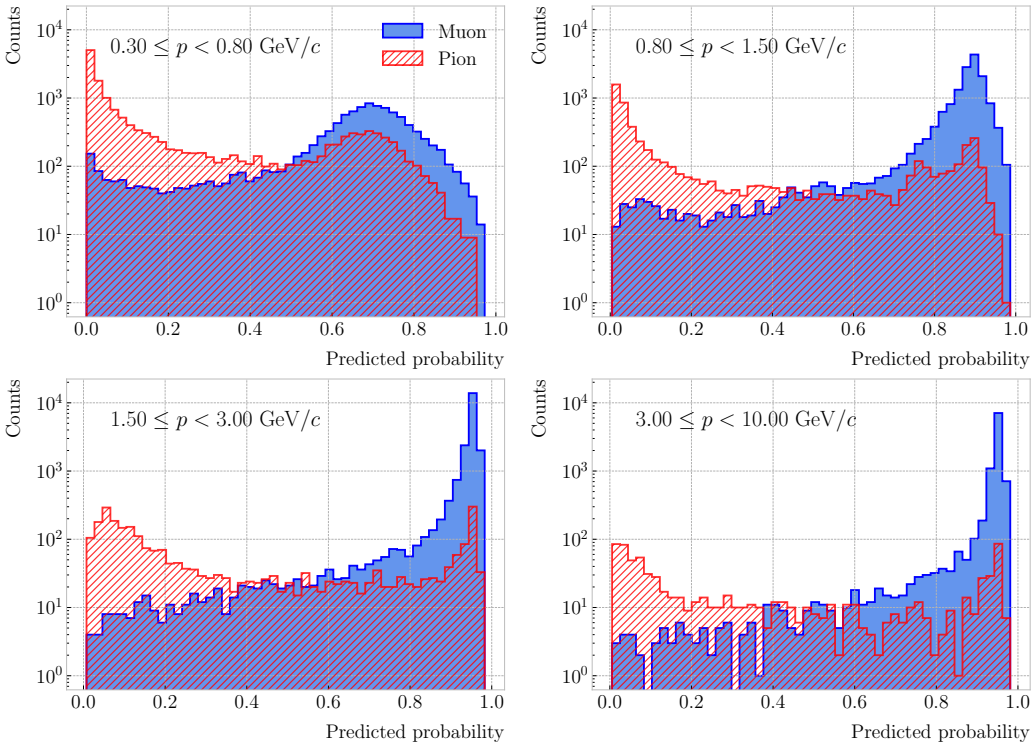


**Figure 6.30:** Calibrated predicted probabilities assigned by the BDT classifiers for the true muons (blue) and charged pions (red) in a FHC neutrino sample.

3188 original, across all the probability range.

3189 One can also compare the responses of the uncalibrated and calibrated classifiers  
 3190 broken down by true particle type, as shown in Fig. 6.29. It can be seen that the  
 3191 distributions for both muons (blue) and charged pions (red) smoothen after calibration,  
 3192 but still the separating power of the classifier remains unchanged.

### 3193 6.3.6 Performance

3194 At this point, having the trained classifiers and the probability calibration parameters, I  
 3195 am able to assess the performance of the classification strategy in a physics-relevant case.  
 3196 For this, I prepared a sample of  $10^5$  FHC neutrino interaction events in the HPgTPC.  
 3197 Using the truth matching information, I select all true muons and pions, and apply the  
 3198 corresponding BDT classifier based on their momentum.

3199 Figure 6.31 shows the resulting calibrated output of the classifiers for the different

### 6.3. MUON AND PION SEPARATION IN THE ECAL AND MUID

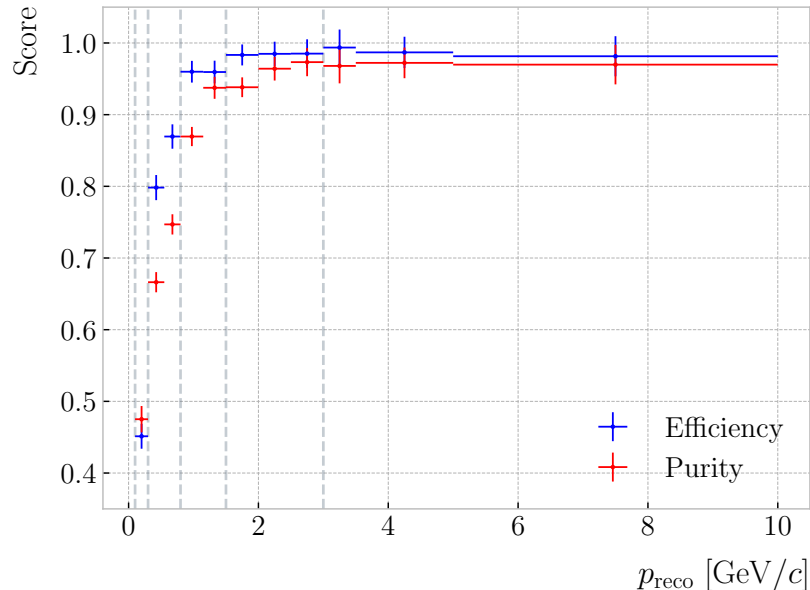


**Figure 6.31:** Efficiency (blue) and purity (red) of the muon selection as a function of the reconstructed momentum for the FHC neutrino sample.

3200 momentum regions. I do not include the first region,  $0.10 \leq p < 0.30$  GeV/ $c$ , as it only  
 3201 contains a small fraction of signal events. The distributions obtained for this validation  
 3202 sample

3203 I also studied the performance of the muon identification in a track-by-track selection.  
 3204 To do so, I apply a simple cut on the output of the BDT classifiers. Every particle  
 3205 with a predicted probability higher than the cut is considered a muon, while the ones  
 3206 not passing the cut are taken to be pions. The results obtained for a cut of 0.50 are  
 3207 shown in Fig. 6.31. Both the efficiency (blue) and the purity (red) of the selection are  
 3208 displayed as a function of the momentum. The binning was chosen so that there were no  
 3209 bins in between different momentum ranges and each had roughly the same number of  
 3210 events. Even without optimising the value of the cut, the performance of the selection  
 3211 is excellent. The only issues the first momentum range, where efficiency and purity sit  
 3212 slightly below 0.50. However, a  $dE/dx$  measurement could help enhance the selection  
 3213 there.

3214 This shows that the method behaves as expected when using unseen data, generalising  
 3215 without problems from single particle to full neutrino events. In the coming Chapter, I



## CHAPTER 6. PARTICLE IDENTIFICATION IN ND-GAr

3216 will study how to use the outputs of the BDT, hereafter referred to as muon scores, to  
3217 perform realistic event selections in ND-GAr.

### 3218 6.4 ECal time-of-flight

3219 Looking at Fig. 6.20, it is clear that for momentum values in the range  $1.0 - 3.0 \text{ GeV}/c$   
3220 it is not possible to separate pions and protons using a  $\langle dE/dx \rangle$  measurement in the  
3221 HPgTPC. However, in the previous section I assumed that protons at those energies  
3222 could be identified by other means, and therefore were not an issue for the muon and  
3223 pion discrimination.

3224 Some detectors, like ALICE [179] or the ILD concept [180], complement the PID  
3225 capabilities of their gaseous trackers with time-of-flight measurements. The use of  
3226 fast timing silicon sensors, with hit time resolutions under 100 ps, would allow for the  
3227 identification of charged hadrons via a ToF measurement up to  $5.0 \text{ GeV}/c$ . In the case  
3228 of ND-GAr, one could think of using the inner layers of the ECal, the ones consisting of  
3229 high-granularity tiles, to obtain a ToF-based PID, with some inputs from the TPC.

3230 Measuring the momentum and the velocity of a charged particle allows for a  
3231 determination of the mass through the relativistic momentum formula:

$$m = \frac{p}{\beta} \sqrt{1 - \beta^2}. \quad (6.19)$$

3232 In our case, the momentum is measured in the TPC, using the curvature and the dip  
3233 angle of the helix inside the magnetic field. The velocity of the particle can be written  
3234 as:

$$\beta = \frac{\ell_{track}}{c\tau}, \quad (6.20)$$

3235 where  $\ell_{track}$  is the length of the track, and  $\tau$  the arrival time to the ECal.

3236 In GArSoft, the track length is computed at the Kalman filter stage. It is simply the  
3237 sum of the line segments along the track, either in the forward or backward fit. In this  
3238 case, because we are only interested in the particles that make it to the ECal, I choose

## 6.4. ECAL TIME-OF-FLIGHT

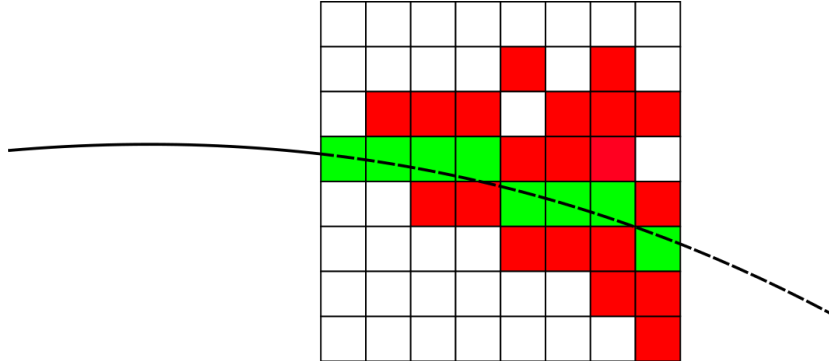


**Figure 6.32:** Schematic of the hit selection used for the ToF measurement. The grid represents the layers of the inner ECal, with coloured squares indicating the tiles with hits. Green squares indicate the selected hits.

3239 the fit direction based on the results of the track-cluster associations.

3240 Additionally, because the last 30 cm of the TPC radius are uninstrumented<sup>11</sup>, I need  
 3241 to correct for the length of the tracks. Using the track fit parameters to propagate the  
 3242 helix to its entry point in the ECal, one can write the total track length as:

$$\ell_{track} = \ell + \left| \frac{\phi_{EP} - \phi}{R^{-1}} \right| \sqrt{1 + \tan^2 \lambda}, \quad (6.21)$$

3243 where  $\phi_{EP}$  is the angle of rotation at the entry point to the calorimeter, and  $\ell$ ,  $\phi$ ,  $R$  and  
 3244  $\lambda$  are the track length, angle of rotation, radius of curvature and dip angle at the last  
 3245 point in the fit, respectively.

3246 To test the idea of performing a ToF measurement with the inner ECal, I generated  
 3247 two data samples. Each consists of 10000 single particle events, either charged pions or  
 3248 protons. Their momenta are uniformly distributed in the range  $0.5 - 5.0$  GeV/ $c$ , and  
 3249 their directions are isotropic. I process each sample using different values of the time  
 3250 resolution, from  $\Delta\tau = 0$ , the perfect time resolution case for comparison, to the current  
 3251 nominal value of  $\Delta\tau = 0.7$  ns, and the worse scenario of  $\Delta\tau = 1.0$  ns.

---

<sup>11</sup>Note to self: check this number.

## CHAPTER 6. PARTICLE IDENTIFICATION IN ND-GAR

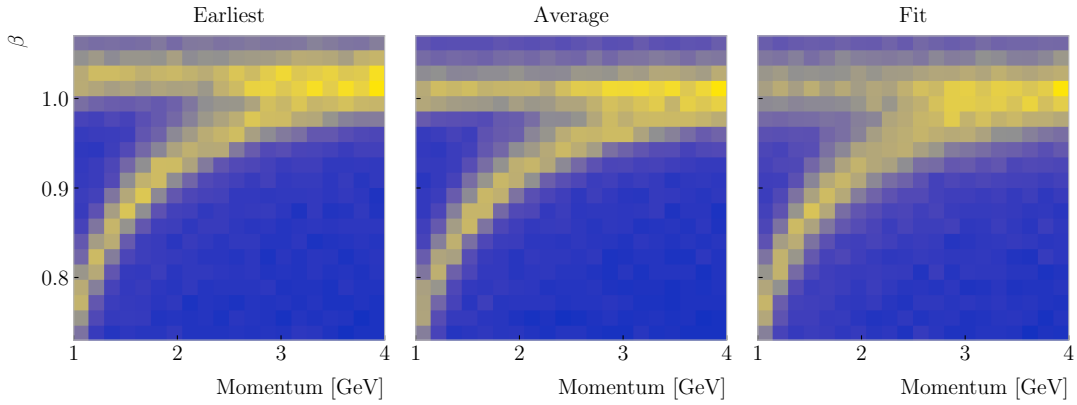


**Figure 6.33:** Particle velocity versus momentum measured with different ECal arrival time estimations. From left to right: earliest hit time, average hit time, and fitted hit time. In all cases the time resolution is  $\Delta\tau = 0.1$  ns.

### 3252 6.4.1 Arrival time estimations

3253 In the simulation, the limited time resolution of the ECal is taken into account by  
 3254 applying a Gaussian smearing to the true hit times. Other effects, like the digitisation  
 3255 of the signals, are not taken into account and fall beyond the scope of this study. After  
 3256 the track-cluster, one ends up with a collection of ECal hits associated to each particle.  
 3257 From these, the arrival time of the particle to the ECal can be extracted.

3258 The simplest possibilities are to either take the time of the earliest hit or the hit  
 3259 closest to the entry point. Because these two coincide, in general, I focused only in  
 3260 the earliest hit time. However, this needs to be corrected, to account for the distance  
 3261 travelled from the entry point to the position of the hit:

$$\tau_{earliest} = \tau_{hit} - \frac{d_{EP-hit}}{c}, \quad (6.22)$$

3262 where  $\tau_{hit}$  is the time of the earliest hit, and  $d_{EP-hit}$  is the distance between that hit  
 3263 and the entry point of the particle to the ECal. This is computed as the arc length  
 3264 between the entry point and the point of the extrapolated helix up to the layer of the  
 3265 hit. This way of correcting the time assumes  $c$  for the propagation of the particle, which  
 3266 may lead to biased estimates.

## 6.4. ECAL TIME-OF-FLIGHT

3267 I also tried to estimate the arrival times using information from the rest of the hits.  
3268 In order to do this, as a simplifying assumption, I approximate the hadronic shower  
3269 considering only its MIP component. For each layer, I keep only the hit in the tile closest  
3270 to the point of the extrapolated track up to that layer. Figure 6.32 shows an example of  
3271 how this hit selection works. The dashed line represents the extrapolated track, while  
3272 the coloured squares are the tiles containing hits. Green indicates the tiles closer to the  
3273 track in each layer (in the sketch they correspond to the grid columns).

3274 Now, I can use these collections of hits to estimate the arrival times. A possibility  
3275 is to take the average of the times of the selected hits, denoted  $\tau_{average}$ . For that to  
3276 work, one needs to correct these times, in a similar way as in Eq. (6.22), before taking  
3277 the average. However, as before, this correction assumes that the particle travels at the  
3278 speed of light inside the ECal. Another option is to perform a linear fit to the hit times  
3279 and the distances to the entry point. In that case, the arrival time would be the fitted  
3280 value of the intercept,  $\tau_{fit}$ . This method would not assume a speed of light propagation.

3281 Figure 6.33 shows the velocity estimations as a function of the particle momentum,  
3282 for the earliest hit time (left panel), average hit time (middle panel), and fitted hit time  
3283 (right panel). The two bands correspond to the  $\pi^\pm$  and the  $p$  particles.  $\Delta\tau = 0.1$  ns.  
3284 Notice how, for the earliest hit time method, the velocities are significantly biased  
3285 towards larger values. For the multi-hit methods, the  $\tau_{fit}$  estimate appears to produce a  
3286 larger variance than when using the  $\tau_{average}$  method.

### 3287 6.4.2 Proton and pion separation

3288 Once we have the velocities of the particles, one can estimate their masses through  
3289 Eq. (6.19). The resulting mass spectra are shown in Fig. 6.34. I computed the masses  
3290 for the three arrival time estimates discussed above, and three different values of the  
3291 time resolution:  $\Delta\tau = 0.00$  (perfect time resolution),  $\Delta\tau = 0.10$  ns, and  $\Delta\tau = 0.70$  ns.  
3292 Although in all cases we have the same number of events, it appears as if the entries  
3293 in the histograms decrease as the time resolution increases. Sometimes, the particles  
3294 get unphysical values of  $\beta > 1$ , and in turn they do not contribute to the mass spectra.

## CHAPTER 6. PARTICLE IDENTIFICATION IN ND-GAR

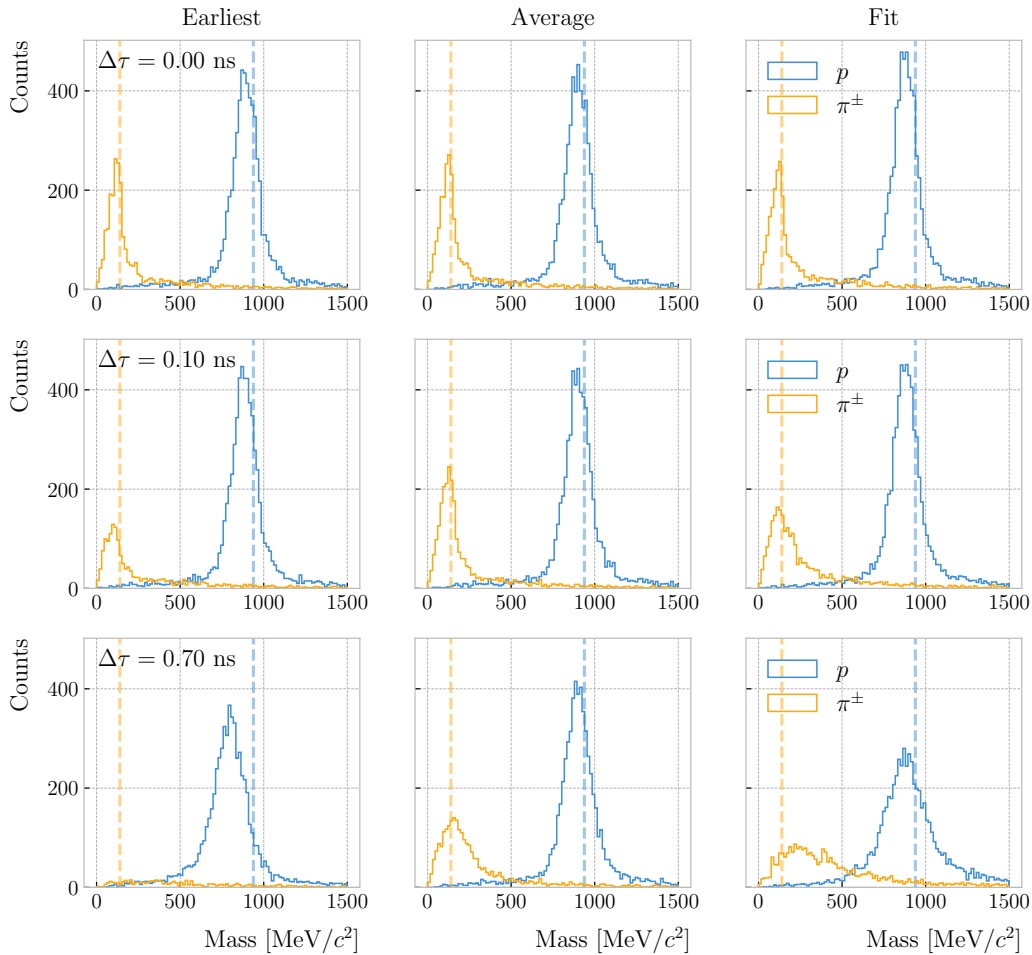


**Figure 6.34:** Mass spectra for  $p$  (blue) and  $\pi^\pm$  (yellow) particles, using different ECal time resolution values (from top to bottom, in ascending order), and arrival time estimates. From left to right: earliest hit time, average hit time, and fitted hit time. The dashed lines indicate the true masses of the particles.

3295 This is more likely to happen for higher values of  $\Delta\tau$ .

3296 As noted before, the average hit time method produces the most robust estimates

3297 when increasing  $\Delta\tau$ . Intuitively this makes sense, as by taking the mean one averages out the effect of the Gaussian smearing. Going forward, I will use this arrival time

3299 estimator, as it appears to be the best performing one.

3300 It is possible to use the velocity estimations to select a sample of protons. In this

3301 case, I do so by dividing the relevant momentum range in bins of  $0.1 \text{ GeV}/c$ . For each

3302 momentum bin, I compute the expected velocity for the protons via the inverse of Eq.

## 6.4. ECAL TIME-OF-FLIGHT

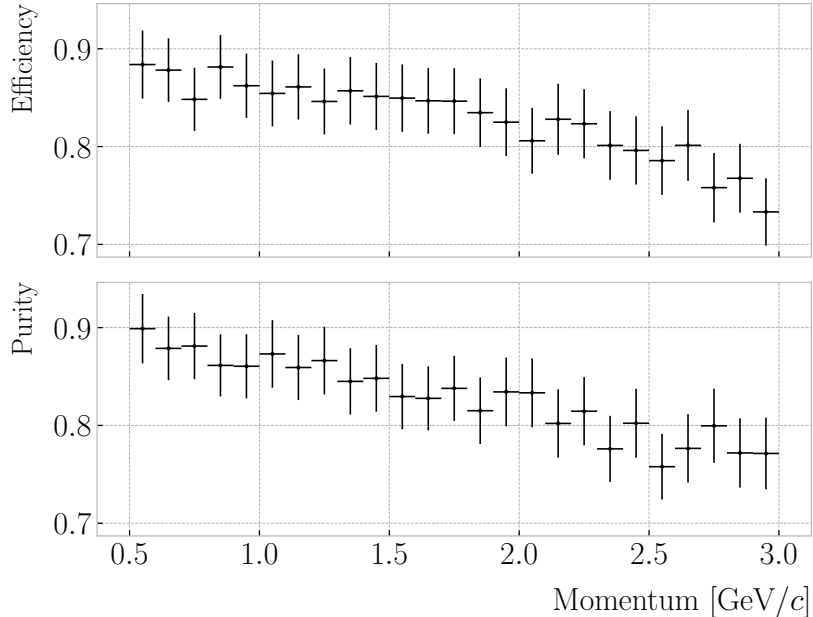


**Figure 6.35:** Efficiency (top panel) and purity (bottom panel) for the proton selection as a function of the momentum, for  $\Delta\tau = 0.10$  ns.

3303 (6.19), and then take the fractional residuals of the measured velocities. Using that  
 3304 distribution, I choose the cut that maximises the  $F_1$ -score of the proton selection.

3305 The results can be seen in Fig. 6.35, for the case  $\Delta\tau = 0.10$  ns. As expected from  
 3306 Fig. 6.33, the performance of the selection degrades rapidly with increasing momentum.  
 3307 However, the purity is still around 75% at 3.0  $\text{GeV}/c$ . This is likely to be sufficient, as  
 3308 we do not expect protons or charged pions with higher energies from the beam neutrino  
 3309 interactions.

3310 Figure 6.36 shows a few examples of the ToF velocity estimation in a FHC neutrino  
 3311 sample. Here, for the different momentum bins, I have taken the fractional residual of  
 3312 the expected value of  $\beta$  for a proton and the measured values (black data points). The  
 3313 coloured lines represent Gaussian fits to the distributions of the different true particle,  
 3314 with the gray line being the sum of these. It can be seen that, even for momenta close  
 3315 to 2.0  $\text{GeV}/c$ , a good proton separation can be achieved. This idea will be explored  
 3316 further later, in the context of the event selection.

## CHAPTER 6. PARTICLE IDENTIFICATION IN ND-GAr

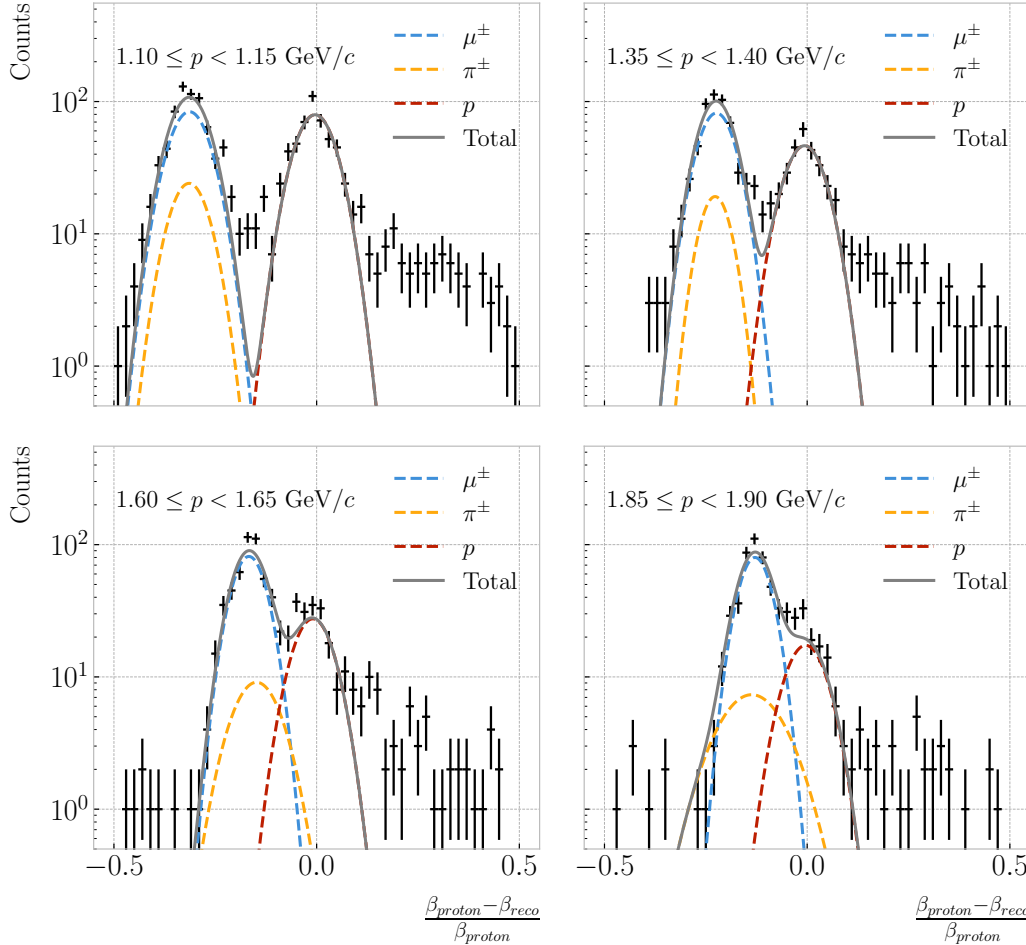


**Figure 6.36:** Distributions of the velocities measured by ToF with the inner ECal, for different momentum bins, in a FHC neutrino interaction sample. The Gaussian fits are performed around the maxima for each particle species.

## 3317 6.5 Charged pion decay in flight

3318 As discussed previously, in GArSoft the TPC tracks are formed after a pattern recognition  
 3319 algorithm and a Kalman filter are applied to the TPC clusters. These two steps can  
 3320 find discontinuities in the track candidates (e.g. due to a particle decay) when these  
 3321 so-called breakpoints are large enough. However, for some, more subtle, cases they may  
 3322 miss them and form a single reconstructed track. It has been noted in the literature  
 3323 that Kalman filters offer, as a by-product, additional information to form test statistics  
 3324 to identify these breakpoints [181, 182].

## 6.5. CHARGED PION DECAY IN FLIGHT

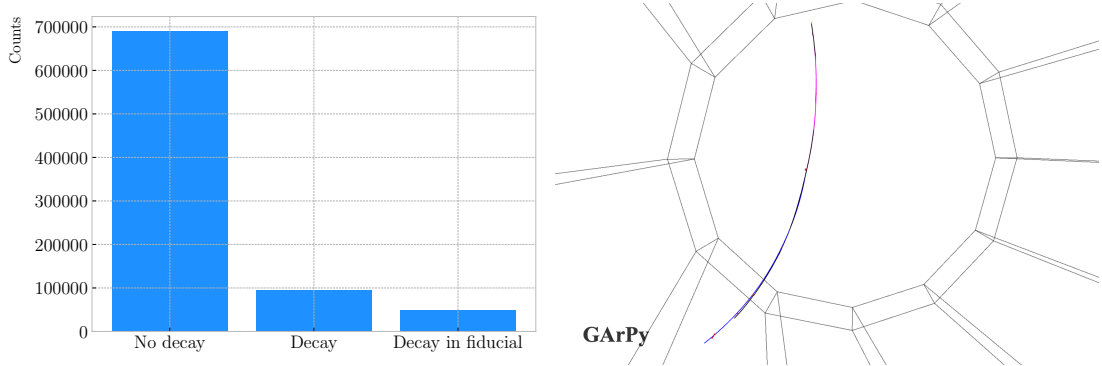


**Figure 6.37:** Left panel: number of non-decaying, decaying and decaying in the fiducial volume pions for a MC sample of 100000,  $p = 500 \text{ MeV}/c$  isotropic positively charged pions inside the TPC. Right panel: event display for a positive pion decaying inside the fiducial volume, with a single reconstructed track for the pion and muon system.

3325 Considering the mean life of the charged pion,  $\tau = (2.6033 \pm 0.0005) \times 10^{-8} \text{ s}$ , one  
 3326 can estimate that about 12% of the pions with momentum  $p \sim \mathcal{O}(500 \text{ MeV}/c)$  (roughly  
 3327 the peak of the pion momentum distribution in  $\nu_\mu$  CC interactions off argon) decay  
 3328 inside the TPC. Figure 6.37 (left panel) shows the amount of charged pions decaying in  
 3329 the full TPC and fiducial volumes from an isotropic, monoenergetic sample of 100000  
 3330 negatively charged pions with  $p = 500 \text{ MeV}/c$ . We see that about 10% of those decayed,  
 3331 with more than half of them decaying inside the TPC fiducial volume.

3332 Figure 6.37 (right panel) shows an example event display of a charged pion (magenta  
 3333 line) decays in flight inside the TPC, but because the angle of the muon (blue line) is  
 3334 small both were reconstructed as one single track (black line). In this case, the composite  
 3335 track reaches the ECal, where it undergoes a muon-like interaction, thus being classified  
 3336 as a muon.

3337 A way to understand what decaying pion tracks were totally or partially reconstructed  
 3338 together with the daughter muon is looking at the relative energy contributions to the  
 3339 reconstructed track. In order to select a sample of such events, I require that a minimum  
 3340 50% of the total energy comes from the pion and at least 20% from the muon.

## CHAPTER 6. PARTICLE IDENTIFICATION IN ND-GAR

### 3341 6.5.1 Track breakpoints

3342 To identify potential decays we can use the information we obtain from the Kalman  
3343 filter at each step of the fitted track. The simplest test we can think about is computing  
3344 the  $\chi^2$  of the mismatch between all the parameters in the forward and the backward fits:

$$\chi_k^{2(FB)} = (\hat{x}_k^B - \hat{x}_k^F)^T [V^{(\hat{x}_k, B)} + V^{(\hat{x}_k, F)}]^{-1} (\hat{x}_k^B - \hat{x}_k^F), \quad (6.23)$$

3345 where  $\hat{x}_k^F$ ,  $\hat{x}_k^B$  are the Kalman filter state vector estimates at step  $k$  in the forward and  
3346 backward fits and  $V^{(\hat{x}_k, F)}$ ,  $V^{(\hat{x}_k, B)}$  the covariance matrices of  $\hat{x}_k^F$  and  $\hat{x}_k^B$  respectively.  
3347 Using the values of the  $\chi^2$  at measurement  $k$  for the forward and backward fits we can  
3348 compute another  $\chi^2$  value that characterises the overall track fit:

$$\chi_{track}^2 = \chi_k^{2(F)} + \chi_k^{2(B)} + \chi_k^{2(FB)}, \quad (6.24)$$

3349 which remains approximately constant for all  $k$ .

3350 An alternative approach proposed in the context of the NOMAD experiment was  
3351 using a fit with a more elaborate breakpoint hypothesis, so we can perform a comparison  
3352 of the  $\chi^2$  with and without breakpoints. This can be achieved by using some alternative  
3353 parametrisation with extra parameters, which allows some of the track parameters to  
3354 be discontinuous at certain points. A decay changes the momentum magnitude and  
3355 direction, so we can use the new state vector:

$$\alpha = (y, z, 1/R_F, 1/R_B, \phi_F, \phi_B, \tan\lambda_F, \tan\lambda_B)^T. \quad (6.25)$$

3356 As we already have the estimates from the standard Kalman filter and their  
3357 covariance matrices at each point, we do not need to repeat the Kalman fit for the new  
3358 parametrisation. Instead, I can compute the values of  $\alpha$  at each point  $k$  that minimise

## 6.5. CHARGED PION DECAY IN FLIGHT

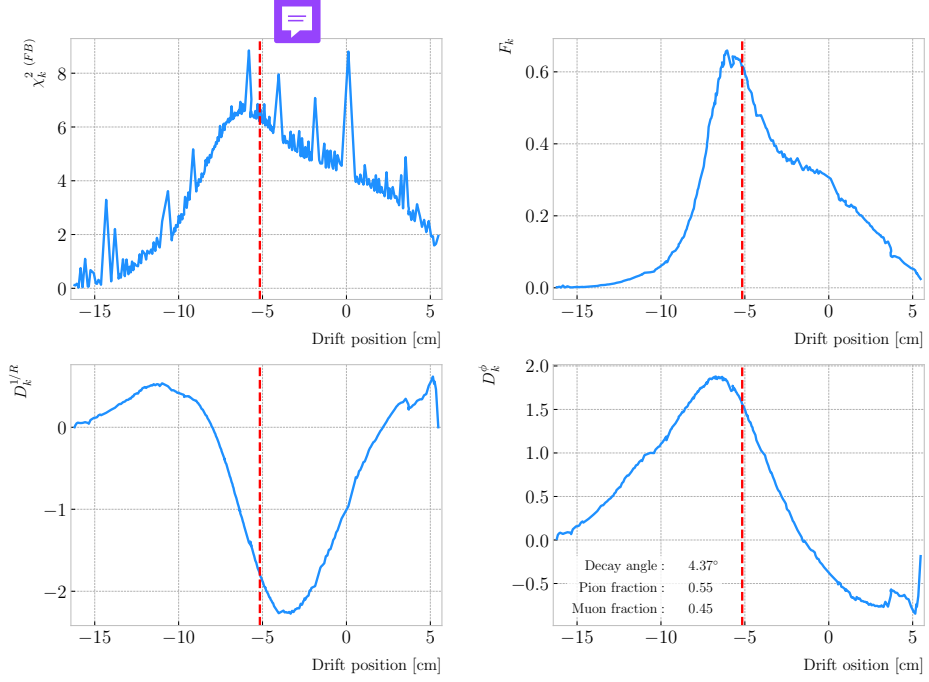


**Figure 6.38:** Values of  $\chi_k^{2(FB)}$  (top left panel),  $F_k$  (top right panel),  $D_k^{1/R}$  (bottom left panel) and  $D_k^\phi$  (bottom right panel) versus position along the drift direction for a reconstructed track in a positive pion decay event. The vertical red dashed line indicates the true location of the decay point.

3359 the  $\chi^2$  resulting from comparing them to  $\{\hat{x}_k^B, \hat{x}_k^F\}$ . Introducing the two  $5 \times 8$  matrices:

$$H^F = \begin{pmatrix} 1 & 0 & 0 & 0 & 0 & 0 & 0 & 0 \\ 0 & 1 & 0 & 0 & 0 & 0 & 0 & 0 \\ 0 & 0 & 1 & 0 & 0 & 0 & 0 & 0 \\ 0 & 0 & 0 & 0 & 1 & 0 & 0 & 0 \\ 0 & 0 & 0 & 0 & 0 & 0 & 1 & 0 \end{pmatrix}, \quad H^B = \begin{pmatrix} 1 & 0 & 0 & 0 & 0 & 0 & 0 & 0 \\ 0 & 1 & 0 & 0 & 0 & 0 & 0 & 0 \\ 0 & 0 & 0 & 1 & 0 & 0 & 0 & 0 \\ 0 & 0 & 0 & 0 & 0 & 1 & 0 & 0 \\ 0 & 0 & 0 & 0 & 0 & 0 & 0 & 1 \end{pmatrix}, \quad (6.26)$$

3360 we can write this as:

$$\begin{aligned} \chi_k^{2(FB)}(\alpha) &= (\hat{x}_k^F - H^F \alpha)^T \left[ V^{(\hat{x}_k, F)} \right]^{-1} (\hat{x}_k^F - H^F \alpha) \\ &\quad + (\hat{x}_k^B - H^B \alpha)^T \left[ V^{(\hat{x}_k, B)} \right]^{-1} (\hat{x}_k^B - H^B \alpha). \end{aligned} \quad (6.27)$$

3361 The minimum of  $\chi_k^{2(FB)}(\alpha)$  is found when the measured new state vector takes the  
3362 value:

$$\hat{\alpha}_k = V^{(\hat{\alpha}_k)} H^T (V^{(\hat{x}_k)})^{-1} \hat{X}, \quad (6.28)$$

## CHAPTER 6. PARTICLE IDENTIFICATION IN ND-GAR

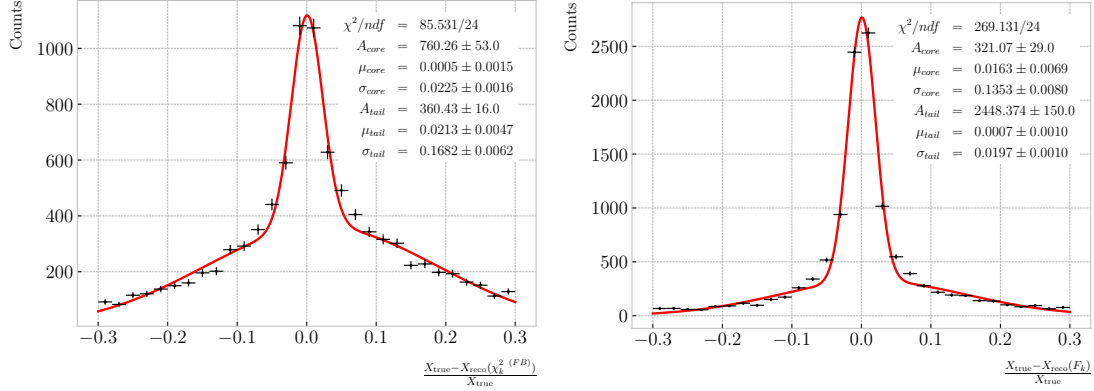


**Figure 6.39:** Fractional residual distributions of the true and reconstructed decay position along the drift coordinate, using the position of the maximum of  $\chi_k^2(FB)$  (left panel) and  $F_k$  (right panel) as estimates of the decay position. Also shown are double Gaussian fits to these points (red lines).

3363 where  $\hat{\mathbf{X}} = \{\hat{\mathbf{x}}_k^B, \hat{\mathbf{x}}_k^F\}$ ,  $V^{(\hat{\mathbf{x}}_k)}$  is the block diagonal matrix formed by  $V^{(\hat{\mathbf{x}}_k, F)}$  and  $V^{(\hat{\mathbf{x}}_k, B)}$   
 3364 and  $V^{(\hat{\alpha}_k)}$  is the covariance matrix of  $\hat{\alpha}_k$ , given by:

$$V^{(\hat{\alpha}_k)} = \left( H^T (V^{(\hat{\mathbf{x}}_k)})^{-1} H \right)^{-1}. \quad (6.29)$$

3365 From these new fit estimates we can compute the  $F$  statistic, which tells us whether  
 3366 the model with breakpoint provides a statistically significant better fit:

$$F_k = \left( \frac{\chi_{\text{track},k}^2 - \chi_{\text{full},k}^2}{8 - 5} \right) / \left( \frac{\chi_{\text{full},k}^2}{N - 8} \right). \quad (6.30)$$

3367 One can also compute the signed difference of the duplicated variables divided by  
 3368 their standard deviation at each point. These represent how significant the discontinuity  
 3369 in each variable is. For any variable  $\eta$  we can write it as:

$$D_k^\eta = \frac{\hat{\eta}_k^B - \hat{\eta}_k^F}{\sqrt{\text{Var}[\hat{\eta}_k^F] + \text{Var}[\hat{\eta}_k^B] - 2\text{Cov}[\hat{\eta}_k^F, \hat{\eta}_k^B]}}. \quad (6.31)$$

3370 In our case, the relevant ones to look at are  $D_k^{1/R}$  and  $D_k^\phi$ .

3371 Figure 6.38 shows the values of  $\chi_k^2(FB)$ ,  $F_k$ ,  $D_k^{1/R}$  and  $D_k^\phi$  as functions of the position  
 3372 along the drift direction, for an example reconstructed track with 55.5% of the energy

## 6.5. CHARGED PION DECAY IN FLIGHT

3373 coming from the charged pion and 45.5% from the daughter muon. The true position of  
 3374 the decay is indicated (dashed red lines). Notice how  $\chi_k^2(FB)$  and  $F_k$ ,  $D_k^{1/R}$  reach their  
 3375 maxima near the decay point. In the former case this indicates a large forward-backward  
 3376 difference in the track fit. In the later it represents that the extended state vector  
 3377 improves the fit particularly around that point.

3378 I can estimate the decay position finding resolution by computing the difference  
 3379 between the  $X$  position of the maxima of  $\chi_k^2(FB)$  and  $F_k$  and the  $X$  position of the  
 3380 true decay. Figure 6.39 represent the the fractional residual distributions for both  
 3381 cases, from the sample of tracks containing pion decays. Fitting a double Gaussian to  
 3382 the distributions (red lines) I find a resolution of  $(3.31 \pm 0.15)\%$  and  $(6.94 \pm 0.31)\%$   
 3383 respectively.

3384 In principle, the  $F$ -statistic should follow a Fisher distribution with  $(8 - 5)$  and  
 3385  $(N - 8)$  degrees of freedom under the null hypothesis. In most of our cases  $N \sim \mathcal{O}(100)$ ,  
 3386 so the probability density functions will look very similar. In this case, it is safe to take  
 3387 the limit  $N \rightarrow \infty$  in the Fisher PDF:

$$\begin{aligned}\tilde{f}(x; a - b) &= \lim_{N \rightarrow \infty} f(x; a - b, N - a) \\ &= \frac{2^{-\frac{a-b}{2}}}{\Gamma\left(\frac{a-b}{2}\right)} (a - b)^{\frac{a-b}{2}} x^{\frac{a-b}{2}-1} e^{-\frac{a-b}{2}x}.\end{aligned}\tag{6.32}$$

3388 In our case  $a - b = 8 - 5 = 3$ , so we would obtain a p-value of 0.05 at  $x = 2.60$ .

3389 Figure 6.40 contains the distributions of the maxima of  $\chi_k^2(FB)$ ,  $F_k$  and  $D_k^\phi$  and the  
 3390 minima of  $D_k^{1/R}$  for a sample of non-decaying pion tracks (blue) and another sample of  
 3391 reconstructed tracks containing part of the pion and the daughter muon from a decay  
 3392 inside the fiducial volume (red). Notice that, even though the values of  $F_k^{(max)}$  for the  
 3393 decay sample are typically larger than for the non-decaying one, just a small fraction of  
 3394 the events go beyond the aforementioned value of  $F = 2.60$ . Therefore, from a practical  
 3395 point of view, it is not the most efficient variable to use for selecting the decay events.

3396 However, looking at the  $D_k^{1/R \ (min)}$  distribution we can see there is a big difference  
 3397 between non-decaying and decaying events in this variable. One can use a combination

## CHAPTER 6. PARTICLE IDENTIFICATION IN ND-GAR

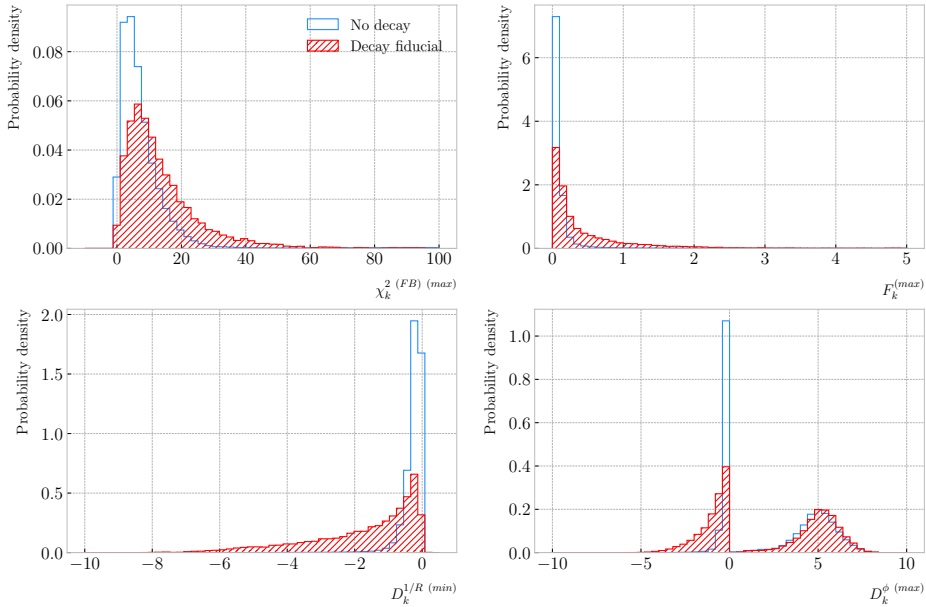


**Figure 6.40:** Distributions of the extreme values of  $\chi_k^2(FB)$  (top left panel),  $F_k$  (top right panel),  $D_k^{1/R}$  (bottom left panel) and  $D_k^\phi$  (bottom right panel) for non-decaying reconstructed pion tracks (blue) and tracks which include the decay inside the fiducial volume (red).

3398 of these four variables to distinguish between the pion decay events (signal) and the  
 3399 non-decaying pions (background).

3400 An approach to this classification could be using a boosted decision tree (BDT). One  
 3401 of the advantages of BDTs is that they are easy to interpret and identify the relative  
 3402 importance of the different input variables. Training a BDT with 400 estimators and a  
 3403 maximum depth of 4 I can obtain an efficient classification without overtraining. Figure  
 3404 6.41 (left panel) shows the distribution of probabilities predicted by the BDT for a test  
 3405 sample. The signal efficiency as a function of background acceptance, the so-called ROC  
 3406 curve, is shown in Fig. 6.41 (right panel). With a relative importance of 0.83, the most  
 3407 important variable turned out to be  $D_k^{1/R}(\min)$ .

3408 One thing we can check is how the resolution to the decay and the signal efficiency in  
 3409 the classification changes with the true decay angle. Using an equal-frequency binning  
 3410 for the decay angles, we can repeat the previous steps for each bin.

3411 Figure 6.42 (left panel) shows the dependence on the decay angle of the decay finding

## 6.5. CHARGED PION DECAY IN FLIGHT

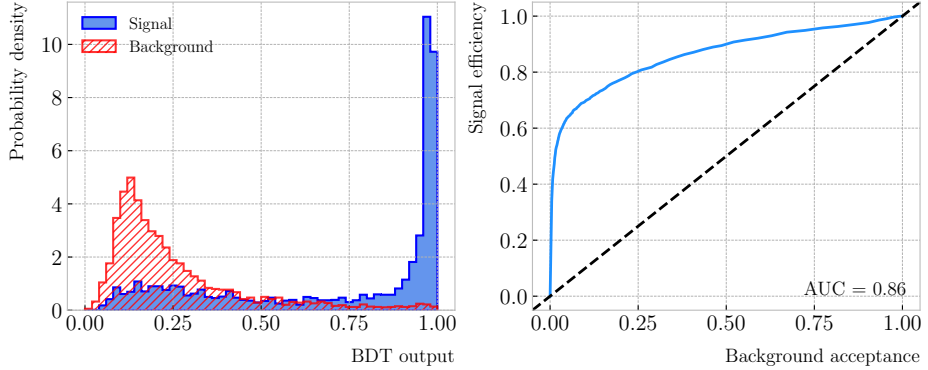


**Figure 6.41:** Left panel: distributions of the predicted probabilities assigned by the BDT classifier to a test sample of decaying pion+muon tracks (blue) and non-decaying pion tracks (red). Left: signal efficiency versus background acceptance (ROC curve) obtained from the BDT for the test sample.

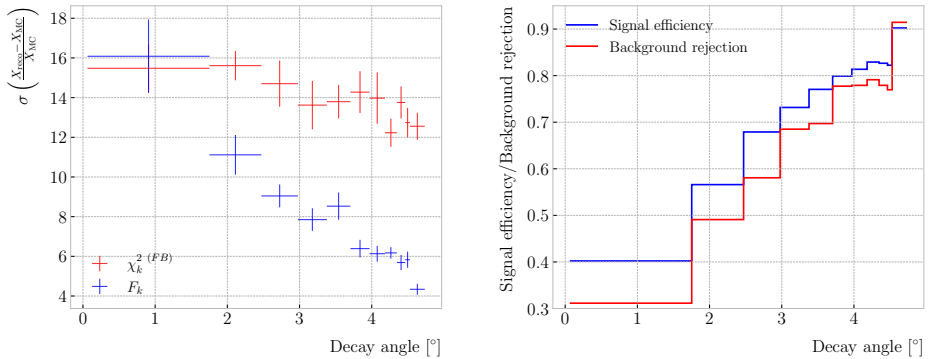


**Figure 6.42:** Left panel: dependence of the decay position finding resolution on the true value of the decay angle for the  $\chi_k^2(FB)$  (red) and  $F_k$  (blue) methods. Right panel: signal efficiency (blue line) and background rejection (red line) from the BDT classifier versus true decay angle.

resolution. We can see that for the  $\chi_k^2(FB)$  maximum location method the resolution consistently lies between 12 to 16%. However, the  $F_k^{(\max)}$  approach gives a significantly better resolution for high angle values, reaching the 4 – 6% range for decay angles  $\geq 4^\circ$ .

For the classification dependence on the angle, I use the same classifier I trained before but evaluating the test sample for each individual angular bin. I compute the signal efficiency in each bin for a fixed value of the background rejection, in this case 90%. Similarly, for the background rejection estimation I use a fixed signal efficiency value of 90%. Figure 6.42 (right panel) represents the change in signal efficiency (blue)



## CHAPTER 6. PARTICLE IDENTIFICATION IN ND-GAr

3420 and background rejection (red) with the value of the true decay angles.

## 3421 6.6 Neutral particle identification

### 3422 6.6.1 ECal clustering

3423 Another important reconstruction item is the clustering algorithm of ECal hits in  
3424 GArSoft. The default module features a NN algorithm that treats all hits in the same  
3425 way, independently of the layer each hit comes from. However, the current ECal design  
3426 of ND-GAr has two very different types of scintillator layers. The inner layers are made  
3427 out of tiles, which provide excellent angular and timing resolutions. On the other hand,  
3428 the outer layers are cross scintillator strips. That way, an algorithm that treats hits  
3429 from both kinds of layers differently may be able to improve the current performance.

3430 Inspired by the reconstruction of T2K's ND280 downstream ECal [183], the idea  
3431 was to put together a clustering module that first builds clusters for the different ECal  
3432 views (tiles, strips segmented in the  $X$  direction and strips segmented in  $Y$  direction),  
3433 and then tries to match them together to form the final clusters.

3434 Working on a module-by-module basis, the algorithm first separates the hits depending  
3435 on the layer type they come from. Then, it performs a NN clustering for the 3 sets of  
3436 hits separately. For the tile hits it clusters together all the hits which are in nearest-  
3437 neighbouring tiles and nearest-neighbouring layers, for strip hits it looks at nearest-  
3438 neighbouring strips and next-to-nearest-neighbouring layers (as the layers with strips  
3439 along the two directions are alternated). For strip clusters an additional cut in the  
3440 direction along the strip length is needed.

3441 After this first clustering I then apply a recursive re-clustering for each collection  
3442 of strip clusters based on a PCA method. In each case, we loop over the clusters with  
3443  $N_{hits} \geq 2$ , computing the centre of mass and three principal components. Propagating  
3444 these axes up to the layers of the rest of the clusters, we check if the propagated point  
3445 and the centre of mass of the second cluster are within next-to-nearest-neighbouring  
3446 strips. An additional cut in the direction along the strip length is also needed. Moreover,

## 6.6. NEUTRAL PARTICLE IDENTIFICATION

**Table 6.5:** Summary of parameters and sampled values used in the optimisation of the clustering algorithm.

Name	Units	Sampled values	Description
PrimMinorCut	strips	2, 3, 4	Distance along strip length in NN clustering
RecMinorCut	strips	3, 5, 8	Distance between propagated point and CM along strip length in re-clustering
RecPerpCut	strips	2, 3, 4	Closest hit pair distance in re-clustering
StripDistCut	strips	3, 5, 8	Distance between CMs in strip cluster merging
StripDirCut	cos	0.5, 0.7, 0.9	Main axes direction cut in strip cluster merging
PointDistCut	tiles	3, 5, 8	Distance between propagated point and CM in strip-tile matching
MergePerpCut	cm	10, 20, 30	Closest hit pair distance in module merging
MergeDirCut	cos	0.5, 0.7, 0.9	Main axes direction cut in module merging

3447 I require that the two closest hits across the two clusters are at most in next-to-nearest-  
3448 neighbouring strips. I merge the clusters if these three conditions are satisfied. The  
3449 re-clustering is repeated until no more cluster pairs pass the cuts.

3450 The clusters in each strip view are combined if their centres of mass are close enough  
3451 and they point in the same direction. An alternative approach for the strip cluster  
3452 merging could be to compute the overlap between the ellipsoids defined by the principal  
3453 axes of the clusters, and then merge the pair if the overlap exceeds some threshold.  
3454 Further study is needed to understand if this change would have an impact in the overall  
3455 clustering performance.

3456 To merge the tile clusters to the combined strip clusters I propagate the principal  
3457 axis of the strip cluster towards the inner layers, up to the centre of mass layer of the  
3458 tile cluster. I merge the clusters if the distance between the propagated point and the  
3459 centre of mass is below a certain cut.

3460 The last step is to check if clusters in neighbouring modules should be merged  
3461 together, both across two barrel modules, across end cap modules and between barrel  
3462 end cap modules. I check the distance between the two closest hits in the pair of clusters  
3463 and merge them if it passes this and an additional direction cut.

## CHAPTER 6. PARTICLE IDENTIFICATION IN ND-GAR

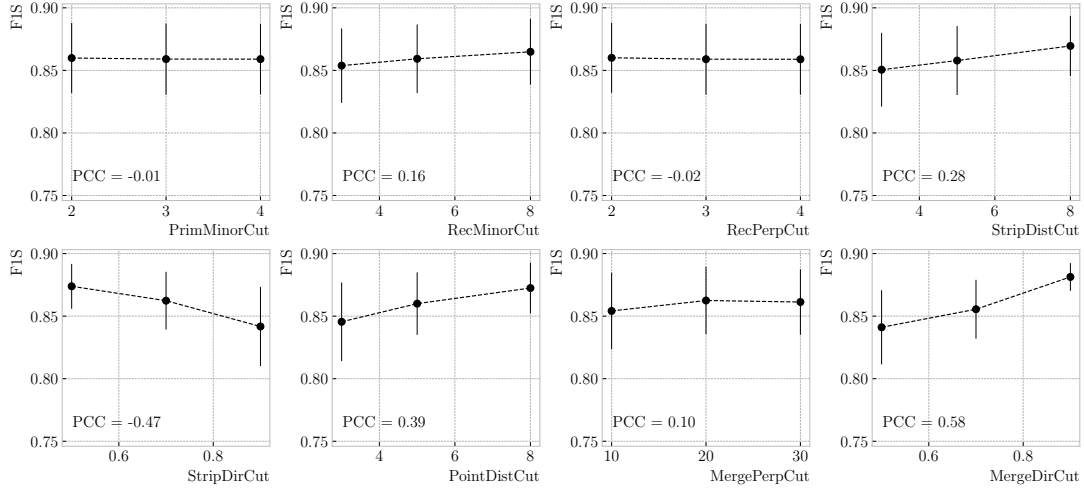


**Figure 6.43:** Mean values of the  $F_1$ -score marginal distributions for the different free parameters of the new clustering algorithm, with the error bars representing one standard deviation around the mean. The  $F_1$ -score values were computed for the 6561 possible parameter configurations using 1000  $\nu_\mu$  CC interaction events.

3464 This algorithm has a total number of eight free parameters that need to be optimised.  
 3465 I used a sample of 1000  $\nu_\mu$  CC interactions in order to obtain the optimal configuration of  
 3466 clustering parameters. This sample was generated up to the default ECal hit clustering  
 3467 level, so then I could run the new clustering algorithm each time with a different  
 3468 configuration of parameters. As the number of parameters is relatively large, I only  
 3469 performed a coarse-grained scan of the parameter space. Sampling each of the eight  
 3470 parameters at three different points each I obtain 6561 different configurations. These  
 3471 parameters, together with the used values, are summarised in Tab. 6.5.

3472 In order to measure the performance of the clustering, I use a binary classification  
 3473 approach. For each formed cluster, I identify the Geant4 Track ID of the matching MC  
 3474 particle and the energy fraction of each hit. Then, I assign to each cluster the Track ID  
 3475 with the highest total energy fraction. For each of the different Track IDs associated to  
 3476 the clusters, I select the cluster with the highest energy (only from the hits with the  
 3477 same Track ID). I identify such a cluster as the main cluster for that Track ID. I count  
 3478 as true positives (TPs) the hits with the correct Track ID in each main cluster. False  
 3479 positives (FPs) are the hits with the incorrect Track ID for the cluster they are in, not

## 6.6. NEUTRAL PARTICLE IDENTIFICATION

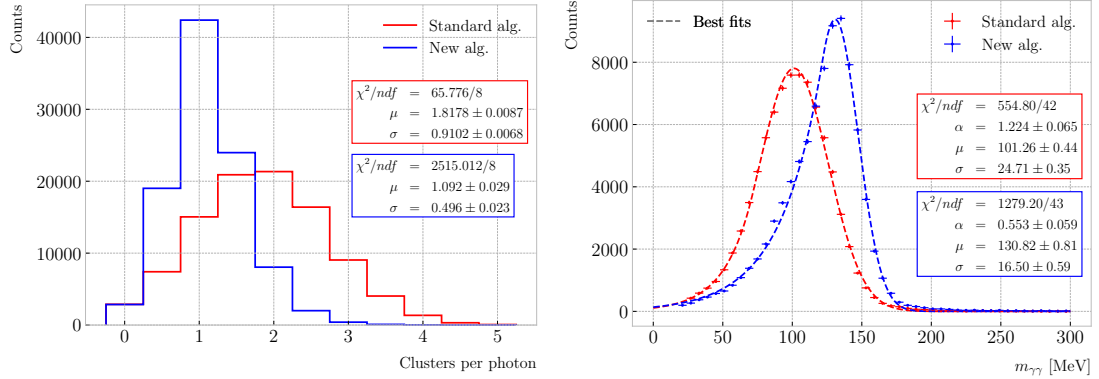


**Figure 6.44:** Left panel: distributions of the number of ECal clusters per photon from  $\pi^0$  decays for the standard (red) and new (blue) clustering algorithms. Right panel: reconstructed invariant mass distributions for photon pairs from single  $\pi^0$  events using the standard (red) and new (blue) ECal clustering algorithms.

only main clusters. The false negatives (FNs) are the hits with the correct Track ID in clusters other than the main.

Figure 6.43 shows the computed  $F_1$ -score values for the different cuts. In each case, the central value represents the mean of the  $F_1$ -score distribution for the specified value of the corresponding variable and the vertical error bar represents one standard deviation around the mean. Also shown are the Pearson correlation coefficients of these central values. We can see that five of the variables have a sizeable effect on the  $F_1$ -score, with an absolute difference between the last and first values as big as 4%.

The working configuration is obtained as follows. I first select all configurations with purity  $\geq 90\%$ . Among those, I choose the combinations that yield the maximum  $F_1$ -score. If more than one configuration remains I select the one with the highest sensitivity. Doing so, I end up with a parameter configuration with an efficiency of 88% and a 90% purity. Compared with the default algorithm, which gives an efficiency of 76% and a purity of 91% for the same sample, I have managed to improve the efficiency by a factor of 1.16.

## CHAPTER 6. PARTICLE IDENTIFICATION IN ND-GAR

### 3495 6.6.2 $\pi^0$ reconstruction

3496 One of the potential applications of the new ECal hit clustering is the reconstruction of  
3497 neutral particles, in particular pions. Neutral pions decay promptly after being produced,  
3498 through the  $\pi^0 \rightarrow \gamma\gamma$  channel ( $98.823 \pm 0.034$ )% of the time. The photon pair does  
3499 not leave any traces in the HPgTPC (unless one or both of them converts into an  
3500 electron-positron pair), but each of them will produce an electromagnetic shower in  
3501 the ECal.

3502 To test the potential impact of the new algorithm in  $\pi^0$  reconstruction, I generated  
3503 a MC sample of single, isotropic neutral pions inside the HPgTPC. All pions were  
3504 generated with a momentum  $p = 500$  MeV and their initial positions were uniformly  
3505 sampled inside a  $2 \times 2 \times 2$  m box aligned with the centre of the TPC. I ran both the  
3506 default and the new clustering algorithms, using for the latter the optimised configuration  
3507 discussed above.

3508 The first thing to notice is that the number of clusters produced per photon has  
3509 decreased. Figure 6.44 (left panel) shows these distributions for the default (red) and  
3510 new (blue) algorithms. Using a simple Gaussian fit, we see that the mean number of  
3511 ECal clusters per photon went from  $1.82 \pm 0.01$  to  $1.09 \pm 0.03$ . This effectively means that  
3512 with the new algorithm the ECal activity of one true particle is typically reconstructed  
3513 as a single object. From the reconstruction point of view this can be an advantage. As  
3514 now most of the photon energy ends up in a single ECal cluster, I can simply use cluster  
3515 pairs to identify the  $\pi^0$  decay.

3516 In general, one calculates the invariant mass of the photon pair as:

$$m_{\gamma\gamma} = \sqrt{2E_1E_2(1 - \cos \theta)}, \quad (6.33)$$

3517 where  $E_i$  are the energies of the photons and  $\theta$  the opening angle between them. In this  
3518 case I can use the energies deposited in the ECal and their incident directions. This  
3519 quantity is computed for all possible pairs of clusters, using their position together with  
3520 the true decay point. In a more realistic scenario, e.g.  $\nu_\mu$  CC interaction, one could use

## 6.7. INTEGRATION IN GArSOFT

3521 the position of the reconstructed primary vertex instead. I also tried to use the principal  
3522 direction of the clusters, but that approach gave considerably worse results. For each  
3523 event I only keep the pair with an invariant mass closer to the true  $\pi^0$  mass value.

3524 Figure 6.44 (right panel) shows the invariant mass distributions for the photon pairs  
3525 we get using the default (red) and the new (blue) ECal clustering algorithms. For the fit  
3526 I used a modified version of the Crystal Ball function [184], obtained by taking the limit  
3527 where the parameter controlling the power-law tail goes to infinity:

$$f(x; N, \mu, \sigma, \alpha) = N \cdot \begin{cases} e^{\frac{\alpha(2x-2\mu+\alpha\sigma)}{2\sigma}}; & x \leq \mu - \alpha\sigma, \\ e^{-\frac{(x-\mu)^2}{2\sigma^2}}; & x > \mu - \alpha\sigma. \end{cases} \quad (6.34)$$

3528 Comparing the fitted mean and standard deviation values for the Gaussian cores, we  
3529 see that the distribution for the new algorithm is a 67% narrower and also peaks much  
3530 closer to the true  $m_{\pi^0}$  value, going from  $101.3 \pm 0.4$  MeV to  $130.8 \pm 0.6$  MeV.

## 3531 6.7 Integration in GArSoft

3532 All the additions and improvements to the reconstruction discussed in this Chapter  
3533 had to be integrated in the GArSoft framework. This is necessary both to allow a  
3534 more streamlined path for development, as this makes testing and adding features  
3535 straightforward, as well as make the changes usable in future productions of simulated  
3536 data. In this section, I outline the current status of the integration in GArSoft of the  
3537 reconstruction work presented above.

3538 The new track-cluster association code has been implemented in GArSoft, under  
3539 the name of `TPCECALAssociation2`, and has now become the new default in the  
3540 reconstruction. The structure of the module is similar to the previous implementation,  
3541 and the data products they output are identical in form. Therefore, any existing code  
3542 using the association objects does not need to be modified.

3543 The computation of the truncated mean  $dE/dx$  of the tracks, the evaluation of  
3544 the muon score for muon and pion separation, and the estimation of the velocity from

## CHAPTER 6. PARTICLE IDENTIFICATION IN ND-GAr

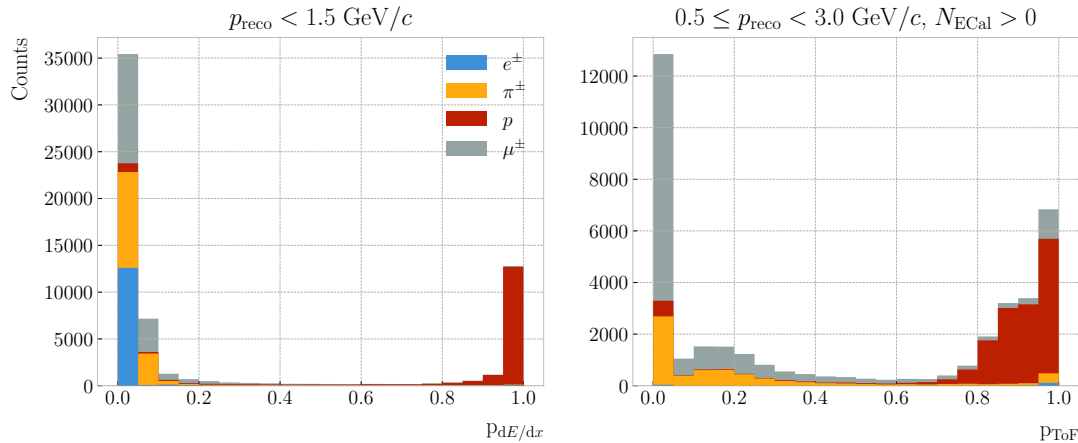


**Figure 6.45:** Distributions of proton  $dE/dx$  (left panel) and ToF (right panel) scores for a sample of 100000 FHC neutrino interactions in the HPgTPC. The distributions are broken down by the true particle type associated to the reconstructed particle.

time-of-flight are all orchestrated by the `CreateRecoParticles` module. Each one of these is implemented as a separate algorithm, which is then called by the parent module. This generates the `gar::rec::RecoParticle` products, a new high-level data object in GArSoft. These combine the information from the HPgTPC, ECal, and  $\mu$ ID to create an object useful for analysers. At the moment, these data products are only generated for charged particles. However, in the future the module can be extended to incorporate other algorithms used for the identification of neutral particles, like neutral pions and neutrons.

Additionally, analogous to the muon score, the `gar::rec::RecoParticle` objects contain two other scores based on the  $\langle dE/dx \rangle$  and ToF estimates which measure the “protoness” of a reconstructed particle. These are obtained in a number of momentum bins, and are a measure of the distance to the point in the corresponding distribution that maximises the  $F_1$ -score for the proton separation. This distance is then transformed applying a sigmoid function, which produces a score in the 0 – 1 range, with coefficients obtained following a procedure similar to the one used to calibrate the response of the muon score. The  $dE/dx$  proton score is defined for all particles with momenta  $p_{\text{reco}} < 1.5 \text{ GeV}/c$ , whereas the ToF proton score is available for the particles with at least one associated hit in the inner ECal and momentum in the range  $0.5 \leq p_{\text{reco}} < 3.0 \text{ GeV}/c$ .

## 6.7. INTEGRATION IN GArSOFT

3563 As an example, Fig. 6.45 shows the distributions of the  $dE/dx$  (left panel) and ToF  
3564 (right panel) proton scores for the reconstructed particles in a 100000 FHC neutrinos  
3565 sample.

3566 The calculation of the track breakpoint variables for pion decay identification is  
3567 currently implemented as an analysis module in GArSoft. It would be interesting to add  
3568 this information to the `gar::rec::RecoParticle` products, possibly calling the code as  
3569 an additional algorithm in the `CreateRecoParticles` module. However, the best way  
3570 to propagate the information to the high-level objects is still unclear.

3571 About the new ECal clustering algorithm, it is still in a development phase, and  
3572 as such it has not replaced the current clustering module. At the moment, its latest  
3573 version is integrated in GArSoft as the `CaloClustering2` module. The algorithm used  
3574 is implemented separately, and then invoked in the main code. The module can be  
3575 run standalone on the outputs of the reconstruction, creating a second instance of the  
3576 `gar::rec::Cluster` collection. In the future it may replace the current algorithm as  
3577 the default in the reconstruction chain. However, more work is needed in order to  
3578 understand its performance in all the different use cases.





## Event selection in ND-GAr

3581        *You have power over your mind, not outside events. Realise this, and you will  
3582            find strength.*

3583

– Marcus Aurelius, *Meditations*

3584        As discussed previously, it is necessary to evaluate the capabilities of ND-GAr at  
3585 identifying different particles. In the context of the LBL analysis, we want ND-GAr to  
3586 provide data samples containing events of specific topologies, like  $\nu_\mu$  CC  $1\pi^\pm$ ,  $\nu_\mu$  CC  
3587  $1p1\pi^\pm$ , etcetera. Thus, developing a strategy for the event selection using the current  
3588 reconstruction is required.

3589        In this Chapter, I present the results of a number of preliminary studies focused on  
3590 the event selection in ND-GAr, particularly the  $\nu_\mu$  CC selection and the pion tagging  
3591 strategies. I also investigate the neutrino energy reconstruction, as well as the systematic  
3592 uncertainties relevant for our detector.

### 3593        7.1 Data sample

3594        For the event selection studies I used a MC sample consisting of  $10^5$  FHC neutrino  
3595 interaction events inside the HPgTPC volume. The version of **GENIE** used was v3\_04\_00,  
3596 with the G18 tune. This is a preliminary version of the re-tune produced from CCQE,  
3597 CC $1\pi$ , CC $2\pi$ , and CC inclusive bubble chamber cross section data [185]. It uses the local  
3598 Fermi gas as a description of the nuclear model. The quasielastic-like events are described  
3599 by the Nieves quasielastic [186] and Valencia 2p2h [187] models. The Berger-Seghal

## CHAPTER 7. EVENT SELECTION IN ND-GAR

3600 model [188, 189] is used for the resonant and coherent pion production. As in all the  
3601 GENIE tunes, the Bodek-Yang model [190] describes the DIS interactions. Finally, the  
3602 FSI are described using the effective intranuclear transport model in INTRANUKE.

3603 For this sample, I used `GArG4` instead of `edep-sim` for the particle propagation.  
3604 Because both `Geant4` wrappers use different configurations for the simulation, the results  
3605 obtained are different. The default `edep-sim` configuration used by the DUNE ND  
3606 is appropriate for ND-LAr, where thresholds for particle production are higher. In  
3607 the case of ND-GAr, these parameters need to be adjusted accordingly. For the time  
3608 being, in these first productions of analysis files, we will use our standalone `Geant4`  
3609 implementation.

3610 The detector simulation and reconstruction used was GArSoft version v02\_21\_00. I  
3611 made use of the standard routines for the readout simulation and the reconstruction,  
3612 which include the additions described in section 6.7. A summary of the GArSoft outputs  
3613 is extracted in the form of a plain `ROOT TTree`. These are then used, together with the  
3614 GENIE output files, to produce the files known within DUNE as common analysis files  
3615 (CAFs). The version of the CAF format used in this analysis is `duneanaobj v3_07_00`.

3616 This sample only includes single interaction events. In the future, we will move  
3617 to simulate full neutrino spills. Also, we will need to include neutrino interactions in  
3618 the other detector volumes (ECal, magnet, . . .), as well as rock muons making it to  
3619 ND-GAr. However, this will require a significant amount of work to go into the so-called  
3620 interaction slicer, the part of the reconstruction in charge of splitting the reconstructed  
3621 events.

3622 Looking forward, these sort of small samples are useful to prepare for launching a  
3623 full production of ND-GAr events. In the original DUNE TDR LBL analysis, the event  
3624 rates are calculated with a  $1.1 \times 10^{21}$  POT/year assumption, which assumes a combined  
3625 uptime and efficiency of the accelerator complex and the LBNF beamline of 57% [59].  
3626 If we have one spill every 1.2 s, that translates into  $7.5 \times 10^{13}$  POT/spill. Therefore,  
3627 assuming that the POT/spill scales linearly with beam power, in Phase II we will have  
3628  $1.3 \times 10^{14}$  POT/spill for the for the 2.1 MW beam. Or equivalently,  $1.9 \times 10^{21}$  POT/year

## 7.2. $\nu_\mu$ CC SELECTION

**Table 7.1:** Estimated event rates in ND-GAr, divided by interaction type and pion multiplicity, for two different values of the POT/year.

Process	Events/ton/year	
	$1.1 \times 10^{21}$ POT/year	$1.9 \times 10^{21}$ POT/year
All $\nu_\mu$ -CC	$1.60 \times 10^6$	$2.83 \times 10^6$
CC $0\pi$	$5.28 \times 10^5$	$9.35 \times 10^5$
CC $1\pi^\pm$	$3.02 \times 10^5$	$5.34 \times 10^5$
CC $1\pi^0$	$1.65 \times 10^5$	$2.92 \times 10^5$
CC $2\pi$	$3.18 \times 10^5$	$5.63 \times 10^5$
CC $3\pi$	$1.36 \times 10^5$	$2.41 \times 10^5$
CC other	$1.52 \times 10^5$	$2.69 \times 10^5$
All $\bar{\nu}_\mu$ -CC	$7.54 \times 10^4$	$1.33 \times 10^5$
All NC	$5.50 \times 10^5$	$9.73 \times 10^5$
All $\nu_e$ -CC	$2.70 \times 10^4$	$4.78 \times 10^4$

3629 using the same efficiency. The event rates per year in ND-GAr computed for these two  
 3630 possible values of the POT/year are shown in Tab. 7.1.

3631 The latest PRISM plan requires  $1.50$  POT · years of data on-axis, followed by  
 3632  $0.25$  POT · years at each off-axis position ( $2, 4, 8, 12, 16, 20, 24$ , and  $28$  m), both for  
 3633 FHC and RHC mode. This implies that a full on-axis ND-GAr production will require  
 3634 a total of  $2.85 \times 10^{21}$  POT for both horn currents. The production of these samples  
 3635 is necessary to understand the impact of ND-GAr on the LBL sensitivities, and the  
 3636 studies presented here should be considered as a first step towards the realisation of  
 3637 such analysis.

## 3638 7.2 $\nu_\mu$ CC selection

3639 In a  $\nu_\mu$  CC inclusive selection, the signal topology we look for is a neutrino-induced  
 3640 muon with or without other final state particles. Here, I also require the neutrino vertex  
 3641 to be located inside the fiducial volume (FV) of ND-GAr.

3642 The FV is defined as a smaller cylinder within the cylindrical volume of the HPgTPC.

## CHAPTER 7. EVENT SELECTION IN ND-GAR

3643 The FV has a radius  $R_{\text{FV}}$  and a half-length  $L_{\text{FV}}$ . For a particle position to lie within  
3644 the FV it must satisfy:

$$\vec{x}_i \in \left\{ \vec{x} \in \mathbb{R}^3 \mid |x_0| \leq L_{\text{FV}} \text{ \& } \sqrt{x_1^2 + x_2^2} \leq R_{\text{FV}} \right\}, \quad (7.1)$$

3645 in the reference frame of the HPgTPC. For convenience, I define:

$$\begin{aligned} \Delta R_{\text{FV}} &= R_{\text{HPgTPC}} - R_{\text{FV}}, \\ \Delta L_{\text{FV}} &= L_{\text{HPgTPC}} - L_{\text{FV}}, \end{aligned} \quad (7.2)$$

3646 where  $R_{\text{HPgTPC}}$  and  $L_{\text{HPgTPC}}$  refer to the radius and the half-length of the HPgTPC,  
3647 respectively. Figure 7.1 shows the HPgTPC volume with the FV inside of it. In that  
3648 representation, the FV is defined as  $\Delta L_{\text{FV}} = 30.0$  cm and  $\Delta R_{\text{FV}} = 30.0$  cm. Also shown  
3649 is the HPgTPC reference frame, with  $x$  being the drift direction and  $z$  aligned along the  
3650 beam direction.

3651 In some cases, it is interesting to divide the signal events in different categories  
3652 based on their true interaction mode. In this work, I will distinguish between charged-  
3653 current quasi-elastic (CCQE), coherent (CCCOH), resonant (CCRES), and deep-inelastic  
3654 (CCDIS) interactions. I also use a separate category for the interactions not included in  
3655 any of the other categories (CCOther).

3656 Any other events are considered backgrounds. For this selection, I use the following  
3657 categorisation of background events:

- 3658 • Out of FV: if the true neutrino vertex lies outside the defined FV.
- 3659 • NC: if the event is a true neutral-current event.
- 3660 •  $\bar{\nu}_\mu$  CC: if the true neutrino candidate is of muon antineutrino flavour.
- 3661 • Other: if the event is not signal nor falls in any of the other background categories.

3662 The key to the CC selection is the identification of a primary muon candidate.  
3663 Typically, this is the longest track in the event. However, sometimes protons and pions

## 7.2. $\nu_\mu$ CC SELECTION

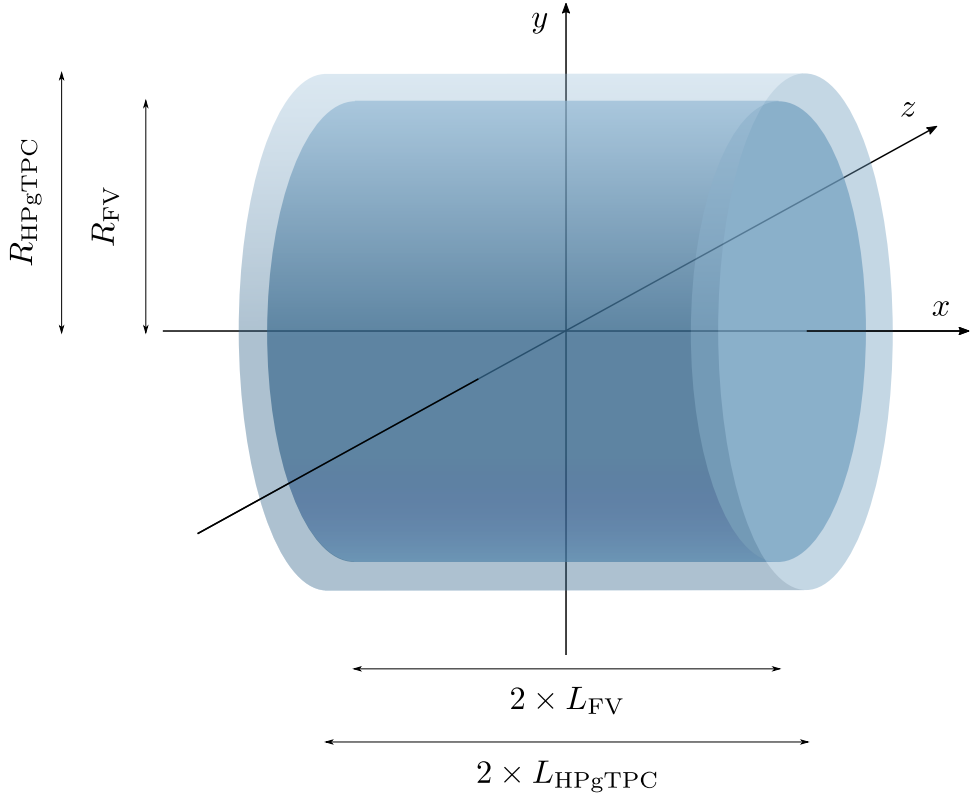


**Figure 7.1:** Schematic diagram of the HPgTPC including the fiducial volume (FV). In this case the FV is given by  $\Delta L_{\text{FV}} = 30.0$  cm and  $\Delta R_{\text{FV}} = 30.0$  cm.

3664 leave tracks longer than that of the muon. This is particularly important in the GAr  
 3665 medium, considerably less dense than the LAr. For this reason, the muon identification  
 3666 in ND-GAr relies heavily on the capabilities of the ECal.

3667 The selection strategy proposed combines the information coming from the three  
 3668 main detection systems of ND-GAr: the HPgTPC charge readout, and the ECal and  
 3669  $\mu$ ID detectors. It consists of five steps:

- 3670 1. Event contains reconstructed particles.
- 3671 2. Select particles with reconstructed negative charge,  $q_{\text{reco}} = -1$ .
- 3672 3. Select particles passing the muon score cut,  $\mu_{\text{score}} \geq \mu_{\text{score}}^{\text{cut}}$ .
- 3673 4. Keep reconstructed particle with the highest momentum,  $\max [p_{\text{reco}}]$ .
- 3674 5. Check that the remaining particle starts within the FV.

## CHAPTER 7. EVENT SELECTION IN ND-GAR

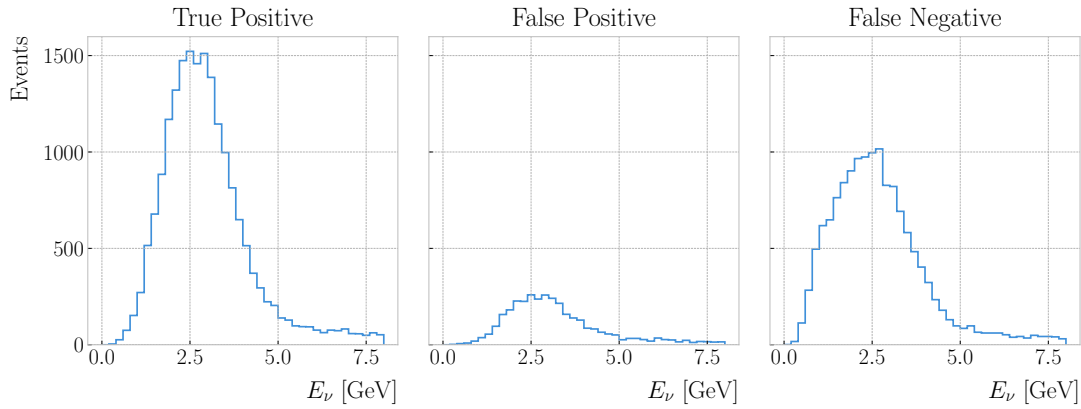


**Figure 7.2:** True positive (left panel), false positive (middle panel), and false negative (right panel) true neutrino energy distributions for the  $\nu_\mu$  CC selection given by a muon score cut of  $\mu_{\text{score}}^{\text{cut}} = 0.75$ , and a FV defined as  $\Delta L_{\text{FV}} = 30.0$  cm and  $\Delta R_{\text{FV}} = 30.0$  cm.

3675 All the events passing these cuts are classified as signal, and the selected particle is  
 3676 regarded as the primary muon candidate.

3677 **7.2.1 Selection optimisation**

3678 I performed an optimisation of this selection, comparing the performance of a number of  
 3679 configurations. For the muon selection, I varied the value of  $\mu_{\text{score}}^{\text{cut}}$  from 0.05 to 0.95,  
 3680 using a step size of 0.05. Additionally, to optimise the FV, I systematically explored a  
 3681 number of different parameter configurations, moving within the 10.0 – 70.0 cm range for  
 3682  $\Delta L_{\text{FV}}$  and 25.0 – 75.0 cm for  $\Delta R_{\text{FV}}$ , in increments of 10.0 cm and 5.0 cm respectively.

3683 For each parameter configuration, I extract three different true neutrino energy  
 3684 distributions. These are built combining the results of the selection described previously,  
 3685 which we can refer to as the “reco” selection, and a “true” selection. The later identifies  
 3686 the true  $\nu_\mu$  CC events using the GENIE event records, and checks that the true neutrino  
 3687 vertices are contained in the FV.

3688 The first distribution consists of the events passing both selections, i.e., these are  
 3689 the true  $\nu_\mu$  CC events which pass the “reco” selection. The second distribution contains  
 3690 the events passing the “reco” selection but failing the “true” selection. These are  
 3691 the background events that the selection misidentifies. Finally, the third distribution

## 7.2. $\nu_\mu$ CC SELECTION

3692 corresponds to the events picked by the “true” selection but not by the “reco” one. In  
 3693 other words, these are the true  $\nu_\mu$  CC events that our selection misses. In analogy to  
 3694 the machine learning jargon, I refer to these distributions as the true positive (TP),  
 3695 false positive (FP), and false negative (FN) spectra, respectively. Figure 7.2 shows an  
 3696 example of these three distributions for the case  $\mu_{\text{score}}^{\text{cut}} = 0.75$ ,  $\Delta L_{\text{FV}} = 30.0$  cm, and  
 3697  $\Delta R_{\text{FV}} = 30.0$  cm.

3698 By making different combinations of these distributions one can compute a series of  
 3699 performance metrics. Using the full information from the spectra allows to obtain the  
 3700 scores as a function of the true neutrino energy, whereas the totals can be obtained by  
 3701 integrating the histograms. This way, the efficiency of the selection is given by:

$$\begin{aligned} \text{Efficiency} &= \frac{\text{Selected true } \nu_\mu \text{ CC events}}{\text{Total true } \nu_\mu \text{ CC events}} \\ &= \frac{\text{TP}}{\text{TP} + \text{FN}}, \end{aligned} \quad (7.3)$$

3702 while the purity can be written as:

$$\begin{aligned} \text{Purity} &= \frac{\text{Selected true } \nu_\mu \text{ CC events}}{\text{Total selected events}} \\ &= \frac{\text{TP}}{\text{TP} + \text{FP}}. \end{aligned} \quad (7.4)$$

3703 Another scoring metric typically used when quantifying the performance of a selection  
 3704 is the significance. It is defined as:

$$\text{Significance} = \frac{S}{\sqrt{S+B}} = \frac{\text{TP}}{\sqrt{\text{TP}+\text{FP}}}. \quad (7.5)$$

3705 The significance measures the relative size of the true signal within the selection,  $S = \text{TP}$   
 3706 with respect to one standard deviation of the counting experiment. Assuming Poisson  
 3707 statistics, the variance is equal to the number of observations, and therefore the standard  
 3708 deviation equals to  $\sqrt{N} = \sqrt{S+B} = \sqrt{\text{TP}+\text{FP}}$ . I use this metric to

3709 Figure 7.3 shows the change in efficiency (blue) and purity (red) of the  $\nu_\mu$  CC  
 3710 selection as a function of the different cuts. From left to right, I vary  $\mu_{\text{score}}^{\text{cut}}$ ,  $\Delta L_{\text{FV}}$ ,

## CHAPTER 7. EVENT SELECTION IN ND-GAR

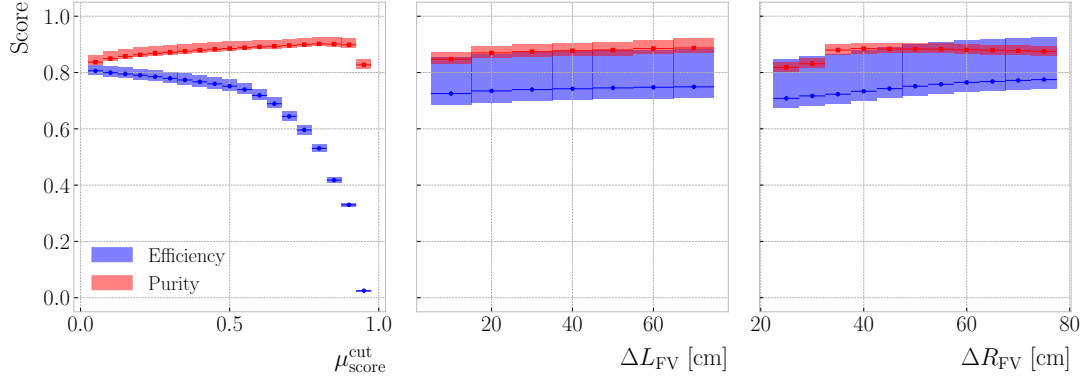


**Figure 7.3:** Efficiency (blue) and purity (red) for the  $\nu_\mu$  CC selection as a function of the muon score cut (left panel), FV half-length cut (middle panel), and radial cut (right panel). The height of the boxes represents the IQR of the conditional distributions, whereas the horizontal line corresponds to the median.

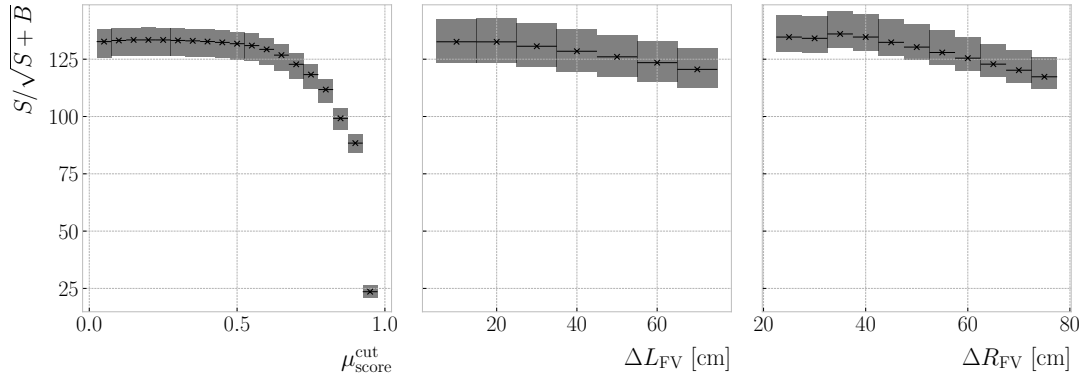


**Figure 7.4:** Significance for the  $\nu_\mu$  CC selection as a function of the muon score cut (left panel), FV half-length cut (middle panel), and radial cut (right panel). The height of the boxes represents the IQR of the conditional distributions, whereas the horizontal line corresponds to the median.

and  $\Delta R_{\text{FV}}$ . For each value of the cuts, I compute the median and IQR (represented by the horizontal lines and the heights of the boxes, respectively) of the corresponding conditional distributions of efficiency and purity. This representation is useful to get an idea of the general trend the scores follow with the cuts, as well as the spread. It is clear that the muon score cut has the biggest impact on the efficiency, which ranges between 0.05 to 0.80, whereas the purity remains stable with values around 0.85.

A similar depiction of the significance can be found in Fig. 7.4. In this case, one can see that the  $S/\sqrt{S+B}$  decreases as the cuts grow tighter. However, there are hints of

## 7.2. $\nu_\mu$ CC SELECTION

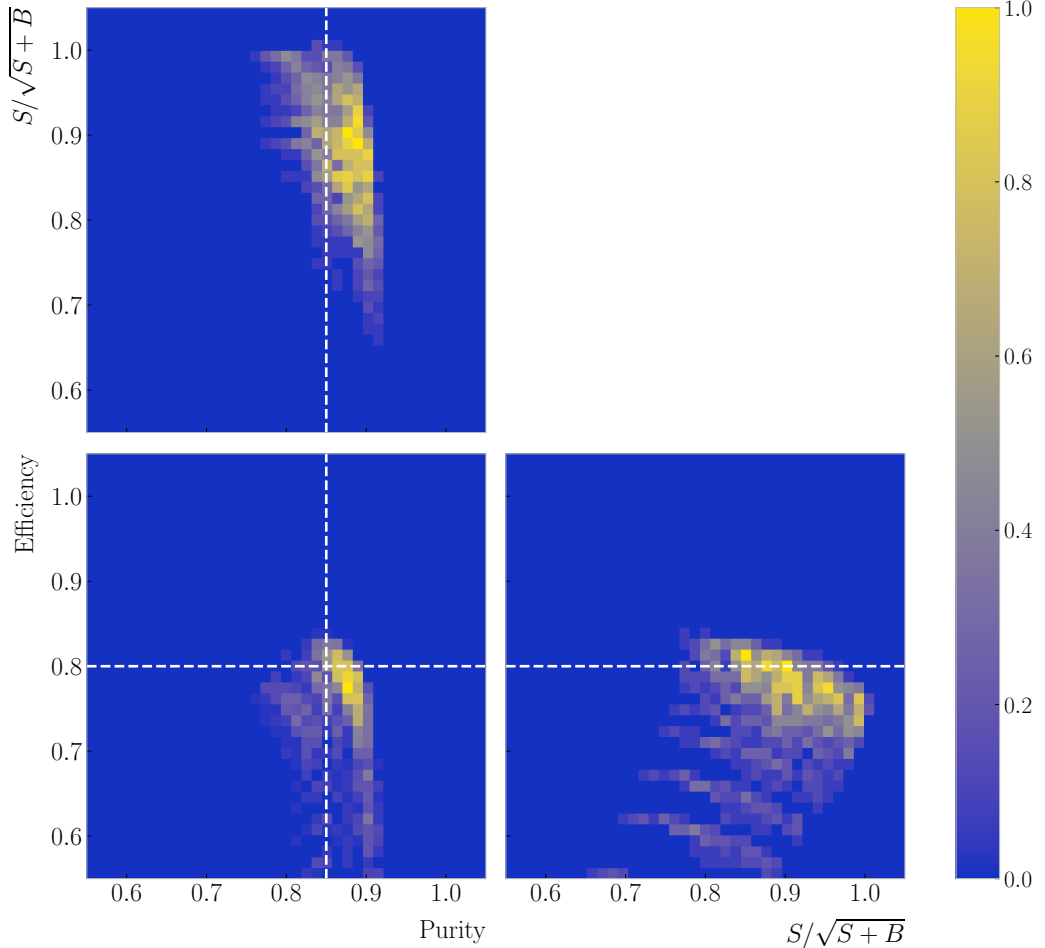


**Figure 7.5:** Normalised 2D distributions of efficiency, purity and significance for the  $\nu_\mu$  CC selection. The  $S/\sqrt{S+B}$  is normalised to the highest value achieved. The vertical dashed line indicates a purity value of 0.85, whereas the horizontal one corresponds to an efficiency of 0.80.

3719 local maxima at intermediate values.

3720 Selecting the cut configuration with the highest significance,  $147 \pm 11$  for the parameter  
 3721 values explored here, results in an efficiency and purity of  $0.754 \pm 0.006$  and  $0.833 \pm 0.007$ ,  
 3722 respectively. Figure 7.5 shows the 2D distributions resulting when combining pairs of  
 3723 efficiency, purity and significance, obtained for the cut configurations explored. The  
 3724 significance is normalised to the highest value obtained in the parameter scan. Looking  
 3725 at this, it is clear that a selection with highest efficiency and purity can be achieved,  
 3726 maintaining a similar significance level.

## CHAPTER 7. EVENT SELECTION IN ND-GAR

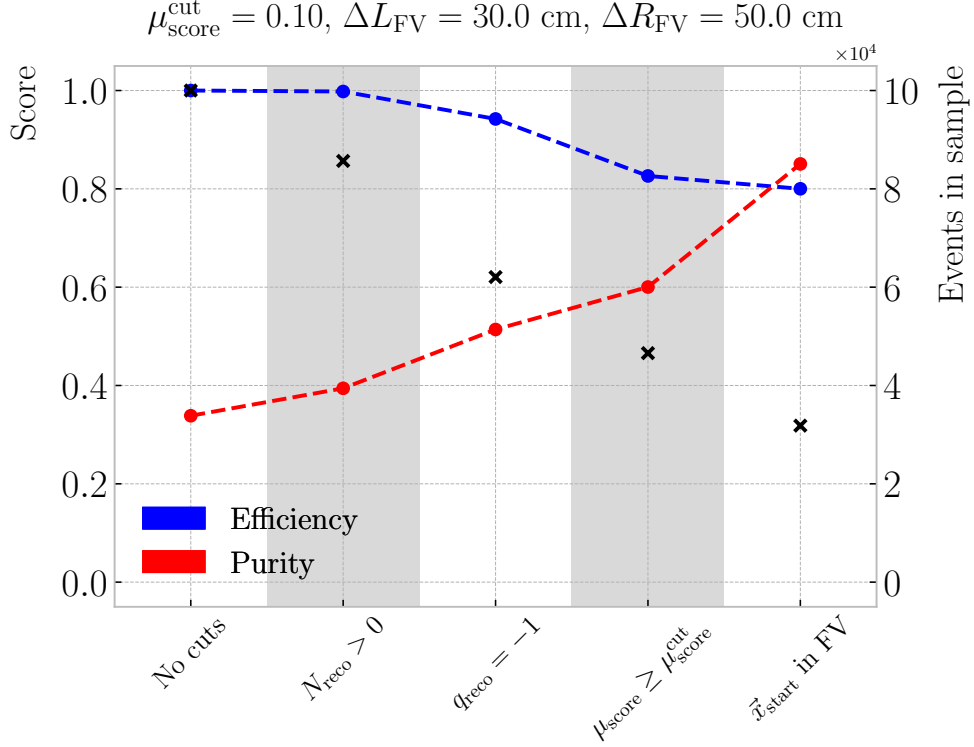


**Figure 7.6:** Cumulative efficiency (blue) and purity (red) of the  $\nu_\mu$  CC selection. The secondary axis indicates the number of events in the sample after each cut (black crosses).

**Table 7.2:** Step-by-step  $\nu_\mu$  CC selection cuts and cumulative passing rates. Relative passing rates are indicated in parentheses.

Cut #	Selection cut	Events	Passing rates
0	Total number of events (No cuts)	100000	100.00% (100.00%)
1	At least one reconstructed particle	85680	85.68% (85.68%)
2	Negatively charged particles only	62054	62.05% (72.43%)
3	$\mu_{\text{score}} \geq \mu_{\text{score}}^{\text{cut}}$	46585	46.59% (75.07%)
4	Candidate $\vec{x}_{\text{start}}$ in FV	31834	31.83% (68.34%)

3727 Therefore, to get a more refined selection, I first select the configurations with a  
 3728 purity and an efficiency higher than 0.85 and 0.80, respectively. After that, I select the  
 3729 tuple of cuts yielding the highest significance. The resulting value for the muon score  
 3730 cut is  $\mu_{\text{score}}^{\text{cut}} = 0.10$ , and the FV is given by  $\Delta L_{\text{FV}} = 30.0 \text{ cm}$  and  $\Delta R_{\text{FV}} = 50.0 \text{ cm}$ .  
 3731 With these, one obtains a total efficiency of  $0.800 \pm 0.007$  and purity of  $0.851 \pm 0.008$ ,

## 7.2. $\nu_\mu$ CC SELECTION

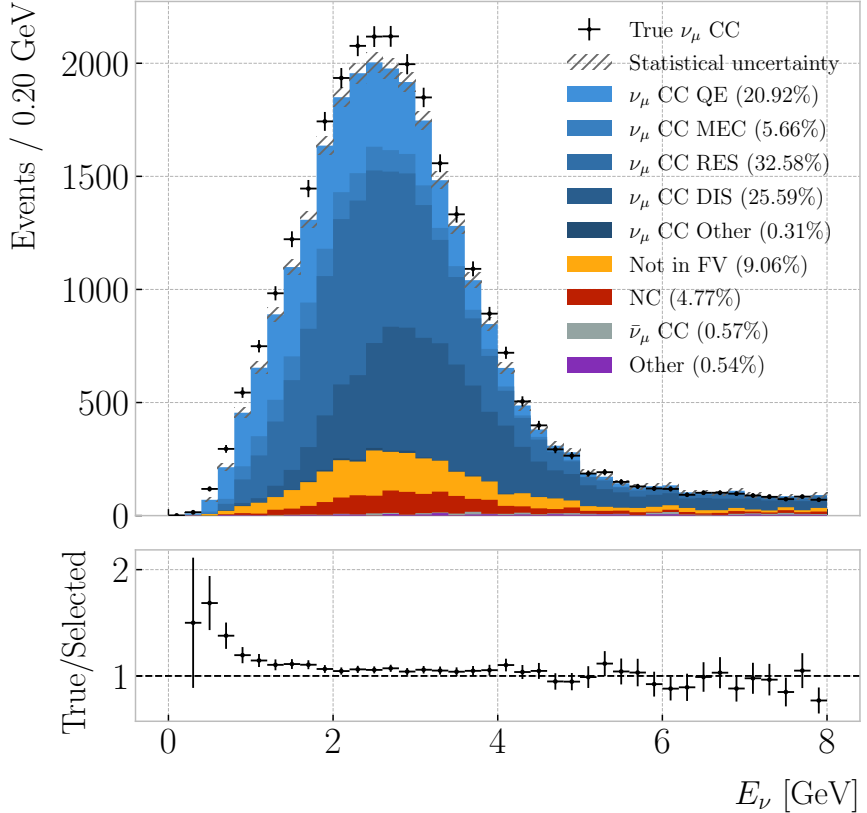


**Figure 7.7:** True neutrino energy spectra for the  $\nu_\mu$  CC selection. The selected events correspond to the coloured stacked histogram, broken down by signal and background subcategories. The statistical uncertainty is drawn in hatched gray. The true distribution is also shown with the black data points. The bottom panel shows the ratio between the number of true and selected  $\nu_\mu$  CC events per bin.

3732 with a significance of  $138 \pm 11$ . Hereafter, I use this optimised selection cuts, unless  
 3733 specified otherwise.

3734 A summary of the selection can be found in Tab. 7.2. It shows the number of  
 3735 events in the selected sample after each selection cut, as well as the absolute and relative  
 3736 passing rates. Figure 7.6 shows the overall efficiencies (blue) and purities (red) after  
 3737 each cut in the event selection is applied. As expected, the efficiency drops while the  
 3738 purity increases with the successive cuts.

3739 Notice how, out of the cuts prior to the FV constraint, the sign selection produces  
 3740 the highest increase in purity. This is one of the advantages of having a magnetised  
 3741 TPC, and can also be used for a  $\bar{\nu}_\mu$  CC selection when running in RHC mode.

## CHAPTER 7. EVENT SELECTION IN ND-GAR

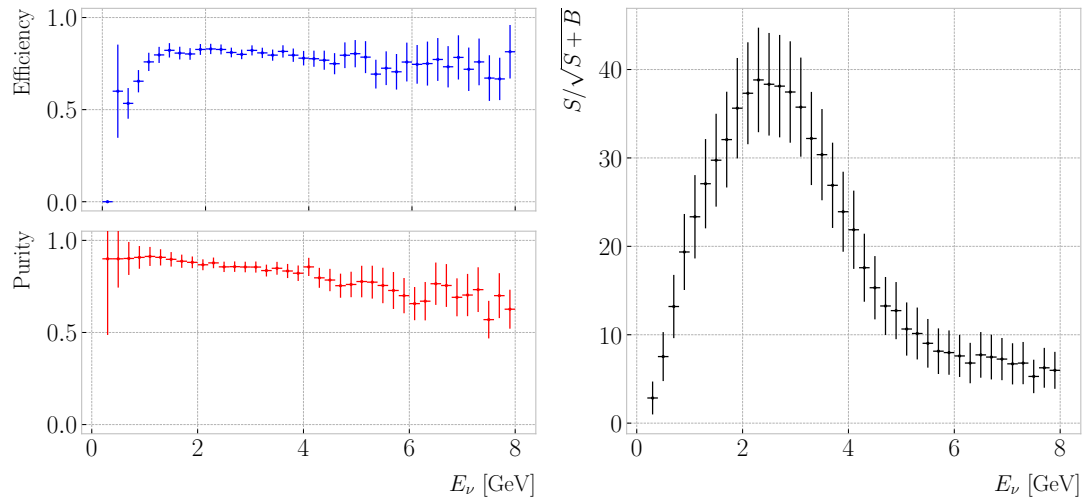


**Figure 7.8:** Left panel: efficiency (top panel) and purity (bottom panel) for the  $\nu_\mu$  CC selection as a function of the true neutrino energy. Right panel: significance for the  $\nu_\mu$  CC selection as a function of the true neutrino energy

### 3742 7.2.2 Selection performance

3743 Using the stored spectra discussed above, the true neutrino energy distribution for the  
 3744 selected events can be recovered doing TP + FP. Similarly, the combination TP + FN  
 3745 gives the true spectrum. Figure 7.7 shows the true (black data points) and selected  
 3746 (coloured stacked histogram)  $E_\nu$  distributions for the optimised  $\nu_\mu$  CC selection. The  
 3747 colours in the selected spectrum indicate the different signal categories and backgrounds,  
 3748 with the overall statistical uncertainty represented by the gray hatched mess. The ratio  
 3749 between the true and selected events is also shown. One can see that it sits around 1 for  
 3750 most of the energy range. However, for energies  $\leq 1$  GeV there is a significant deficit of  
 3751 selected events.

3752 These spectra also allow to compute the efficiency and purity of the selection as  
 3753 a function of the true neutrino energy, as shown in Fig. 7.8 (left panel). As it could  
 3754 be expected from the previous ratio plot, the efficiency is low at low neutrino energies.  
 3755 Nonetheless, it raises quickly with the energy, until it stabilises around a value of 0.80.  
 3756 Looking at the purity, one may notice that, although it starts at around 0.90, there is a  
 3757 significant decrease towards the high end of the spectrum. Figure 7.8 (right panel) also

## 7.2. $\nu_\mu$ CC SELECTION

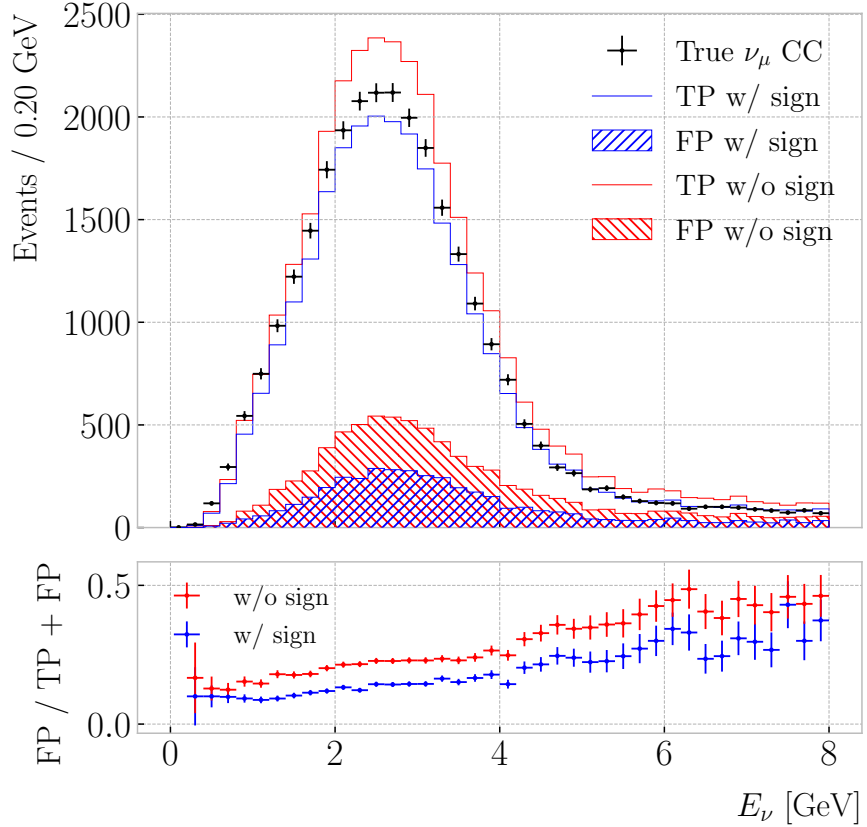


**Figure 7.9:** True neutrino energy spectra for the  $\nu_\mu$  CC selection with (blue) and without (red) sign selection. The selected events are broken down by true positives (signal) and false positives (background). The true distribution is also shown (black data points). The bottom panel shows the ratios between the number of false positives and total selected events per bin.

3758 shows the significance as a function of the energy. In this case, the highest  $S/\sqrt{S+B}$  is  
 3759 achieved around the energies where the spectrum peaks.

3760 A variation of the  $\nu_\mu$  CC selection one can try is to apply it without the reconstructed  
 3761 charge cut. Figure 7.9 (top panel) shows the  $E_\nu$  distributions corresponding to the  
 3762 selection with (blue stacked histogram) and without (red stacked histogram) the sign  
 3763 selection. In the former case, the out of FV contamination amounts to 9.06% of the  
 3764 total, while the NC contamination results 4.77% and the wrong-sign contamination  
 3765 0.57%. For the later, these backgrounds account for the 10.01%, 10.82%, and 2.18%  
 3766 of the selected events, respectively. As expected, removing the positive particles does  
 3767 not change the FV-related effects noticeably. However, the sign selection proves its

## CHAPTER 7. EVENT SELECTION IN ND-GAR

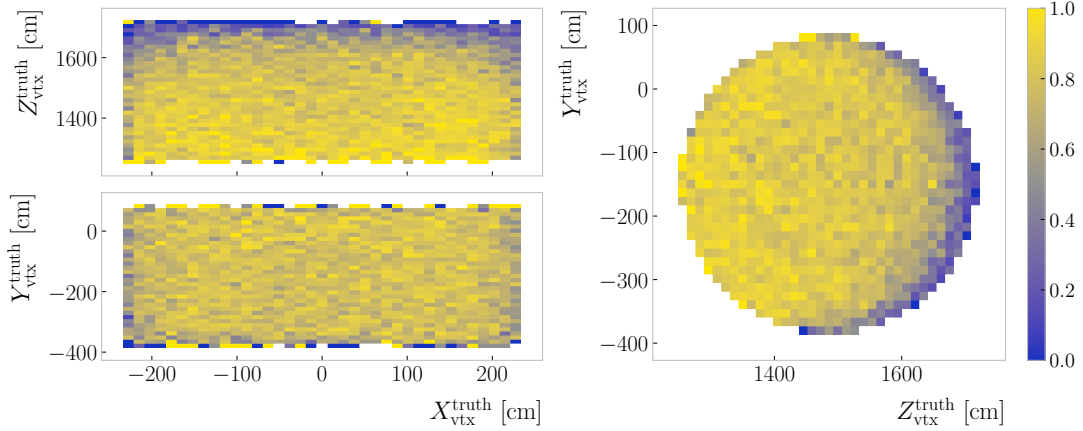


**Figure 7.10:** Efficiency 2D distributions for the  $\nu_\mu$  CC selection given the true position of the interaction vertex.

3768 worth in the rejection of  $\bar{\nu}_\mu$  CC events, which drop almost by one order of magnitude.

3769 Additionally, the charge selection cuts the NC events in half, as it reduces the chances

3770 of misidentifying a positively charged hadron for a muon.

3771 As an additional check, I explored how the performance of the  $\nu_\mu$  CC selection  
 3772 depends on the position of the neutrino interaction within the HPgTPC. Maps of the  
 3773 selection efficiency for the  $X, Z$  (top left panel),  $X, Y$  (bottom left panel), and  $Z, Y$   
 3774 (right panel) true vertex position pairs are given in Fig. 7.10. It can be seen that the  
 3775 efficiency remains stable along the drift direction, only slightly degrading close to the  
 3776 edges of the FV. Regarding the radial direction, it is clear that an important number of  
 3777 events with high  $Z_{\text{vtx}}^{\text{truth}}$  are not being selected. Intuitively, the muons arising from these  
 3778 interactions will leave short tracks. As their directions are typically aligned with the  
 3779 beam direction, they enter the ECal shortly after production. This is likely to affect  
 3780 the tracking, and therefore their identification. As a result, the regions with the lowest  
 3781 efficiency are the downstream corners of the HPgTPC, i.e. the areas with high  $|X_{\text{vtx}}^{\text{truth}}|$   
 3782 and  $Z_{\text{vtx}}^{\text{truth}}$ .

### 3783 7.2.3 Primary muon kinematics

3784 This  $\nu_\mu$  CC selection relies on the identification of the a primary muon, meaning that  
 3785 for each selected event a particle is picked out as the muon candidate. It is because of

## 7.2. $\nu_\mu$ CC SELECTION

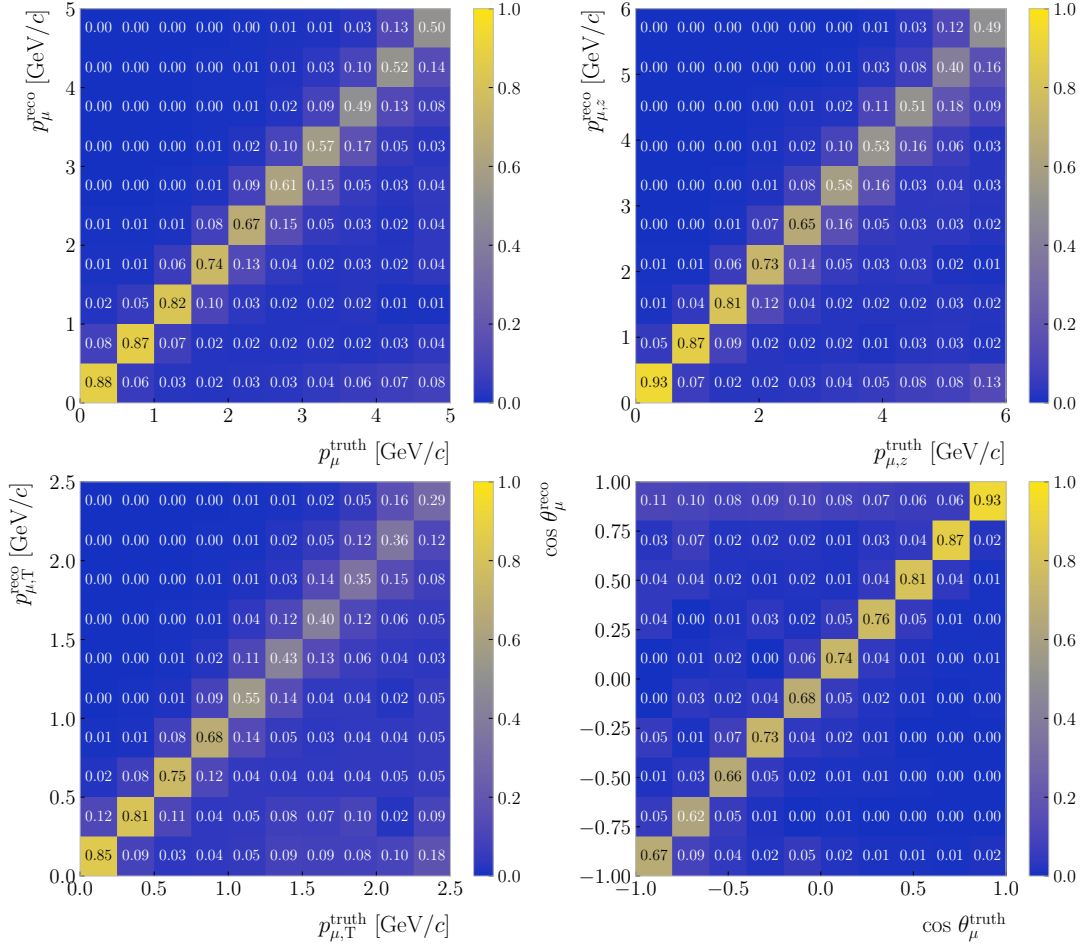


**Figure 7.11:** Distributions for the reconstructed versus truth generated primary muon momentum (top left panel), longitudinal momentum (top right panel), transverse momentum (bottom left panel), and beam angle (bottom right panel). The reconstructed values correspond to the selected primary muon candidate, whereas the truth values come from the true primary muon in the event.

3786 this that one can study the kinematics of these selected primary muons.

3787 Figure 7.11 shows a comparison between some of the reconstructed and truth primary  
 3788 muon kinematic variables. From top to bottom, left to right, we have muon momentum,  
 3789 longitudinal momentum, transverse momentum and beam angle. The histograms are  
 3790 column-normalised, and so the diagonal entries give an idea of the resolution for the  
 3791 different variables. The match between truth and reconstructed values can only be done  
 3792 for the selected true  $\nu_\mu$  CC events, as the others do not have a primary muon. However,  
 3793 for this comparison I do not require the events to start inside the FV.

## CHAPTER 7. EVENT SELECTION IN ND-GAR

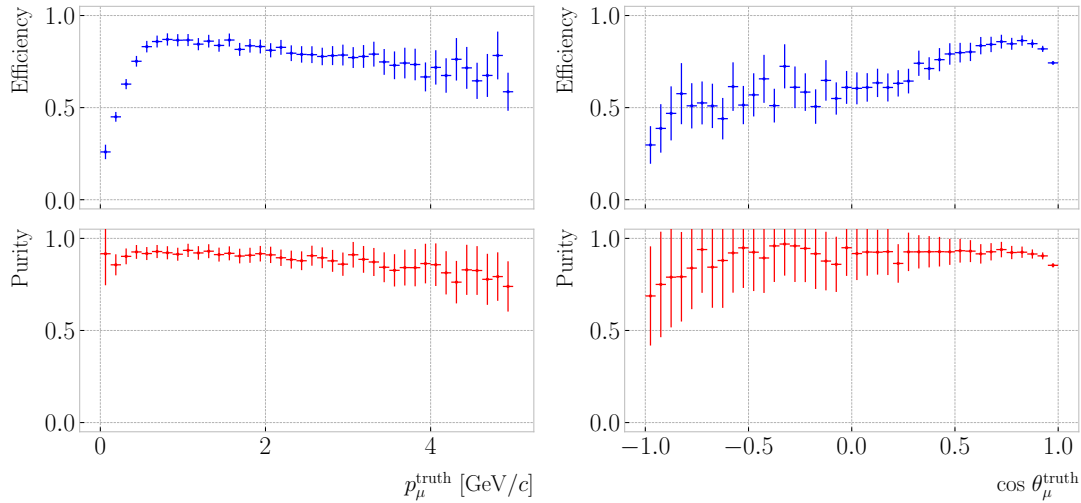


**Figure 7.12:** Efficiency (blue) and purity (red) of the  $\nu_\mu$  CC selection as a function of the primary muon true momentum (left panel) and beam angle (right panel).

3794 Notice that, for the reconstructed values, the variables do not necessarily come  
 3795 from a reconstructed particle that matches the true primary muon. In other words,  
 3796 sometimes, even though the event was correctly identified, the primary muon may have  
 3797 been confused with another particle. That means that in these distributions include  
 3798 both reconstruction and selection deficiencies.

3799 I also studied the performance of the  $\nu_\mu$  CC selection as a function of the kinematic  
 3800 variables of the primary muon. As before, these metrics are only possible to compute for  
 3801 true  $\nu_\mu$  CC events. The efficiency (top panels) and purity (bottom panels) as a function  
 3802 of the truth muon momentum (left) and beam angle (right) are shown in Fig. 7.12. One  
 3803 can see that there are some similarities in the behaviour of both metrics between the  
 3804 true neutrino energy and the muon momentum cases. This is to be expected, as these  
 3805 two variables are highly correlated. For the efficiency, there is a rapid increase at low  
 3806 momentum values until it peaks at around 1 GeV/c, after which it starts decreasing  
 3807 slowly. The purity remains relatively constant, with a slight drop towards high  $p_\mu^{\text{truth}}$   
 3808 values. In the case of the muon angle, the decrease in efficiency at high  $\theta_\mu^{\text{truth}}$  is more  
 3809 noticeable. However, note that the number of events with backward-going muons is  
 3810 much smaller than those aimed towards the forward direction, as can be seen from the

## 7.2. $\nu_\mu$ CC SELECTION

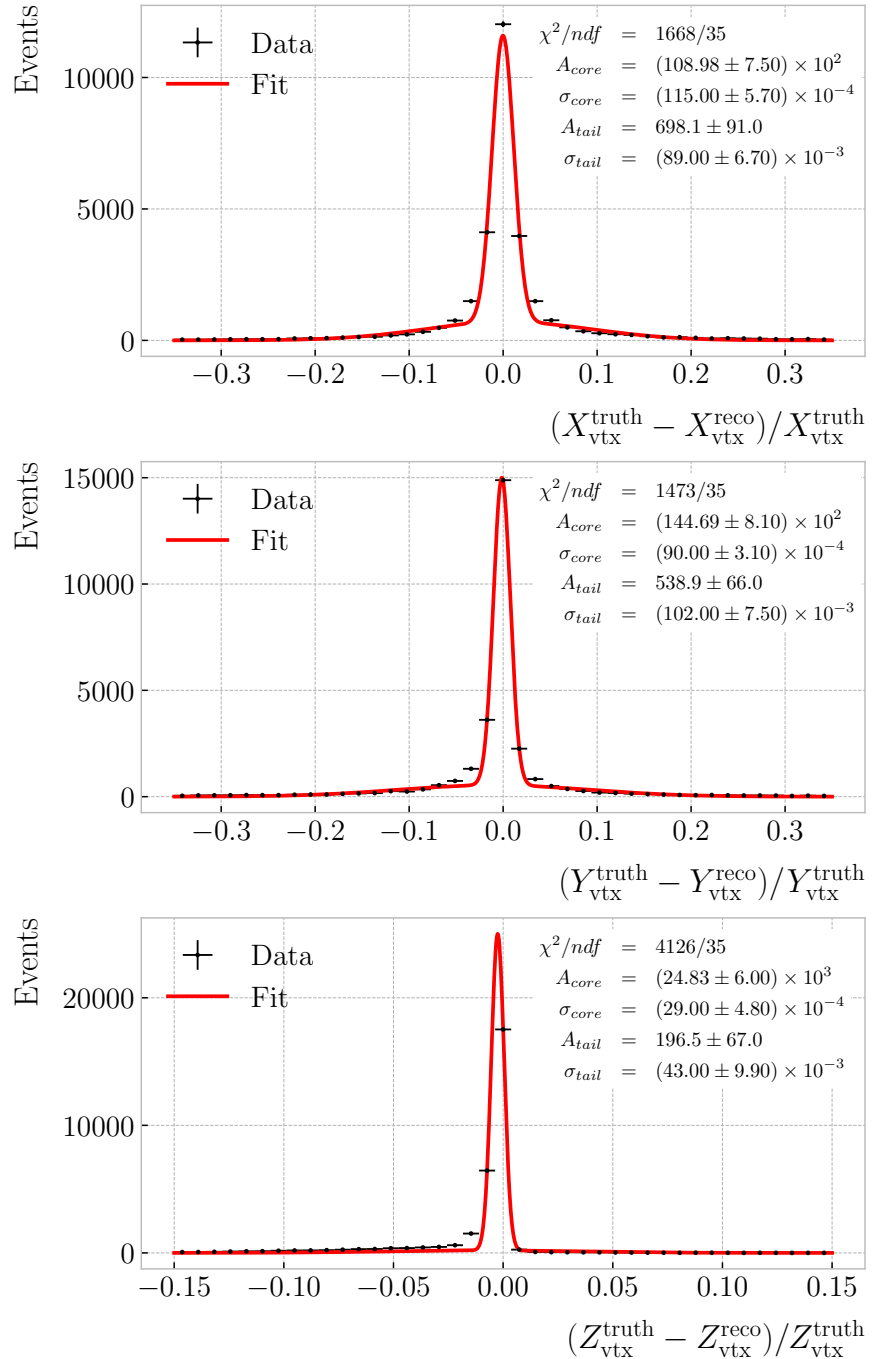


**Figure 7.13:** Fractional residual distributions for the position of the primary vertex in the  $\nu_\mu$  CC selection. The best fits to a double Gaussian function are also shown (red lines).

## CHAPTER 7. EVENT SELECTION IN ND-GAR

3811 size of the vertical error bars. There is also a decline in the purity with the beam angle,  
3812 but this effect is much smaller.

3813 A byproduct of selecting the primary lepton in the interaction is the position  
3814 of the reconstructed neutrino vertex candidate. Checking how the position of the  
3815 selected reconstructed primary vertex and the true vertex position compare is needed to  
3816 understand the validity of our method. Figure 7.13 shows the distributions of fractional  
3817 residuals between the truth and reconstructed vertex positions in the  $X$  (top panel),  
3818  $Y$  (middle panel), and  $Z$  (bottom panel) directions. Performing a double Gaussian fit  
3819 to the distributions (red lines), I estimate the reconstructed vertex resolution achieved  
3820 with this method to be  $1.62 \pm 0.08\%$ ,  $1.23 \pm 0.05\%$ , and  $0.32 \pm 0.05\%$  for the  $X$ ,  $Y$ ,  
3821 and  $Z$  directions, respectively. As expected, the resolution along the drift direction.  
3822 However, the significant difference in resolution between the two transverse directions is  
3823 worth noting. Not only the resolution is better for the  $Z$  direction, but the layout of the  
3824 residual distribution is highly asymmetrical. This may be related to the variability in  
3825 the selection efficiency along that direction.

### 3826 7.3 Charged pion identification

3827 Now that I have checked the robustness of the proposed  $\nu_\mu$  CC selection, it can be  
3828 used as a starting point for other, more convoluted, selections. One of the priorities  
3829 of ND-GAr, as mentioned previously, is the identification of pions. With its lower  
3830 tracking thresholds, ND-GAr is expected to do better regarding  $\pi^\pm$  identification than  
3831 the traditional LArTPCs, like ND-LAr. Moreover, it can make use of the different  
3832 detector subcomponents to tag the charged pions.

3833 The  $\nu_\mu$  CC selection provides a starting point for the pion identification. The first  
3834 thing one can do is rule out the selected primary muon candidate. Then, by looking at  
3835 the properties of the rest of the reconstructed particles, one can start the counting of  
3836 the charged pions.

3837 The two proton scores, the one based on the  $dE/dx$  in the HPgTPC and the one

### 7.3. CHARGED PION IDENTIFICATION

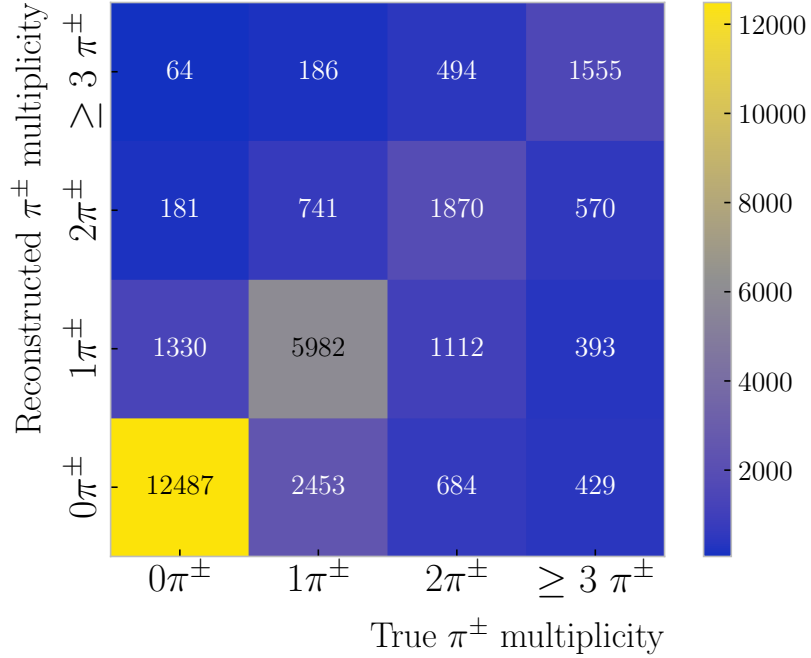


**Figure 7.14:** Distribution of events given their true and reconstructed  $\pi^\pm$  multiplicity, for the selection given by  $p_{dE/dx}^{\text{cut}} = p_{\text{ToF}}^{\text{cut}} = 0.50$ ,  $\Delta_{dE/dx}^{\pi^\pm} = 0.20$ , and  $d_\mu^{\text{cut}} = 50.0$  cm.

3838 obtained from the ToF measurement in the ECal, can be used to separate the protons  
 3839 from the sample of charged pions. By providing appropriate cuts for these, a good  
 3840 separation can be achieved.

3841 Another source of information available is the  $dE/dx$  of the track associated to the  
 3842 reconstructed particle. To select the charged pions, we can require that the measured  
 3843 mean  $dE/dx$  is compatible with the expectation for a true  $\pi^\pm$ , in other words:

$$\left\langle \frac{dE}{dx} \right\rangle_{\pi^\pm} \left( 1 - \Delta_{dE/dx}^{\pi^\pm} \right) \leq \left\langle \frac{dE}{dx} \right\rangle_{\text{meas.}} < \left\langle \frac{dE}{dx} \right\rangle_{\pi^\pm} \left( 1 + \Delta_{dE/dx}^{\pi^\pm} \right), \quad (7.6)$$

3844 where the parameter  $\Delta_{dE/dx}^{\pi^\pm}$  measures the fractional variation one allows around the  
 3845 theoretical expectation. To obtain the expected mean  $dE/dx$  of a charged pion with a  
 3846 given momentum, I use the ALEPH parametrisation with the parameter values obtained  
 3847 previously.

3848 Also, as we are only interested in the primary pions, and because these are by  
 3849 definition close to the interaction vertex, one can apply an additional distance cut. Using

## CHAPTER 7. EVENT SELECTION IN ND-GAR

3850 the start position of the muon candidate, we can restrict the starting point of pions to a  
3851 certain volume around the vertex.

3852 Combining all these ideas, I propose the following procedure to identify the charged  
3853 pions in an event:

- 3854 1. Apply  $\nu_\mu$  CC selection.
- 3855 2. Disregard particle selected as primary muon.
- 3856 3. Remove particles with momentum below threshold.
- 3857 4. Select particles with proton  $dE/dx$  score below threshold.
- 3858 5. Select particles with proton ToF score below threshold.
- 3859 6. Select particles with mean  $dE/dx$  around the expected value for a pion.
- 3860 7. Remove particles with a distance between the start of the track and the primary  
3861 vertex greater than the cut.

3862 The remaining particles after all these cuts are taken to be charged pion candidates.

3863 This counting method depends on four cuts, denoted by  $p_{dE/dx}^{\text{cut}}$ ,  $p_{\text{ToF}}^{\text{cut}}$ ,  $\Delta_{dE/dx}^{\pi^\pm}$ , and  
3864  $d_\mu^{\text{cut}}$  in order of appearance. The momentum threshold is necessary to compare with  
3865 the true multiplicity. For values of the kinetic energy lower than 10 – 20 MeV, we  
3866 do not expect to be able to tag individual pions. Such low energy particles just leave  
3867 small traces in the TPC which, together with the busy environment of the neutrino  
3868 interaction vertex, leaves one with no other option but to only account for their energy  
3869 calorimetrically. As such, the true pion counting also features this momentum threshold.

3870 I performed an optimisation of the charged pion counting by scanning the space of  
3871 possible cut configurations. For the two proton scores, I let them vary between 0.10 to  
3872 0.90, in increments of 0.10. Similarly, the parameter  $\Delta_{dE/dx}^{\pi^\pm}$  takes values in the range  
3873 0.05 – 0.25, with a step size of 0.05. Finally, the distance cut changes in 10 cm steps,  
3874 from 10 to 120 cm.

### 7.3. CHARGED PION IDENTIFICATION

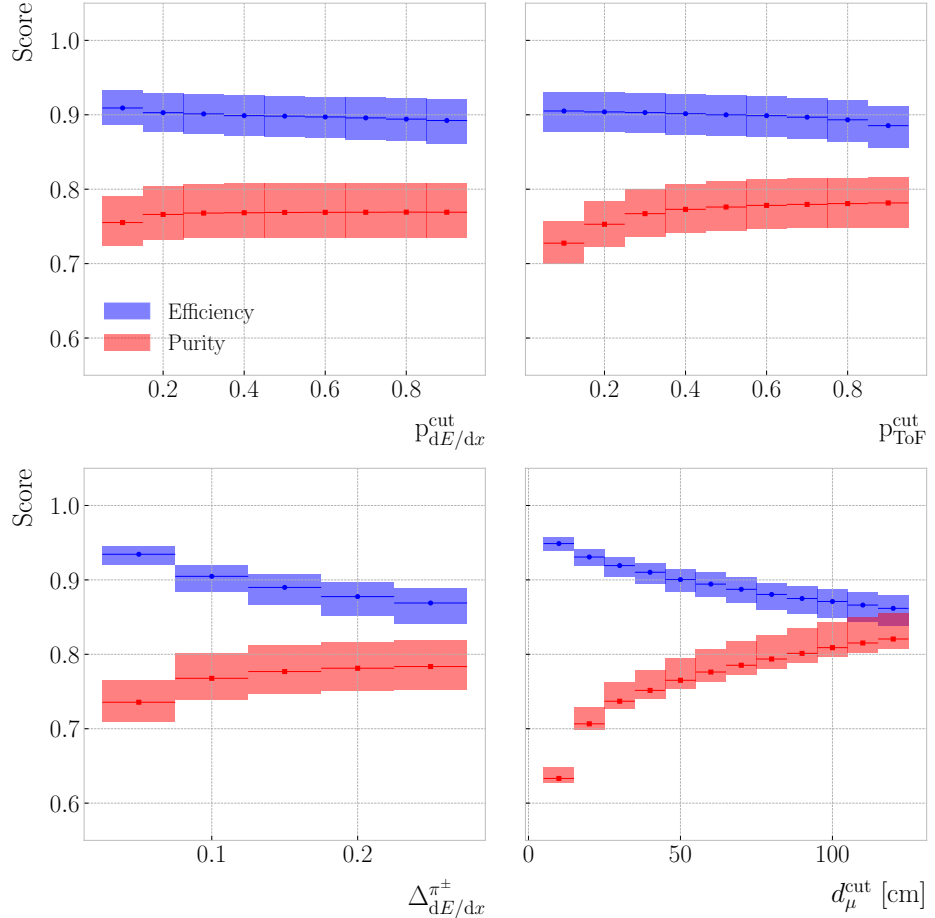


**Figure 7.15:** Efficiency (blue) and purity (red) for the  $\nu_\mu$  CC  $0\pi^\pm$  selection as a function of the proton  $dE/dx$  score cut (top left panel), proton ToF score cut (top right panel), pion  $dE/dx$  cut (bottom left panel), and distance to muon cut (bottom right panel). The height of the boxes represents the IQR of the conditional distributions, whereas the line corresponds to the median.

3875 For each combination of selection cuts, I compare the true charged pion multiplicity  
 3876 given by GENIE with the number of charged pion candidates I count with this method,  
 3877 hereafter referred to as the reconstructed  $\pi^\pm$  multiplicity. The result of this comparison  
 3878 is a matrix, with columns and rows indicating true and reconstructed charged pion  
 3879 multiplicity, respectively. An example of one of these matrices, obtained for a certain  
 3880 configuration of cuts, can be seen in Fig. 7.14. From these multiplicity matrices one can  
 3881 extract performance metrics, like efficiency, purity, and significance.

3882 Given a multiplicity matrix  $\mathbf{M}$ , the efficiency for the  $i$ -th multiplicity value can be

## CHAPTER 7. EVENT SELECTION IN ND-GAR

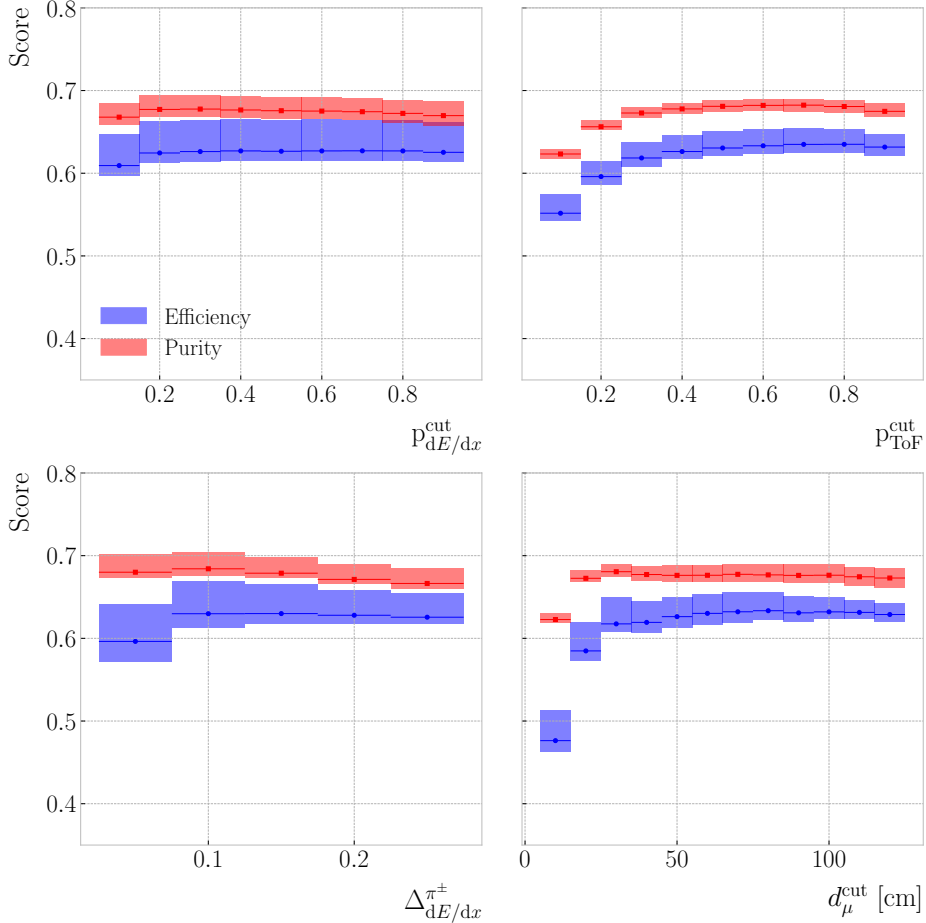


**Figure 7.16:** Efficiency (blue) and purity (red) for the  $\nu_\mu$  CC  $1\pi^\pm$  selection as a function of the proton  $dE/dx$  score cut (top left panel), proton ToF score cut (top right panel), pion  $dE/dx$  cut (bottom left panel), and distance to muon cut (bottom right panel). The height of the boxes represents the IQR of the conditional distributions, whereas the line corresponds to the median.

3883 computed as:

$$\text{Efficiency}|_i = \frac{M_{ii}}{\sum_j M_{ij}}, \quad (7.7)$$

3884 or in other words, dividing the corresponding diagonal entry by the sum of all the entries

3885 in the same column. On the other hand, the purity is given by:

$$\text{Purity}|_i = \frac{M_{ii}}{\sum_j M_{ji}}, \quad (7.8)$$

3886 which is just the ratio between the diagonal entry and the sum of the entries in the

### 7.3. CHARGED PION IDENTIFICATION

3887 corresponding row. Similarly, the significance is obtained by taking the square root of  
 3888 the denominator in the previous expression:

$$\text{Significance}|_i = \frac{S}{\sqrt{S+B}}|_i = \frac{M_{ii}}{\sqrt{\sum_j M_{ji}}}. \quad (7.9)$$

3889 Figures 7.15 and 7.16 show the efficiency (blue) and the purity (red) for the  $\nu_\mu$   
 3890 CC  $0\pi^\pm$  and  $1\pi^\pm$  selections, respectively, as a function of the different cut values. In  
 3891 the figures, each box represents the IQR of the conditional distribution for the fixed  
 3892 value of the corresponding cut, and the horizontal lines correspond to the medians. The  
 3893 first thing one notices is that the efficiency is always higher than the purity in the  $0\pi^\pm$   
 3894 selection, while the opposite is true for the  $1\pi^\pm$  selection. Also, it is clear that the range  
 3895 within these metrics fluctuate in the  $0\pi^\pm$  selection is significantly higher than it is for  
 3896 the  $1\pi^\pm$  case. This shows that it is easier to assess that no charged pions are present in  
 3897 the event than actually tagging them.

3898 For the  $\nu_\mu$  CC  $0\pi^\pm$  selection, the performance metrics follow the expected tendency.  
 3899 As the purity grows with a cut value, the efficiency decreases. Interestingly, this is not  
 3900 the case for the  $1\pi^\pm$  selection, where both efficiency and purity follow roughly the same  
 3901 trends along the different cuts. This makes sense when one comprehends that this is not  
 3902 a traditional cut-based selection, but more of a counting exercise. Some restrictive cut  
 3903 configurations will not tag any particles as pions. On the contrary, loose cuts will render  
 3904 every particle as a  $\pi^\pm$ . Therefore, when looking at a specific multiplicity, the relation  
 3905 between the cut value and the performance metrics is not obvious. Thus, sometimes  
 3906 efficiency and purity can both increase, as the cuts refine the definition of a reconstructed  
 3907 pion.

3908 To have a working point for our studies, I chose the cut configuration that yields  
 3909 the maximum significance for the  $\nu_\mu$  CC  $1\pi^\pm$  selection. Of course, other cuts would be  
 3910 more appropriate in certain scenarios. However, this provides us with a starting point  
 3911 to understand the performance of the selection. A significance of  $66 \pm 7$  for the  $1\pi^\pm$   
 3912 selection is achieved for the cut values  $p_{dE/dx}^{\text{cut}} = 0.30$ ,  $p_{\text{ToF}}^{\text{cut}} = 0.70$ ,  $\Delta_{dE/dx}^{\pi^\pm} = 0.10$ , and

## CHAPTER 7. EVENT SELECTION IN ND-GAR

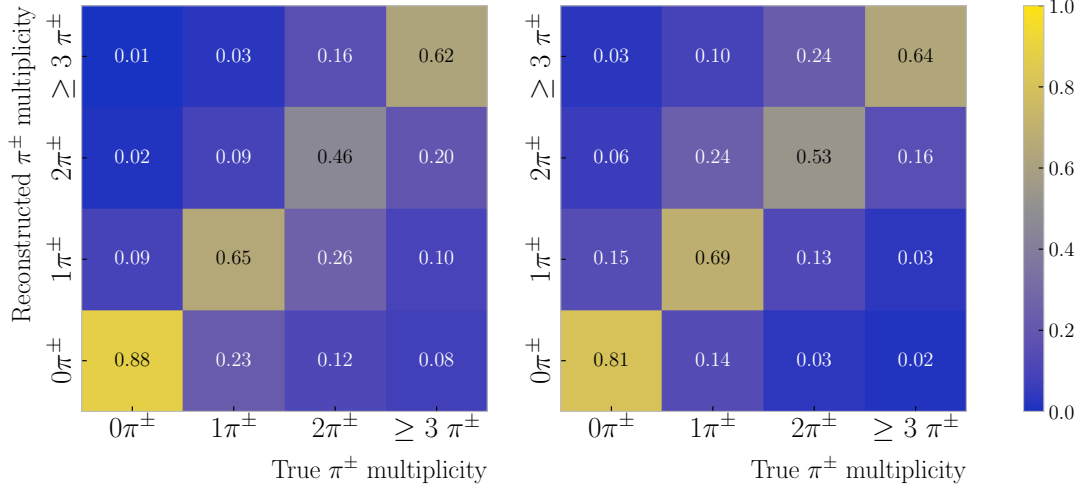


**Figure 7.17:** Distribution of events given their true and reconstructed  $\pi^\pm$  multiplicity, both column-wise (left panel) and row-wise (right panel) normalised, for the selection that maximises the significance of the  $\nu_\mu$  CC  $1\pi^\pm$  selection. The column normalisation yields the efficiency in the diagonal entries, whereas the row normalisation reveals the purity.

3913  $d_\mu^{\text{cut}} = 110.0$  cm.

3914 Figure 7.17 shows the multiplicity matrices resulting from this optimised  $\nu_\mu$  CC  $1\pi^\pm$   
 3915 selection. Although both matrices are produced with the same selection cuts, one is  
 3916 column normalised (left panel), whereas the other is row normalised (right panel). It  
 3917 follows from the definitions in Eqs. (7.7) and ((7.8)) that the diagonal entries of these  
 3918 matrices correspond to the efficiencies and the purities, respectively, for each of the  
 3919 possible charged pion multiplicity selections.

3920 An additional check to make is understand how this configuration performs when  
 3921 applied to the other selections, like  $\nu_\mu$  CC  $0\pi^\pm$ , and how it compares to the other  
 3922 possible configurations. A comparison between the different pion multiplicity selections,  
 3923 indicated with colours, in the purity versus efficiency space is shown in Fig. 7.18. For  
 3924 each of the possible multiplicity choices, the performance obtained for the  $1\pi^\pm$  optimised  
 3925 selection is indicated by an outlined point. From this, one can see that the selected  
 3926 configuration performs reasonably well, within the limits of what can be achieved in  
 3927 each case, across the different multiplicities.

3928 At this point, one can study the charged pion selection performance as a function of

### 7.3. CHARGED PION IDENTIFICATION

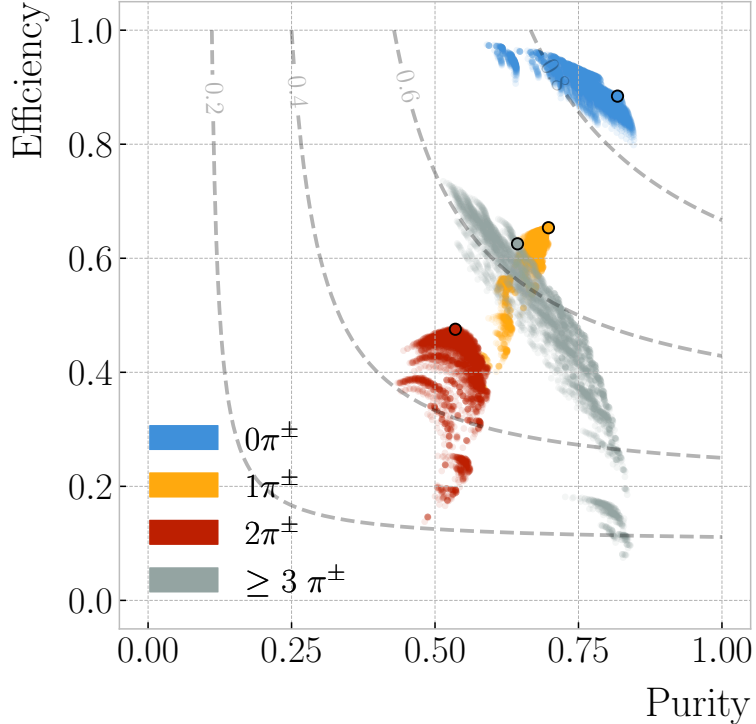


**Figure 7.18:** Purity versus efficiency achieved for the different cut configurations explored separated by the various  $\nu_\mu$  CC  $N\pi^\pm$  selections. The outlined points indicate the state for each possible multiplicity when using the configuration that maximises the significance of the  $\nu_\mu$  CC  $1\pi^\pm$  selection. The contours indicate the surfaces of equal  $F_1$ -score.

3929 other quantities of interest. A natural variable to check is the hadronic invariant mass.

3930 It is defined as:

$$W = \sqrt{-Q^2 + 2m_n q_0 + m_n^2} \quad (7.10)$$

3931 where  $Q^2$  is the momentum transfer from the neutrino to the primary muon,  $q_0$  the  
 3932 energy transfer, and  $m_n$  the mass of the nucleon. This quantity is related to the elasticity  
 3933 of the neutrino interaction, and defines the transitions between the QEL, RES and DIS  
 3934 regions. An interesting invariant mass range for DUNE is the one that extends between  
 3935 the mass of the  $\Delta$  resonance, even though it is typically extended down to  $m_p + m_{\pi^\pm}$ ,  
 3936 and 2.0 GeV. It is estimated that roughly 7 in every 10 events in our ND will take  
 3937 place in this region. Although the RES production dominates at these  $W$  values, this  
 3938 range also includes the transition to the DIS regime. Thus, it is often called the shallow

## CHAPTER 7. EVENT SELECTION IN ND-GAR

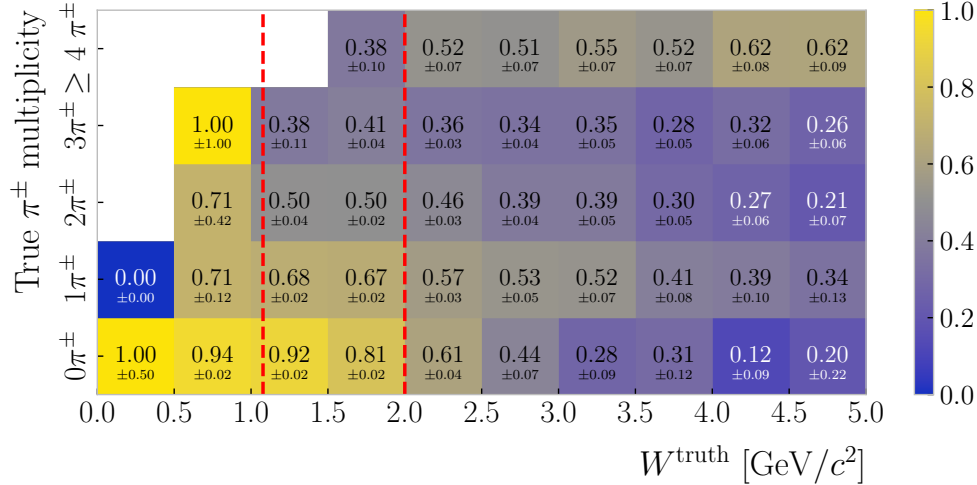


**Figure 7.19:** Efficiency of the various  $\nu_\mu$  CC  $N\pi^\pm$  selections as a function of the true hadronic invariant mass. The dashed vertical lines correspond (from left to right) to the values  $m_p + m_{\pi^\pm}$  and  $2.0 \text{ GeV}/c^2$ , which define the shallow inelastic scattering region.

3939 inelastic scattering (SIS) region.

3940 Within these boundaries, the resonant events produce either 1 or 2 charged pions,  
 3941 whereas the multipion events are typically associated to non-resonant production.  
 3942 Therefore, our ability of correctly select events with  $\geq 2\pi^\pm$  in the SIS region will  
 3943 impact our ability of constraining this poorly understood regime. Figure 7.19 shows the  
 3944 efficiency of the various charged pion multiplicity selections in a number of hadronic  
 3945 invariant mass bins. The two red dashed lines indicate the boundaries of the SIS region.  
 3946 One can see that, although not as good as the single pion selection, the efficiency for the  
 3947 multipion events is reasonable in the relevant invariant mass range. The total efficiency  
 3948 for the  $\nu_\mu$  CC  $\geq 2\pi^\pm$  selection in the SIS regime is estimated to be  $0.65 \pm 0.02$ .

### 3949 7.3.1 $\nu_\mu$ CC $1\pi^\pm$ selection

3950 By focusing on the  $1\pi^\pm$  selection, one can study the kinematics of the selected pion.  
 3951 This allows one to understand how well the charged pions are tagged. This is difficult  
 3952 to do only using the multiplicity matrices, as with them one can only check that the  
 3953 number of charged pions is the same as in the truth. Sometime, even if the estimated  
 3954 pion multiplicity is correct, the identified particles may not be true pions.

### 7.3. CHARGED PION IDENTIFICATION

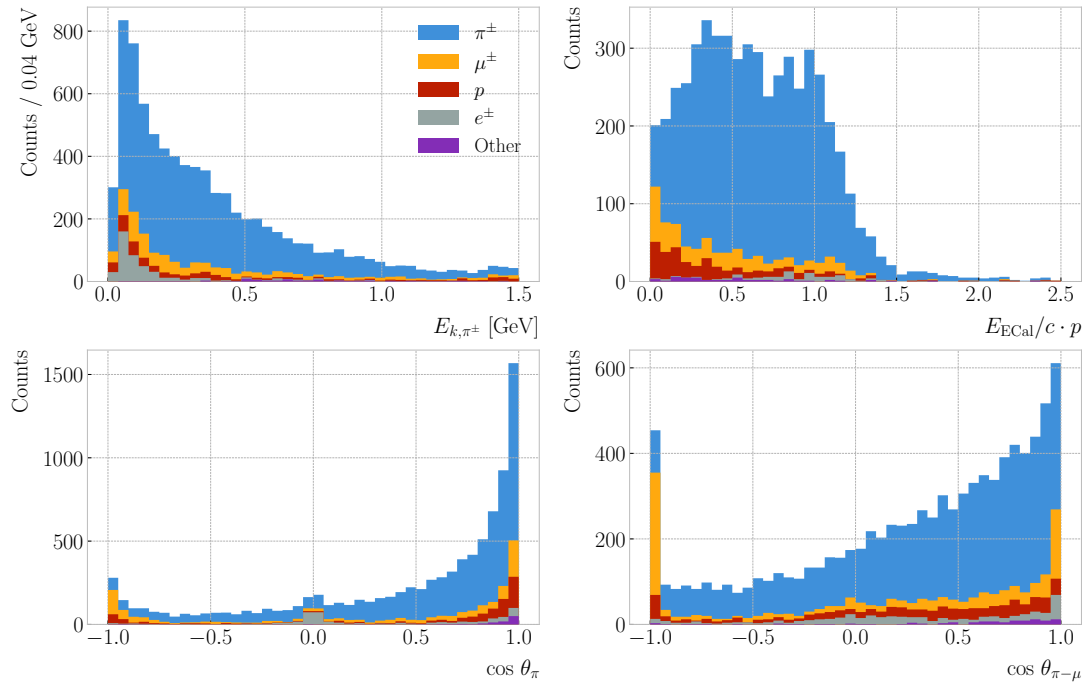


**Figure 7.20:** Reconstructed kinematic distributions for the pion candidate in the  $\nu_\mu$  CC  $1\pi^\pm$  selection, broken down by true ID of the particle. From left to right, top to bottom, we have the kinetic energy given the pion hypothesis, the ratio between the energy deposited in the ECal and the momentum, the pion angle, and the angle between the muon and pion candidates.

3955        Figure 7.20 displays the distributions of various reconstructed kinematic variables  
 3956        for the selected pion candidate. The different colours indicate the ID of the true particle  
 3957        associated to the reconstructed pion.

3958        First, we have the kinetic energy distribution. For this set of reconstructed particles,  
 3959        because they have been tagged as charged pions, the kinetic energy is computed using their  
 3960        momentum assuming the pion hypothesis. One can see that most of the contaminants  
 3961        sit in low energy range, up to around 0.2 GeV.

3962        The next distribution presents the ratio between the energy deposited in the ECal  
 3963        associated to the particle over the momentum measured in the HPgTPC. This variable is  
 3964        restricted to particles with at least one associated hit in the ECal. It is interesting to see  
 3965        two peak structure in the true pion distribution. The first one presumably corresponds  
 3966        to the pions punching-through the ECal, while the latter is probably due to the ones

## CHAPTER 7. EVENT SELECTION IN ND-GAR

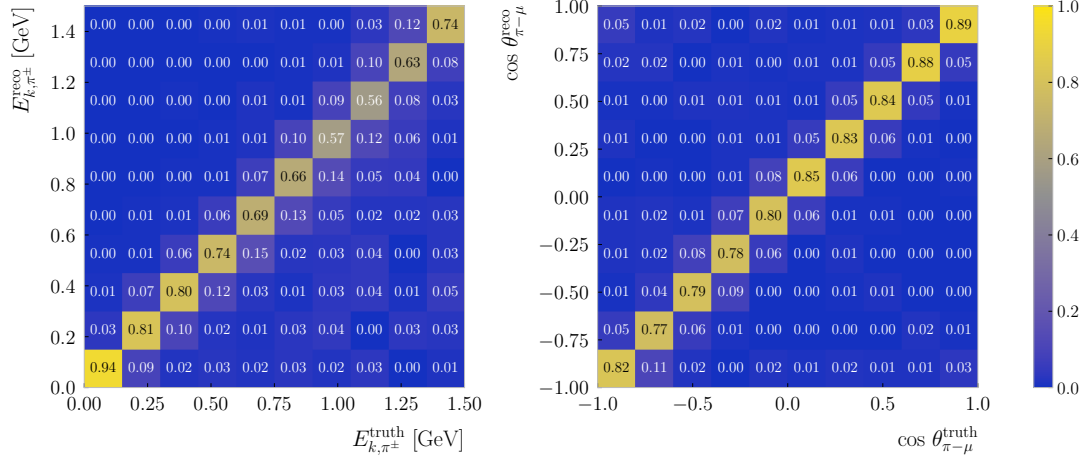


**Figure 7.21:** Distributions for the reconstructed versus truth generated pion kinetic energy (left panel) and cosine of the angle between the pion and muon (right panel). The reconstructed values correspond to the selected primary muon and pion candidates in the  $\nu_\mu$  CC  $1\pi^\pm$  selection, whereas the truth values come from the true primary muon and pion in the events.

3967 stopping in it. On the other hand, the misidentified particles, other than the electrons,  
 3968 tend to lower ratios. This is expected for protons, as this could not be higher than 0.5  
 3969 for momenta  $\leq 1$  GeV/ $c$  even if they stopped, but for the muons it may point to a  
 3970 misreconstruction.

3971 The following distribution shows the angle of the pion candidates with respect to the  
 3972 beam direction. Although most of them are aimed in the forward direction, it can be  
 3973 noted that an important number of the misidentified muons seem to be backward-going.  
 3974 This is likely a reconstruction artifact, produced by broken tracks that got assigned the  
 3975 wrong propagation direction. Also, there is a sizeable number of true electrons with  
 3976 directions perpendicular to the beam, probably delta electrons from the primary muon.

3977 Finally, I included the reconstructed pion-muon angular distribution. Even though  
 3978 it shares some similarities with the previous distribution, as the primary muon typically  
 3979 goes forward, the pion distribution is not as prominently forward-going in this case.  
 3980 Also, it may be noted that approximately 25% of the muons misidentified as pions have  
 3981  $\cos \theta_{\pi-\mu} \leq -0.95$ . Therefore, putting an additional angular cut improves the purity of  
 3982 the charged pion selection from  $0.74 \pm 0.01$  to  $0.77 \pm 0.01$ , while not loosing a substantial

## 7.4. NEUTRAL PION IDENTIFICATION

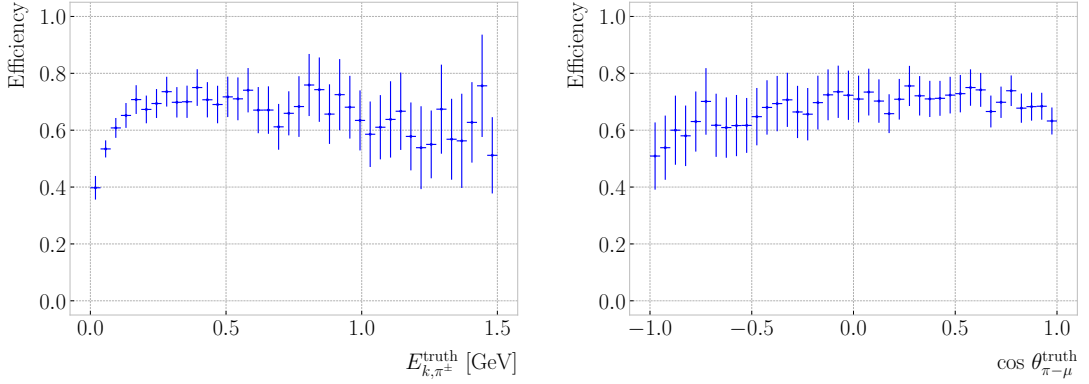


**Figure 7.22:** Efficiency of the  $\nu_\mu$  CC  $1\pi^\pm$  selection as a function of the true pion kinetic energy (left panel) and pion-muon angle (right panel).

3983 amount of true pions.

3984 A comparison between the true and the reconstructed values of the pion kinetic  
 3985 energy (left panel) and pion-muon angle (right panel) is shown in Fig. 7.21. The  
 3986 distributions are column normalised, which allows to see the fraction of events in the  
 3987 correct bins. For this, I selected the events where only one reconstructed pion and  
 3988 one true pion were identified, as that is the only case where a pairing of the variables is  
 3989 possible. It showcases the excellent agreement between the reconstruction and the truth  
 3990 information.

3991 One can also study the performance of the pion selection as a function of the  
 3992 truth pion kinematics. Fig. 7.22 shows the selection efficiency versus the true kinetic  
 3993 energy (left panel) and the angle between the true primary pion and muon (right panel).  
 3994 The efficiency is computed from the events with a single true and reconstructed pion,  
 3995 comparing their number to the total of events with one true pion. Notice how the  
 3996 efficiency, although it starts with relatively low values, plateaus around 0.70 quickly  
 3997 after 0.20 GeV. In terms of the pion-muon angle, the efficiency looks relatively flat, only  
 3998 dropping slightly towards the back-to-back case.

## CHAPTER 7. EVENT SELECTION IN ND-GAR

### 3999 7.4 Neutral pion identification

4000 The  $\nu_\mu$  CC selection can also be used as a stepping stone for the identification of  
4001 neutral pions. Although these particles do not leave any traces in the HPgTPC, using a  
4002 combination of the different detectors within ND-GAr. Being able to tag the neutral  
4003 pions is a valuable asset for the estimation of the reconstructed neutrino energy, as both  
4004 their kinetic and mass components can then be added in the calculation.

4005 In the case that both photons from the  $\pi^0$  decay do not undergo pair production  
4006 of a  $e^+e^-$  pair, they will reach the ECal where they will produce an electromagnetic  
4007 shower. This activity inside the ECal will not be associated to any charged particle track  
4008 inside the HPgTPC, unless there is a reconstruction failure. Thus, having a neutrino  
4009 interaction vertex candidate from the  $\nu_\mu$  CC selection, one can reconstruct the mass of  
4010 the  $\pi^0$  using the energy and position of the photons. I already used this same technique  
4011 in section 6.6 for a single  $\pi^0$  sample. However, here I apply it to neutrino interaction  
4012 events, and the vertex position is not cheated but selected from the reconstruction  
4013 products.

4014 The idea is to look for all the ECal clusters that were not associated to tracks in  
4015 each event. Then, if two or more were identified, compute the invariant mass for all  
4016 possible combinations. At this point, I select the pair whose invariant mass is closest to  
4017  $m_{\pi^0}$ , remove the pairs containing any of the two selected clusters from the collection,  
4018 and iterate until no more pairs can be formed.

4019 I repeat this procedure for the events with 0, 1, 2 and 3 or more true neutral pions.  
4020 For each of them, I extract the invariant mass of the first three cluster pair candidates  
4021 (in order of proximity to  $m_{\pi^0}$ ), in case they can be formed. If the number of the cluster  
4022 pair is lower than the true neutral pion multiplicity of the event, that entry will be  
4023 counted as signal. The additional candidates for an event of a given multiplicity are  
4024 considered background. The resulting distribution is shown in Fig. 7.23 (black data  
4025 points).

## 7.4. NEUTRAL PION IDENTIFICATION

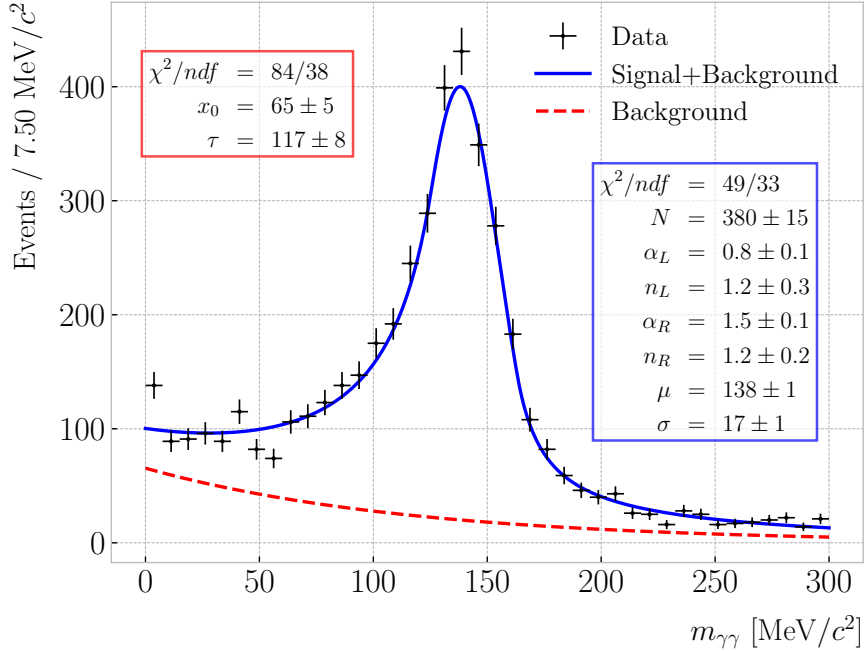


**Figure 7.23:** Invariant mass distribution obtained for the unassociated ECal cluster pair in the event with the value closest to the true  $\pi^0$  mass. The best fits for signal plus background (solid blue line) and background only (dashed red line) are also shown.

4026

I fit the signal distribution to a double-sided Crystal Ball function:

$$f_s(x; \alpha_{L,R}, n_{L,R}, \mu, \sigma, N) = N \begin{cases} A_L \left( B_L - \frac{x-\mu}{\sigma} \right)^{-n_L}, & \text{for } \frac{x-\mu}{\sigma} < -\alpha_L, \\ e^{-\frac{(x-\mu)^2}{2\sigma^2}}, & \text{for } -\alpha_L \leq \frac{x-\mu}{\sigma} \leq \alpha_R, \\ A_R \left( B_R + \frac{x-\mu}{\sigma} \right)^{-n_R}, & \text{for } \frac{x-\mu}{\sigma} > \alpha_R, \end{cases} \quad (7.11)$$

4027

where  $A_{L,R}$  and  $B_{L,R}$  are given by:

$$A_{L,R} = \left( \frac{n_{L,R}}{|\alpha_{L,R}|} \right)^{n_{L,R}} e^{-\frac{|\alpha_{L,R}|^2}{2}}, \quad (7.12)$$

$$B_{L,R} = \frac{n_{L,R}}{|\alpha_{L,R}|} - |\alpha_{L,R}|.$$

4028 The tails of this distribution accommodate the asymmetric shape of the misreconstruction  
 4029 effects. The values obtained for the best fit parameters are indicated in Fig. 7.23 (blue  
 4030 box).

## CHAPTER 7. EVENT SELECTION IN ND-GAR

4031 The background is characterised by an exponential function of the form:

$$f_b(x; x_0, \tau) = x_0 e^{-x/\tau}. \quad (7.13)$$

4032 Similarly, the best fit values can be seen in Fig. 7.23 (red box).

4033 Figure 7.23 also shows the results of the fits for the signal plus background (blue line)  
 4034 and the background only (dashed red line) cases. Using these, I estimate the tagging  
 4035 efficiency of this method to be  $0.90 \pm 0.01$  with a purity of  $0.85 \pm 0.01$ , when selecting  
 4036 the candidates with an invariant mass in the range  $54.0 - 288.0 \text{ GeV}/c^2$ .

4037 This is a robust method to identify the photon pair from the  $\pi^0$  decay. However,  
 4038 this approach is not enough to efficiently identify all the events containing neutral pions  
 4039 in the sample. A quick calculation reveals that only 20% of the  $\nu_\mu$  CC  $1\pi^0$  events can  
 4040 be correctly identified with it.

4041 This approach can be complemented with the identification of the secondary vertices  
 4042 from the  $e^+e^-$  conversions. This will make it possible to cover the cases when either  
 4043 one or both photons convert in the HPgTPC. In those cases, one can try pairing the  
 4044  $e^+e^-$  with unassociated activities in the ECal, or matching pairs of secondary vertices.  
 4045 However, this will require further work on the reconstruction, and thus falls out of the  
 4046 scope of this analysis.

## 4047 7.5 Neutrino energy reconstruction

4048 In a neutrino-nucleus CC interaction, where alongside the charged lepton  $N$  nucleons  
 4049 where knocked out and  $M$  mesons produced, the reconstructed neutrino energy can be  
 4050 computed as:

$$E_{\text{rec}} = S_n + E_\ell + \sum_{i=0}^N E_{k,n_i} + \sum_{j=0}^M E_{m_j}, \quad (7.14)$$

4051 where  $S_n$  is the average single-nucleon separation energy,  $E_\ell$  the energy of the primary  
 4052 lepton,  $E_{k,n_i}$  is the kinetic energy of the  $i$ -th knocked-out nucleon and  $E_{m_j}$  the total  
 4053 energy of the  $j$ -th produced meson.

## 7.5. NEUTRINO ENERGY RECONSTRUCTION

4054 This represents the ideal scenario, where all the kinetic energy of the nucleons is  
 4055 visible in the detector and one can identify all mesons produced in the interaction. In a  
 4056 real experiment, some of these energy components will not be , and this needs to be  
 4057 accounted for in any estimation of the reconstructed energy.

4058 For instance, in ND-GAr neutrons are complicated to account for, as they do not  
 4059 produce tracks in the TPC. They may be identified either from scatterings off Ar nuclei  
 4060 in the HPgTPC, or performing a ToF measurement in the ECal. However, these methods  
 4061 are not fully mature in the current reconstruction, and their development is beyond the  
 4062 scope of this study. So, in the following, I will completely ignore the contribution of  
 4063 neutrons.

4064 Also, with a real detector we can not expect to tag all the charged pions irrespective  
 4065 of their energy. This is why one has to introduce detection thresholds in the energy  
 4066 estimation. Thus, in the reconstructed energy calculation I will add only the kinetic  
 4067 energy for the charged pions below the threshold, and the total energy for the pions  
 4068 above the threshold.

4069 Likewise, the identification of all neutral pions in the sample is challenging. As  
 4070 discussed in the previous section, with our ECal we are able to identify the photons  
 4071 from the  $\pi^0$  decays, but that selection still needs to be completed with other methods.  
 4072 Therefore, for this first study I do not take into account the energy contribution of the  
 4073 neutral pions.

4074 With all this in mind, using the truth information from the events I compute the  
 4075 reconstructed neutrino energy as:

$$E_{\text{rec}}^{\text{truth}} = S_n + E_\ell + \sum_{i=0}^{N_p} E_{k,p_i} + \sum_{j=0}^{M_{\pi^\pm}^<} E_{k,\pi_j^\pm} + \sum_{k=0}^{M_{\pi^\pm}^>} E_{\pi_k^\pm}, \quad (7.15)$$

4076 where  $N_p$  is the number of protons, and  $M_{\pi^\pm}^<$  and  $M_{\pi^\pm}^>$  the number of charged pions  
 4077 below and above the threshold, respectively. As before, I assume a kinetic energy  
 4078 threshold of 20 MeV for the charged pions.

4079 At the reconstruction level, I use the energy of the primary muon candidate, computed

## CHAPTER 7. EVENT SELECTION IN ND-GAR

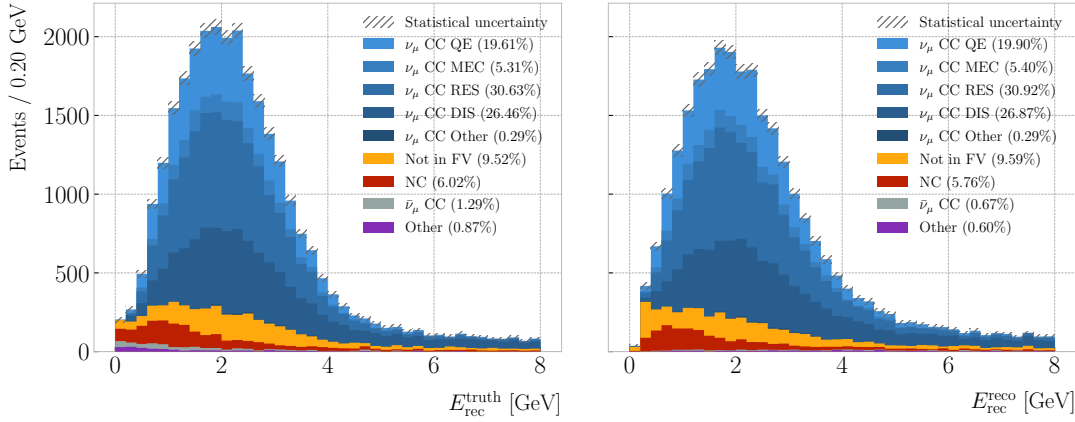


**Figure 7.24:** Reconstructed neutrino energy spectra for the  $\nu_\mu$  CC selection obtained using the truth (left panel) and reconstructed (right panel) information. The selected events are broken down by signal and background subcategories. The statistical uncertainty is drawn in hatched gray.

from its momentum, as the starting point for the neutrino energy calculation. Then, I add the total energy contributions from the identified charged pions, again using their momenta. After that, I try to identify the protons by looking at the two proton scores. If any of them are above threshold (here the thresholds used are the same as for the pion identification), the kinetic energy of the particle is added to the total. Finally, I check if any of the remaining particles are fully contained within the FV. I add their kinetic contributions using the total energy they deposited in the HPgTPC.

Figure 7.24 shows the resulting distributions of reconstructed neutrino energy obtained from the truth (left panel) and reconstructed (right panel) particle collections. The overall shape of the distributions is similar, with the reconstructed one having a slightly larger high energy tail. Note also that the background events from outside the FV tend to have a smaller energy in the reconstructed case. This is likely due to a misreconstruction of the primary muon, which clearly does not affect the other computation.

I also compared the reconstructed energies to the true energy of the neutrino. Figure 7.25 displays the ratio of the energy residuals to the true energy for the truth (left panel) and reconstructed (right panel) cases. As expected, using the true particles one never overestimates the neutrino energy. Also, using the reconstructed objects one is more

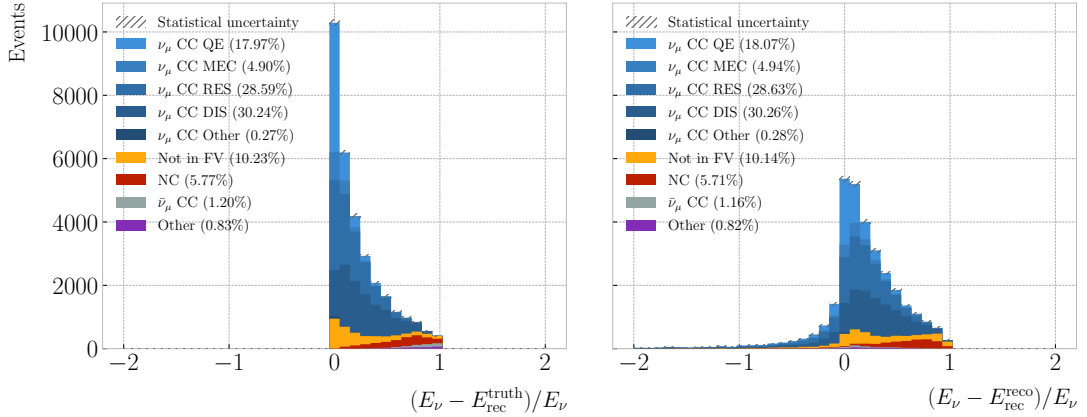


**Figure 7.25:** Neutrino energy residuals distributions for the  $\nu_\mu$  CC selection obtained using the truth (left panel) and reconstructed (right panel) information. The selected events are broken down by signal and background subcategories. The statistical uncertainty is drawn in hatched gray.

4098 prone to underestimate the neutrino energy, due to deficiencies in the reconstruction.

## 4099 7.6 Systematic uncertainties

4100 Although the implementation and study of the systematic uncertainties relevant for  
 4101 ND-GAr is out of the scope of this preliminary analysis, in this section I give an extended  
 4102 overview of the topic. can be classified in three categories: neutrino flux uncertainties,  
 4103 neutrino-nucleus interaction model uncertainties, and detector response uncertainties.

### 4104 7.6.1 Flux uncertainties

4105 The neutrino flux prediction is affected by systematic uncertainties arising from two  
 4106 sources: the uncertainties in the production of hadrons in the target and the uncertainties  
 4107 in the design parameters of the beamline itself. These fluxes and their uncertainties are  
 4108 generated with the G4LBNF simulation [83], a Geant4 implementation of the LBNF  
 4109 beamline, and the Package to Predict the FluX (PPFX) framework, originally developed  
 4110 for MINERvA [191].

4111 The hadron production uncertainties are associated to the kinematic distributions  
 4112 of the hadrons produced when the protons interact with the carbon target, as well

## CHAPTER 7. EVENT SELECTION IN ND-GAR

as the possible interactions of the hadrons with the beamline materials. The PPFX package estimates these uncertainties by performing a number of random throws of the production model parameters [192]. This way, different predictions of the LBNF flux are generated, which can be compared to the nominal prediction to build a matrix of the covariances between neutrino energies, flavours and running modes (either FHC or RHC). The resulting hadron production uncertainties are described by the eigenvectors associated to the largest eigenvalues in this matrix, obtained performing a PCA analysis.

The other set of uncertainties affecting the neutrino flux prediction come from the limited precision with which we know the parameters of the different components in the beamline. These include the specifications of the target, the dimensions of the decay pipe, and the current and alignment of the magnetic horns. The effects on the flux predictions of these uncertainties are estimated using the G4LBNF simulation. For each of the parameters, the simulation runs with said parameter shifted by  $\pm 1\sigma$  from the nominal value, and the resulting flux prediction is compared to the nominal one.

### 7.6.2 Cross section uncertainties

As discussed previously in section 2.6, the neutrino-nucleus interaction model is of great importance for neutrino experiments, as it maps the true neutrino energy to the kinematics of the final state particles. The uncertainties on the cross section model are implemented in three ways: varying the parameters used in the GENIE simulation, using weights that parametrise cross section effects not accounted for in GENIE, and comparing the GENIE predictions to other interaction models.

Within the DUNE TDR LBL analysis, the default interaction model was that implemented in GENIE v2\_12\_10 [121]. A summary of the cross section systematic parameters present in GENIE used in that analysis is presented in Tab. 7.3. The additional systematic parameters used in the analysis are described in Tab. 7.4.

In this default GENIE configuration, the initial state of the nucleons is described by the Bodek-Ritchie global Fermi gas model [193]. The model is known give a poor agreement whe compared to neutrino-nucleon data [194]. Because of the limitations of

## 7.6. SYSTEMATIC UNCERTAINTIES

**Table 7.3:** Neutrino interaction systematic parameters implemented in GENIE used in the DUNE TDR LBL analysis. Events with low  $W$  that are not QE are mainly RES, whereas DIS events dominate at high  $W$ . The initials BY refer to the Bodek-Yang model. Table adapted from Ref. [121].

Systematic	$1\sigma$ value
<b>Quasielastic</b>	
Axial mass for CCQE	$+0.25_{-0.15}$ GeV
CCQE vector form factor shape	N/A
Fermi surface momentum for Pauli blocking	$\pm 30\%$
<b>Low <math>W</math></b>	
Axial mass for CC resonance	$\pm 0.05$ GeV
Vector mass for CC resonance	$\pm 10\%$
$\theta_\pi$ distribution for $\Delta$ decay	N/A
<b>High <math>W</math> (BY model)</b>	
$A_{HT}$	$\pm 25\%$
$B_{HT}$	$\pm 25\%$
$C_{v1u}$	$\pm 30\%$
$C_{v2u}$	$\pm 40\%$
<b>Other neutral current</b>	
Axial mass for NC resonance	$\pm 10\%$
Vector mass for NC resonance	$\pm 5\%$
<b>Intra-nuclear</b>	
Nucleon charge exchange	$\pm 50\%$
Nucleon elastic reaction	$\pm 30\%$
Nucleon inelastic reaction	$\pm 40\%$
Nucleon absorption	$\pm 20\%$
Nucleon $\pi$ -production	$\pm 20\%$
$\pi$ charge exchange	$\pm 50\%$
$\pi$ elastic reaction	$\pm 10\%$
$\pi$ inelastic reaction	$\pm 40\%$
$\pi$ absorption	$\pm 20\%$
$\pi$ $\pi$ -production	$\pm 20\%$

## CHAPTER 7. EVENT SELECTION IN ND-GAR

**Table 7.4:** Neutrino interaction systematic parameters used in the DUNE TDR LBL analysis not present in **GENIE**. I have omitted the parameters only relevant for the FD. Table adapted from Ref. [121].

Systematic	Mode	Description
BeRPA	$1p1h/\text{QE}$	Nuclear model suppression
ArC2p2h	$2p2h \text{ Ar/C}$	Electron scattering SRC pairs
$E_{2p2h}$	$2p2h$	$2p2h$ energy dependence
CC non-resonant	CC DIS $1\pi$	$\nu + n/p \rightarrow \ell + 1\pi$
Other non-resonant	DIS $N\pi$	$1 < W < 5 \text{ GeV}/c^2$
NC normalisation	NC	$\pm 20\%$ to all NC events at the ND

4141 the model, the current versions of **GENIE** use the local Fermi gas approach, which takes  
 4142 into account the correlation between the momentum of the nucleons and their location  
 4143 within the nucleus.

4144 For the CCQE events, the dominant model uncertainties arise from the axial form  
 4145 factor of the nucleon, for which a dipole parametrisation is used, and the nuclear  
 4146 correlation effects computed using the random phase approximation (RPA). In the  
 4147 analysis, a parametrisation of the Valencia RPA effect [187] is used. This consists of  
 4148 a third-order Bernstein polynomial up to  $Q^2 = 1.2 \text{ GeV}^2$  followed by an exponential  
 4149 decay (BeRPA), originally proposed by the T2K collaboration [195].

4150 The  $2p2h$  interactions are included using the Valencia model [187], with an additional  
 4151 correction following the observation of an underprediction of these events in MINERvA  
 4152 [196]. Additional uncertainties for the energy dependence of the missing strength were  
 4153 added. Also, the uncertainties in the scaling from carbon to argon are included, based  
 4154 on measurements of electron scattering off short-range correlated (SRC) nucleon pairs  
 4155 on multiple targets [197].

4156 In this version of **GENIE**, the Rein-Sehgal model describes the single pion resonant  
 4157 production events [198]. It includes 16 different resonances, with no interference between  
 4158 them. Two parameters account for the uncertainties on the axial and vector masses of  
 4159 the resonances. In subsequent **GENIE** tunes, like the one used in the studies presented in  
 4160 this Chapter, the Berger-Sehgal model is used [188]. This is an improved version of the

## 7.6. SYSTEMATIC UNCERTAINTIES

4161 Rein-Sehgal model, which includes the lepton mass effects in the calculations.

4162 The Bodek-Yang parametrisation is used to describe the DIS events [190]. The  
4163 parameters  $A_{\text{HT}}$  and  $B_{\text{HT}}$  account for higher twist effects in the scaling variable, while  
4164  $C_{v1u}$  and  $C_{v2u}$  control the form of the valence quark  $K$  factors. For the analysis, the  
4165 uncertainties on the values of these parameters are taken into consideration. Also, due to  
4166 the difficulties of GENIE at describing the transition region between RES and DIS events,  
4167 a set of systematic parameters affecting the different non-resonant pion production  
4168 channels were developed, following the example of NOvA [199]. There are independent  
4169 parameters for the interactions on protons and neutrons, except for the CC DIS  $1\pi$  case  
4170 where they are merged. All start with an uncertainty of 50% for  $W \leq 3 \text{ GeV}/c^2$ , which  
4171 linearly decreases until reaching a 5% at  $W = 5 \text{ GeV}/c^2$ .

4172 For the TDR analysis, an additional 20% normalisation uncertainty was added to all  
4173 NC events in the ND. It was implemented to understand if the NC events passing the  
4174 selection cuts affected the results of the analysis [121].

4175 Finally, the effective intranuclear transport model (often denoted as  $hA$ ) is a part  
4176 of GENIE, implemented in the INTRANUKE module. GENIE features a large number of  
4177 parameters for the uncertainties on the intranuclear cascade model, which are summarised  
4178 in the last portion of Tab. 7.3. In following GENIE releases, updated versions of the  
4179 INTRANUKE model are used.

4180 Although part of this cross section systematic treatment is outdated, as the tunes  
4181 currently used feature different models, it gives a good idea of what systematic effects  
4182 are relevant for the different measurements we may want to perform in the future. At  
4183 the moment, a significant effort is channeled to the creation of new tunes specifically  
4184 tailored for DUNE, including the development of parametrisations particularly relevant  
4185 for ND-GAr.

### 4186 7.6.3 Detector uncertainties

4187 The DUNE ND CDR [89] presents a number of studies on the performance of ND-GAr.  
4188 These were based on the reference design described in section 3.5. Because the detector

## CHAPTER 7. EVENT SELECTION IN ND-GAR

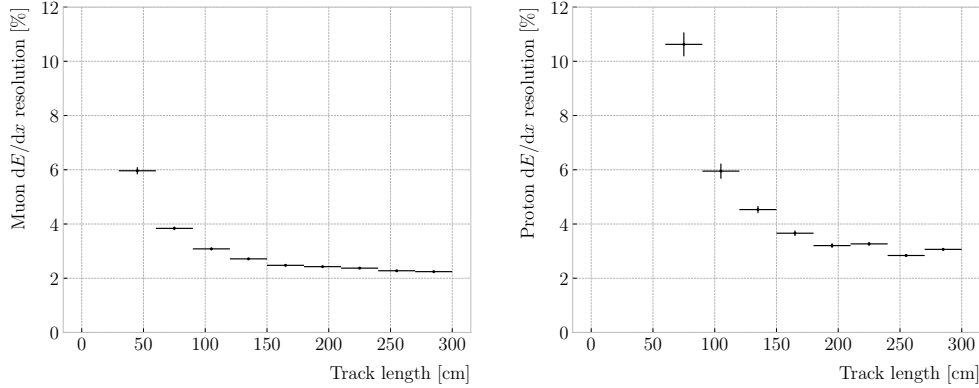


**Figure 7.26:** Estimated  $dE/dx$  resolution as a function of the track length for true muons (left panel) and protons (right panel) in a  $\nu_\mu$  CC sample.

is still in an R&D stage, with the design continually evolving, these performance metrics will need to be revisited in the future. However, they still provide valuable information. These studies help understand what detector requirements are needed to achieve the physics goals of the experiment, and on what design aspects we need to improve.

Since the reference design of ND-GAr repurposes the ALICE MWPCs and other hardware components, the ALICE TPC operation experience point of reference for the spatial resolution performance. They reported a single hit resolution of 0.25 mm and 1.50 mm in the directions perpendicular and parallel to the drift direction, respectively [93]. Nevertheless, the MWPCs are not the leading option for the charge readout anymore. Current efforts focus on the study of the effects of different pixelisation choices. of the GEMs setups.

For other performance metrics, a fairer comparison for the ND-GAr HPgTPC could be the PEP-4. It operated with a 80:20 Ar:CH<sub>4</sub> mixture at 8.5 bar, achieving a two-track separation of 1 cm [200, 201]. This metric is particularly relevant in our case, as the neutrino interaction vertex can be an area of very high track multiplicity. Thus, our track separation capabilities will have a direct impact on the primary vertex identification and resolution. There are several difference between our HPgTPC and PEP-4. The operating pressure of ND-GAr will be higher, and the gas mixture likely to contain a higher fraction of Ar.

## 7.6. SYSTEMATIC UNCERTAINTIES

4208 In terms of the ionisation measurement, both the experience from ALICE and PEP-4  
4209 are relevant, as this depends on the readout and the running conditions (pressure and  
4210 gas mixture). They obtained resolutions of 4.5% and 3.0% for typical track lengths of  
4211 160 and 75 cm, respectively. According to previous studies on the  $dE/dx$  resolution in  
4212 gaseous detectors [202], ND-GAr can achieve a 2% resolution for a typical track length of  
4213 200 cm. Figure 7.26 shows the values of the resolution I estimate for muons (left panel)  
4214 and proton (right panel) tracks with different lengths, using the procedure described in  
4215 section 6.2.

4216 The tracking capabilities of ND-GAr were studied in the context of  $\nu_\mu$  CC interactions.  
4217 Using a sample of reconstructed tracks from true muons and charged pions, the tracking  
4218 efficiency was estimated to be above 90% for momenta  $\geq 40 \text{ MeV}/c$ , with it steadily  
4219 rising with the momentum. As a function of the angle with respect to the beam direction,  
4220 the efficiency was almost flat for particles with  $p \geq 200 \text{ MeV}/c$ . In the case of protons,  
4221 the tracking performs for kinetic energies  $\geq 20 \text{ MeV}$ . A machine learning algorithm is  
4222 being developed for low energy proton track identification near the interaction vertex.  
4223 Preliminary results show an efficiency of 30% at 5 MeV for this method.

4224 The same samples used for the tracking studies were employed to estimate the  
4225 momentum resolution. The momentum is computed from the curvature of the tracks  
4226 in the magnetic field, and is therefore limited by the track length in the direction  
4227 perpendicular to the field. Focusing on the tracks associated to true muons, a double  
4228 Gaussian fit revealed a width of 2.7% and 12% for the core and tails of the momentum  
4229 distribution. This same study determined the 3D angular resolution in the HPgTPC to  
4230 be  $0.80^\circ$ .

4231 The main source of uncertainty in the momentum measurement is the value of the  
4232 magnetic field. The magnetic field simulations indicate that the overall uncertainty on  
4233 the central field value is  $< 0.05\%$ . A preliminary study investigated the use of  $K_s^0$  decays  
4234 in the HPgTPC to measure any deviations of the magnetic field from its nominal 0.5 T  
4235 value. This showed that even a magnetic field bias of 1% will shift the reconstructed  
4236 invariant mass distribution significantly.

## CHAPTER 7. EVENT SELECTION IN ND-GAR

4237     The results presented for the ECal in Ref. [89] use an outdated version of the  
4238     geometry, where the entire ECal sits outside of the pressure vessel and the layers consist  
4239     of 5 mm of scintillator and 2 mm of Cu. The sample used consists of single photons in  
4240     a  $20^\circ$  cone aligned with the beam direction. In the simulation, an energy threshold of  
4241     200 keV and a time resolution of 0.25 ns are assumed.

4242     The energy resolution of the photons is obtained from a Gaussian fit. The resulting  
4243     resolutions are then fitted to a function of the form:

$$\frac{\sigma_E}{E} = \frac{A}{\sqrt{E}} \oplus \frac{B}{E} \oplus C, \quad (7.16)$$

4244     where  $A$  is the stochastic term,  $B$  the noise term and  $C$  the constant term. The best fit  
4245     finds the values  $A = 6.1\%$ ,  $B = 1.6\%$ , and  $C = 4.5\%$ . The photon angle is estimated  
4246     using a PCA analysis of the associated ECal cluster, taken to be the direction of the  
4247     first principal component. The angular resolution is computed from a Gaussian fit to  
4248     the core of the distribution. As a function of the photon energy, the values obtained are  
4249      $\frac{8.17^\circ}{\sqrt{E}} + 4.18^\circ$ . Different arrangements of the layers and alternative absorber choices may  
4250     improve these results.

## Conclusion and outlook

4253        *Our plans miscarry because they have no aim. When a man does not know  
4254        what harbour he is making for, no wind is the right wind.*

4255                          – Lucio Anneo Seneca, *Epistulae morales ad Lucilium*

4256        This thesis is a compilation of three different projects within DUNE. However,  
4257        the idea behind each one of them is the same. The common theme is the prospect  
4258        of improving or extending the physics of DUNE. In the first case, by enhancing the  
4259        production of TPs in the induction channels what I seek is to provide more useful  
4260        information to the FD data selection. The investigations with both data and MC, as  
4261        well as the opportunity to run with a live detector, showed that such an enhancement  
4262        is possible and should be pursued. Next, the solar DM analysis adds to the already  
4263        rich BSM programme of DUNE. With the results of these preliminary studies, I want  
4264        to show that DUNE can be complementary to the large-volume neutrino detectors in  
4265        this kind of searches. Finally, the goal of the ND-GAr reconstruction improvements  
4266        was the development of the PID strategy of the detector. For this, I tried to extract all  
4267        the possible information from its different subcomponents. With the PID at hand, it  
4268        is possible to form the selections of the different ND-GAr samples, as I have shown in  
4269        this work. These will help understand how the detector is going to further constrain the  
4270        neutrino interaction uncertainties in DUNE Phase II, which will eventually allow DUNE  
4271        to reach its ultimate physics goals.

4272        The DAQ system of the DUNE FD relies on the online identification of hits on

## CHAPTER 8. CONCLUSION AND OUTLOOK

4273 channels, the so-called TPs, to form decisions data to store. The goal of Chapter 4  
4274 is to motivate a method to enhance the production of TPs in the induction channels  
4275 of the detectors. Forming TPs from all the charge readout planes will improve the  
4276 redundancy of the trigger algorithms. Not only that, but this may be the key to have  
4277 more complex trigger logic that requires directional information. The aspect I focused on  
4278 to improve the hit finding is the filtering of the waveforms. In section 4.3 I use a sample  
4279 of ProtoDUNE-SP cosmic data to show how different low-pass FIR filters affect the S/N  
4280 in the collection and induction planes. Then, I introduce the concept of the matched  
4281 filter in section 4.4. Using the same dataset, I demonstrate that the improvement in the  
4282 S/N of the induction channels achieved with these filters can be significantly higher than  
4283 with the standard filter approach. A series of studies using MC samples are presented in  
4284 section 4.5. These allow to study the dependence of the filtering on the orientation and  
4285 the energy of the tracks. I also use them to assess the impact of this method on the hit  
4286 sensitivity. Finally, in section 4.6 I briefly summarise the results from the VD ColdBox  
4287 runs which featured the matched filter.

4288 With these studies, I showed that the matched filter puts the production of TPs in  
4289 the induction and collection planes on the same level. The natural next step will be to  
4290 understand the impact that this has in the context of the current trigger algorithms.  
4291 Then, explore the development of new trigger routines, like triggers based on coincidence  
4292 across planes. At the same time, these alternative hit finder chains should be implemented  
4293 in the trigger simulations currently under development.

4294 The solar DM analysis is covered in Chapter 5. There I explain how the DUNE  
4295 FD can be used to probe DM interactions by measuring the neutrino flux coming from  
4296 DM annihilations in the core of the Sun. After introducing the topic of DM capture  
4297 and annihilation in a massive object like the Sun, I describe what kind of neutrino  
4298 signals one can expect from such events in section 5.2. Later, I comment on how  
4299 DUNE could constrain the DM parameter space by performing counting experiments.  
4300 In section 5.5 I study the selection efficiency for the  $\tau^+\tau^-$  and  $b\bar{b}$  channels. I focus  
4301 on two different kinematic regimes: the high energy neutrinos where DIS interactions

4302 with argon dominate, and the low energy part of the spectrum where neutrinos mainly  
4303 undergo QEL interactions. This allows me to compute the projected generator-level DM  
4304 cross section sensitivities, showing how DUNE can be complementary to other indirect  
4305 DM searches. Additionally, I explore two specific realisations of the DM interactions,  
4306 namely Kaluza-Klein and leptophilic DM.

4307 At this stage, this analysis already shows the potential of DUNE to explore these  
4308 scenarios. However, including the full simulation and reconstruction of the events will  
4309 be necessary moving forward. At the moment, a significant effort is aimed towards the  
4310 reconstruction of atmospheric neutrinos in the DUNE FD, which could be relevant for  
4311 the case at hand. Also, following iterations of the analysis should include all the relevant  
4312 systematic uncertainties. A summary of these is presented in section 5.7.

4313 Chapter 6 reviews my work on the reconstruction for ND-GAr. In section 6.2 I try  
4314 to establish the relation between the measured charge in the readout and the deposited  
4315 energy from a stopping proton sample, using the residual range of the tracks. This  
4316 calibration allows to compute the mean  $dE/dx$  for the particles. I finish the section  
4317 providing a parametrisation for how this depends on the momentum. The problem of the  
4318 muon and pion separation is the topic of section 6.3. I propose to use the information  
4319 from the ECal to achieve this classification. In this section, I describe the features and  
4320 the procedure I follow to train the classifier, showing its performance as a function of  
4321 the particle momentum. In section 6.4 I explore the possibility of performing a ToF  
4322 measurement with the ECal. With this, I achieve a separation between pions and protons  
4323 in a momentum range beyond the reach of the HPgTPC alone. Section 6.5 is devoted to  
4324 the identification of charged particle decays inside the HPgTPC where the parent plus  
4325 (charged) daughter system is reconstructed as a single track. I use the information from  
4326 the track fit to construct a series of variables which can identify the tracks containing  
4327 decays, as well as locate their position. I finish the Chapter introducing a new clustering  
4328 algorithm for the ECal hits in section 6.6. It aims at having a one-to-one correspondence  
4329 between particles and clusters, which will facilitate the reconstruction of neutral particles  
4330 in the ECal.

## CHAPTER 8. CONCLUSION AND OUTLOOK

4331 The goal of these developments was establishing a robust PID strategy for ND-GAr,  
4332 that allows to reconstruct the multiplicity of pions and other hadrons in the neutrino  
4333 interactions final states. In section 6.7 I describe the status of the integration of the  
4334 different additions to the reconstruction chain.

4335 Finally, in Chapter 7 I apply to the event selection in ND-GAr. I start by describing  
4336 a method for selecting  $\nu_\mu$  CC events in section 7.2. This is mainly based on the muon  
4337 score derived from the muon/pion classification I developed. Additionally, I perform  
4338 an optimisation of the FV. As part of this study, I also examined the kinematics of  
4339 the selected primary muon and the reconstructed interaction vertex. Next, in section  
4340 7.3 I explore the capabilities of ND-GAr and its reconstruction at identifying charged  
4341 pions. I optimise a selection based on the reconstructed charged pion multiplicity, for  
4342 events with 0, 1, 2, and  $\geq 3\pi^\pm$  in the final state. I the performance of the selection as a  
4343 function of the truth hadronic invariant mass, as well as the true pion kinematics for the  
4344  $\nu_\mu$  CC  $1\pi^\pm$  case. I briefly discuss the possibility of tagging events with neutral pions  
4345 by reconstructing the invariant mass of the photon pairs from their decay in section  
4346 7.4. Lastly, in section 7.5 I study the neutrino energy reconstruction of the selected  $\nu_\mu$   
4347 CC events using a calorimetric approach. For this, I compare the values obtained using  
4348 generator-level and reconstructed information.

4349 These studies constitute the first try at an event selection in ND-GAr using full  
4350 simulation and reconstruction. It will serve as a stepping stone for the development  
4351 of other selections and analyses. Ultimately, the goal is to quantify the impact of  
4352 ND-GAr on the LBL analysis in DUNE. For this, including the effect of the systematic  
4353 uncertainties outlined in section 7.6 will be necessary.

4354 In summary, this thesis provides an overview of three novel topics within DUNE. As  
4355 a single sentence, in this work I investigate the enhancement of the triggering capabilities  
4356 of the FD, study the sensitivity of the FD to solar DM signatures, and develop the  
4357 particle identification and event selection strategies for the Phase II ND. Each Chapter  
4358 aims to be a comprehensive summary of the status of the different studies. I hope they  
4359 can be helpful guides for future work both in the ND and FD.

## Bibliography

- 4361 [1] S.L. Glashow, *Partial-symmetries of weak interactions*, *Nuclear Physics* **22** 579.  
 4362 33, 37
- 4363 [2] S. Weinberg, *A model of leptons*, *Physical Review Letters* **19** 1264. 33, 37
- 4364 [3] A. Salam, *Weak and Electromagnetic Interactions*, *Conf. Proc. C* **680519** (1968)  
 4365 367. 33, 37
- 4366 [4] J. Erler and M. Schott, *Electroweak Precision Tests of the Standard Model after*  
 4367 *the Discovery of the Higgs Boson*, *Prog. Part. Nucl. Phys.* **106** (2019) 68  
 4368 [1902.05142]. 33
- 4369 [5] L. Canetti, M. Drewes and M. Shaposhnikov, *Matter and Antimatter in the*  
 4370 *Universe*, *New J. Phys.* **14** (2012) 095012 [1204.4186]. 33
- 4371 [6] G. Bertone, D. Hooper and J. Silk, *Particle dark matter: Evidence, candidates*  
 4372 *and constraints*, *Phys. Rept.* **405** (2005) 279 [[hep-ph/0404175](#)]. 33
- 4373 [7] S.F. King, A. Merle, S. Morisi, Y. Shimizu and M. Tanimoto, *Neutrino Mass and*  
 4374 *Mixing: from Theory to Experiment*, *New J. Phys.* **16** (2014) 045018 [1402.4271].  
 4375 33
- 4376 [8] A.D. Sakharov, *Violation of CP Invariance, C asymmetry, and baryon asymmetry*  
 4377 *of the universe*, *Pisma Zh. Eksp. Teor. Fiz.* **5** (1967) 32. 33
- 4378 [9] M.B. Gavela, P. Hernandez, J. Orloff and O. Pene, *Standard model CP violation*  
 4379 *and baryon asymmetry*, *Mod. Phys. Lett. A* **9** (1994) 795 [[hep-ph/9312215](#)]. 33

## BIBLIOGRAPHY

- 4380 [10] E.K. Akhmedov, V.A. Rubakov and A.Y. Smirnov, *Baryogenesis via neutrino*  
4381 *oscillations*, *Phys. Rev. Lett.* **81** (1998) 1359 [[hep-ph/9803255](#)]. 33
- 4382 [11] B.W. Lee and S. Weinberg, *Cosmological Lower Bound on Heavy Neutrino*  
4383 *Masses*, *Phys. Rev. Lett.* **39** (1977) 165. 34
- 4384 [12] G. Jungman, M. Kamionkowski and K. Griest, *Supersymmetric dark matter*, *Phys.*  
4385 *Rept.* **267** (1996) 195 [[hep-ph/9506380](#)]. 34
- 4386 [13] G. Arcadi, D. Cabo-Almeida, M. Dutra, P. Ghosh, M. Lindner, Y. Mambrini  
4387 et al., *The Waning of the WIMP: Endgame?*, [2403.15860](#). 34
- 4388 [14] DUNE collaboration, *Deep Underground Neutrino Experiment (DUNE), Far*  
4389 *Detector Technical Design Report, Volume I Introduction to DUNE*, *JINST* **15**  
4390 (2020) T08008 [[2002.02967](#)]. 34, 61, 62, 63, 69, 70, 79, 80, 81, 82
- 4391 [15] W. Pauli, *Dear radioactive ladies and gentlemen*, *Phys. Today* **31N9** (1978) 27. 37
- 4392 [16] F. Reines and C.L. Cowan, *Detection of the free neutrino*, *Phys. Rev.* **92** (1953)  
4393 830. 37
- 4394 [17] A. Pich, *The Standard Model of Electroweak Interactions*, in *2010 European*  
4395 *School of High Energy Physics*, pp. 1–50, 1, 2012 [[1201.0537](#)]. 38
- 4396 [18] ALEPH, DELPHI, L3, OPAL, SLD, LEP ELECTROWEAK WORKING GROUP,  
4397 SLD ELECTROWEAK GROUP, SLD HEAVY FLAVOUR GROUP collaboration,  
4398 *Precision electroweak measurements on the Z resonance*, *Phys. Rept.* **427** (2006)  
4399 257 [[hep-ex/0509008](#)]. 41
- 4400 [19] R. Davis, D.S. Harmer and K.C. Hoffman, *Search for neutrinos from the sun*,  
4401 *Physical Review Letters* **20** 1205. 42
- 4402 [20] J.N. Bahcall, A.M. Serenelli and S. Basu, *New solar opacities, abundances,*  
4403 *helioseismology, and neutrino fluxes*, *Astrophys. J. Lett.* **621** (2005) L85  
4404 [[astro-ph/0412440](#)]. 42, 127, 129

## BIBLIOGRAPHY

- 4405 [21] J.N. Bahcall, N.A. Bahcall and G. Shaviv, *Present Status of the Theoretical*  
 4406 *Predictions for the  $^{37}\text{Cl}$  Solar-Neutrino Experiment*, . 42
- 4407 [22] B.T. Cleveland, T. Daily, R. Davis, Jr., J.R. Distel, K. Lande, C.K. Lee et al.,  
 4408 *Measurement of the solar electron neutrino flux with the Homestake chlorine*  
 4409 *detector, Astrophys. J.* **496** (1998) 505. 42
- 4410 [23] SAGE collaboration, *Measurement of the solar neutrino capture rate with gallium*  
 4411 *metal. III: Results for the 2002–2007 data-taking period, Phys. Rev. C* **80** (2009)  
 4412 015807 [0901.2200]. 42, 54
- 4413 [24] F. Kaether, W. Hampel, G. Heusser, J. Kiko and T. Kirsten, *Reanalysis of the*  
 4414 *GALLEX solar neutrino flux and source experiments, Phys. Lett. B* **685** (2010) 47  
 4415 [1001.2731]. 42, 54
- 4416 [25] Q.R. Ahmad, R.C. Allen, T.C. Andersen, J.D. Anglin, G. Bühler, J.C. Barton  
 4417 et al., *Measurement of the Rate of  $\nu_e + d \rightarrow p + p + e^-$  Interactions Produced by*  
 4418  *$^8\text{B}$  Solar Neutrinos at the Sudbury Neutrino Observatory*, . 43
- 4419 [26] Q.R. Ahmad, R.C. Allen, T.C. Andersen, J. D. Anglin, J.C. Barton, E.W. Beier  
 4420 et al., *Direct Evidence for Neutrino Flavor Transformation from Neutral-Current*  
 4421 *Interactions in the Sudbury Neutrino Observatory*, . 43
- 4422 [27] T.K. Gaisser and M. Honda, *Flux of atmospheric neutrinos*, . 43
- 4423 [28] K. Hirata, T. Kajita, M. Koshiba, M. Nakahata, S. Ohara, Y. Oyama et al.,  
 4424 *Experimental study of the atmospheric neutrino flux*, . 44
- 4425 [29] D. Casper, R. Becker-Szendy, C.B. Bratton, D.R. Cady, R. Claus, S.T. Dye et al.,  
 4426 *Measurement of atmospheric neutrino composition with the imb-3 detector*, . 44
- 4427 [30] M. Ambrosio, R. Antolini, C. Aramo, G. Auriemma, A. Baldini, G. C. Barbarino  
 4428 et al., *Measurement of the atmospheric neutrino-induced upgoing muon flux using*  
 4429 *macro*, . 44

## BIBLIOGRAPHY

- 4430 [31] W. Allison, G. Alner, D. Ayres, W. Barrett, C. Bode, P. Border et al.,  
4431 *Measurement of the atmospheric neutrino flavour composition in soudan 2*, . 44
- 4432 [32] SUPER-KAMIOKANDE collaboration, *Evidence for oscillation of atmospheric*  
4433 *neutrinos*, *Phys. Rev. Lett.* **81** (1998) 1562 [[hep-ex/9807003](#)]. 44
- 4434 [33] P. Minkowski,  $\mu \rightarrow e\gamma$  at a Rate of One Out of  $10^9$  Muon Decays?, *Phys. Lett. B*  
4435 **67** (1977) 421. 47
- 4436 [34] M. Gell-Mann, P. Ramond and R. Slansky, *Complex Spinors and Unified Theories*,  
4437 *Conf. Proc. C* **790927** (1979) 315 [[1306.4669](#)]. 47
- 4438 [35] T. Yanagida, *Horizontal gauge symmetry and masses of neutrinos*, *Conf. Proc. C*  
4439 **7902131** (1979) 95. 47
- 4440 [36] R.N. Mohapatra and G. Senjanovic, *Neutrino Mass and Spontaneous Parity*  
4441 *Nonconservation*, *Phys. Rev. Lett.* **44** (1980) 912. 47
- 4442 [37] J. Schechter and J.W.F. Valle, *Neutrino Masses in  $SU(2) \times U(1)$  Theories*, *Phys.*  
4443 *Rev. D* **22** (1980) 2227. 47
- 4444 [38] B. Pontecorvo, *Mesonium and anti-mesonium*, *Sov. Phys. JETP* **6** (1957) 429. 47
- 4445 [39] M. Gell-Mann and A. Pais, *Behavior of neutral particles under charge conjugation*,  
4446 . 47
- 4447 [40] B. Pontecorvo, *Neutrino Experiments and the Problem of Conservation of*  
4448 *Leptonic Charge*, *Zh. Eksp. Teor. Fiz.* **53** (1967) 1717. 48
- 4449 [41] B. Pontecorvo, *Inverse beta processes and nonconservation of lepton charge*, *Zh.*  
4450 *Eksp. Teor. Fiz.* **34** (1957) 247. 49
- 4451 [42] Z. Maki, M. Nakagawa and S. Sakata, *Remarks on the unified model of elementary*  
4452 *particles*, *Prog. Theor. Phys.* **28** (1962) 870. 49
- 4453 [43] PARTICLE DATA GROUP collaboration, *Review of particle physics*, *Phys. Rev. D*  
4454 **110** (2024) 030001. 51

## BIBLIOGRAPHY

- 4455 [44] L. Wolfenstein, *Neutrino Oscillations in Matter*, *Phys. Rev. D* **17** (1978) 2369. 52
- 4456 [45] B.T. Cleveland, T. Daily, R. Davis, Jr., J.R. Distel, K. Lande, C.K. Lee et al.,  
4457 *Measurement of the solar electron neutrino flux with the Homestake chlorine*  
4458 *detector*, *Astrophys. J.* **496** (1998) 505. 54
- 4459 [46] G. Bellini et al., *Precision measurement of the  ${}^7\text{Be}$  solar neutrino interaction rate*  
4460 *in Borexino*, *Phys. Rev. Lett.* **107** (2011) 141302 [[1104.1816](#)]. 54
- 4461 [47] SUPER-KAMIOKANDE collaboration, *Solar neutrino measurements in*  
4462 *super-Kamiokande-I*, *Phys. Rev. D* **73** (2006) 112001 [[hep-ex/0508053](#)]. 54
- 4463 [48] SNO collaboration, *Combined Analysis of all Three Phases of Solar Neutrino*  
4464 *Data from the Sudbury Neutrino Observatory*, *Phys. Rev. C* **88** (2013) 025501  
4465 [[1109.0763](#)]. 54
- 4466 [49] SUPER-KAMIOKANDE collaboration, *Atmospheric neutrino oscillation analysis*  
4467 *with external constraints in Super-Kamiokande I-IV*, *Phys. Rev. D* **97** (2018)  
4468 072001 [[1710.09126](#)]. 54, 157
- 4469 [50] ICECUBE collaboration, *Measurement of Atmospheric Neutrino Oscillations at*  
4470 *6–56 GeV with IceCube DeepCore*, *Phys. Rev. Lett.* **120** (2018) 071801  
4471 [[1707.07081](#)]. 54
- 4472 [51] KAMLAND collaboration, *Reactor On-Off Antineutrino Measurement with*  
4473 *KamLAND*, *Phys. Rev. D* **88** (2013) 033001 [[1303.4667](#)]. 55
- 4474 [52] RENO collaboration, *Measurement of Reactor Antineutrino Oscillation Amplitude*  
4475 *and Frequency at RENO*, *Phys. Rev. Lett.* **121** (2018) 201801 [[1806.00248](#)]. 55
- 4476 [53] DAYA BAY collaboration, *Measurement of the Electron Antineutrino Oscillation*  
4477 *with 1958 Days of Operation at Daya Bay*, *Phys. Rev. Lett.* **121** (2018) 241805  
4478 [[1809.02261](#)]. 55

## BIBLIOGRAPHY

- 4479 [54] K.J. Kelly, P.A.N. Machado, S.J. Parke, Y.F. Perez-Gonzalez and R.Z. Funchal,  
4480 *Neutrino mass ordering in light of recent data*, *Phys. Rev. D* **103** (2021) 013004.  
4481 55
- 4482 [55] P. Dunne, “Latest Neutrino Oscillation Results from T2K.” Jul, 2020. 55
- 4483 [56] MINOS collaboration, *Combined analysis of  $\nu_\mu$  disappearance and  $\nu_\mu \rightarrow \nu_e$*   
4484 *appearance in MINOS using accelerator and atmospheric neutrinos*, *Phys. Rev.*  
4485 *Lett.* **112** (2014) 191801 [[1403.0867](#)]. 55
- 4486 [57] OPERA collaboration, *Final Results of the OPERA Experiment on  $\nu_\tau$*   
4487 *Appearance in the CNGS Neutrino Beam*, *Phys. Rev. Lett.* **120** (2018) 211801  
4488 [[1804.04912](#)]. 55
- 4489 [58] K2K collaboration, *Measurement of Neutrino Oscillation by the K2K Experiment*,  
4490 *Phys. Rev. D* **74** (2006) 072003 [[hep-ex/0606032](#)]. 55
- 4491 [59] DUNE collaboration, *Long-baseline neutrino oscillation physics potential of the*  
4492 *DUNE experiment*, *Eur. Phys. J. C* **80** (2020) 978 [[2006.16043](#)]. 55, 238
- 4493 [60] HYPER-KAMIOKANDE collaboration, *Physics potential of Hyper-Kamiokande for*  
4494 *neutrino oscillation measurements*, *PoS NuFact2019* (2019) 040. 55
- 4495 [61] P.F. de Salas, D.V. Forero, S. Gariazzo, P. Martínez-Miravé, O. Mena,  
4496 C.A. Ternes et al., *2020 global reassessment of the neutrino oscillation picture*,  
4497 *JHEP* **02** (2021) 071 [[2006.11237](#)]. 55, 63
- 4498 [62] SUPERNEMO collaboration, *Probing New Physics Models of Neutrinoless Double*  
4499 *Beta Decay with SuperNEMO*, *Eur. Phys. J. C* **70** (2010) 927 [[1005.1241](#)]. 56
- 4500 [63] SNO+ collaboration, *Current Status and Future Prospects of the SNO+*  
4501 *Experiment*, *Adv. High Energy Phys.* **2016** (2016) 6194250 [[1508.05759](#)]. 56
- 4502 [64] NEXT collaboration, *Sensitivity of a tonne-scale NEXT detector for neutrinoless*  
4503 *double beta decay searches*, *JHEP* **2021** (2021) 164 [[2005.06467](#)]. 56

## BIBLIOGRAPHY

- 4504 [65] P. Coloma and P. Huber, *Impact of nuclear effects on the extraction of neutrino  
4505 oscillation parameters*, *Phys. Rev. Lett.* **111** (2013) 221802 [[1307.1243](#)]. 57
- 4506 [66] P. Coloma, P. Huber, C.-M. Jen and C. Mariani, *Neutrino-nucleus interaction  
4507 models and their impact on oscillation analyses*, *Phys. Rev. D* **89** (2014) 073015  
4508 [[1311.4506](#)]. 57
- 4509 [67] U. Mosel, *Neutrino Interactions with Nucleons and Nuclei: Importance for  
4510 Long-Baseline Experiments*, *Ann. Rev. Nucl. Part. Sci.* **66** (2016) 171  
4511 [[1602.00696](#)]. 57
- 4512 [68] J.A. Formaggio and G.P. Zeller, *From ev to eev: Neutrino cross sections across  
4513 energy scales*, *Rev. Mod. Phys.* **84** (2012) 1307 [[1305.7513](#)]. 58
- 4514 [69] L. Bathe-Peters, S. Gardiner and R. Guenette, *Comparing generator predictions  
4515 of transverse kinematic imbalance in neutrino-argon scattering*, [2201.04664](#). 59
- 4516 [70] R.A. Smith and E.J. Moniz, *Neutrino reactions on nuclear targets*, *Nucl. Phys. B*  
4517 **43** (1972) 605. 59
- 4518 [71] H. Nakamura and R. Seki, *Quasi-elastic neutrino-nucleus scattering and spectral  
4519 function*, *Nuclear Physics B - Proceedings Supplements* **112** 197. 59
- 4520 [72] V. Pandey, N. Jachowicz, T. Van Cuyck, J. Ryckebusch and M. Martini,  
4521 *Low-energy excitations and quasielastic contribution to electron-nucleus and  
4522 neutrino-nucleus scattering in the continuum random-phase approximation*, *Phys.  
4523 Rev. C* **92** (2015) 024606 [[1412.4624](#)]. 59
- 4524 [73] A. Nikolakopoulos, R. González-Jiménez, N. Jachowicz, K. Niewczas, F. Sánchez  
4525 and J.M. Udías, *Benchmarking intranuclear cascade models for neutrino  
4526 scattering with relativistic optical potentials*, *Phys. Rev. C* **105** (2022) 054603  
4527 [[2202.01689](#)]. 59

## BIBLIOGRAPHY

- 4528 [74] MINIBoONE collaboration, *First Measurement of the Muon Neutrino Charged*  
4529 *Current Quasielastic Double Differential Cross Section*, *Phys. Rev. D* **81** (2010)  
4530 092005 [1002.2680]. 60
- 4531 [75] MINERvA collaboration, *Measurements of the Inclusive Neutrino and*  
4532 *Antineutrino Charged Current Cross Sections in MINERvA Using the Low- $\nu$  Flux*  
4533 *Method*, *Phys. Rev. D* **94** (2016) 112007 [1610.04746]. 60
- 4534 [76] MICROBoONE collaboration, *First Measurement of Energy-Dependent Inclusive*  
4535 *Muon Neutrino Charged-Current Cross Sections on Argon with the MicroBooNE*  
4536 *Detector*, *Phys. Rev. Lett.* **128** (2022) 151801 [2110.14023]. 60
- 4537 [77] SBND collaboration, *Neutrino cross-section measurement prospects with SBND*,  
4538 *PoS NuFact2017* (2018) 067. 60
- 4539 [78] NOvA collaboration, *Measurement of the double-differential muon-neutrino*  
4540 *charged-current inclusive cross section in the NOvA near detector*, *Phys. Rev. D*  
4541 **107** (2023) 052011 [2109.12220]. 60
- 4542 [79] T2K collaboration, *Measurement of the  $\nu_\mu$  charged-current cross sections on*  
4543 *water, hydrocarbon, iron, and their ratios with the T2K on-axis detectors*, *PTEP*  
4544 **2019** (2019) 093C02 [1904.09611]. 60
- 4545 [80] \$\\\$PRISM collaboration,  *$\nu$ PRISM: A new way of probing neutrino*  
4546 *interactions*, *PoS NUFAC2014* (2015) 046. 60
- 4547 [81] C. Hasnip, *DUNE-PRISM – A New Method to Measure Neutrino Oscillations*,  
4548 Ph.D. thesis, Oxford U., 2023. 60, 71
- 4549 [82] DUNE collaboration, *Snowmass Neutrino Frontier: DUNE Physics Summary*,  
4550 2203.06100. 63, 64
- 4551 [83] DUNE collaboration, *Deep Underground Neutrino Experiment (DUNE), Far*  
4552 *Detector Technical Design Report, Volume II: DUNE Physics*, 2002.03005. 63, 65,  
4553 67, 73, 133, 142, 146, 271

## BIBLIOGRAPHY

- 4554 [84] SUPER-KAMIOKANDE collaboration, *Search for Proton Decay via  $p \rightarrow e^+ \pi_0$  and*
- 4555  $p \rightarrow \mu^+ \pi_0$  in a Large Water Cherenkov Detector, *Phys. Rev. Lett.* **102** (2009)
- 4556 141801 [0903.0676]. 64
- 4557 [85] S. Raby, *Grand Unified Theories*, in *2nd World Summit: Physics Beyond the*
- 4558 *Standard Model*, 8, 2006 [[hep-ph/0608183](#)]. 64
- 4559 [86] KAMIOKANDE-II collaboration, *Observation of a Neutrino Burst from the*
- 4560 *Supernova SN 1987a*, *Phys. Rev. Lett.* **58** (1987) 1490. 65
- 4561 [87] R.M. Bionta et al., *Observation of a Neutrino Burst in Coincidence with*
- 4562 *Supernova SN 1987a in the Large Magellanic Cloud*, *Phys. Rev. Lett.* **58** (1987)
- 4563 1494. 65
- 4564 [88] J. Strait, E. McCluskey, T. Lundin, J. Willhite, T. Hamernik, V. Papadimitriou
- 4565 et al., *Long-baseline neutrino facility (lbnf) and deep underground neutrino*
- 4566 *experiment (dune) conceptual design report volume 3: Long-baseline neutrino*
- 4567 *facility for dune june 24, 2015*, 1601.05823. 65, 66
- 4568 [89] DUNE collaboration, *Deep Underground Neutrino Experiment (DUNE) Near*
- 4569 *Detector Conceptual Design Report, Instruments* **5** (2021) 31 [[2103.13910](#)]. 68,
- 4570 72, 73, 74, 75, 275, 278
- 4571 [90] J. Asaadi et al., *A New Concept for Kilotonne Scale Liquid Argon Time*
- 4572 *Projection Chambers, Instruments* **4** (2020) 6 [[1908.10956](#)]. 69
- 4573 [91] DUNE collaboration, *DUNE Phase II: Scientific Opportunities, Detector*
- 4574 *Concepts, Technological Solutions*, 2408.12725. 71, 74, 76
- 4575 [92] DUNE collaboration, *A Gaseous Argon-Based Near Detector to Enhance the*
- 4576 *Physics Capabilities of DUNE*, 2203.06281. 73
- 4577 [93] ALICE collaboration, *Alice: Physics performance report, volume ii*, . 74, 276

## BIBLIOGRAPHY

- 4578 [94] F. Sauli, *Gem: A new concept for electron amplification in gas detectors*, *Nuclear*  
4579 *Instruments and Methods in Physics Research Section A: Accelerators,*  
4580 *Spectrometers, Detectors and Associated Equipment* **386** 531. 74, 78
- 4581 [95] DUNE collaboration, *SPY: a conceptual design study of a magnet system for a*  
4582 *high-pressure gaseous TPC neutrino detector*, *JINST* **19** (2024) P06018  
4583 [2311.16063]. 76
- 4584 [96] A. Ritchie-Yates et al., *First operation of an ALICE OROC operated in high*  
4585 *pressure Ar-CO<sub>2</sub> and Ar-CH<sub>4</sub>*, *Eur. Phys. J. C* **83** (2023) 1139 [2305.08822]. 77
- 4586 [97] ALICE TPC collaboration, *The upgrade of the ALICE TPC with GEMs and*  
4587 *continuous readout*, *JINST* **16** (2021) P03022 [2012.09518]. 77
- 4588 [98] F. Sauli, *The gas electron multiplier (gem): Operating principles and applications*,  
4589 *Nuclear Instruments and Methods in Physics Research Section A: Accelerators,*  
4590 *Spectrometers, Detectors and Associated Equipment* **805** 2. 78
- 4591 [99] C. Lippmann, *A continuous read-out tpc for the alice upgrade*, *Nuclear*  
4592 *Instruments and Methods in Physics Research Section A: Accelerators,*  
4593 *Spectrometers, Detectors and Associated Equipment* **824** 543. 78
- 4594 [100] C. Calabria, *Large-size triple gem detectors for the cms forward muon upgrade*,  
4595 *Nuclear and Particle Physics Proceedings* **273–275** 1042. 78
- 4596 [101] DUNE collaboration, *The DUNE Far Detector Vertical Drift Technology*,  
4597 *Technical Design Report*, 2312.03130. 83, 84
- 4598 [102] DUNE collaboration, *Deep Underground Neutrino Experiment (DUNE), Far*  
4599 *Detector Technical Design Report, Volume IV: Far Detector Single-phase*  
4600 *Technology*, *JINST* **15** (2020) T08010 [2002.03010]. 85
- 4601 [103] DUNE DAQ Project, “Trigger and Data AcQuisition (TDAQ) System Design.”  
4602 EDMS-2826454, 2022. 87

## BIBLIOGRAPHY

- 4603 [104] DUNE DAQ, “dtp-firmware.”  
4604 <https://gitlab.cern.ch/dune-daq/readout/dtp-firmware>, 2020. 88
- 4605 [105] J. McClellan and T. Parks, *A personal history of the Parks-McClellan algorithm*,  
4606 *IEEE Signal Processing Magazine* **22** (2005) 82. 91
- 4607 [106] L. Weinberg and P. Slepian, *Takahasi’s results on tchebycheff and butterworth*  
4608 *ladder networks*, *IRE Transactions on Circuit Theory* **7** (1960) 88. 91
- 4609 [107] G. Turin, *An introduction to matched filters*, *IEEE Transactions on Information*  
4610 *Theory* **6** (1960) 311. 95
- 4611 [108] J.W. Goodman, *Statistical Optics*, Wiley (1985). 96
- 4612 [109] B. Dwork, *Detection of a pulse superimposed on fluctuation noise*, *Proceedings of*  
4613 *the IRE* **38** (1950) 771. 97
- 4614 [110] L. Wainstein and V. Zubakov, *Extraction of Signals from Noise*, Prentice-Hall  
4615 (1962). 98
- 4616 [111] E.D. Church, *Larsoft: A software package for liquid argon time projection drift*  
4617 *chambers*, [1311.6774](https://cds.cern.ch/record/1311.6774). 101
- 4618 [112] S.V. Stehman, *Selecting and interpreting measures of thematic classification*  
4619 *accuracy*, *Remote Sensing of Environment* **62** (1997) 77. 114
- 4620 [113] A.A. Taha and A. Hanbury, *Metrics for evaluating 3d medical image*  
4621 *segmentation: analysis, selection, and tool*, *BMC Medical Imaging* **15** (2015) . 115
- 4622 [114] J. Silk, K.A. Olive and M. Srednicki, *The Photino, the Sun and High-Energy*  
4623 *Neutrinos*, *Phys. Rev. Lett.* **55** (1985) 257. 123
- 4624 [115] M. Srednicki, K.A. Olive and J. Silk, *High-Energy Neutrinos from the Sun and*  
4625 *Cold Dark Matter*, *Nucl. Phys. B* **279** (1987) 804. 123
- 4626 [116] J.S. Hagelin, K.W. Ng and K.A. Olive, *A High-energy Neutrino Signature From*  
4627 *Supersymmetric Relics*, *Phys. Lett. B* **180** (1986) 375. 123

## BIBLIOGRAPHY

- 4628 [117] T.K. Gaisser, G. Steigman and S. Tilav, *Limits on Cold Dark Matter Candidates*  
4629 *from Deep Underground Detectors*, *Phys. Rev. D* **34** (1986) 2206. 123
- 4630 [118] N. Bernal, J. Martín-Albo and S. Palomares-Ruiz, *A novel way of constraining*  
4631 *WIMPs annihilations in the Sun: MeV neutrinos*, *JCAP* **08** (2013) 011  
4632 [1208.0834]. 123, 124, 125, 127, 131
- 4633 [119] C. Rott, J. Siegal-Gaskins and J.F. Beacom, *New Sensitivity to Solar WIMP*  
4634 *Annihilation using Low-Energy Neutrinos*, *Phys. Rev. D* **88** (2013) 055005  
4635 [1208.0827]. 123, 130
- 4636 [120] C. Rott, S. In, J. Kumar and D. Yaylali, *Dark Matter Searches for Monoenergetic*  
4637 *Neutrinos Arising from Stopped Meson Decay in the Sun*, *JCAP* **11** (2015) 039  
4638 [1510.00170]. 123
- 4639 [121] DUNE collaboration, *Searching for solar KDAR with DUNE*, *JCAP* **10** (2021)  
4640 065 [2107.09109]. 123, 272, 273, 274, 275
- 4641 [122] G. Busoni, A. De Simone and W.-C. Huang, *On the Minimum Dark Matter Mass*  
4642 *Testable by Neutrinos from the Sun*, *JCAP* **07** (2013) 010 [1305.1817]. 124
- 4643 [123] J.N. Bahcall and M.H. Pinsonneault, *Solar models with helium and heavy element*  
4644 *diffusion*, *Rev. Mod. Phys.* **67** (1995) 781 [hep-ph/9505425]. 124
- 4645 [124] R. Garani and S. Palomares-Ruiz, *Dark matter in the Sun: scattering off electrons*  
4646 *vs nucleons*, *JCAP* **05** (2017) 007 [1702.02768]. 125, 126, 128, 129, 130, 153
- 4647 [125] V.A. Bednyakov and F. Simkovic, *Nuclear spin structure in dark matter search:*  
4648 *The Zero momentum transfer limit*, *Phys. Part. Nucl.* **36** (2005) 131  
4649 [hep-ph/0406218]. 125
- 4650 [126] R. Catena and B. Schwabe, *Form factors for dark matter capture by the Sun in*  
4651 *effective theories*, *JCAP* **04** (2015) 042 [1501.03729]. 125

## BIBLIOGRAPHY

- 4652 [127] A. Gould, *WIMP Distribution in and Evaporation From the Sun*, *Astrophys. J.* **321** (1987) 560. 125, 126
- 4654 [128] A. Gould, *Resonant Enhancements in WIMP Capture by the Earth*, *Astrophys. J.* **321** (1987) 571. 127
- 4656 [129] T. Bringmann, J. Edsjö, P. Gondolo, P. Ullio and L. Bergström, *DarkSUSY 6 : An Advanced Tool to Compute Dark Matter Properties Numerically*, *JCAP* **07** (2018) 033 [[1802.03399](#)]. 128
- 4659 [130] J.N. Bahcall, M.H. Pinsonneault and S. Basu, *Solar models: Current epoch and time dependences, neutrinos, and helioseismological properties*, *Astrophys. J.* **555** (2001) 990 [[astro-ph/0010346](#)]. 128
- 4662 [131] T. Golan, J.T. Sobczyk and J. Zmuda, *NuWro: the Wroclaw Monte Carlo Generator of Neutrino Interactions*, *Nucl. Phys. B Proc. Suppl.* **229-232** (2012) 499. 132
- 4665 [132] M. Honda, M. Sajjad Athar, T. Kajita, K. Kasahara and S. Midorikawa, *Atmospheric neutrino flux calculation using the NRLMSISE-00 atmospheric model*, *Phys. Rev. D* **92** (2015) 023004 [[1502.03916](#)]. 133, 134
- 4668 [133] G. Cowan, K. Cranmer, E. Gross and O. Vitells, *Asymptotic formulae for likelihood-based tests of new physics*, *Eur. Phys. J. C* **71** (2011) 1554 [[1007.1727](#)]. 133
- 4671 [134] T. Kaluza, *Zum Unitätsproblem der Physik, Sitzungsber. Preuss. Akad. Wiss. Berlin (Math. Phys.)* **1921** (1921) 966 [[1803.08616](#)]. 135
- 4673 [135] O. Klein, *Quantum Theory and Five-Dimensional Theory of Relativity. (In German and English)*, *Z. Phys.* **37** (1926) 895. 135
- 4675 [136] T. Appelquist, H.-C. Cheng and B.A. Dobrescu, *Bounds on universal extra dimensions*, *Phys. Rev. D* **64** (2001) 035002 [[hep-ph/0012100](#)]. 135

## BIBLIOGRAPHY

- 4677 [137] N. Arkani-Hamed, S. Dimopoulos and G.R. Dvali, *The Hierarchy problem and new*  
4678 *dimensions at a millimeter*, *Phys. Lett. B* **429** (1998) 263 [[hep-ph/9803315](#)]. 135
- 4679 [138] L. Randall and R. Sundrum, *A Large mass hierarchy from a small extra*  
4680 *dimension*, *Phys. Rev. Lett.* **83** (1999) 3370 [[hep-ph/9905221](#)]. 135
- 4681 [139] G. Servant and T.M.P. Tait, *Is the lightest Kaluza-Klein particle a viable dark*  
4682 *matter candidate?*, *Nucl. Phys. B* **650** (2003) 391 [[hep-ph/0206071](#)]. 135
- 4683 [140] H.-C. Cheng, K.T. Matchev and M. Schmaltz, *Radiative corrections to*  
4684 *Kaluza-Klein masses*, *Phys. Rev. D* **66** (2002) 036005 [[hep-ph/0204342](#)]. 135, 137
- 4685 [141] M. Blennow, J. Edsjö and T. Ohlsson, *Neutrinos from WIMP annihilations using*  
4686 *a full three-flavor Monte Carlo*, *JCAP* **01** (2008) 021 [[0709.3898](#)]. 137, 140
- 4687 [142] J. Edsjö, J. Elevant and C. Niblaeus, *WimpSim Neutrino Monte Carlo*. 137, 140
- 4688 [143] M. Colom i Bernadich and C. Pérez de los Heros, *Limits on Kaluza-Klein dark*  
4689 *matter annihilation in the Sun from recent IceCube results*, *Eur. Phys. J. C*, **80** 2  
4690 (*2020*) **129** **80** (2019) [[1912.04585](#)]. 138
- 4691 [144] ANTARES collaboration, *Search for Dark Matter in the Sun with the ANTARES*  
4692 *Neutrino Telescope in the CMSSM and mUED frameworks*, *Nucl. Instrum. Meth.*  
4693 *A* **725** (2013) 76 [[1204.5290](#)]. 138
- 4694 [145] N. Deutschmann, T. Flacke and J.S. Kim, *Current LHC Constraints on Minimal*  
4695 *Universal Extra Dimensions*, *Phys. Lett. B* **771** (2017) 515 [[1702.00410](#)]. 138, 139
- 4696 [146] U. Haisch and A. Weiler, *Bound on minimal universal extra dimensions from*  
4697 *anti-B → X(s)gamma*, *Phys. Rev. D* **76** (2007) 034014 [[hep-ph/0703064](#)]. 139
- 4698 [147] A. Freitas and U. Haisch, *Anti-B → X(s) gamma in two universal extra*  
4699 *dimensions*, *Phys. Rev. D* **77** (2008) 093008 [[0801.4346](#)]. 139

## BIBLIOGRAPHY

- 4700 [148] C. Rott, D. Jeong, J. Kumar and D. Yaylali, *Neutrino Topology Reconstruction at*  
 4701 *DUNE and Applications to Searches for Dark Matter Annihilation in the Sun*,  
 4702 *JCAP* **07** (2019) 006 [[1903.04175](#)]. 142
- 4703 [149] F. Pedregosa, G. Varoquaux, A. Gramfort, V. Michel, B. Thirion, O. Grisel et al.,  
 4704 *Scikit-learn: Machine learning in Python*, *Journal of Machine Learning Research*  
 4705 **12** (2011) 2825. 148
- 4706 [150] ICECUBE collaboration, *Search for GeV-scale dark matter annihilation in the Sun*  
 4707 *with IceCube DeepCore*, *Phys. Rev. D* **105** (2022) 062004 [[2111.09970](#)]. 150
- 4708 [151] C.-S. Chen, F.-F. Lee, G.-L. Lin and Y.-H. Lin, *Probing Dark Matter*  
 4709 *Self-Interaction in the Sun with IceCube-PINGU*, *JCAP* **10** (2014) 049  
 4710 [[1408.5471](#)]. 150
- 4711 [152] N.F. Bell, M.J. Dolan and S. Robles, *Searching for dark matter in the Sun using*  
 4712 *Hyper-Kamiokande*, *JCAP* **11** (2021) 004 [[2107.04216](#)]. 150
- 4713 [153] E. Behnke et al., *Final Results of the PICASSO Dark Matter Search Experiment*,  
 4714 *Astropart. Phys.* **90** (2017) 85 [[1611.01499](#)]. 150
- 4715 [154] PICO collaboration, *Dark Matter Search Results from the Complete Exposure of*  
 4716 *the PICO-60 C<sub>3</sub>F<sub>8</sub> Bubble Chamber*, *Phys. Rev. D* **100** (2019) 022001  
 4717 [[1902.04031](#)]. 150
- 4718 [155] J. Kopp, V. Niro, T. Schwetz and J. Zupan, *DAMA/LIBRA and leptonically*  
 4719 *interacting Dark Matter*, *Phys. Rev. D* **80** (2009) 083502 [[0907.3159](#)]. 152
- 4720 [156] PARTICLE DATA GROUP collaboration, *Review of Particle Physics*, *PTEP* **2020**  
 4721 (2020) 083C01. 153
- 4722 [157] M. Beltran, D. Hooper, E.W. Kolb and Z.C. Krusberg, *Deducing the nature of*  
 4723 *dark matter from direct and indirect detection experiments in the absence of*  
 4724 *collider signatures of new physics*, *Phys. Rev. D* **80** (2009) 043509 [[0808.3384](#)].  
 4725 153

## BIBLIOGRAPHY

- 4726 [158] PLANCK collaboration, *Planck 2018 results. VI. Cosmological parameters, Astron.*  
4727 *Astrophys.* **641** (2020) A6 [[1807.06209](#)]. 154
- 4728 [159] XENON collaboration, *Light Dark Matter Search with Ionization Signals in*  
4729 *XENON1T, Phys. Rev. Lett.* **123** (2019) 251801 [[1907.11485](#)]. 154, 155
- 4730 [160] DARKSIDE collaboration, *Search for Dark Matter Particle Interactions with*  
4731 *Electron Final States with DarkSide-50, Phys. Rev. Lett.* **130** (2023) 101002  
4732 [[2207.11968](#)]. 154, 155
- 4733 [161] PANDAX-II collaboration, *Search for Light Dark Matter-Electron Scatterings in*  
4734 *the PandaX-II Experiment, Phys. Rev. Lett.* **126** (2021) 211803 [[2101.07479](#)].  
4735 154, 155
- 4736 [162] C. Principato, *An Indirect Search for Weakly Interacting Massive Particles in the*  
4737 *Sun Using Upward-going Muons in NOvA*, Ph.D. thesis, Virginia U., 2021.  
4738 [10.18130/x5z2-1466](#). 156, 157
- 4739 [163] G. Wikström and J. Edsjö, *Limits on the wimp-nucleon scattering cross-section*  
4740 *from neutrino telescopes*, [0903.2986](#). 156
- 4741 [164] SUPER-KAMIOKANDE collaboration, *Search for neutrinos from annihilation of*  
4742 *captured low-mass dark matter particles in the Sun by Super-Kamiokande, Phys.*  
4743 *Rev. Lett.* **114** (2015) 141301 [[1503.04858](#)]. 156, 157
- 4744 [165] C. Rott, T. Tanaka and Y. Itow, *Enhanced sensitivity to dark matter*  
4745 *self-annihilations in the sun using neutrino spectral information*, [1107.3182](#). 156
- 4746 [166] M.M. Boliev, S.V. Demidov, S.P. Mikheyev and O.V. Suvorova, *Search for muon*  
4747 *signal from dark matter annihilations in the Sun with the Baksan Underground*  
4748 *Scintillator Telescope for 24.12 years, JCAP* **09** (2013) 019 [[1301.1138](#)]. 156, 157,  
4749 158

## BIBLIOGRAPHY

- 4750 [167] M. Honda, T. Kajita, K. Kasahara, S. Midorikawa and T. Sanuki, *Calculation of  
4751 atmospheric neutrino flux using the interaction model calibrated with atmospheric  
4752 muon data*, *Phys. Rev. D* **75** (2007) 043006 [[astro-ph/0611418](#)]. 158
- 4753 [168] C. Green, J. Kowalkowski, M. Paterno, M. Fischler, L. Garren and Q. Lu, *The  
4754 Art Framework*, *J. Phys. Conf. Ser.* **396** (2012) 022020. 159
- 4755 [169] H. Bethe, *Zur theorie des durchgangs schneller korpuskularstrahlen durch materie,  
4756 Annalen der Physik* **397** (1930) 325. 165
- 4757 [170] E. Fermi, *The ionization loss of energy in gases and in condensed materials,  
4758 Physical Review* **57** (1940) 485. 165
- 4759 [171] R. Sternheimer, M. Berger and S. Seltzer, *Density effect for the ionization loss of  
4760 charged particles in various substances*, *Atomic Data and Nuclear Data Tables* **30**  
4761 (1984) 261. 165
- 4762 [172] W.W.M. Allison and J.H. Cobb, *Relativistic Charged Particle Identification by  
4763 Energy Loss*, *Ann. Rev. Nucl. Part. Sci.* **30** (1980) 253. 165
- 4764 [173] W. Blum, L. Rolandi and W. Riegler, *Particle detection with drift chambers,  
4765 Particle Acceleration and Detection* (2008), 10.1007/978-3-540-76684-1. 166
- 4766 [174] ALICE TPC collaboration, *Particle identification of the ALICE TPC via dE/dx,  
4767 Nucl. Instrum. Meth. A* **706** (2013) 55. 166
- 4768 [175] L. Landau, *On the energy loss of fast particles by ionization*, *J. Phys. (USSR)* **8**  
4769 (1944) 201. 169
- 4770 [176] W. Ulmer and E. Matsinos, *Theoretical methods for the calculation of Bragg  
4771 curves and 3D distributions of proton beams*, *The European Physical Journal  
4772 Special Topics* **190** (2010) 1. 170
- 4773 [177] E. Aprile, A.E. Bolotnikov, A.L. Bolozdynya and T. Doke, *Noble Gas Detectors,  
4774 Wiley* (Oct., 2008), 10.1002/9783527610020. 172

## BIBLIOGRAPHY

- 4775 [178] D.S. Wilks, *Statistical Methods in the Atmospheric Sciences*, Academic Press. 210
- 4776 [179] ALICE collaboration, *Production of pions, kaons and protons in pp collisions at*  
4777  $\sqrt{s} = 900 \text{ gev with alice at the lhc}$ , 1101.4110. 214
- 4778 [180] U. Einhaus, *Charged hadron identification with de/dx and time-of-flight at future*  
4779 *higgs factories*, 2110.15115. 214
- 4780 [181] R. Frühwirth, *Application of filter methods to the reconstruction of tracks and*  
4781 *vertices in events of experimental high energy physics*, Ph.D. thesis, Technischen  
4782 Universität Wien, 1988. 220
- 4783 [182] P. Astier, A. Cardini, R.D. Cousins, A. Letessier-Selvon, B.A. Popov and  
4784 T. Vinogradova, *Kalman filter track fits and track breakpoint analysis*, Nuclear  
4785 *Instruments and Methods in Physics Research Section A: Accelerators,*  
4786 *Spectrometers, Detectors and Associated Equipment* **450** (2000) 138. 220
- 4787 [183] T2K UK collaboration, *The Electromagnetic Calorimeter for the T2K Near*  
4788 *Detector ND280*, JINST **8** (2013) P10019 [1308.3445]. 228
- 4789 [184] J.E. Gaiser, *Charmonium Spectroscopy From Radiative Decays of the J/ψ and ψ'*,  
4790 Ph.D. thesis, Stanford University, 1982. 233
- 4791 [185] GENIE collaboration, *Neutrino-nucleon cross-section model tuning in GENIE v3*,  
4792 *Phys. Rev. D* **104** (2021) 072009 [2104.09179]. 237
- 4793 [186] J. Nieves, J.E. Amaro and M. Valverde, *Inclusive quasi-elastic neutrino reactions*,  
4794 *Phys. Rev. C* **70** (2004) 055503 [nucl-th/0408005]. 237
- 4795 [187] J. Nieves, I. Ruiz Simo and M.J. Vicente Vacas, *Inclusive Charged-Current*  
4796 *Neutrino-Nucleus Reactions*, *Phys. Rev. C* **83** (2011) 045501 [1102.2777]. 237,  
4797 274
- 4798 [188] C. Berger and L.M. Sehgal, *Lepton mass effects in single pion production by*  
4799 *neutrinos*, *Phys. Rev. D* **76** (2007) 113004 [0709.4378]. 238, 274

## BIBLIOGRAPHY

- 4800 [189] C. Berger and L.M. Sehgal, *PCAC and coherent pion production by low energy*  
 4801 *neutrinos*, *Phys. Rev. D* **79** (2009) 053003 [[0812.2653](#)]. 238
- 4802 [190] A. Bodek and U.K. Yang, *Modeling deep inelastic cross-sections in the few GeV*  
 4803 *region*, *Nucl. Phys. B Proc. Suppl.* **112** (2002) 70 [[hep-ex/0203009](#)]. 238, 275
- 4804 [191] T. Golan, L. Aliaga and M. Kordosky, *Minerva's flux prediction*, in *Proceedings of*  
 4805 *the 10th International Workshop on Neutrino-Nucleus Interactions in Few-GeV*  
 4806 *Region (NuInt15)*, Journal of the Physical Society of Japan, DOI. 271
- 4807 [192] A. Bashyal, H. Schellman and L. Fields, *Ppfx implementation in deep underground*  
 4808 *neutrino experiment*, . 272
- 4809 [193] A. Bodek and J.L. Ritchie, *Fermi Motion Effects in Deep Inelastic Lepton*  
 4810 *Scattering from Nuclear Targets*, *Phys. Rev. D* **23** (1981) 1070. 272
- 4811 [194] C. Wilkinson et al., *Testing charged current quasi-elastic and multinucleon*  
 4812 *interaction models in the NEUT neutrino interaction generator with published*  
 4813 *datasets from the MiniBooNE and MINERνA experiments*, *Phys. Rev. D* **93**  
 4814 (2016) 072010 [[1601.05592](#)]. 272
- 4815 [195] T2K collaboration, *Search for CP Violation in Neutrino and Antineutrino*  
 4816 *Oscillations by the T2K Experiment with  $2.2 \times 10^{21}$  Protons on Target*, *Phys. Rev.*  
 4817 *Lett.* **121** (2018) 171802 [[1807.07891](#)]. 274
- 4818 [196] MINERνA collaboration, *Identification of nuclear effects in neutrino-carbon*  
 4819 *interactions at low three-momentum transfer*, *Phys. Rev. Lett.* **116** (2016) 071802  
 4820 [[1511.05944](#)]. 274
- 4821 [197] C. Colle, O. Hen, W. Cosyn, I. Korover, E. Piasetzky, J. Ryckebusch et al.,  
 4822 *Extracting the mass dependence and quantum numbers of short-range correlated*  
 4823 *pairs from  $a(e, e' p)$  and  $a(e, e' pp)$  scattering*, *Phys. Rev. C* **92** (2015) 024604. 274
- 4824 [198] D. Rein and L.M. Sehgal, *Neutrino Excitation of Baryon Resonances and Single*  
 4825 *Pion Production*, *Annals Phys.* **133** (1981) 79. 274

## BIBLIOGRAPHY

- 4826 [199] M. Sanchez, "NOvA Results and Prospects." June, 2018. 275
- 4827 [200] D.H. Stork, *First operation of the tpc facility at peplbl, ucla, uc riverside , johns*  
4828 *hopkins , tokyo, yale (pep4 collaboration)*, . 276
- 4829 [201] H. Aihara, M. Alston-Garnjost, D.H. Badtke, J.A. Bakken, A. Barbaro-Galtieri,  
4830 A.V. Barnes et al., *Spatial resolution of the pep-4 time projection chamber*, . 276
- 4831 [202] I. Lehraus, *Progress in particle identification by ionization sampling, Nucl.*  
4832 *Instrum. Meth.* **217** (1983) 43. 277